

---

# The history of stellar mass in the most massive galaxies at $z < 3.5$

Carl Joseph Mundy



UNITED KINGDOM • CHINA • MALAYSIA

Thesis submitted to The University of Nottingham  
for the degree of Doctor of Philosophy, September 2016

---

*“Astronomy is useful because it raises us above ourselves; it is useful because it is grand. It shows us how small is mans body, how great his mind, since his intelligence can embrace the whole of this dazzling immensity, where his body is only an obscure point, and enjoy its silent harmony.”*

– **Jules Henri Poincaré**

**Supervisor:** Prof. Christopher J. Conselice

**Examiners:** Dr Simon Dye

Dr Kevin Pimblet

**Submitted:** 30<sup>th</sup> September 2016

**Examined:** 19<sup>th</sup> December 2016

**Resubmitted:** 20<sup>th</sup> February 2017

# Contents

<b>Abstract</b>	<b>5</b>
<b>Published Work</b>	<b>7</b>
<b>List of Figures</b>	<b>9</b>
<b>List of Tables</b>	<b>12</b>
<b>Acknowledgements</b>	<b>13</b>
<b>1 Introduction</b>	<b>15</b>
1.1 The galaxy zoo . . . . .	15
1.2 The many pathways to galaxy growth . . . . .	17
1.3 Cosmic collisions . . . . .	21
1.4 Dark side of the Universe . . . . .	23
1.5 The oldest light . . . . .	24
1.6 Simulating the Universe . . . . .	25
1.7 Remaining questions . . . . .	27
1.8 Outline of thesis structure . . . . .	29
<b>2 Tracing Massive Galaxies in Cosmological Simulations</b>	<b>31</b>
2.1 Introduction . . . . .	31
2.2 Data Description . . . . .	34
2.2.1 Simulated Data . . . . .	35
2.2.2 Selection Method Metrics . . . . .	36
2.2.3 Velocity Dispersion Selection . . . . .	38
2.3 Stellar mass selections . . . . .	39
2.3.1 Descendants . . . . .	39
2.3.2 Progenitors . . . . .	44
2.3.3 Fitting forms . . . . .	44
2.4 Inferred velocity dispersion selections . . . . .	49
2.4.1 Descendants . . . . .	50
2.4.2 Progenitors . . . . .	50

2.5	Discussion . . . . .	53
2.5.1	Where are the progenitors of $z = 0$ massive galaxies at high redshift? . . . . .	56
2.5.2	How do mergers affect the selections? . . . . .	57
2.5.3	Can we infer velocity dispersion in a semi-analytical model? . . . . .	60
2.5.4	Comparison with previous works . . . . .	61
2.6	Summary . . . . .	61
<b>3</b>	<b>Measuring galaxy merger histories</b>	<b>64</b>
3.1	A short history of measuring merger histories . . . . .	64
3.2	Counting close-pairs with <b>Pyrus</b> . . . . .	67
3.2.1	Initial close-pair selection . . . . .	67
3.2.2	The pair probability function . . . . .	67
3.2.3	Close-pair constraints . . . . .	68
3.2.4	Selection effect corrections . . . . .	69
3.2.5	The close-pair fraction . . . . .	71
<b>4</b>	<b>The major merger histories of massive galaxies</b>	<b>73</b>
4.1	Introduction . . . . .	73
4.2	Data . . . . .	76
4.2.1	UKIDSS Ultra Deep Survey (UDS) . . . . .	76
4.2.2	UltraVISTA . . . . .	77
4.2.3	VIDEO . . . . .	77
4.2.4	GAMA . . . . .	78
4.2.5	Simulated Data . . . . .	79
4.3	Data Products . . . . .	79
4.3.1	Photometric redshifts . . . . .	79
4.3.1.1	Photometric redshift confidence intervals . . . . .	81
4.3.1.2	Best-fit solutions . . . . .	82
4.3.2	Stellar mass estimates . . . . .	83
4.4	The major merger fraction at $z < 3.5$ . . . . .	89
4.4.1	Constant stellar mass selected samples . . . . .	89
4.4.1.1	Massive galaxies ( $\mathcal{M}_* > 10^{11} \text{M}_\odot$ ) . . . . .	89
4.4.1.2	Intermediate mass galaxies ( $\mathcal{M}_* > 10^{10} \text{M}_\odot$ ) . . . . .	95
4.4.2	Constant number density selected samples . . . . .	96
4.4.3	Comparison between spectroscopically and photometrically determined merger fractions . . . . .	99
4.5	The major merger rate at $z < 3.5$ . . . . .	101



4.5.1	Calculating the merger rate from the pair fraction . . . . .	101
4.5.2	Number of major merger events at $z < 3.5$ . . . . .	106
4.5.3	Major merger rates at a constant cumulative number density	109
4.6	Discussion . . . . .	110
4.6.1	Comparison with semi-analytic models and hydrodynamical simulations . . . . .	111
4.6.2	Field-to-field variation . . . . .	112
4.6.3	Tests on the merger fraction . . . . .	113
4.6.3.1	Galaxy stellar mass function choice . . . . .	114
4.7	Conclusions . . . . .	115
<b>5</b>	<b>The total merger histories of massive galaxies at <math>z &lt; 3.5</math></b>	<b>117</b>
5.1	Introduction . . . . .	117
5.2	Data overview . . . . .	119
5.3	Pair fractions measurements . . . . .	120
5.3.1	Total merger pair fraction . . . . .	120
5.3.2	The minor merger pair fraction . . . . .	125
5.4	Total Merger rate estimations . . . . .	128
5.4.1	Massive galaxies ( $> 10^{11} M_{\odot}$ ) . . . . .	128
5.4.2	Intermediate mass galaxies ( $> 10^{10} M_{\odot}$ ) . . . . .	131
5.4.3	Galaxies at a constant number density . . . . .	133
5.5	Discussion . . . . .	135
5.5.1	Number of merger events at $z < 3.5$ . . . . .	136
5.6	Conclusions . . . . .	137
<b>6</b>	<b>The build-up of stellar mass in massive galaxies at <math>z &lt; 3.5</math></b>	<b>139</b>
6.1	Introduction . . . . .	139
6.2	Stellar mass added by mergers . . . . .	140
6.2.1	Major merger stellar mass accretion rate density . . . . .	141
6.2.2	Minor merger stellar mass accretion rate density . . . . .	143
6.2.3	Comparison to hydrodynamical simulations . . . . .	146
6.3	Stellar mass added by star-formation . . . . .	148
6.4	Comparing star-formation to major and minor mergers in the build up of stellar mass . . . . .	152
6.5	Role of mergers in size evolution . . . . .	153
6.6	Conclusions . . . . .	157

<b>7</b>	<b>Conclusions</b>	<b>159</b>
7.1	Future work . . . . .	160
<b>A</b>	<b>VIDEO completeness simulations</b>	<b>163</b>
<b>B</b>	<b>Supplementary minor merger pair fraction estimations</b>	<b>165</b>
<b>C</b>	<b>Additional SFR density estimates</b>	<b>171</b>
	<b>Bibliography</b>	<b>173</b>

# Abstract

Observations have shown that galaxies have undergone intense transformations over the past 11 Gyr, increasing both their size and stellar mass in the process. Uncovering and understanding the mechanisms behind such changes remains one of the aims of modern astronomy. This Thesis presents an investigation into two mechanisms — star-formation and galaxy mergers — which may be responsible for these observed changes. This is achieved through the analyses of several publicly available semi-analytic models of galaxy formation and evolution, combined with a large sample of approximately 350,000 galaxies at  $0.005 < z < 3.5$ .

Firstly, a comprehensive study is detailed comparing two methods which aim to connect galaxies across cosmic time, to ascertain the best method of tracing the true evolution of a galaxy population's most fundamental properties across large redshift ranges. This is done using a suite of semi-analytic models and selecting galaxies at either a constant stellar mass, or a constant cumulative number density ranked by stellar mass. It is found that the latter selection is better at tracing the true evolution in stellar mass and star-formation rate of a galaxy population, both forwards and backwards in time, compared to the former method. The method allows these properties to be recovered within a factor of 2–3 across a redshift range of  $0 < z < 3$ , with the systematic offset proportional to the redshift range probed. This contrasts with a constant stellar mass selection — used throughout the literature — which often overestimates these physical properties by up to a factor of  $\sim 20$ , depending on the mass range probed.

Secondly, this Thesis introduces a method allowing for the measurement of the close-pair fraction for galaxies selected by stellar mass from a flux-limited survey. Previous measurements of the merger fraction suffered from small volumes or uncertain statistical corrections for projected close-pairs of galaxies. The method presented herein, adapted from that presented in López-Sanjuan *et al.* (2015), uses the full redshift probability distribution to measure the pair fraction of galaxies at  $> 10^{10} M_{\odot}$ , and at a constant cumulative number density of  $10^{-4} \text{ Mpc}^{-3}$ , representing the best constraints on the pair fraction at  $z < 3.5$  to date. Major and minor

merger pair fractions approximately a factor of  $\sim 2$  smaller than previous works are found and subsequently converted to merger *rates*. The major merger rate is found to be similar for galaxies at  $> 10^{11} M_{\odot}$  and  $> 10^{10} M_{\odot}$ , while the minor merger rate is larger for the most massive galaxies by a factor of  $\sim 2$ .

Finally, the relative role of galaxy mergers and star-formation in the build up of stellar mass is explored. Using star-formation rate estimates, a statistical estimation of the star-formation rate density and the merger accretion rate density of stellar mass-selected samples are compared and contrasted. From this analysis, it is found that star-formation remained the dominant source of stellar mass growth in massive galaxies until  $z \sim 0.5$ , with major merger becoming comparable in more recent times and minor mergers a factor of  $\sim 10$  smaller even today. Furthermore, simple virial arguments are used to show that major and minor mergers are likely not the dominant mechanism in the size evolution of massive galaxies at  $z < 3.5$ , increasing their sizes by a factor of  $\sim 1.6$  at most.

In summary, the results presented in this Thesis explore the stellar mass, star-formation and size evolution of massive galaxies over the past 11 Gyr, and shed new light on the mechanisms responsible. By taking advantage of the latest wide-area, deep surveys, the largest sample of galaxies is used to constrain the merger histories of massive galaxies and infer their role in the evolution of massive galaxies in a consistent manner.

# Published Work

The vast majority of the work presented in this Thesis has been presented in the following publications:

- I **Mundy, C. J.**; Conselice, C. J.; Ownsworth, J. R., “*Tracing galaxy populations through cosmic time: a critical test of methods for connecting the same galaxies between different redshifts at  $z < 3$* ”, Monthly Notices of the Royal Astronomical Society (2015), Volume 450, Issue 4, p.3696-3707.
- II **Mundy, C. J.**; Conselice, C. J.; Duncan, K. J.; Almaini, O.; Häußler, B.; Hartley, W., “*The major merger histories of the most massive galaxies at  $z < 3.5$* ”, submitted to MNRAS.

Additionally, the overwhelming majority of the work presented in this Thesis is the sole work of the author. The methodology for the galaxy merger analysis presented in Chapter 3 has been created, programmed and implemented in an equal collaborative effort with Dr Kenneth J. Duncan. Furthermore, associated work and work that was the genesis for several projects described in this Thesis are presented in the following publications:

- III Ownsworth, J. R.; Conselice, C. J.; Mortlock, A.; Hartley, W. G.; Almaini, O.; Duncan, K. J.; **Mundy, C. J.**, “*Minor versus major mergers: the stellar mass growth of massive galaxies from  $z = 3$  using number density selection techniques*”, Monthly Notices of the Royal Astronomical Society (2014), Volume 445, Issue 3, p.2198-2213.
- IV Ownsworth, J. R.; Conselice, C. J.; **Mundy, C. J.**; Mortlock, A.; Hartley, W. G.; Duncan, K. J.; Almaini, O., “*The evolution of galaxies at constant number density: a less biased view of star formation, quenching, and structural formation*”, Monthly Notices of the Royal Astronomical Society (2016), Volume 461, Issue 1, p.1112-1129.

V Duncan, K.; Conselice, C. J.; **Mundy, C. J.**; Lu, Y.; Guo, Y.; Ferguson, H. C. and the CANDELS collaboration, “*Towards a complete history of galaxy assembly: Major merger rates at  $2 \leq z \leq 6$  in the CANDELS fields*”, in preparation.

Paper I is a collaboration between the author (85%), Christopher Conselice (10%) and Jamie Ownsworth (5%). The contents of this publication are presented in Chapter 2. Paper II was the result of work by the author (70%), Kenneth Duncan (15%), Christopher Conselice (10%) and Omar Almaini, William Hartley and Boris Häußler (5%). The results of this study are presented in Chapter 4. The author made a contribution to Paper III in the form of simple recovery fraction calculations within semi-analytic models. This contribution was the genesis for the study presented in Chapter 2. A similar contribution was made by the author to Paper IV in addition to performing calculations of stellar mass and rest-frame UVJ measurements. Paper V uses the methodology presented in Chapter 3 to calculate merger fractions. This was an equal contribution collaboration between the author and Dr Kenneth J. Duncan.

# List of Figures

1.1	Hubble tuning fork diagram . . . . .	16
1.2	Cosmic star-formation rate density at $z < 8$ . . . . .	19
1.3	A compilation of the merger fraction, $f_m(z)$ , evolution for galaxies with stellar masses $> 10^{10} M_\odot$ . . . . .	22
1.4	Cosmic Microwave Background (CMB) . . . . .	24
1.5	Redshift evolution in the Illustris simulation . . . . .	28
2.1	Descendant recovery metrics at constant stellar mass . . . . .	40
2.2	Descendant recovery metrics at constant number density in stellar mass . . . . .	41
2.3	Progenitor recovery metrics at constant stellar mass . . . . .	45
2.4	Progenitor recovery metrics at constant number density in stellar mass	46
2.5	Descendant recovery metrics at constant velocity dispersion . . . . .	51
2.6	Descendant recovery metrics at constant number density in velocity dispersion . . . . .	52
2.7	Progenitor recovery metrics at constant velocity dispersion . . . . .	54
2.8	Progenitor recovery metrics at constant number density in velocity dispersion . . . . .	55
2.9	Progenitor mass distributions in the Guo <i>et al.</i> (2013) SAM . . . . .	58
4.1	$K_s$ -band magnitude priors used in photometric redshift calculations	81
4.2	Comparison between photometric and spectroscopic redshifts in the UKIDSS UDS, VIDEO, COSMOS and GAMA regions . . . . .	84
4.3	Stellar mass distributions as a function of redshift in the UKIDSS UDS, VIDEO, COSMOS and GAMA regions . . . . .	85
4.6	Major merger pair fractions for galaxies at $> 10^{11} M_\odot$ . . . . .	91
4.7	Major merger pair fractions for galaxies at $> 10^{10} M_\odot$ . . . . .	95
4.8	Stellar mass limits for a constant cumulative number density of $1 \times$ $10^{-4} \text{ Mpc}^{-3}$ . . . . .	97

4.9	Stellar mass limits for a constant cumulative number density of $5 \times 10^{-4} \text{ Mpc}^{-3}$ . . . . .	98
4.10	Volume-averaged, $\Gamma_{\text{merg}}(z)$ , and fractional, $\mathcal{R}_{\text{merg}}(z)$ , merger rates for galaxies at $> 10^{11} \text{ M}_{\odot}$ and 5–30 kpc. . . . .	107
4.11	Volume-averaged, $\Gamma_{\text{merg}}(z)$ , and fractional, $\mathcal{R}_{\text{merg}}(z)$ , merger rates for galaxies at $> 10^{10} \text{ M}_{\odot}$ and 5–30 kpc. . . . .	108
4.12	Volume-averaged, $\Gamma_{\text{merg}}(z)$ , and fractional, $\mathcal{R}_{\text{merg}}(z)$ , merger rates for galaxies at $n = 1 \times 10^{-4} \text{ Mpc}^{-3}$ and 5–30 kpc. . . . .	109
5.1	Evolution of total (minor + major) merger pair fractions . . . . .	122
5.2	Evolution of total, major and minor merger pair fractions . . . . .	126
5.3	Minor merger rates for galaxies at $> 10^{11} \text{ M}_{\odot}$ . . . . .	129
5.4	Total merger rates for galaxies at $> 10^{10} \text{ M}_{\odot}$ . . . . .	132
5.5	Minor merger rates for galaxies at $n(> \mathcal{M}_*) = 1 \times 10^{-4} \text{ Mpc}^{-3}$ . . .	134
6.1	Major merger accretion rate density, $\rho_{1/4}$ , for constant stellar mass and constant number density samples . . . . .	142
6.2	Minor merger accretion rate density, $\rho_{1/10}$ , for constant stellar mass and constant number density samples . . . . .	146
6.3	Star-formation rate distributions as a function of stellar mass and redshift . . . . .	149
6.4	Estimated star-formation rate densities, $\rho_{\Psi}$ , for constant stellar mass and constant number density samples . . . . .	151
6.5	The ratio of star-formation rate density to major and minor merger accretion rate density . . . . .	154
6.6	Size evolution of massive galaxies due to major and minor mergers at $z < 3.5$ . . . . .	156
A.1	VIDEO completeness simulation example image and completeness curve . . . . .	164
B.1	Total, major and minor merger pair fractions for galaxies with $\mathcal{M}_* > 10^{11} \text{ M}_{\odot}$ . . . . .	168
B.2	Total, major and minor merger pair fractions for galaxies with $\mathcal{M}_* > 10^{10} \text{ M}_{\odot}$ . . . . .	169
B.3	Total, major and minor merger pair fractions for galaxies selected at $n = 1 \times 10^{-4} \text{ Mpc}^{-3}$ . . . . .	170



C.1	Estimations of the major merger accretion rate density and star-formation rate density using SFR estimates of Laigle <i>et al.</i> (2016)	172
-----	---	-----

# List of Tables

2.1	Progenitor and descendant constant stellar mass limits in the various SAMs . . . . .	43
2.2	Recovery metric fitting parameters for descendants and progenitors selected at a constant cumulative number density . . . . .	48
2.3	Inferred velocity dispersion limits . . . . .	53
4.1	Photometric redshift quality metrics for the UDS, VIDEO, COSMOS and GAMA regions . . . . .	83
4.2	Major merger ( $\mu > 1/4$ ) pair fractions . . . . .	90
4.3	Major merger ( $\mu > 1/4$ ) pair fraction fitting parameters . . . . .	94
4.4	Major merger ( $\mu > 1/4$ ) pair fractions for constant cumulative number density selections . . . . .	100
4.5	Volume-averaged merger rate, $\Gamma_{\text{merg}}(z)$ , fitting parameters . . . . .	104
4.6	Fractional merger rate, $\mathcal{R}_{\text{merg}}(z)$ , fitting parameters . . . . .	105
5.1	Total merger ( $\mu > 1/10$ ) pair fractions . . . . .	121
5.2	Total merger ( $\mu > 1/10$ ) pair fraction fitting parameters . . . . .	123
5.3	Minor merger ( $1/10 < \mu < 1/4$ ) pair fraction fitting parameters . . . . .	127
5.4	Total merger ( $\mu > 1/10$ ) rates fitting parameters . . . . .	133
5.5	Estimates of the number of merger events, $N_{\text{merg}}$ , at $z < 3.5$ . . . . .	136
6.2	Star-formation rate density, $\rho_{\Psi}(z)$ , fitting parameters . . . . .	152
6.3	Fitting parameters for the ratio of star-formation rate density to merger accretion rate density . . . . .	153

# Acknowledgements

Firstly, I owe an immense debt of gratitude to my supervisor, Chris Conselice, for his help, advice and guidance over these past four years. This document would have been unrecognisable without him. I am also indebted to the army of postgraduate students and post-docs that have graced our group meetings over the years whom have had an undeniable impact on the work presented in this Thesis. Special thanks must go to Will Hartley, Alice Mortlock, Jamie Ownsworth and Kenneth Duncan for their library of code, bottomless knowledge and timely advice which greatly accelerated the process of my research and immeasurably improved its quality. Hard times were made less so by their and others' kindness and friendship. I was also lucky enough to experience lunchtime ramblings and religiously regular trips to the pub with Sophie Morris, Caterina Lani, Lyndsay Old and others which repeatedly resulted in uncontrollable fits of laughter. I can honestly say I will cherish these times forever.

From my cosy corner of the office I have had the pleasure of chatting with amazing people over the years. Kate Rowlands, Nathan Bourne, Julian Onions and Evelyn Johnston made me feel incredibly welcome when I first arrived. Two traitors — James Nightingale and Ross Hart — came and went (I'm kidding of course). Most recently, Berta Margalef, James Stevenson, Kshitija Kelkar, Lizzie Cooke, Rach Bhatawdekar and Rachel Asquith have made every single day that little bit easier (and filled with a lot more laughter). I sincerely wish everyone all the best of luck in the future.

I can honestly say this particular journey has not been an easy one for me. However, I want to thank Omar Almaini and Simon Dye in particular for their advice and kind words, as well as always sounding genuinely interested in my answer when they asked how things were going. To Frazer Pearce I say thank you for your *honesty* during my talks which always led to significant changes in the direction of my work for the better. Thank you also to Meghan Gray whose candid Journal Club talks helped me reduce the pressure I piled upon my shoulders — power poses really do work! Of course a massive thanks is directed at Phil Parry for always

sorting out IT problems and going the extra mile to ensure I could undertake my research. It must be said that Jules and Mel have been instrumental during my eight years at The University of Nottingham. I have enjoyed our conversations and the privilege of working on the open days, and, of course, I cannot thank you both enough for lending me an umbrella on the numerous occasions when I wore shorts in the torrential rain.

From the final year of my undergraduate degree until the third year of my PhD I was incredibly lucky to be part of The Science Show. I have the absolute pleasure to call some incredible people friends because of this — I'm talking about you: Emma Bradshaw, Dave Farmer, Grace Lowe, George O'Neill, David Brander, Ben Henderson, Rosie Shanahan, Joe Archer, Daniel Payne, Alex Summerfield, Jenna Flye and Carl Alexander. A special mention must also be extended to Paul Munday who supported every ridiculous idea we came up with. I can say without any doubt that producing and presenting this show with you all was the most rewarding and enjoyable thing I have ever done. I cannot explain how proud I am of the ~60 hours of radio we created together. Thank you all for the memories, most of which are recorded for future generations to laugh at on demand.

I have to say thank you to my parents who, while not always understanding my research, always pretended to and supported me throughout my studies. Finally, and most importantly, I want to thank Charlotte Marshall. The very fact this text exists at all rests on the pillar of your unwavering support and encouragement over the past two years. When I first met you eight years ago I would not have imagined in my wildest dreams that we would be together and now, finishing our PhDs, beginning a new chapter of our lives together. You are my very best friend.

*This thesis is dedicated to Julie and Debra.*

# Chapter 1

## Introduction

Astronomy is arguably the most beautiful of the sciences, in both a visual and theoretical sense. Spectacular images of the cosmos produced by the veteran Hubble Space Telescope (HST) are some of the most obvious and ingrained mascots for the field, with future observatories promising a revolution in both science and outreach. Modern astronomy, which has existed in its recognisable form for just a century, has uncovered remarkable truths about the Universe and the physical laws that define it.

Over millennia it has come to be known that our place in the Universe is quite unremarkable. Where once our home planet was naively placed at the centre of everything, the scientific method applied to observations of the heavens uncovered the heliocentric nature of our existence. Subsequent observations with larger telescopes and better techniques have revealed the Solar System to be one of many that exist within the Milky Way, with our home galaxy but one oasis in a vast cosmic desert sparkling with similar but no less magnificent collections of gas, dust and stars.

### 1.1 The galaxy zoo

Observations made by Edwin Hubble are arguably the foundation of modern extragalactic astronomy. His realisation (Hubble, 1926) that so-called spiral nebulae were in fact separate, independent galaxies found beyond the bounds of the Milky Way immeasurably expanded the limits of the known Universe. Hubble subsequently constructed a classification scheme for galaxies, placing them within distinct classes based on their physical appearance (i.e. morphology). This scheme, displayed in Figure 1.1 and often called the ‘Hubble Tuning Fork Diagram’, remains in use to this day. However, its construction implied an evolutionary sequence along which galaxies travelled during the course of their lives. Labels such as ‘early-type’, ap-

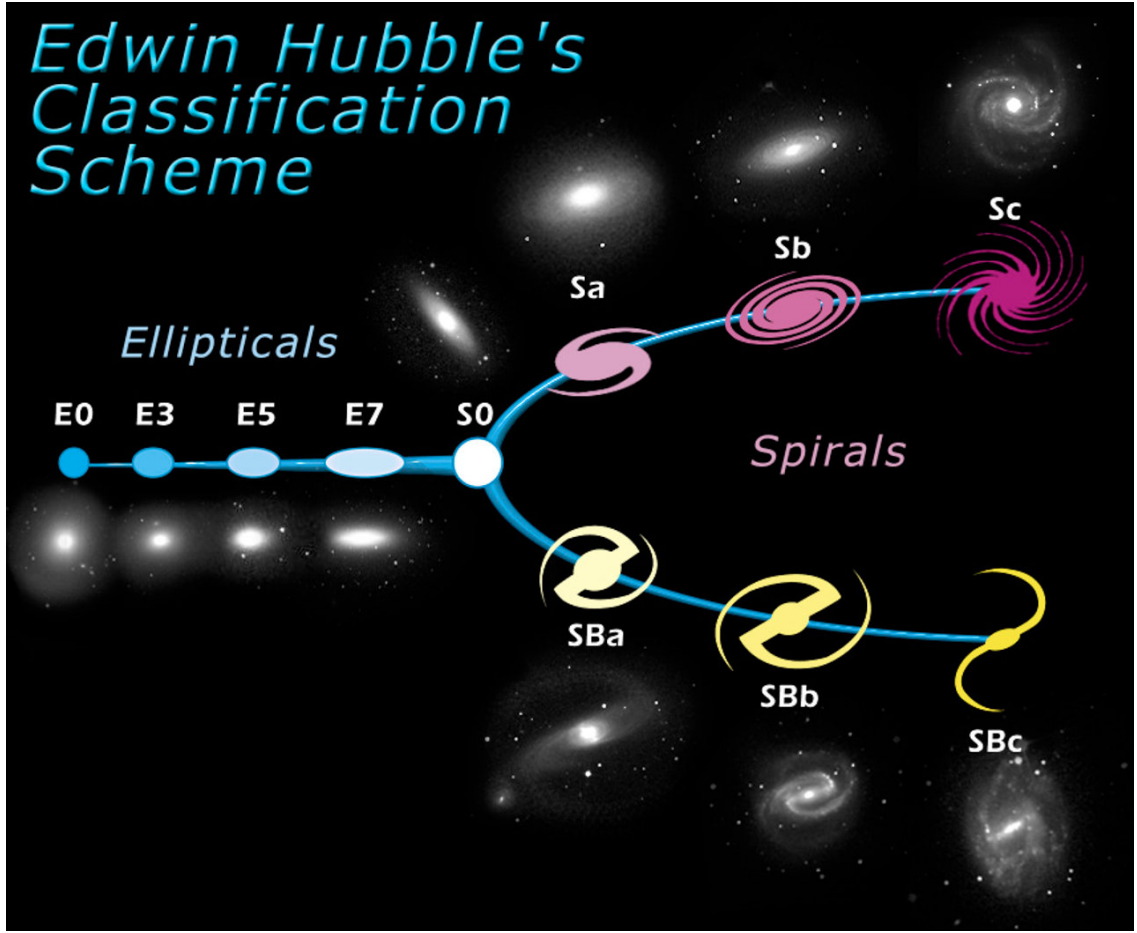


**Figure 1.1:** The Hubble Tuning Fork Diagram, using a selection of galaxies observed with the Hubble Space Telescope, describing the zoo of galaxies observed by Edwin Hubble. (Credit: NASA/ESA.)

plied to the ellipticals, and ‘late-type’, applied to the spiral galaxies, gave this impression. Such an evolutionary journey is now known to be almost certainly incorrect, however the exact evolutionary path taken by galaxies still remains a largely unanswered question in modern astronomy.

Furthermore, striking correlations between various galaxy properties (e.g., colour, size, luminosity) and galaxy morphology — among other characteristics — have been revealed (e.g., Faber & Jackson, 1976; Tully & Fisher, 1977) which permit deductions on galaxy evolution to be made. For example, early-type galaxies are found to almost exclusively possess relatively ‘red’ colours compared to late-type galaxies. Indeed, a bimodality in the colour distribution of galaxies is well documented and has been studied extensively for nearly two decades (e.g., Kauffmann *et al.*, 2003; Taylor *et al.*, 2015).

Understanding just how this bimodality came to be, and identifying the physical mechanisms that control the evolutionary journeys of different galaxy types is just one particular aim of modern astronomy. Probing the stellar populations and

kinematics of different types of galaxies allows constraints to be placed on their formation histories, and thus brings the field a step closer to understanding their evolution.

## 1.2 The many pathways to galaxy growth

The Universe can be best described via a model with four components: normal baryonic matter, dark matter, dark energy and radiation. In this  $\Lambda$ CDM paradigm, galaxies — a collection of gas, dust and stars — sit at the centre of a dark matter halo’s gravitational potential well. In this hierarchical picture, galaxies accrue baryonic matter through the repeated mergers of small systems which form larger ones over time. This is indeed the sole source of dark matter halo growth in the Universe. On the other hand, the stellar mass of a galaxy — the baryonic mass in the form of stars — can grow through a number of different pathways and is a relatively easy quantity to measure observationally.

As the light from any galaxy we observe is the integrated light of its amassed stellar populations, a galaxy’s colour is useful for placing constraints on its evolutionary history. More massive, younger stars are short-lived but extremely luminous, and only a relatively small amount of these stars are required to cause a galaxy to possess ‘blue’ colours (Ellis, Abraham & Dickinson, 2001). Blue colours are therefore a strong indicator of ongoing star-formation. The bulk of the stellar mass, however, is typically contained in older, redder, and less massive stars which are many times more numerous. Thus, it is near-IR wavelengths that better trace the integrated stellar mass of a galaxy due to the fact that evolved stars exhibit little change in their colour with age.

Measuring the stellar mass of a galaxy is in reality more complicated than a simple conversion of near-IR luminosity. The most widely used technique is to use the colours of a galaxy (if photometric measurements are available), or indeed the spectral energy distribution (SED; if spectroscopic measurements have been made), for the process of template fitting. Typically, a large set of template SEDs of a given unit stellar mass are generated by stellar population synthesis models (e.g., Bruzual & Charlot, 2003; Maraston, 2005) that encompass a range of stellar population parameters (e.g., star-formation history, age, dust attenuation, and IMF) are fit to the available photometry for a galaxy. An estimate of the stellar mass is then simply given by the normalisation needed to match the galaxy photometry. While some parameters that can be estimated this way are degenerate (e.g., age, dust attenuation, and metallicity), the stellar mass and indeed the star-formation rate

are generally well constrained given good photometric coverage of spectral features, such as the Balmer and 4000Å breaks, which are correlated with age (Conroy, 2013).

While the rest-frame near-IR photometry is theoretically a better tracer of the integrated stellar mass of a galaxy, some evidence suggests that including rest-frame near-IR photometry in SED-fitting techniques does not improve estimates of a galaxy’s stellar mass. Taylor *et al.* (2011) find that agreement of stellar population parameters is found between model sets when using just the UV to optical photometry of a galaxy. They suggest that stellar population synthesis models are not well constrained in the near-IR wavelength regime at this time. However, the stellar mass estimates for galaxies with ‘normal’ SEDs are most likely accurate to within a factor of  $< 2$  (Conroy, 2013).

With their caveats understood, SED fitting techniques can also provide valuable estimates of a galaxy’s star-formation rate (SFR) — the amount of stellar mass generated from a galaxy’s cold gas reservoir per unit time. In order to achieve this an assumption is typically made on the form of a galaxy’s star-formation history (SFH). The most commonly used parametrisation is that of an exponentially declining (or increasing) SFH, defined as

$$\Psi(t) = \Psi_0 \times \exp\left(-\frac{t}{\tau}\right), \quad (1.1)$$

where  $\Psi$  is the SFR,  $\Psi_0$  is the initial star-formation rate of the galaxy, and  $\tau$  is the exponential scale time over which the SFR declines (or increases). For the purposes of SED modelling, the observed SFR is that when  $t$  is set to the age of the model SED. Other common parametrisations include a constant SFH ( $\tau \rightarrow \infty$ ), and multiple bursts at different ages. There are even recent suggestions that galaxies may follow a log-normal SFH (Abramson *et al.*, 2015), although this is not a particularly common assumption. While resulting SFR values are sensitive to the priors placed on the stellar population parameters, and indeed the SFH, comparisons between SED-based and emission line SFRs result in excellent agreement, at least at low-redshift (e.g., Salim *et al.*, 2007).

Much progress has been made in the development of methods to infer the SFR of a galaxy. The Ultraviolet (UV) and Infrared (IR) wavelength regimes possess useful indicators of star-formation that can be analysed. The UV traces light from young, massive stars that dominate the luminosity output of a stellar population, while the IR traces (mostly) UV light absorbed by dust that is re-radiated at mid-IR to far-IR wavelengths. As the vast majority of UV emission is attributed to the process of star-formation, a galaxy’s IR luminosity can be said to be directly proportional to



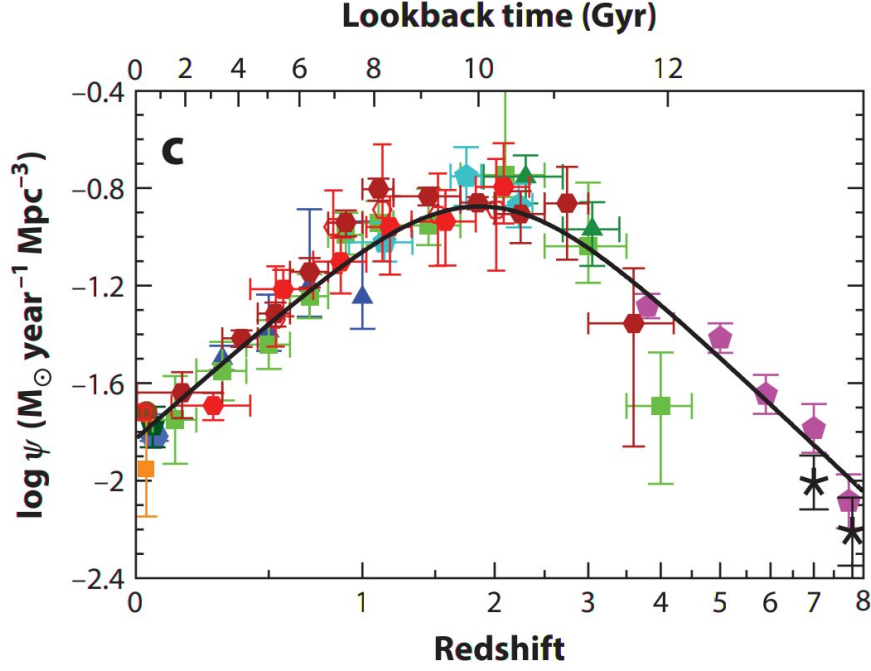


**Figure 1.2:** Compilation of the FUV+IR cosmic (volume-averaged) star-formation rate density at  $z < 8$ . The peak of cosmic star-formation occurred at  $z \sim 2$ , when the Universe was approximately  $\sim 3$  Gyr old. (Figure from Madau & Dickinson 2014.)

the absorbed star-formation light (neglecting complexities from AGN, for example). While in this sense dust within a galaxy is a useful tool, it also complicates matters by attenuating the observed UV emission.

Figure 1.2 illustrates a representative sample of cosmologically averaged star-formation rate density measurements from the literature compiled by Madau & Dickinson (2014). This quantity,  $\rho_\Psi$  (given as  $\Psi$  in the figure), encodes the typical rate of star-formation per unit time and volume in the Universe. A wealth of observations in the UV (e.g., Robotham & Driver, 2011; Bouwens *et al.*, 2012) and IR (e.g., Magnelli *et al.*, 2013) paint a consistent picture of the cosmic SFH. At  $3 < z < 8$   $\rho_*$  steadily increases  $\propto (1+z)^{-2.9}$ , peaking when the Universe was  $\sim 3$  Gyr old at  $z \approx 2$ . This peak is then followed at lower redshift by a steady decline to present day, with  $\rho_* \propto (1+z)^{2.7}$ . While the exact redshift of peak  $\rho_*$  depends on the assumptions used (e.g., Behroozi *et al.*, 2013), the general evolution in the star-formation rate density is remarkably well constrained over the last  $\sim 13$  Gyr.

Many of the most fundamental astronomical observables involve counting objects in the night sky. The evolution in the number of objects over time can place useful constraints on the evolution of galaxies. The galaxy stellar mass function (GSMF) is the embodiment of this method, and quantifies the number density of galaxies

as a function of their stellar mass. Much effort has been expended to explore how the number density of galaxies has changed over large swathes of time. Indeed, only within the last decade has assembling large samples of galaxies in the high redshift Universe been possible, due in part to the Hubble Space Telescope and deep, square degree-sized near-IR surveys of the cosmos. The ability to estimate stellar masses and photometric redshifts was vital to permitting this revolution in observational astronomy. Investigating the GSMF of different galaxy populations allows the physical processes which govern stellar mass growth as well as the types of galaxies affected by these physical processes to be understood.

Most notably it is found that the massive end ( $> 10^{11} M_{\odot}$ ) of the GSMF is dominated almost exclusively by red and dead galaxies, while lower masses are dominated by blue, star-forming systems. Studies have shown that the number density of massive galaxies has increased with time, such that the most massive galaxies have at most doubled their stellar mass since  $z \sim 4$ , and that lower stellar mass ( $\sim 10^{10.5} M_{\odot}$ ) galaxies have increased their stellar mass by approximately an order of magnitude (Bell *et al.*, 2003; Marchesini *et al.*, 2009; Mortlock *et al.*, 2011; Muzzin *et al.*, 2013a; Duncan *et al.*, 2014). The observed constantness in the number density of the most massive galaxies is evidence towards the idea of ‘downsizing’, where the most massive galaxies form their stellar mass before lower mass systems (e.g., Cowie *et al.*, 1996).

Dissecting galaxies into ‘quiescent’ and ‘star-forming’ through some selection in rest-frame  $UVJ$  colour-colour space (e.g., Labbé *et al.* 2005; Williams *et al.* 2009), for example, or Sérsic index, has revealed disparate evolutionary pathways for galaxies in these populations (e.g., Muzzin *et al.*, 2013a; Mortlock *et al.*, 2015). Increasing number density growth towards lower stellar masses indicate that quiescent galaxies undergo stellar mass growth that is mass dependent, and that low-mass systems are quenching relatively rapidly. One suggestion for this mass dependence in the quiescent population is different methods of quenching the star-formation in galaxies, for example mass quenching (where hot gas in massive halos halts star-formation) and environmental quenching (Peng *et al.*, 2010). In contrast, the GSMF for star-forming systems is observed to evolve very little over time, which paints a particular picture of galaxy evolution where the number densities of star-forming galaxies are approximately conserved at all masses, even as galaxies evolve, build up their mass and move along the star-formation main sequence.

### 1.3 Cosmic collisions

A third process implicated in the transformation of galaxies (i.e., from blue, star-forming systems to red, passive ones; or from less massive to more massive) is the process of merging — the coalescence of two or more galaxies. Many studies have shown that merging can result in wide ranging changes to a host galaxy. These include, but are not limited to, morphological transformation (e.g., Toomre & Toomre, 1972; Kauffmann, White & Guiderdoni, 1993), cessation of star-formation, and also rejuvenation of star-formation (e.g., Karman *et al.*, 2015). These different outcomes depend on many variables including orbital parameters, stellar mass (or flux) ratio, and the available gas reservoirs — usually parametrised as the gas fraction  $f_{\text{gas}}$  (Lotz *et al.*, 2010). Indeed, the ability of astronomers to observe mergers also depends on these properties and the method used to probe them. Many studies have attempted to measure mergers observationally, quantified in their most basic form as the fraction of galaxies in a particular sample undergoing a merger event.

Arguably the most simple method of achieving this measurement has been to count galaxies in close proximity — typically less than 20–50 kpc — which possess a high probability of merging in the future. Generally a search is made for *projected* close-pairs of galaxies and a statistical correction made for the expected number of anomalous line-of-sight projections. Other studies have searched for the distinct morphological signatures of *ongoing* mergers using galaxy structural parameters. Over time, a general consensus has emerged that over the last 9 Gyr ( $z < 1.5$ ) the merger rate for massive galaxies has increased. Figure 1.3, taken from Conselice (2014), displays collated observational (markers) and theoretical (lines) measurements of the merger fraction,  $f_m(z)$ , at  $z < 3$  for galaxies with  $> 10^{10} M_\odot$  (left panel) and  $> 10^{11} M_\odot$  (right panel). Agreement within the errors is found for low-redshift ( $z < 1$ ) measurements of the merger fraction using different selections and methodologies.

It is clear, however, that an emerging discrepancy between studies exists at earlier times ( $z > 1.5$ ). Some studies suggest the fraction of merging galaxies increases or remains steady (e.g., Bluck *et al.*, 2009; Man *et al.*, 2012; López-Sanjuan *et al.*, 2015), while others suggest a decline (e.g., Williams, Quadri & Franx, 2011; Newman *et al.*, 2012). Recently, this discrepancy has been explained in part due to the nuances of making merger ratio selections using stellar mass or flux. Selecting mergers by *H*-band flux ratio selects gas-rich systems at high redshift ( $z > 1.5$ ) that a selection in stellar mass may otherwise miss, providing larger measured

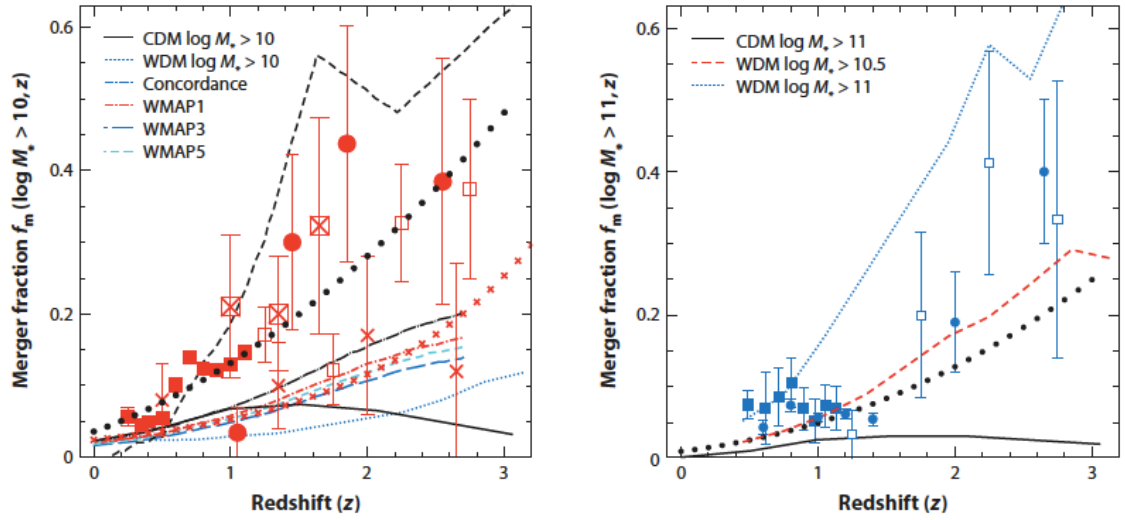


**Figure 1.3:** A compilation of the merger fraction,  $f_m(z)$ , evolution for galaxies with stellar masses  $> 10^{10} M_\odot$  (left panel) and  $> 10^{11} M_\odot$  (right panel). Observational measurements Conselice *et al.* (2003, solid circles), Conselice (2009, solid boxes), Mortlock *et al.* (2013, open boxes), Man *et al.* (2012, crosses), López-Sanjuan *et al.* (2009, open boxes with crosses), Bluck *et al.* (2009, 2012, solid circles) are given by the markers while theoretical predictions are given by the lines. The line comprised of black solid circles is the best fit relation for a merger fraction parametrisation as  $\sim (1+z)^m$  while the blue dotted lines and the red dashed line show the predicted merger history within warm dark matter (WDM) simulations. The solid black line shows predictions from cold dark matter (CDM) simulations. (Credit: Conselice 2014)

pair fractions in the process. It is argued that a selection using flux is therefore more representative the total baryonic mass involved in mergers (Man, Zirm & Toft, 2014). While many separate studies have painted a picture of galaxy merger histories, the literature is dogged by cosmic variance issues, selection differences and a plethora of methodologies that mean a significant and self-consistent study over the vast majority of cosmic time has not yet been performed.

Regardless, the observational and theoretical study of mergers can enlighten astronomers about the evolution of galaxies. For example, it is observed that massive galaxies have increased their physical size by a factor of 2–4 (e.g., Ilbert *et al.*, 2010; Mortlock *et al.*, 2015; Ownsworth *et al.*, 2016), and their stellar masses by a factor of 3–5 (e.g., Daddi *et al.*, 2005; Buitrago *et al.*, 2008) since  $z \sim 2$ . Mergers are an obvious source of ex situ stellar mass growth and their contribution and simple virial theorem arguments suggest they have the ability to increase the sizes of galaxies (e.g., Bezanson *et al.*, 2009). Various works have attempted to quantify the contribution from mergers towards this observed evolution. However, the large spread in merger fraction measurements ultimately results in estimates of the merger *rate* and therefore some authors come to the conclusion that mergers could be the dominant driver of the observed size evolution (e.g., Bluck *et al.*, 2012), while others do not (e.g., Man, Zirm & Toft, 2014). The current state of affairs, therefore, is that little consensus exists on the merger fraction or merger rate at high redshift. Surprisingly, arguably more consensus exists regarding the side of the Universe we cannot directly observe which directly influences the merger history of galaxies.

## 1.4 Dark side of the Universe

Evidence for something other than the ‘normal’ matter that can be observed with conventional telescopes first begun accumulating with observations of galaxy clusters detailed in 1933. Zwicky observed the Coma Cluster (Zwicky, 1933). Although the cluster was assumed to be in a state of virial equilibrium, Zwicky discovered that the mass obtained using the mass-to-light ratio was at odds to the mass required to satisfy the conditions of virial equilibrium. This extra ‘missing’ mass was dubbed by Zwicky as *dunkle materie* — dark matter — which is the term used to this day.

More recently, observations of distant ( $0.2 < z < 1.0$ ) Type 1a supernovae (Perlmutter *et al.*, 1998; Riess *et al.*, 1998) unambiguously favoured the accelerating expansion of the Universe, driven by a positive non-zero contribution from a ‘cosmological constant’, sometimes labelled the vacuum energy density. This cos-

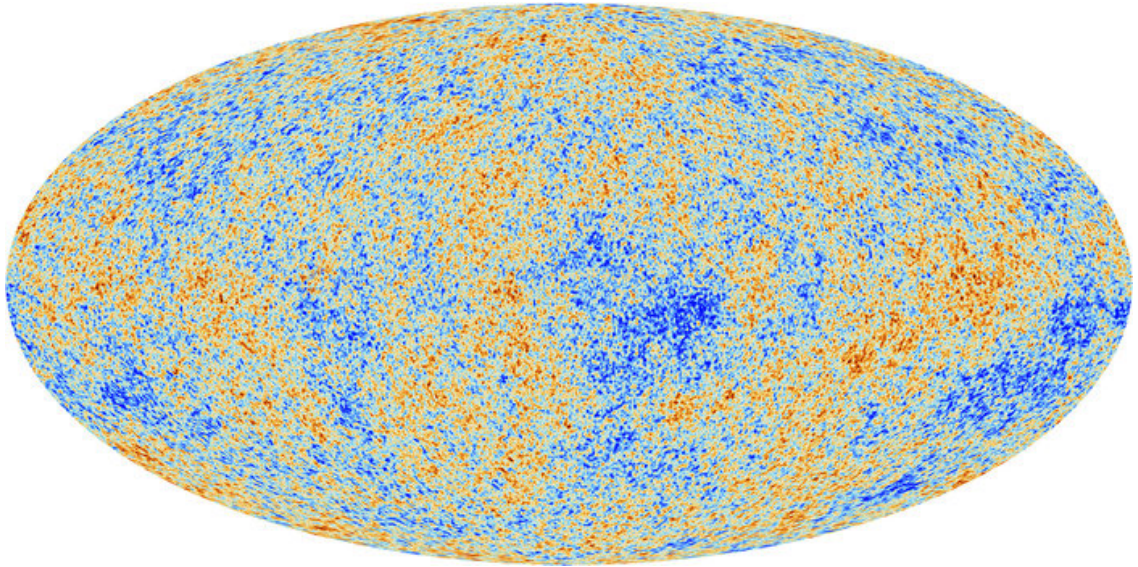


**Figure 1.4:** The anisotropies of the Cosmic Microwave Background (CMB) as observed by Planck. It depicts the tiny temperature fluctuations that correspond to regions of under- and over-density, representing the seeds of all large-scale structure seen in the Universe today. (Credit: ESA and the Planck Collaboration.)

mological constant term has subsequently been dubbed dark energy. It has been the driving force behind the field of cosmology to probe these most mysterious of substances, and to this end there have been many observations performed in the intervening decades which have shone a light on the dark side of the Universe.

## 1.5 The oldest light

The revolutionary prediction, subsequent observation and analysis of the oldest light in the Universe, the Cosmic Microwave Background (CMB; Figure 1.4), is arguably the crowning achievement of cosmology to date. Infamously discovered serendipitously by Arno Penzias and Robert Wilson in 1964 (Penzias & Wilson, 1965), the CMB was produced at the point of de-coupling between matter and radiation as the early Universe expanded and cooled. It is these photons that have travelled across the vastness of space and time to enter our telescopes and detectors.

Since these initial measurements of the the CMB, a stream of instruments have been deployed on the ground and in space to measure and characterise the CMB with increased precision. These missions discovered minuscule anisotropies in the temperature of the CMB on small scales which, due to more recent observatories such as Planck, are strongly interpreted as evidence in support for the favoured model of a  $\Lambda$ -Cold Dark Matter ( $\Lambda$ CMD) cosmology. Indeed, the relative contribution from the Universe's various components have been uncovered thanks to detailed

analysis of this first light. It is now known that the Universe is comprised of exactly  $31.56 \pm 0.91\%$  matter of which a paltry  $\sim 5\%$  is the regular matter we are able to directly observe, and the rest is comprised of Zwicky’s dark matter. The remaining  $68.44 \pm 0.91\%$  of the Universe is comprised of another mysterious substance; dark energy (Planck Collaboration *et al.*, 2015). Even now, dark matter and dark energy remain enigmatic components with many more questions than answers surrounding them.

The CMB not only allows precise constraints to be placed on cosmological parameters, but it also depicts (both visually and statistically) the primordial fluctuations that existed when the Universe was extremely young. While normal baryonic matter coupled to the electromagnetic radiation field, erasing any inhomogeneities in the process, dark matter was unable to do so. As such, dark matter formed tiny over-densities which, due to gravity, collapsed into larger halos with time. Only after recombination — decoupling baryonic matter from the radiation — were baryons permitted to be compelled by gravity and fall into the gravitational potentials of dark matter halos.

These over-densities are thought to have grown in a hierarchical fashion over the next few hundred million years, whereby larger halos were produced through the merging together of smaller halos. The conditions of the baryonic matter at the centre of the most massive halos were eventually such that neutral molecular hydrogen gas was able to radiate energy away and cool. Doing so allowed the baryonic matter to collapse further and reach the required conditions favourable for nuclear fusion to occur. This is the moment the first stars were formed. The exact details surrounding their formation is unclear, therefore multiple efforts have recently been made to both simulate and observe these stars and their closest descendants (Bromm, 2013; Crighton, O’Meara & Murphy, 2016; Safranek-Shrader *et al.*, 2016). With the ignition of nuclear fusion, the Universe was, in part, unshackled from the darkness.

Merging, whether between galaxies or dark matter halos, is the cornerstone on which the Universe and the idea of hierarchical assembly is built. It is therefore not surprising that every effort has been made to simulate these events and inform our understanding of the cosmos.

## 1.6 Simulating the Universe

Numerous observations, for example of the ‘Bullet Cluster’ (Markevitch *et al.*, 2004; Clowe, Gonzalez & Markevitch, 2004), have suggested dark matter to be a colli-

sionless, neutral particle which interacts only through the force of gravity. As dark matter is known to outweigh normal baryonic matter by a factor of  $\sim 5$ , astronomers have reasonably disregarded normal baryonic matter and the electromagnetic interactions that govern them. Vast, cosmological simulations of dark matter have therefore been a popular method with which to probe large scale structure in the Universe (e.g., Peebles, 1970; Frenk *et al.*, 1988; Springel *et al.*, 2005).

Such simulations have grown in both size and complexity over the intervening decades, taking advantage of the increase in computing power that has followed. The simulations made predictions on the large scale structure of the Universe that was ultimately corroborated by painstakingly precise observations of galaxy positions (e.g., Colless *et al.*, 2001). While dark matter is useful for understanding the larger structures in the Universe, by itself it can provide little information on the galaxies that are presumed to sit at the centres of dark matter halos. Special algorithms, grouped under the umbrella of ‘halo finders’, have been developed to search for and define dark matter halos within the simulations. Such algorithms allow for halos to be traced through time and therefore reveal their formation history in the form of merger trees.

Often complex models have therefore been developed to populate the resulting simulated dark matter halos with galaxies. These models – most commonly referred to as semi-analytic models of galaxy formation and evolution – employ various prescriptions for physical processes such as star-formation and AGN feedback that are derived from observations and theoretical studies. The overarching aim of this endeavour has been to match observations, typically through tuning model parameters until agreement is reached, and make predictions of galaxy formation and evolution at higher redshifts. The most common form these models take is that of the semi-analytic model, first detailed in White & Frenk (1991). Theoretically and observationally motivated prescriptions for physical processes such as gas cooling, star-formation, supernova feedback and galaxy merging are used to define the physical properties of galaxies residing in the simulated dark matter halos.

A suite of models has been constantly updated in the two decades plus since White & Frenk (1991), with the most common models found in two ‘flavours’: Munich (e.g., Kauffmann, White & Guiderdoni, 1993; Croton *et al.*, 2006; Henriques *et al.*, 2015), and Durham (e.g., Cole *et al.*, 1994; Bower *et al.*, 2006; Lagos, Lacey & Baugh, 2013). The most obvious differences between these ‘flavours’ are the recipes for physical processes, the dark matter halo finders used to identify halos within N-body simulations, and the way in which model parameters are tuned. In this time, models have become increasingly complex and now successfully predict many com-



mon scaling relations (e.g., stellar mass-size relation) and parameter distributions (e.g., luminosity function) at increasingly high redshift regimes. Recently, cosmological simulations that follow the co-evolution of both dark and baryonic matter — rather than ‘painting’ baryonic matter properties onto dark halos — have been performed, e.g. EAGLE (Schaye *et al.*, 2015). These hydrodynamical simulations are arguably a truer representation of the Universe whereby gravitational interactions in and between the dark and baryonic matter do occur. Figure 1.5 displays the redshift evolution of the dark matter density, gas density, gas temperature and gas metallicity of a volume centred on a large cluster of galaxies within the Illustris hydrodynamical simulation (Vogelsberger *et al.*, 2014a). Simulations that include gas physics are the natural next step in the field’s attempt to understand galaxy evolution. Much as it was found semi-analytic models required feedback from supernovae and AGN to match the galaxy luminosity and stellar mass functions, there is no doubt that future hydrodynamical simulations will also help inform our observations of the cosmos.

Whether a dark matter-only or hydrodynamical simulation, the core principle is that of gravity and the hierarchical assembly of structure over time. Thus the most basic comparisons that can be made between model and observation is the build up of mass over time.

## 1.7 Remaining questions

Although much progress has been made, many questions surrounding the formation and evolution of galaxies remain unanswered. What physical processes cause the observed galaxy colour bimodality (e.g., Strateva *et al.*, 2001; Baldry *et al.*, 2004)? What mechanism(s) cause galaxies to stop forming stars (e.g., Bundy *et al.*, 2006)? Among these questions are arguable some of the most fundamental questions that can be asked about the evolution of galaxies: just how many mergers have galaxies undergone (e.g., Conselice *et al.*, 2003)? What is the integrated impact of mergers on a galaxy (e.g., Mihos & Hernquist, 1996; Conselice, Yang & Bluck, 2009)? Additionally, a question that was never asked until recently: what is the best way to observationally connect populations of galaxies over large periods of time (e.g., Leja, van Dokkum & Franx, 2013)? These are the questions this thesis focuses on and attempts to shed light on.

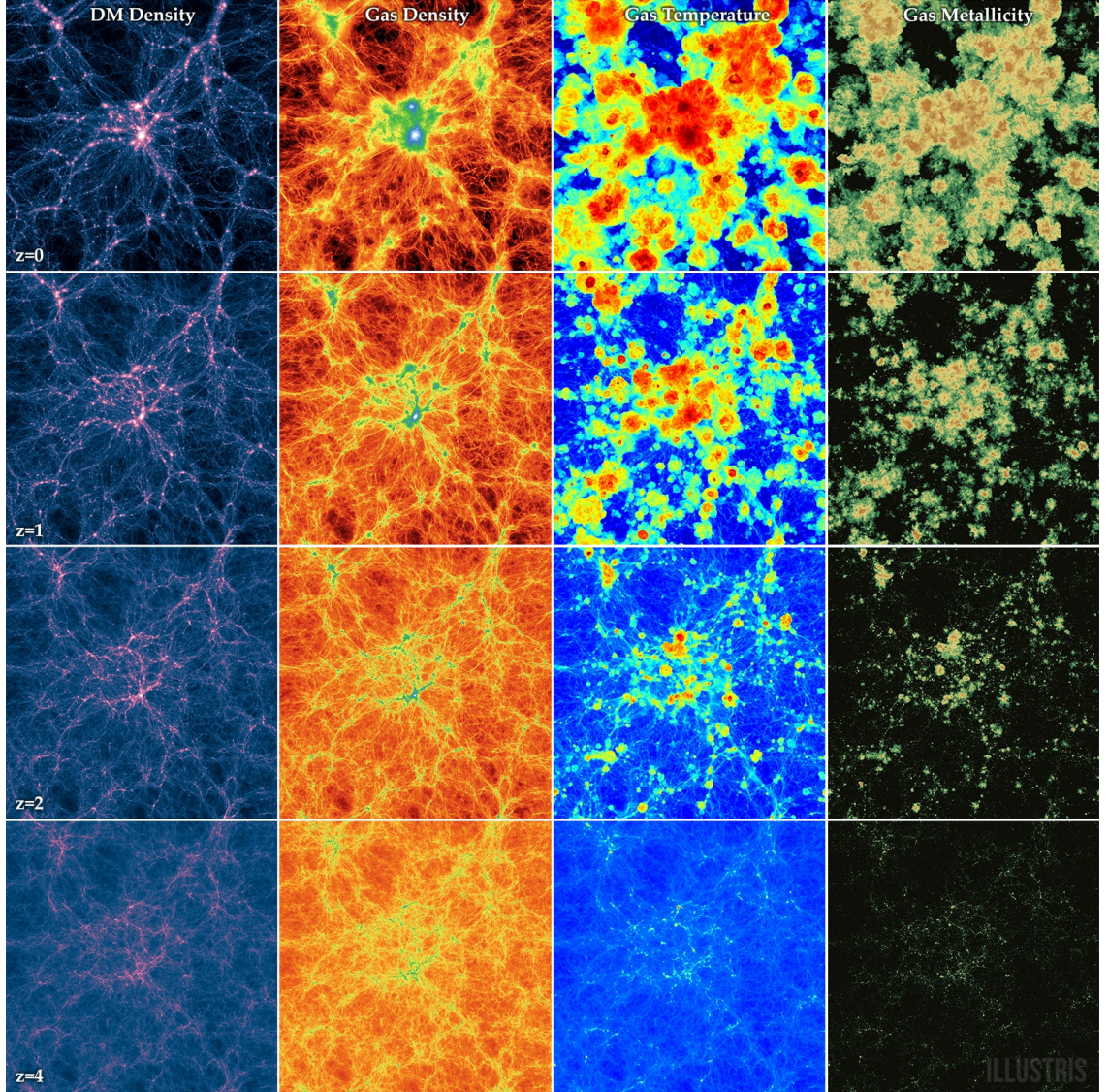


**Figure 1.5:** Redshift evolution in the Illustris simulation of a whole box slice from  $z = 4$  to  $z = 0$ , showing four projections (from left to right): dark matter density, gas density, gas temperature, and gas metallicity. (Credit: Illustris Collaboration).

## 1.8 Outline of thesis structure

The primary aim of this thesis is to improve our understanding of the growth of galaxies over the last 12 billion years. This is achieved by exploring the best method to use in order to trace galaxy populations (both backwards and forwards) in time, and applying this method to measure the merger histories of massive galaxies in a robust and statistical manner. This pathway to galaxy growth is then compared to star-formation and a consistent and self-consistent picture of galaxy growth painted for the first time.

**Chapter 2** uses a suite of semi-analytical models of galaxy formation and evolution applied to the Millenium Run cosmological N-body simulation to test and compare two methods which aim to connect galaxy populations across time. Selecting galaxies above a constant stellar mass, and selecting galaxies at a constant cumulative number density are tested on their ability to recover the true evolution in stellar mass, star-formation rate and star-formation rate density at  $z < 3$ . The use of velocity dispersion in place of stellar mass as the ranked quantity is also explored.

**Chapter 3** details the current methods used to determine the merger histories of galaxies at high redshift, and discusses the pros and cons inherent to each method. A new approach to measuring photometric close-pair statistics, named **Pyrus**, which circumvents the issues afflicting past studies of the merger fraction of stellar mass selected samples of galaxies out to high redshift is described.

**Chapter 4** and **Chapter 5** applies **Pyrus** to a sample of  $\sim 350,000$  galaxies collated from the GAMA, UKIDSS UDS, VIDEO and UltraVISTA/COSMOS survey regions. These fields provide an area of  $144 \text{ deg}^2$  at  $0.005 < z < 0.2$  and  $3.25 \text{ deg}^2$  at  $0.2 < z < 3.5$  in order to measure the major and minor merger fractions of galaxies with  $> 10^{10} M_{\odot}$  drawn from flux-limited samples consistently over such a large redshift range for the first time.

**Chapter 6** explores the build-up of stellar mass in massive galaxies at  $z < 3$  by measuring the relative roles of star-formation and (major and minor) mergers using the results of the previous chapter and a new method to statistically measure the star-formation rate density of stellar mass selected samples of galaxies.

The final chapter discusses the conclusions drawn from the work presented in the

aforementioned chapters, and considers the future work that can build upon these results.

## Chapter 2

# Tracing Massive Galaxies in Cosmological Simulations

In this chapter, a suite of semi-analytic models applied to the Millennium Run (Springel *et al.*, 2005; Lemson & Consortium, 2006) cosmological N-body simulation are used to test and compare two observational techniques which aim to connect populations of massive galaxies across time. Selections of galaxies made above a constant stellar mass, and at a constant cumulative number density are made. Several metrics that quantify the accuracy to which these selections recover genuine galaxy descendants and progenitors, as well as the true stellar mass and star-formation rate of galaxy populations are analysed at  $z < 3$  representing the vast majority of cosmic time. Finally, the use of velocity dispersion in place of stellar mass to select galaxies is investigated in a similar manner. This chapter concludes by making suggestions on the appropriate method to use when performing an observational analysis that requires connections to be made between galaxy populations over a large redshift range.

### 2.1 Introduction

In the now commonly accepted paradigm, galaxies form in the gravitational wells of collapsed cold dark matter halos, which themselves are seeded by primordial quantum fluctuations in the Universe's first moments. In this hierarchical picture of galaxy formation and evolution, galaxies build up stellar mass through both in-situ star-formation and galaxy mergers, where more massive galaxies merge with smaller systems which result in more massive descendants. Over time, these processes produce the array of galaxies and the environments within which they are observed. In order to understand how galaxies form and evolve, the evolution in

their properties (e.g. stellar mass, size) must be observed. As the most massive, and thus the brightest, galaxies are the easiest systems to observe out to high redshift, it is these galaxies and their properties that observations attempt to study. This has typically been achieved by selecting galaxies in two ways.

Historically, selecting galaxies across a redshift range of interest using a constant stellar mass cut has been used to study the evolution of the most massive galaxies (e.g., Conselice *et al.*, 2003; Mortlock *et al.*, 2013). Use of this selection method intrinsically assumes galaxies have more or less been a passively evolving population from high redshift. However, processes such as major galaxy mergers and bursts of star-formation interfere with these assumptions and contaminate the selection by changing the rank order of galaxies. Thus, the wider the redshift range this method is applied to, the less accurately it may trace the galaxies of the original selection.

Selecting galaxies at a constant cumulative comoving number density, when ranked by some physical property such as stellar mass or luminosity, has proven a popular alternative in the recent literature when observing both field and cluster galaxy evolution (e.g., Lin *et al.*, 2013). Using this technique, the averaged star-formation history of a constant number density selected sample of galaxies over the redshift range  $3 < z < 8$  has been shown to be able to account for the stellar mass growth of these galaxies (Papovich *et al.*, 2010). The average stellar mass of the most massive galaxies (those with  $\log M_* > 11.0$  at  $z = 0$ , and  $\log n [\text{Mpc}^{-3}] = -4.0$ ) has been found to increase by a factor of  $\sim 4$  over the redshift range  $0.3 < z < 3$ . However, the integrated star-formation history appears unable to account for the growth in stellar mass at  $z < 1.5$ . Therefore, the influence of both major and minor galaxy mergers is required to account for this discrepancy at low redshift (Ownsworth *et al.*, 2014).

Furthermore, studies have observed the evolution in  $\text{H}\alpha$  equivalent width, structural properties and colours of galaxy populations selected at various number densities (e.g., Fumagalli *et al.*, 2012; Marchesini *et al.*, 2014). Stellar mass measured inside a radius of  $r = 5\text{kpc}$  on stacked images of massive galaxies (selected at  $\log n [\text{Mpc}^{-3}] = -3.7$  corresponding to galaxies with  $\log M^* [M_\odot] > 11.4$  and  $\log M^* [M_\odot] > 11.1$  at  $z = 0.1$  and  $z = 2.0$  respectively) is found to be approximately constant over the redshift range  $0.6 < z < 2.0$ . On the other hand, the stellar mass content beyond this radius is found to increase by a factor of  $\sim 4$  (van Dokkum *et al.*, 2010). Conselice *et al.* (2013) compare the derived gas fractions of massive galaxies ( $M_* > 10^{11} M_\odot$ ) with their star-formation histories in the redshift range  $1.5 < z < 3$ , selecting galaxies at a merger-adjusted constant number density. They conclude that gas accretion is the dominant source of observed stellar mass

production for these galaxies over this redshift range.

Investigation into the efficacy of either selection method has not been fully explored. Numerical calculations presented in van Dokkum *et al.* (2010) suggest the influence of galaxy mergers has little influence on stellar mass growth when measured using a constant number density selected sample. Papovich *et al.* (2010) used dark matter halo merger trees from the Millennium Simulation<sup>1</sup> (MS; Springel *et al.*, 2005; Lemson & Consortium, 2006) to show that the recovery fraction of descendant halos at redshifts  $3 < z < 8$  is  $\sim 50\%$ . Behroozi *et al.* (2013) found a small change in the cumulative number density of the most massive ( $M_* > 10^{11.5} M_\odot$ )  $z = 0$  progenitor galaxies of  $+0.22$  dex per unit  $\Delta z$ . Furthermore, they find that this change and thus the mass histories of descendants and progenitors are different. More directly, Leja, van Dokkum & Franx (2013) used the Guo *et al.* (2011, G11) semi-analytical model (SAM) applied to the MS in order to test the validity of the underlying assumptions of constant number density selection. They find that, within this particular SAM, the median stellar mass of descendant galaxies can be recovered over the redshift range  $0 < z < 3$  to within  $\sim 40\%$  of the true value. Corrections for stellar mass growth rate scatter, galaxy mergers and quenching are found to reduce this discrepancy to within  $\sim 12\%$  - well within typical observational error attributed to the calculation of stellar masses. These results, however, are model and cosmology dependent and are sensitive to the dark matter merger trees and the recipes used to determine galaxy properties. How the stellar mass is calculated is a prime example. Different methods of calculating this may introduce different levels of scatter into the rank order of galaxies across redshifts. Sensibly investigating the efficacy of these techniques requires a mixture of SAMs, merger trees and cosmology to gauge the amount of variance in the results.

While stellar mass is used in the studies mentioned previously, it may not be the most appropriate property with which to rank and select galaxies in order to trace their properties. Increasing evidence has suggested that the central velocity dispersion of a galaxy is a good predictor of galaxy properties, including star-formation rate (SFR) and colour, across large redshift ranges. Furthermore, it is thought to be a more stable quantity with redshift compared to, for example, stellar mass (e.g., Bezanson, vanDokkum & Franx, 2012; Wake, vanDokkum & Franx, 2012), partly due to the weak dependence of velocity dispersion on both stellar mass and galaxy size, with  $\sigma \propto (M_*/R_e)^{\frac{1}{2}}$ . Leja, van Dokkum & Franx (2013) briefly investigated the change in velocity dispersion for descendants of  $z = 3$  galaxies selected at a constant cumulative number density. They found a small change ( $< 0.15$  dex in

---

<sup>1</sup><http://www.mpa-garching.mpg.de/galform/virgo/millennium/>



$\log \sigma$ ) in the average inferred velocity dispersion from  $0 < z < 3$  in the G11 SAM. Similarly, simulations of massive galaxies ( $\log M_\star > 10.8$ ) presented in Oser *et al.* (2012) find an increase in velocity dispersion of  $\Delta\sigma = 0.2$  dex over the redshift range from  $z = 2$  to  $z = 0$ , consistent with observational estimates (e.g., Javier Cenarro & Trujillo, 2009; Martinez-Manso *et al.*, 2011). These observations warrant a detailed study into the use of inferred velocity dispersion in place of stellar mass.

To generate an accurate framework for how galaxies form and evolve, one must observe the evolution of their properties over time. With these observations, models can be crafted to explain them. If, however, the evolution is not traced correctly, these frameworks can deviate from the truth. Although the aforementioned literature works provide some arguments to support the use of their selection methods, no study has attempted to quantify the recovery efficiency of these methods. To this end, this Chapter presents a detailed study on the ability of these selection methods to trace individual galaxies, as well as their stellar mass and star-formation properties over cosmic time. This is achieved through the use of galaxy evolution models to investigate the ability of galaxy selections which are a) above a constant stellar mass limit; b) at a constant cumulative comoving number density in stellar mass; c) above a constant stellar velocity dispersion limit; and d) at a constant cumulative comoving number density in stellar velocity dispersion. How well these methods trace the true evolution of progenitor and descendant populations initially selected at redshifts  $z = 0$  and  $z = 3$  respectively is tested.

## 2.2 Data Description

This Chapter explores the efficacy of two different methods in recovering the direct (i.e. most massive) progenitors and descendants of the most massive galaxies from initial selections at redshifts of  $z = 0$  and  $z = 3$ , respectively. The first selection method is at a constant limit (in either stellar mass or velocity dispersion), above which galaxies are selected. The second selection is at a constant cumulative comoving number density. This is achieved by integrating the galaxy stellar mass function (GSMF), or the galaxy velocity dispersion function (GVDF) if velocity dispersion is used, to obtain the integrated number density as a function of stellar mass (or velocity dispersion). From this the stellar mass limit above which all the galaxies are below a certain number density can be obtained. The sample examined at that redshift thus contains all galaxies with a stellar mass greater than this value. Additionally, it is prudent to quantify how well each selection method recovers both the average and sum total stellar mass in the descendant or progenitor



populations, as well as the average SFR. The combination of cosmological dark matter simulations and semi-analytical recipes, as well as cosmological hydrodynamical simulations, continue to provide the only environments in which to conduct such an investigation.

### 2.2.1 Simulated Data

To this end, the output of the Millennium Simulation and the catalogues of four SAMs applied to it and its variants are used. The Millennium Simulation combined with the web-based database (Lemson & Consortium, 2006) of SAMs applied to it offer an unparalleled dataset with which to perform this study. The original simulation consists of  $2160^3$  dark matter particles of mass  $8.6 \times 10^8 h^{-1} M_\odot$  within a comoving box of size  $500 h^{-1}$  Mpc on a side. The MS uses a  $\Lambda$ CDM cosmological model with a matter density  $\Omega_m = 0.25$ , baryonic matter density  $\Omega_b = 0.045$ , Hubble constant  $h = 0.73$  in units of  $100 \text{ km s}^{-1} \text{ Mpc}^{-1}$ , dark energy density  $\Omega_\Lambda = 0.75$ , scalar spectrum power-law index  $n_s = 1$  and root-mean-square (r.m.s.) linear mass fluctuation within a sphere of radius  $8 h^{-1}$  Mpc  $\sigma_8 = 0.9$ . The Guo *et al.* (2013, G13) SAM utilises a subsequent simulation which follows  $2160^3$  particles of mass  $9.3 \times 10^8 h^{-1} M_\odot$  using an updated WMAP7 (Komatsu *et al.*, 2011) cosmology with  $\Omega_m = 0.272$ ,  $\Omega_b = 0.0455$ ,  $h = 0.704$ ,  $\Omega_\Lambda = 0.728$ ,  $n_s = 0.967$  and  $\sigma_8 = 0.81$ . The main difference between these two simulations is the value of the linear power spectrum amplitude on scales of  $8 h^{-1}$  Mpc,  $\sigma_8$ . This parameter essentially quantifies the clustering expected on such a scale and therefore a larger value of  $\sigma_8$  would roughly translate to larger measured merger rates (Conselice *et al.*, 2014).

Bower *et al.* (2006, B06) presents an updated variant of the Durham SAM of galaxy formation (Cole *et al.*, 2002) in which the treatment of active galactic nuclei (AGN) and stellar feedback on halo quenching is improved. They find that these updated treatments reduce the number densities of higher mass galaxies and remove cooling flows from rich clusters. De Lucia & Blaizot (2006, D06) applied their model to the output of the MS with updated treatments for stellar populations, dust attenuation and cooling flow suppression via AGN feedback. They find that supernovae and AGN feedback processes play a vital role in the early quenching of star-formation in the progenitors of local brightest cluster galaxies (BCGs). G11 describe an updated model of galaxy formation and evolution with new recipes for supernovae feedback and galaxy bulge sizes among others. They find that the simulated abundance of massive galaxies, with  $\log M_\star [M_\odot] > 11.0$ , are consistent with observations out to  $z \sim 1.0$ . However, they over predict galaxies of lower stellar mass beyond  $z \sim 0.6$  and under predict massive galaxies at  $z > 1.0$  by at

least an order of magnitude (see Fig. 23 in G11). Finally, G13 describe the results of implementing their SAM in a WMAP7 cosmology. They find a requirement for weaker feedback and star-formation efficiency than a WMAP1 cosmology in order to reproduce the observed local GSMF. Merger trees used by B06 are described in Harker *et al.* (2006) while those employed by the remaining SAMs are presented in Springel *et al.* (2005). It is these models based upon these merger trees extracted from the Millennium Simulation from which the observational selection methods are studied.

Physically motivated models of galaxy formation (see, for example, Bower *et al.*, 2006; Vogelsberger *et al.*, 2014a) applied to cosmological dark matter simulations, such as the MS, provide an unparalleled tool to probe the evolution of dark matter halos and the galaxies that reside within them. Simulations and observations at low redshift ( $z < 2$ ) are found to be consistent in many respects (e.g. luminosity functions), however SAMs have varying degrees of success in matching observational quantities beyond this. Comparison of different SAMs and other models show simulated galaxy stellar mass functions are generally consistent with most observations out to  $z \sim 2$  if feedback mechanisms from AGN and supernovae are included (e.g., Croton *et al.*, 2006; Lu *et al.*, 2014). This agreement extends to comparison between simulated and observed major mergers for the most massive galaxies inside the MS, but not for lower mass systems (Bertone & Conselice, 2009).

### 2.2.2 Selection Method Metrics

It is prudent to measure how accurately each selection method samples the progenitors or descendants of the galaxy population being studied. In this work, descendants of an initial  $z = 3$  selection are identified by following the ‘descendantId’ property in the SAM output catalogues. At each step, duplicate descendants (due to mergers between two or more galaxies) are removed such that the number of true descendants decreases with time. On the other hand, progenitors of an initial  $z = 0$  selection are defined as the most massive galaxy in the previous redshift snapshot that came to be the galaxy in the current snapshot. Descendants and progenitors of any mass ratio (down to the resolution of the simulation) are traced with this method. These definitions allow traversing of different branches along merger trees depending on the direction we take. In summary, this work measures the ability of each selection method to recover galaxy properties using various metrics.

Firstly, the recovery fraction quantifies how many of the available progenitors or descendants are recovered at different redshifts in the sample obtained using a

given selection method such that

$$f_{\text{rec}} = N_s / N_{\text{tot}}, \quad (2.1)$$

where  $N_s$  is the number of descendants/progenitors included in the observational selection, and  $N_{\text{tot}}$  is the total number of descendants/progenitors available to be selected.

Although helpful, it may not strictly be necessary to sample the descendants or progenitors of interest to reproduce the true evolution of galaxy properties - sampling different galaxies from the true progenitors or descendants might be sufficient if the galaxies replacing those lost have similar properties. Therefore a low recovery fraction may not necessarily correspond to an inability to recover the true evolution in, for example, average stellar mass or SFR. Because of this, the fraction of the observed sample that is not a galaxy of interest is considered. This quantity, the contamination fraction, is defined as

$$f_{\text{contam}} = (N_{\text{sel}} - N_s) / N_{\text{sel}} \quad (2.2)$$

where  $N_{\text{sel}}$  is the number of galaxies within the observed selection and  $N_s$  is the number of true (i.e. most massive) descendants/progenitors included in the selection. This Chapter also compares the true mean stellar mass,  $\tilde{m}_{\text{true}}^* = \sum m_{\text{true}}^* / N_{\text{true}}$ , of the progenitors or descendants to that observed using each selection method,  $\tilde{m}_{\text{obs}}^* = \sum m_{\text{obs}}^* / N_{\text{obs}}$ , defined as

$$\kappa_{m^*} = (\tilde{m}_{\text{obs}}^* - \tilde{m}_{\text{true}}^*) / \tilde{m}_{\text{true}}^* = \Delta \tilde{m}^* / \tilde{m}_{\text{true}}^*. \quad (2.3)$$

In a similar fashion, the ability to trace the evolution of the stellar mass density, or sum of the stellar mass, is important to understand the build up of stellar mass in galaxies over time. We compare the observational selection techniques' abilities to return the true mean stellar mass density, quantified as

$$\kappa_{\rho^*} = \Delta(\Sigma m^*) / \Sigma m_{\text{true}}^* \quad (2.4)$$

where  $(\Sigma m^*)$  is the sum of stellar masses. It follows from these definitions that the recovery metric for average stellar mass,  $\kappa_{m^*}$ , can be written in terms of the recovery metric for stellar mass density,  $\kappa_{\rho^*}$ , as

$$\kappa_{m^*} = \left( \frac{N_{\text{true}}}{N_{\text{obs}}} \kappa_{\rho^*} \right) + \frac{N_{\text{true}}}{N_{\text{obs}}} - 1. \quad (2.5)$$

Finally, this is extended to the average SFR of the galaxies in a similar fashion such that the discrepancy between the true and observed is defined as

$$\Delta\tilde{\Psi}^* / \tilde{\Psi}_{\text{true}}^* \quad (2.6)$$

where  $\tilde{\Psi}^*$  is the mean SFR. The choice to study these galaxy properties in particular is made because they are the most fundamental, and the most used in the literature thus far. Additionally, it is investigated whether each selection method is best applied to tracing progenitor or descendant galaxy populations, i.e. whether the selection methods are best applied forwards or backwards in time.

### 2.2.3 Velocity Dispersion Selection

As central velocity dispersion has been shown to exhibit a shallow evolution over time, it is prudent to investigate this physical property as a tracer. From scalar virial theory the stellar velocity dispersion of a system can be estimated by

$$\sigma^2 = \frac{GM_\star}{5R_{\frac{1}{2}}} \quad (2.7)$$

where  $G$  is Newton's gravitational constant,  $M_\star$  is the total stellar mass and  $R$  is the half-mass radius (see, e.g., Cappellari *et al.*, 2006). Using the reported total and bulge stellar masses and sizes, the same method as described in Leja, van Dokkum & Franx (2013) is used to estimate the half-mass radius of each simulated galaxy as

$$R_{\frac{1}{2}} = \frac{M_b R_b + M_d R_d}{M_b + M_d}. \quad (2.8)$$

As before,  $M$  is stellar mass,  $R$  is the half-mass radius and subscripts  $b$  and  $d$  correspond to the bulge and disk components, respectively. The SAMs considered in this work do report bulge and disk component masses as well as half-mass radius of the bulge. However they do not report the half-mass radii of the disk but instead provide a disk scale radius which is equal to three times the scale length of the disk. This scale length,  $R_{\text{scale}}$ , is corrected to convert it to a half-mass (effective) radius such that  $R_d = 1.678R_{\text{scale}}$ . This relation is ideally obtained numerically, however approximations are available for a range of Sérsic (1963) indices. Graham & Driver (2005) derive, calculate and provide various Sérsic-related quantities including ef-

fective radius as a function of disk scale length and Sérsic index (Equation 16). The above conversion corresponds to  $n = 1$  exponential profile.

The aforementioned metrics are calculated using both stellar mass and velocity dispersion at four constant number density selections and four constant limits. Number density values are chosen to cover a wide range, allowing comparison with previous work, and to be representative of what number densities are currently applicable to observational studies. Constant limits in both stellar mass and velocity dispersion are chosen to enable comparison with the number density selections. Constant stellar mass limits are defined as the mass limit of a number density selection at either  $z = 0$  or  $z = 3$ , depending on whether progenitors or descendants are being investigated. In short, the limits are chosen such that the initial selections, whether at  $z = 0$  or  $z = 3$ , are the same. Section §2.3 reports on the results of using stellar mass as the ranking property, while Section §2.4 details the results of using inferred velocity dispersion.

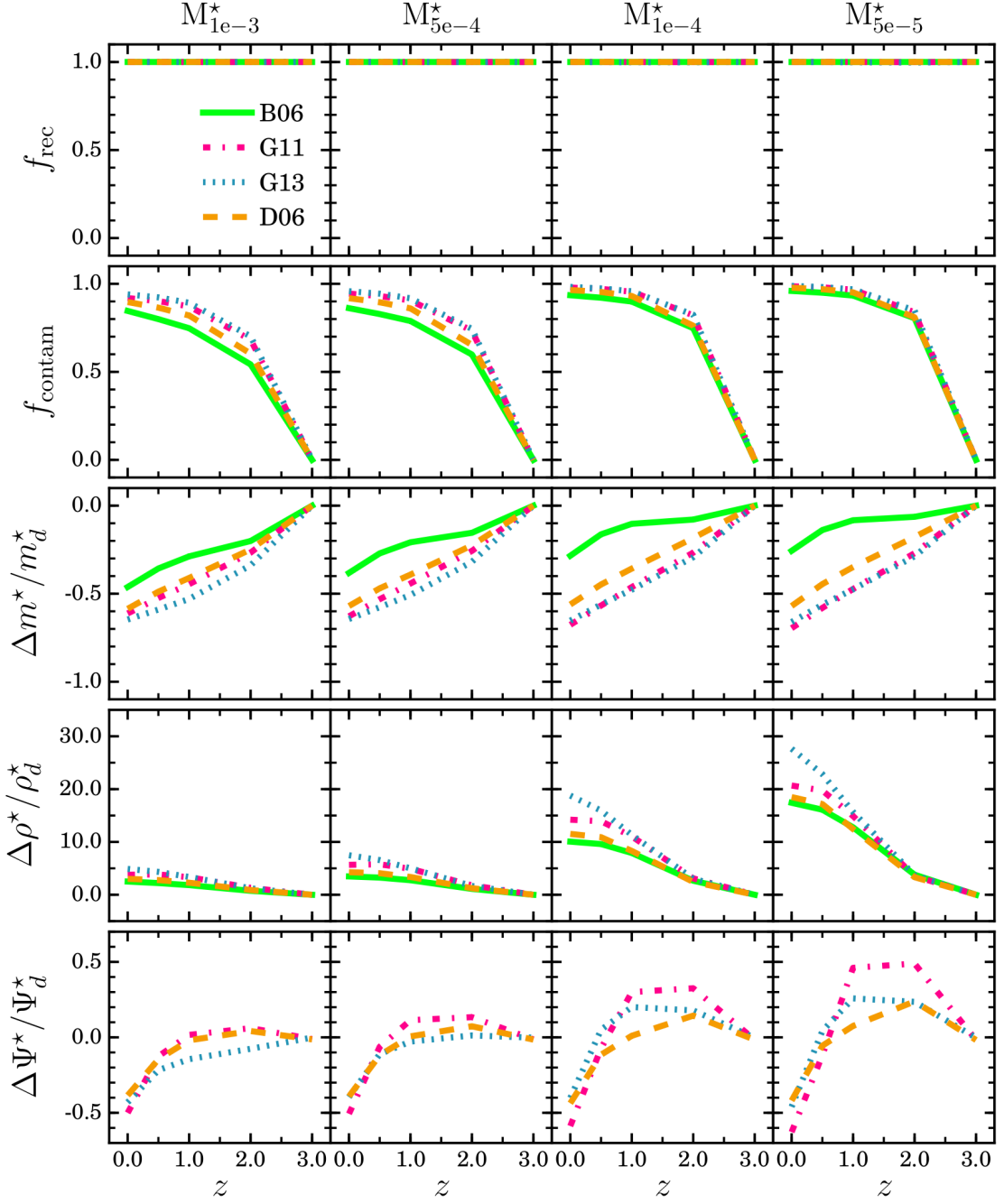
## 2.3 Stellar mass selections

The investigation now focuses on the ability of two different galaxy selection methods, using two different galaxy properties, to recover the mean stellar mass, stellar mass density, mean velocity dispersion and average SFR of progenitor and descendant populations.

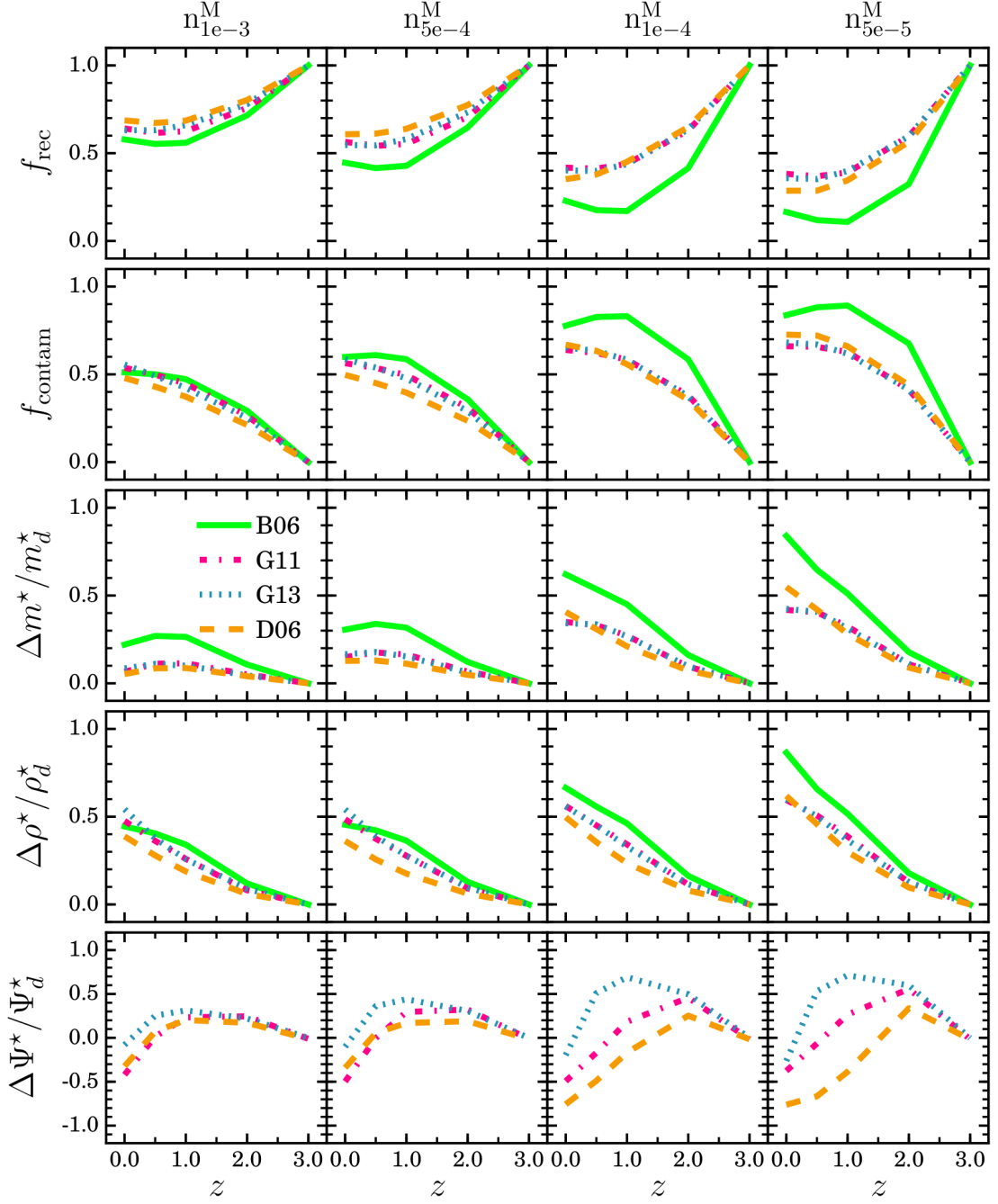
### 2.3.1 Descendants

Figure 2.1 presents the results of selecting descendants at four constant stellar mass limits, described in Table 2.1. This is defined as the stellar mass limit for a number density selection beginning at  $z = 3$  and examining evolution at lower redshift. As one might expect, all constant stellar mass selections recovered all available descendant galaxies at every redshift (top panel), as galaxies typically experience a net gain in stellar mass over these redshift ranges. However, the fraction of the selected sample that are not descendants of interest,  $f_{\text{contam}}$ , increases to  $\sim 50\%$  by  $z = 2$ . By  $z = 0$ , samples selected above each stellar mass limit are almost completely contaminated ( $> 80\%$ ). This shows that using a constant mass cut at  $z = 3$  selects essentially none of the same galaxies (descendants) at lower redshift.

Contrary to what this metric might suggest, the difference between the observed and true mean stellar mass is underestimated by only  $\sim 50\%$  by  $z = 0$ , decreasing linearly at lower redshift. This seems to be largely independent of the stellar mass



**Figure 2.1:** Recovery fraction of individual descendants, their average stellar mass, stellar mass density and average SFR (rows) for four constant stellar mass limit selections (columns) covering the stellar mass range at  $z = 3$  of  $\log M_* > 10.7, 10.6, 10.4, 10.2$ . Initial stellar mass selection limits for each SAM are given in the third column of Table 2.1. SAMs used are Bower *et al.* (2006, B06), De Lucia & Blaizot (2006, D06), Guo *et al.* (2011, G11) and Guo *et al.* (2013, G13), represented by solid green, dashed orange, dashed-dotted magenta and dotted blue lines respectively.



**Figure 2.2:** Recovery fraction of individual descendants, their average stellar mass, stellar mass density and average SFR (rows) for four constant number density selections (columns) covering the number density range  $-4.3 < \log n < -3.0$ . These approximately correspond to stellar masses at  $z = 3$  of  $\log M_* > 10.7, 10.6, 10.4, 10.2$ . Initial stellar mass selection limits for each SAM are given in the third column of Table 2.1. SAMs used are Bower *et al.* (2006, B06), De Lucia & Blaizot (2006, D06), Guo *et al.* (2011, G11) and Guo *et al.* (2013, G13), represented by solid green, dashed orange, dashed-dotted magenta and dotted blue lines respectively.

limit in all but the B06 SAM which fares relatively better at higher limits. Recovery of the median stellar mass is indistinguishable from the mean stellar mass for the two smallest number densities. At the two largest choices however, the median stellar mass is further underestimated towards lower redshift such that at  $z = 0$ , this property is underestimated by  $\sim 60\%$ . The stellar mass density is overestimated by a factor of  $\sim 4$  ( $\sim 20$ ) at the lowest (highest) mass limit in all SAMs by  $z = 0$ . As the B06 SAM does not report SFRs in its catalogues, only the remaining three SAMs are considered in recovery of the mean SFR. At the lowest stellar mass limit, this is recovered to within  $\sim 10\%$  down to  $z = 1$ . At lower redshifts, however, the SFR begins to be increasingly underestimated and by  $z = 0$  it is underestimated by  $\sim 50\%$ .

Results displayed in Figure 2.2 reveal that using a constant number density selection the recovery fraction,  $f_{\text{rec}}$ , decreases exponentially with decreasing redshift such that by  $z = 0$  between 30% and 60% of the available descendants are selected. The contamination fraction is found to vary between half and three quarters of the sample at the highest and lowest number densities respectively. Mean stellar mass is overestimated by a factor that increases with both number density and redshift, overestimating the true value by a factor of 1.3 and 1.6 by  $z = 0$ . While not plotted, the median stellar mass is qualitatively similar above  $z \sim 0.5$ . Below this, the median stellar mass is further overestimated by up to 30% more at  $z = 0$ . Similarly, the stellar mass density is eventually overestimated by a factor of 1.5 (1.8) at the largest (smallest) number densities. Finally, over the entire redshift range the SFR is recovered to within  $\sim 50\%$  in all SAMs and at all number density choices.

It is worth noting that the top row of Figure 2.2, and indeed other figures, illustrate that the recovery fraction actually improves towards the lowest redshifts ( $z < 1$ ) in the vast majority of SAMs. This is caused by galaxies initially lost from the selection gaining the required stellar mass to be included. Viewing the merger trees for these particular galaxies, it is found that this extra stellar mass is mostly the result of halo mergers within the simulation. This suggests that mergers become an important source of mass growth at low redshift and demonstrates the non-constantness of the stellar mass rank ordering of galaxies.

Compared to a constant stellar mass selection, a constant number density selection recovers far fewer of the true descendants at lower redshift. However, at all number density choices, the lower redshift selections have considerably less contamination.



**Table 2.1:** Constant stellar mass limits for progenitors and descendants, defined as the stellar mass limit for a number density selection at  $z = 0$  and  $z = 3$  respectively.

SAM	$n$ [ $\text{Mpc}^{-3} h^3$ ]	Descendants ( $z = 3$ )	Progenitors ( $z = 0$ )
		$M_{\text{lim}}$ [ $\log M_{\odot}/h$ ]	$M_{\text{lim}}$ [ $\log M_{\odot}/h$ ]
B06	$1 \times 10^{-3}$	10.32	10.87
	$5 \times 10^{-4}$	10.51	11.01
	$1 \times 10^{-4}$	10.76	11.22
	$5 \times 10^{-5}$	10.82	11.30
D06	$1 \times 10^{-3}$	10.31	10.92
	$5 \times 10^{-4}$	10.46	11.04
	$1 \times 10^{-4}$	10.68	11.29
	$5 \times 10^{-5}$	10.74	11.39
G11	$1 \times 10^{-3}$	10.21	10.84
	$5 \times 10^{-4}$	10.33	10.97
	$1 \times 10^{-4}$	10.52	11.24
	$5 \times 10^{-5}$	10.59	11.35
G13	$1 \times 10^{-3}$	10.00	10.77
	$5 \times 10^{-4}$	10.15	10.89
	$1 \times 10^{-4}$	10.40	11.12
	$5 \times 10^{-5}$	10.48	11.21

### 2.3.2 Progenitors

Now an initial selection at  $z = 0$  is taken and the most massive progenitors traced back in time towards higher redshifts. As Figure 2.3 shows, the recovery of individual progenitors using a constant stellar mass limit (detailed in Table 2.1) deteriorates exponentially such that at  $z = 1$ , only 30% are recovered in the selection at the smallest stellar mass limit and less than 5% at the largest stellar mass limit (smallest number density). The sample's contamination fraction increases immediately and, at all stellar mass limits, the sample is  $> 95\%$  contamination by  $z = 3$ .

The discrepancy between the true and observed mean stellar mass of the progenitors increases approximately exponentially with redshift, overestimating the mean mass by a factor of three at  $z = 3$ , independent of stellar mass limit and weakly dependent on the choice of SAM. Recovery of the median stellar mass is again indistinguishable from the mean recovery at the two largest stellar mass limits. At the two highest, the median mass is overestimated by factors of 3 – 7 times. Furthermore, observed stellar mass density is increasingly underestimated with redshift in all SAMs. Finally, the mean SFR is recovered to within a factor of  $\sim 4$  by  $z = 3$ .

Selecting progenitors at a constant number density fares relatively better, as shown in Figure 2.4. Out to  $z = 3$ , no less than  $\sim 50\%$  ( $\sim 30\%$ ) of progenitors are recovered at the largest (smallest) selections. The mean stellar mass is recovered to within a factor of  $\sim 1.5$  at  $z = 3$  in all SAMs and choices of  $n$ , and the observed stellar mass density follows a very similar trend. Median stellar mass recovery is indistinguishable from the mean recovery except at the largest number density where the overestimation is larger at  $z \sim 2$  by approximately 50%. Lastly, the mean SFR is recovered to within  $\pm 20\%$  at all number density selections except for D06, which overestimates the SFR at a peak of  $\sim 50\%$  at  $z = 1$ .

Comparing these results with the descendant population (§2.3.1), it is found that that a constant cumulative comoving number density selection recovers all descendent population properties within a factor of two of the true value. Similarly, all the progenitor properties are recovered to within a factor of 1.5 of the true value. Furthermore, a constant number density selection appears to trace the ensemble progenitor properties of  $z = 0$  massive galaxies better than the descendants of those at  $z = 3$ .

### 2.3.3 Fitting forms

For convenience, metrics in the previous figures are fit with parametric functions (described below) for a constant number density selected sample of galaxies. These

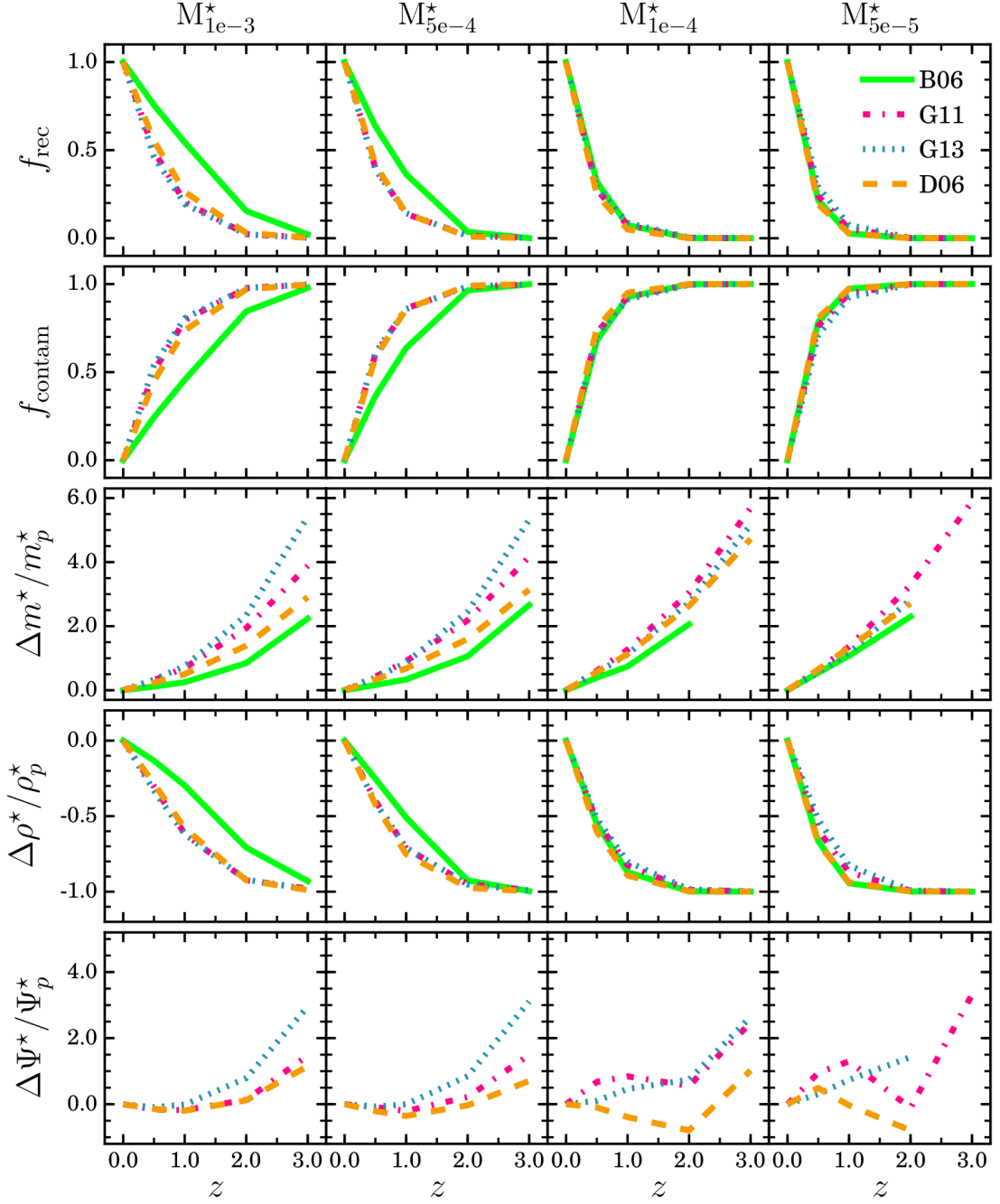


**Figure 2.3:** Recovery of individual progenitors, their average stellar mass, stellar mass density and average SFR (rows) for four constant stellar mass limit selections (columns) covering the number density range  $-4.3 < \log n < -3.0$ . The B06, D06, G11 and G13 models represented by solid green, dashed orange, dashed-dotted magenta and dotted blue lines respectively. Progenitor stellar mass limits for each SAM are given in the third column of Table 2.1.

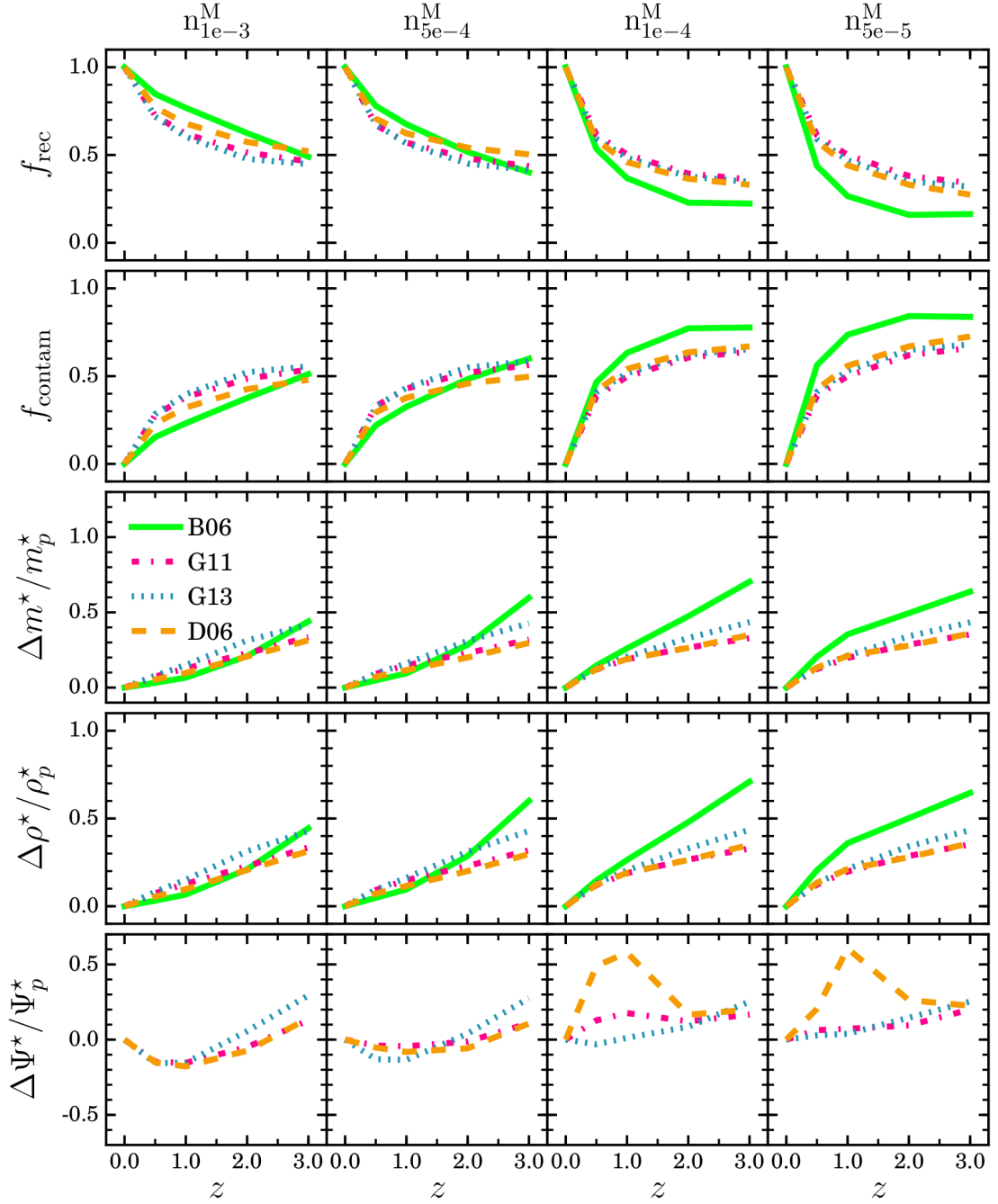


**Figure 2.4:** Recovery of individual progenitors, their average stellar mass, stellar mass density and average SFR (rows) for four constant number density selections (columns) covering the number density range  $-4.3 < \log n < -3.0$ . The B06, D06, G11 and G13 models represented by solid green, dashed orange, dashed-dotted magenta and dotted blue lines respectively.

fits are strictly valid over the redshift range  $0 < z < 3$ . For each metric (e.g.,  $f_{\text{rec}}$ ), the mean value of all SAMs at each redshift is taken. Next, at each redshift, a Gaussian of width equal to the spread between SAMs centred on the mean value is sampled. The function is then fit to these sampled points in order to take into account the differences between SAMs. These steps are repeated  $10^4$  times to obtain the average parameters and their associated errors for each metric at each number density. The detailed results of fitting for all number densities are reported in Table 2.2.

**Table 2.2:** Fitting parameters, described in §2.3.3, for descendants and progenitors selected at a constant cumulative number density across the redshift range  $0 < z < 3$ . Note: for the contamination fraction descendants use Equation 2.9 and progenitors use Equation 2.11 for fitting.

Metric	Descendants			Progenitors		
	<i>a</i>	<i>b</i>	<i>c</i>	<i>a</i>	<i>b</i>	<i>c</i>
$n = 1 \times 10^{-3} [\text{Mpc}^{-3} h^3]$						
$f_{\text{rec}}$	$0.000 \pm 0.000$	$0.480 \pm 0.030$	$0.175 \pm 0.018$	$0.000 \pm 0.000$	$1.212 \pm 0.055$	$-0.260 \pm 0.027$
$f_{\text{contam}}$	$0.511 \pm 0.019$	$-0.010 \pm 0.001$	$1.000 \pm 0.000$	$-0.708 \pm 0.070$	$-0.235 \pm 0.056$	$0.563 \pm 0.064$
$\kappa_{m^*}$	$0.191 \pm 0.066$	$-0.044 \pm 0.019$	-	$-0.131 \pm 0.030$	$0.125 \pm 0.017$	-
$\kappa_{\rho^*}$	$0.592 \pm 0.050$	$-0.156 \pm 0.015$	-	$-0.132 \pm 0.031$	$0.126 \pm 0.018$	-
$n = 5 \times 10^{-4} [\text{Mpc}^{-3} h^3]$						
$f_{\text{rec}}$	$0.000 \pm 0.000$	$0.372 \pm 0.044$	$0.240 \pm 0.032$	$0.000 \pm 0.000$	$1.234 \pm 0.057$	$-0.302 \pm 0.029$
$f_{\text{contam}}$	$0.568 \pm 0.032$	$-0.011 \pm 0.001$	$1.000 \pm 0.000$	$-0.670 \pm 0.035$	$-0.242 \pm 0.017$	$0.580 \pm 0.009$
$\kappa_{m^*}$	$0.294 \pm 0.070$	$-0.071 \pm 0.020$	-	$-0.134 \pm 0.058$	$0.134 \pm 0.036$	-
$\kappa_{\rho^*}$	$0.596 \pm 0.061$	$-0.156 \pm 0.018$	-	$-0.134 \pm 0.058$	$0.134 \pm 0.036$	-
$n = 1 \times 10^{-4} [\text{Mpc}^{-3} h^3]$						
$f_{\text{rec}}$	$0.000 \pm 0.000$	$0.180 \pm 0.047$	$0.430 \pm 0.071$	$0.000 \pm 0.000$	$1.516 \pm 0.155$	$-0.519 \pm 0.079$
$f_{\text{contam}}$	$0.725 \pm 0.050$	$-0.014 \pm 0.001$	$1.000 \pm 0.000$	$-0.623 \pm 0.036$	$-0.216 \pm 0.019$	$0.582 \pm 0.005$
$\kappa_{m^*}$	$0.691 \pm 0.099$	$-0.151 \pm 0.029$	-	$-0.107 \pm 0.072$	$0.144 \pm 0.045$	-
$\kappa_{\rho^*}$	$0.742 \pm 0.062$	$-0.194 \pm 0.018$	-	$-0.107 \pm 0.073$	$0.145 \pm 0.046$	-
$n = 5 \times 10^{-5} [\text{Mpc}^{-3} h^3]$						
$f_{\text{rec}}$	$0.000 \pm 0.000$	$0.128 \pm 0.044$	$0.522 \pm 0.096$	$0.000 \pm 0.000$	$1.723 \pm 0.321$	$-0.626 \pm 0.144$
$f_{\text{contam}}$	$0.787 \pm 0.054$	$-0.014 \pm 0.001$	$1.000 \pm 0.000$	$-0.621 \pm 0.058$	$-0.204 \pm 0.026$	$0.582 \pm 0.009$
$\kappa_{m^*}$	$0.747 \pm 0.136$	$-0.198 \pm 0.041$	-	$-0.083 \pm 0.062$	$0.139 \pm 0.036$	-
$\kappa_{\rho^*}$	$0.868 \pm 0.093$	$-0.228 \pm 0.028$	-	$-0.085 \pm 0.064$	$0.141 \pm 0.037$	-

The descendant galaxy recovery and contamination fraction is fit with a function of form

$$f = a + b \times \exp(c \times (1 + z)), \quad (2.9)$$

where  $a$ ,  $b$  and  $c$  are free parameters. It is observed that forcing  $a$  to zero for the recovery fraction, and  $c$  to unity for the contamination fraction, gives better fits and is more ‘physical’ than allowing it to be a free parameter. The recovery of average stellar mass ( $\kappa_{m^*}$ ) and stellar mass density ( $\kappa_{\rho^*}$ ) are then parametrised as

$$\kappa = a + b \times (1 + z). \quad (2.10)$$

To fit the progenitor galaxy contamination fraction, the parametrisation is modified such that

$$f' = a + b \times (1 + z) + (1 + z)^c. \quad (2.11)$$

Fitted parameters and associated errors are available in Table 2.2 for constant cumulative number density selected samples.

## 2.4 Inferred velocity dispersion selections

In an era of ever larger and deeper spectroscopic surveys, the extra information these observations afford of internal properties could possibly be employed as a better tracer of progenitor or descendant galaxy properties. One product of such a survey is the measurement of the central stellar velocity dispersion of a galaxy.

As the SAM catalogues do not report the velocity dispersions of galaxies, this quantity is inferred using Equations 2.7 and 2.8. The inferred velocity dispersion, as defined here, is a relatively direct observable at the redshifts probed because the stellar mass and half-mass radius are observable. This Chapter reports on the results of using this property in place of stellar mass as the ranking property. As a reminder, this would be achieved observationally by integrating the galaxy velocity dispersion function ( $\sigma_*$  analogue of the GSMF) to obtain the cumulative number density of galaxies as a function of their velocity dispersion. The velocity dispersion limit, above which all galaxies are at a number density  $n$ , can simply be read off.

### 2.4.1 Descendants

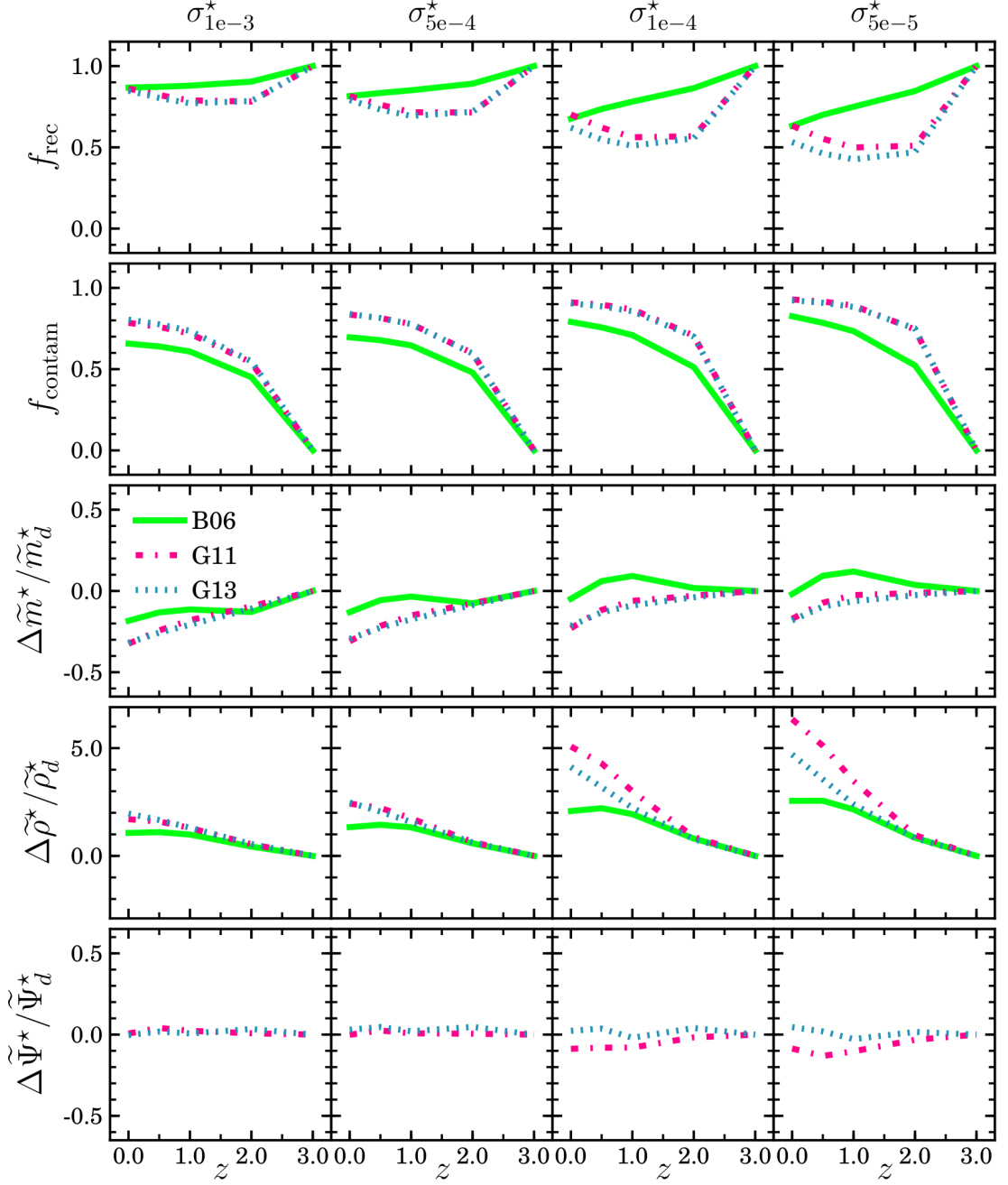
As displayed in Figure 2.5, selecting galaxies above a constant inferred velocity dispersion limit, given in Table 2.3, results in slowly losing descendants with decreasing redshift in the B06 SAM. However, in the G11 and G13 SAMs, the recovery fraction increases below  $z < 2$ . At  $z = 0$ , 90% and 60% of descendant galaxies are selected above the lowest and highest inferred velocity dispersion limits respectively. As with selection above a constant stellar mass limit, the contamination fraction increases exponentially towards lower redshift. At the lowest (highest) velocity dispersion limits there is significant contamination in the observed sample at the level of 70% (90%). Recovery of the descendant mean stellar mass is increasingly underestimated. The true value is maximally underestimated at  $z = 0$  at all inferred velocity dispersion limits by 30%. Conversely, the stellar mass density is increasingly overestimated with time by up to a factor of  $\sim 5$  times the true value. Finally, a constant inferred velocity dispersion selection recovers the descendants' average SFR to within 10% at all limit choices and redshifts.

Figure 2.6 displays the result of a selection at a constant cumulative number density in inferred velocity dispersion. Inferred velocity dispersion is, as defined in this paper, a function of and proportional to stellar mass for each galaxy type (early and late) and so it is not surprising that the results are similar to those obtained in §2.3. Comparing with the stellar mass selections described in §2.3.1, these results suggest inferred velocity dispersion is just as competent a tracer as stellar mass, and even more accurate in some cases. However, any improvements are small over the use of stellar mass at the mass and redshift regimes probed in this work.

### 2.4.2 Progenitors

Figures 2.7 and 2.8 display the results of attempting to trace the progenitors of  $z = 0$  galaxies via selection above a constant inferred velocity dispersion and at a constant cumulative number density, ordered by inferred velocity dispersion, respectively. Selection above a constant limit loses progenitor galaxies from the sample with increasing redshift. By  $z = 3$ , only 10% of true progenitors are sampled at all velocity dispersion limits and SAMs. The average stellar mass is increasingly overestimated with redshift, by 50 – 100% at  $z = 3$ . The stellar mass density is increasingly underestimated. In the B06 SAM, it is even more underestimated at higher inferred velocity dispersion limits than at smaller limits. However, in the G11 and G13 SAMs, it is underestimated by 70% at all limits by  $z = 3$ . Similarly, the SFR is recovered to within 50% in the two SAMs considered.





**Figure 2.5:** Recovery of individual descendants, their average stellar mass, stellar mass density and average SFR (rows) at four constant inferred velocity dispersion selections (columns) covering the range  $-4.3 < \log n < -3.0$ . The B06, G11 and G13 models are represented by solid green, dashed-dotted magenta and dotted blue lines respectively. Inferred velocity dispersion limits given in Table 2.3.

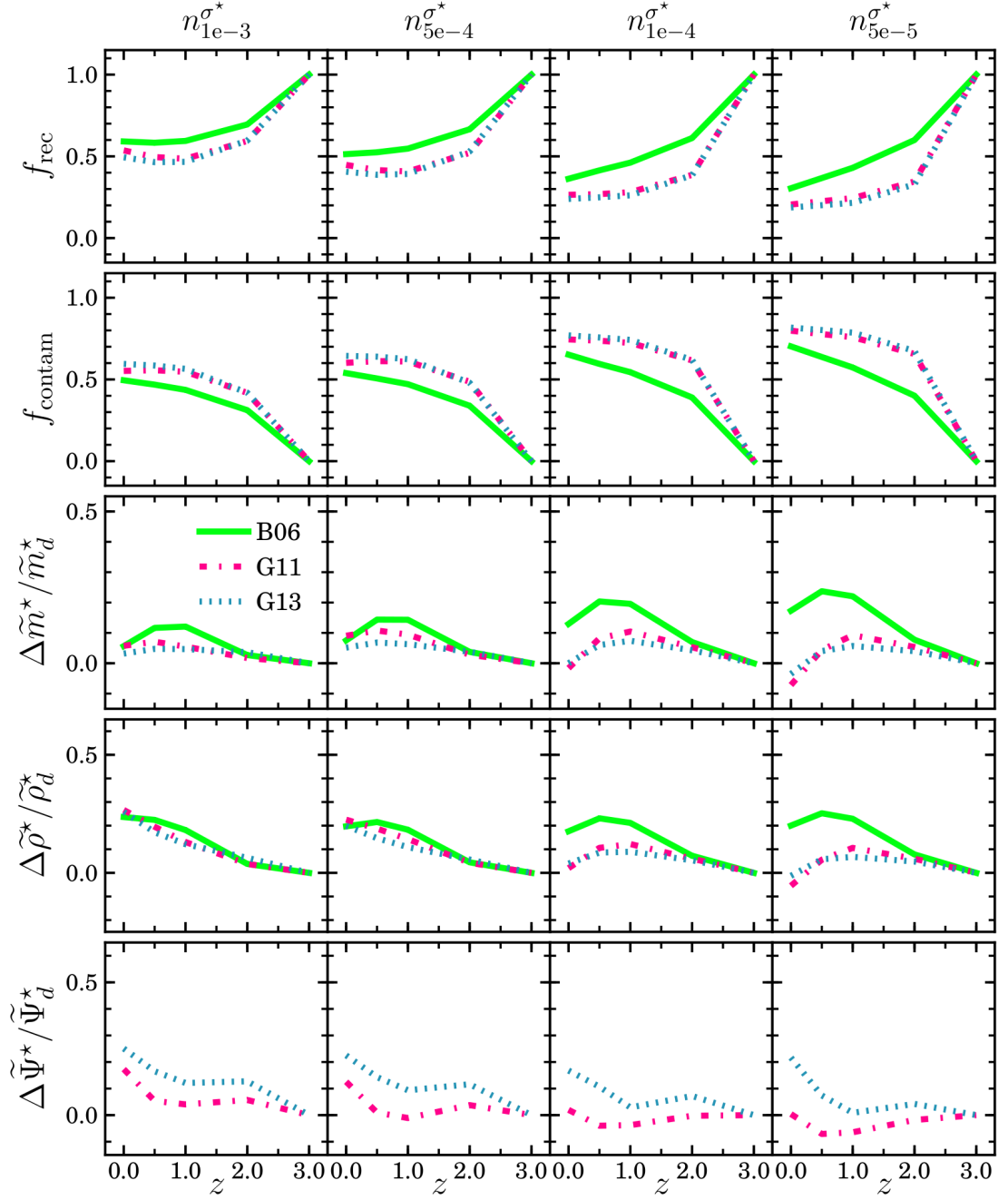


**Figure 2.6:** Recovery of individual descendants, their average stellar mass, stellar mass density and average SFR (rows) for four constant number density selections (columns) covering the range  $-4.3 < \log n < -3.0$ . The B06, G11 and G13 models are represented by solid green, dashed-dotted magenta and dotted blue lines respectively.

**Table 2.3:** Inferred velocity dispersion limits for progenitors and descendants, defined as the minimum inferred velocity dispersion for a number density selection at  $z = 0$  and  $z = 3$  respectively. Inferred velocity dispersions are calculated using Equation 2.7 with the galaxy component stellar masses and sizes reported by each SAM.

SAM	$n$ [ $\text{Mpc}^{-3} h^3$ ]	Descendants	Progenitors
		$\sigma_{\text{lim}}$ [ $\text{km s}^{-1}$ ]	$\sigma_{\text{lim}}$ [ $\text{km s}^{-1}$ ]
B06	$1 \times 10^{-3}$	133.1	198.2
	$5 \times 10^{-4}$	181.7	263.5
	$1 \times 10^{-4}$	309.3	424.5
	$5 \times 10^{-5}$	365.4	502.4
G11	$1 \times 10^{-3}$	83.7	131.8
	$5 \times 10^{-4}$	100.2	156.9
	$1 \times 10^{-4}$	142.1	208.9
	$5 \times 10^{-5}$	161.6	231.0
G13	$1 \times 10^{-3}$	69.3	109.6
	$5 \times 10^{-4}$	84.7	131.8
	$1 \times 10^{-4}$	124.7	181.1
	$5 \times 10^{-5}$	143.8	202.6

Selection at a constant cumulative number density, ordered by inferred velocity dispersion, results in recovery fractions similar to the number density selection using stellar mass. It is found to decrease exponentially from  $z = 0$ , 50% (30%) at the largest (smallest) number densities. Both the average stellar mass and the stellar mass density are recovered to within 40% of the true value across all redshifts, SAMs and number densities investigated in this Chapter. Finally, the SFR is recovered to within 20% at all times.

## 2.5 Discussion

Firstly, let the use of a constant stellar mass selected sample be contrasted against a constant number density (in stellar mass) selected sample. As one may have expected, the former recovers all descendants of an initial high redshift sample. This is due to the definition of a descendant used in this work, and that the stellar mass of systems can only increase with time inside these simulations. Even though the recovery fraction is high, the contamination fraction increases to  $> 80\%$  within  $\sim 2$  Gyr as galaxies, initially unsampled, increase their stellar mass and move into

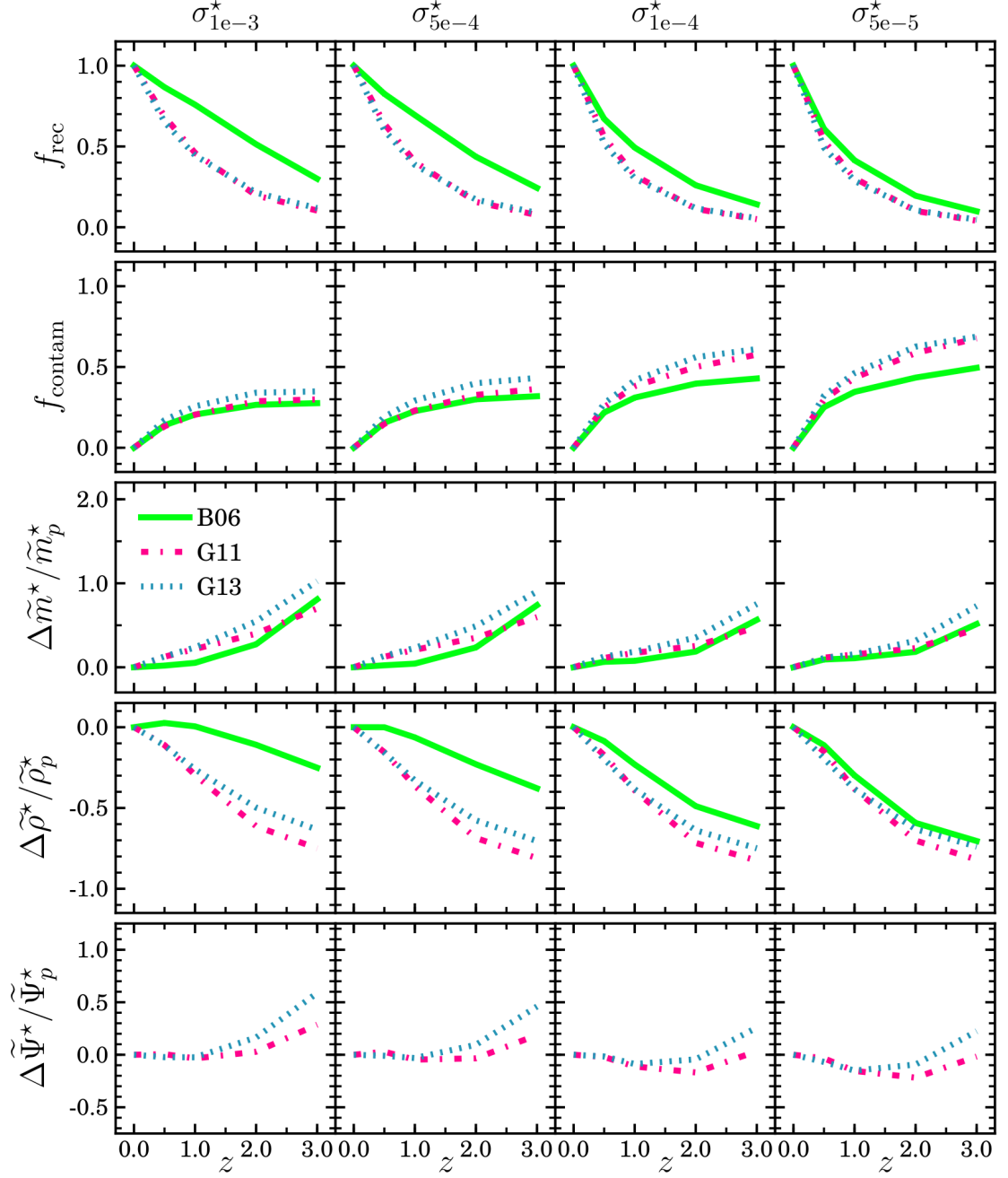


**Figure 2.7:** Recovery of individual progenitors, their average stellar mass, stellar mass density and average SFR (rows) at four constant inferred velocity dispersion selections (columns) covering the range  $-4.3 < \log n < -3.0$ . The B06, G11 and G13 models are represented by solid green, dashed-dotted magenta and dotted blue lines respectively. Inferred velocity dispersion limits given in Table 2.3.

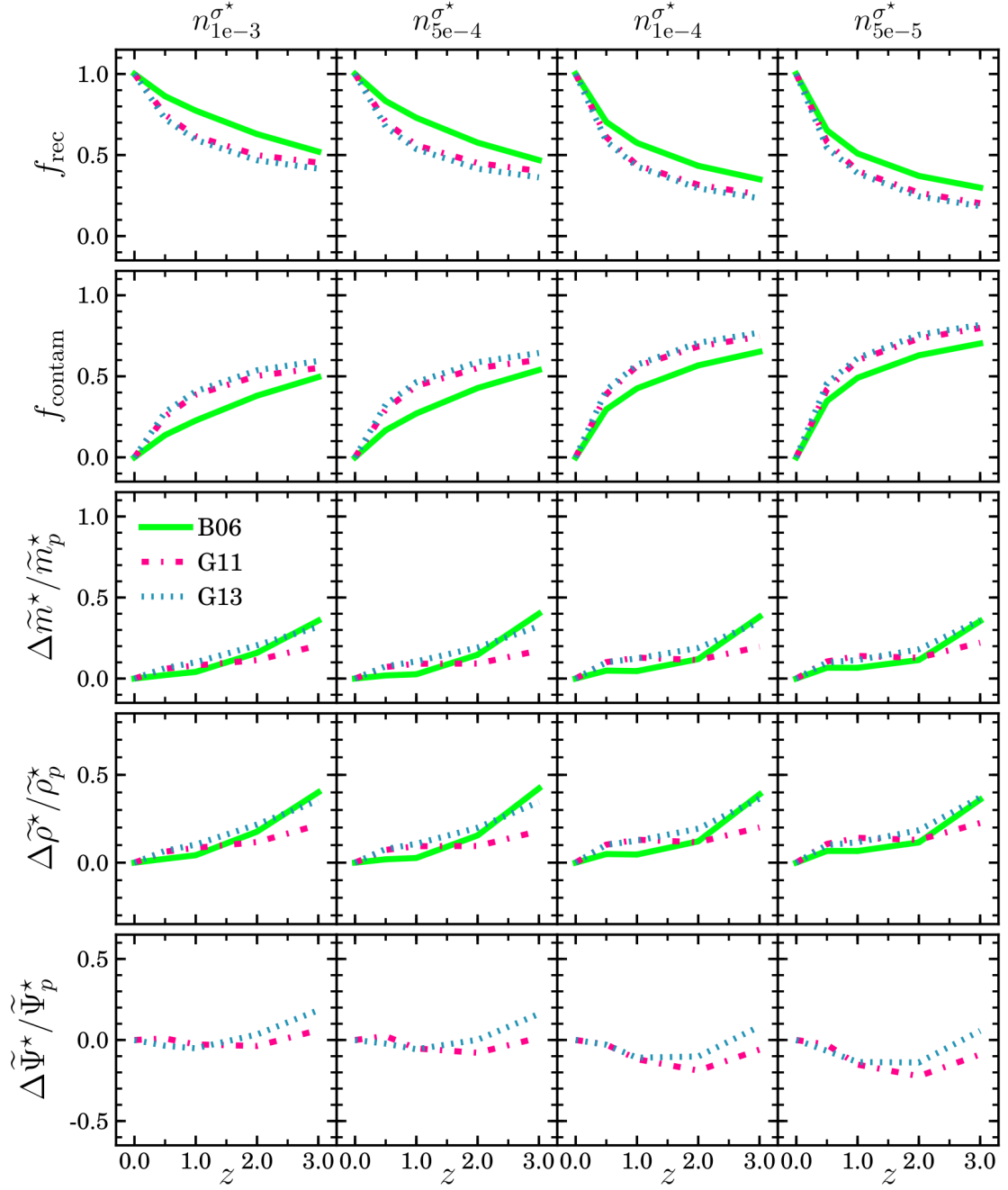


**Figure 2.8:** Recovery of individual progenitors, their average stellar mass, stellar mass density and average SFR (rows) for four constant number density selections (columns) covering the range  $-4.3 < \log n < -3.0$ . The B06, G11 and G13 models are represented by solid green, dashed-dotted magenta and dotted blue lines respectively.

the selection.

Comparing the recovery and contamination fractions obtained through constant number density selections of descendants and progenitors, one can infer how these populations have evolved. Taking the smallest number density choice of  $n = 5 \times 10^{-5} \text{ Mpc}^{-3} h^3$ , at  $z = 0$  30% of the available descendants and nearly three quarters of our selection is contamination. Similarly, at  $z = 3$  just 30% of the progenitors are recovered, and 70% of the sample is contamination. These results suggest that a large fraction of the progenitors of the most massive local galaxies are not the most massive at higher redshifts. Conversely, a large fraction of the most massive galaxies at high redshift are not among the most massive at lower redshifts. The one-to-one mapping in stellar mass rank order that this selection method assumes does not occur within these simulations. Furthermore, lower mass systems from below the selection at high redshift increase their stellar mass at a higher rate than those more massive systems and become most of the most massive galaxies in the local Universe.

It is worth noting that all of the SAMs used in this work fail to match observed galaxy stellar mass functions beyond some redshift (typically  $z \sim 1.5$ ) meaning that they also fail to reproduce the observed evolution of certain galaxy populations. A known problem with the original MS is the cosmology used. Use of a larger  $\sigma_8$  than currently observed (Komatsu *et al.*, 2011; Planck Collaboration *et al.*, 2015) will increase the merger rate and therefore the scatter in the rank order of galaxy stellar mass. Furthermore, this cosmology produces a larger population of quenched galaxies earlier than observed. This requires the SAMs to build up the low mass end of the GSMF at early times in order to match the observed local stellar mass function. See Leja, van Dokkum & Franx (2013) and Guo *et al.* (2011) for an in-depth discussion into this and other issues. Therefore one would expect less scatter in the real Universe, and therefore better recovery of galaxy properties compared to the results obtained here. Cosmological hydrodynamical simulations, e.g. Furlong *et al.* (2015) and Genel *et al.* (2014), show closer agreement with observed galaxy stellar mass functions out to high redshift and may offer a better environment in which to conduct these tests.

### 2.5.1 Where are the progenitors of $z = 0$ massive galaxies at high redshift?

A simple question is where exactly in the ranking (in either stellar velocity dispersion or stellar mass) are the progenitors of the most massive galaxies at  $z = 0$  at

earlier times. Taking the two extremes of the number density choices in this work ( $\log n = -4.3, -3.0$ ), Figure 2.9 presents the stellar mass distributions of the most massive progenitors of  $z = 0$  galaxies (top row). At each redshift the stellar mass distributions are fit with a Gaussian function and show in the middle panels that fit residuals (difference between the fitted Gaussian function and the distribution of stellar masses) are minimal at  $< 5\%$ . This is done to quantify the changes in these distributions as a function of redshift. Shown in the bottom row of the Figure are the properties of these distributions as a function of redshift. The mean and widths (distribution standard deviation) are shown in the bottom left and bottom right panels respectively.

At higher redshift the mass distributions move systematically towards smaller mass galaxies and the stellar mass distributions widen. At the highest redshift, the distributions are found to have standard deviations of  $\sigma = 0.32 [\log M_\odot h^{-1}]$  and  $\sigma = 0.21 [\log M_\odot h^{-1}]$  for the largest and smallest number density selections. In both cases, the distributions increase in width by a factor of  $\sim 3$  since  $z = 0$ .

Furthermore, the selections made by a constant number density (the mass limits of which are indicated by the vertical dashed lines in the top panels of Figure 2.9) show that beyond  $z > 1$ , the majority of the progenitors are below this limit (i.e. the peak of the actual progenitor stellar mass distribution is found at a lower stellar mass than the selection's stellar mass limit). Therefore, within the Millennium Simulation at the very least, the progenitors of the most massive local galaxies are not only the most massive galaxies at higher redshifts - they span a wide range of masses at higher redshifts. For example, the most massive progenitors span more than an order of magnitude ( $> 1$  dex) in stellar mass for the largest initial number density selection (top right panel) and  $\sim 0.5$  dex for the smallest number density at  $z = 3$ . As shown in this work however, this does not appear to significantly impact the ability of a number density selected sample to recover the average stellar mass, star-formation rate or stellar mass density.

### 2.5.2 How do mergers affect the selections?

The number of progenitors or descendant galaxies can change over time due to mergers between objects within the initial sample. Selecting galaxies at a constant number density ignores these changes, and potentially contributes to the over- or underestimation of ensemble properties.

To determine the extent of this, the number of mergers between the descendants of an initial selection at  $z = 3$  are calculated within the B06 and G13 SAMs, as these are based on different dark matter merger trees from the MS. In B06, 1.3%

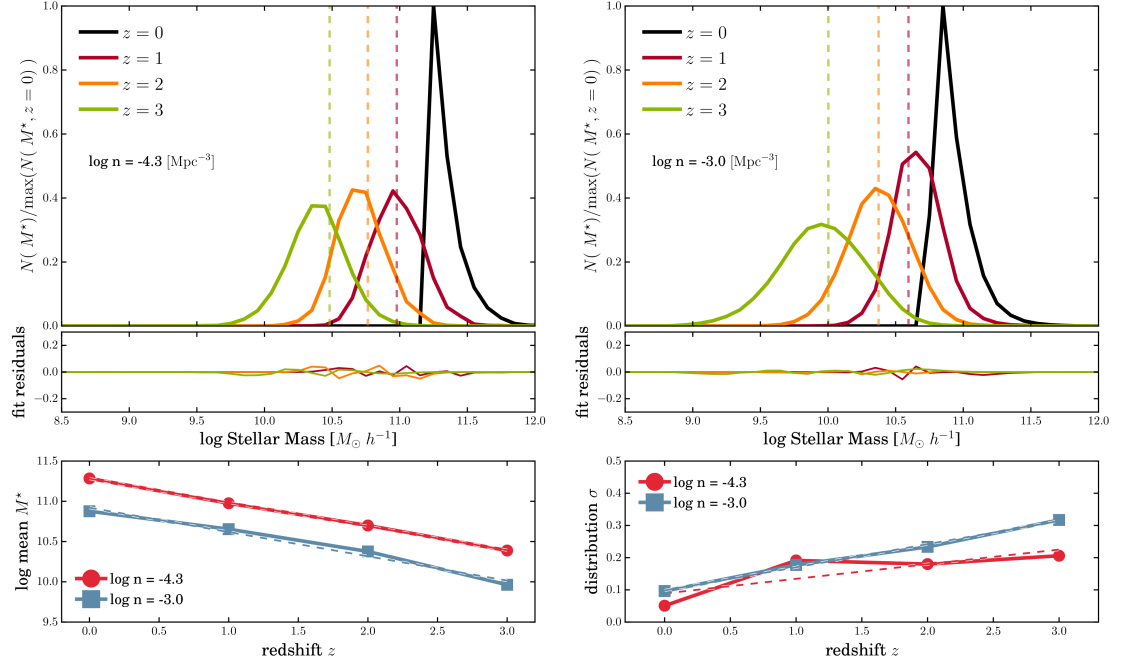


**Figure 2.9:** Progenitor mass distributions in the Guo *et al.* (2013) SAM for  $z = 0$  galaxy selections at constant number densities  $\log n = -4.3 \text{ Mpc}^{-3} h^3$  (top left) and  $\log n = -3.0 \text{ Mpc}^{-3} h^3$  (top right). These number densities correspond to galaxies with a  $z = 0$  stellar mass of  $\log M^* > 11.21 [M_\odot h^{-1}]$  and  $\log M^* > 10.77 [M_\odot h^{-1}]$ , respectively. Stellar mass distributions at  $z = 0, 1, 2, 3$  are given in black, red, orange and green solid lines. Dashed vertical lines represent the stellar mass cuts inferred from a number density cut at each redshift. Residuals from Gaussian fits to these distributions are displayed in the middle panels. Parameters from Gaussian fits to the progenitor masses are shown in the bottom row, with the mean stellar mass and standard deviation at bottom left and bottom right respectively with the largest (blue squares) and smallest (red circles) number densities plotted as a function of redshift.



and 15.5% of galaxies in the initial selection are lost due to mergers from  $z = 3$  to  $z = 0$  at the smallest and largest number density selections. In the G13 SAM however, these measurements are higher at 10.9% and 29.6%, respectively. For the most massive galaxies, this translates to approximately 3 – 5 mergers per massive galaxy (see Table 2.1 for mass limits) over the redshift range  $0 < z < 3$ . It must be noted that these numbers represent all (total) mergers, and are not major mergers as they may include some mergers with mass ratios greater than 1 : 4, the most widely used definition. These measurements are slightly higher compared with pair fraction and morphological observations of major mergers in comparably massive galaxies (see, e.g., Bluck *et al.*, 2009; Conselice, Yang & Bluck, 2009; Man *et al.*, 2012).

An intriguing feature of Figure 2.2 is the recovery metrics for the average stellar mass and stellar mass density. A naive expectation would be for these metrics to be equal as the selection is made at a constant cumulative number density and therefore  $N_{\text{true}} = N_{\text{obs}}$ . However, the internal mergers mentioned above mean that  $N_{\text{true}} \leq N_{\text{obs}}$  and thus  $\kappa_{m*} \leq \kappa_{\rho*}$ . Using Equation 2.5, the effect of internal mergers on these recovery metrics can be predicted. As  $\approx 1\%$  ( $\approx 16\%$ ) of galaxies within the initial selection are lost within the smallest (largest) number density selection from  $z = 3$  to  $z = 0$ , it would be expected at  $z = 0$  that  $\kappa_{m*} = 0.99\kappa_{\rho*} - 0.01 \approx 0.83$  ( $\kappa_{m*} = 0.84\kappa_{\rho*} - 0.16 \approx 0.22$ ). Similar results are expected for the G13 SAM. It can be seen from the plot that these are the values that are found and so the difference between these two metrics for a constant number density selection can be entirely attributed to internal mergers reducing the number of galaxies within the initial selection. Additionally, it can be seen in Figure 2.4 that  $\kappa_{m*} = \kappa_{\rho*}$  for galaxy progenitors selected at a constant number density. As every galaxy has a progenitor, it means that the number of galaxies within the initial  $z = 0$  selection does not change.

At increasingly larger number densities, mergers within the descendant population may become increasingly important. As such, selection at a constant number density may not be applicable over such a redshift range. It may be appropriate to correct the number density between redshift bins to account for mergers that have occurred within the sample. However, the reduction of the number density in response to descendant galaxy mergers does not result in the desired effect. Qualitatively, reducing the number density at each redshift results in higher stellar mass limits. The average stellar mass of the observed sample would therefore increase. As the average stellar mass and stellar mass density are already overestimated, this discrepancy would only increase. On the other hand, the ‘un-merging’ of galaxies

going backwards in time would increase the number density used to trace progenitor galaxies. This would lower the stellar mass limit used to select the samples and thus decrease the measured average stellar mass of the observed samples. As this quantity is also overestimated, this discrepancy would be reduced. However, as the number density would increase, contamination would also increase. It is thus a matter of trade-off.

### 2.5.3 Can we infer velocity dispersion in a semi-analytical model?

This work investigates inferred velocity dispersion in place of stellar mass as a ranking property due to evidence of a shallower and more stable evolution with redshift. It is prudent to ask whether this quantity can be accurately obtained from the SAMs used in this work. Use of Equation 2.7 implicitly assumes a spherically symmetric system and would correspond to a system with a Sérsic index of  $n \approx 5.5$  (Cappellari *et al.*, 2006). However, the factor in the denominator doesn't account for multiple components (i.e. a combination of a bulge and disk) and is influenced not only by Sérsic index but also galaxy black hole mass. Thus the value calculated using this equation is a simplistic estimate at best and not strictly applicable to every type of galaxy. Furthermore, disk-dominated systems are not spherical and isotropic and thus this equation is not strictly applicable to these types of systems.

Using the bulge-to-total stellar mass ratio (B/T) as a proxy for disk and bulge dominated morphologies, it is found that the most massive galaxies at  $z = 0$  ( $z = 3$ ) in the B06 SAM are typically bulge dominated with only 30% (40%) having  $B/T < 0.5$ . While this suggests Equation 2.7 is applicable at these redshifts, this SAM does not reproduce observations of larger disk-dominated fractions at high redshift (Bluck *et al.*, 2014; Bruce *et al.*, 2014). The G13 SAM reproduces observations more closely with 50% (95%) of systems having  $B/T < 0.5$  at  $z = 0$  ( $z = 3$ ). Because of this, the velocity dispersions inferred within this SAM at the highest redshifts probed can be considered discrepant with observations only at the highest redshifts. While these caveats must be taken into consideration, the values of velocity dispersion inferred are physical and generally in agreement with observations of spheroidal/passive systems (Bernardi *et al.*, 2010; Oser *et al.*, 2012), with  $\sigma_*$   $\sim 60$ –500 km/s depending on the SAM.

It is also essential to consider whether the physical sizes of the simulated galaxy components can be used to infer the velocity dispersion. In G11 and G13, the resulting mass-size relations are shallower than the observations (see, e.g., Lani

*et al.*, 2013; van der Wel *et al.*, 2014) with both masses and sizes larger (smaller) at low (high) redshift (Guo *et al.*, 2011). For the purposes of this work however, the only criteria is that the evolution in  $M/R$  is correctly reproduced, and it is possible that, at least within G11 and G13, this may not be the case. From this it is concluded that inferred velocity dispersion could provide a useful property with which to trace the evolving properties of the most massive galaxies. However, more detailed future simulations that accurately reproduce the evolution in both stellar mass and galaxy component sizes, or that report a value for velocity dispersion directly, are needed to confirm these findings.

#### 2.5.4 Comparison with previous works

The results presented in this Chapter are consistent with the work of Leja, van Dokkum & Franx (2013) who investigate cumulative number density selection of descendant galaxies over  $0 < z < 3$  in the range  $0.5 < n [10^{-4} \text{ Mpc}^{-3}] < 8.0$  using the G11 SAM. Uncorrected for mergers and growth scatter, they show that for the two smallest number densities, the median stellar mass evolution is overestimated by between 0.05 – 0.15 dex (12 – 41%) by  $z = 0$ . Using the mean stellar mass, this work finds an overestimate at  $n = 5 \times 10^{-5} \text{ Mpc}^{-3}$  of 40% in the G11 and G13 SAMs. Most recently, Henriques *et al.* (2015, H15) contrasted the mean stellar mass of progenitors derived from a constant number density selection with the values obtained from their SAM using a Planck (Ade *et al.*, 2014) cosmology. They found that mean stellar mass evolution is overestimated by a factor of 3 – 5 for the progenitors of galaxies with a  $z = 0$  stellar mass between  $10.25 < \log M_* [\text{M}_\odot \text{ h}^{-2}] < 11.25$ . This is a larger increase than we find for similar mass galaxies. It is suggested that this discrepancy is due to the ability of H16 to correctly reproduce the abundance of massive galaxies out to higher redshift. With less massive and passive galaxies, H06 must produce a larger evolution in stellar mass from high redshift to match the local stellar mass function.

## 2.6 Summary

This Chapter has presented comparisons of the use of two popular galaxy selection methods which aim to trace galaxy populations across large swathes of time. Furthermore, it has contrasted the use of galaxy stellar mass and inferred velocity dispersion in semi-analytical models based on the output of the Millennium Simulation over the redshift range  $0 < z < 3$ . Galaxies selected above a constant limit of

stellar mass in this redshift range are probed, and the main results for this selection are:

- Descendants can be fully recovered over the entire redshift range regardless of mass limit choice. However, progenitors of  $z = 0$  galaxies are lost from the selection with at least 80% below the stellar mass limit at  $z = 1$ .
- Average descendant ensemble stellar mass is increasingly underestimated with increasing redshift by an amount that varies between SAMs but is, on average, around 50% at  $z = 0$ . Similarly, the average stellar mass of progenitors is increasingly overestimated. At  $z = 0$ , average progenitor stellar mass is overestimated by a factor of  $\sim 5$ .

Additionally, selecting galaxies at a constant cumulative number density in stellar mass, it is concluded that:

- Recovery of individual descendant galaxies falls exponentially with a time scale dependent on choice of number density. Just 30% of the most massive galaxies (selected at  $\log n = -4.3 \text{ Mpc}^{-3} h^3$  at  $z = 3$ ) are at the same cumulative number density at the lowest redshift. For the largest number density selection, this increases to 60%. Recovery of progenitors is similar, but with 50 – 30% recovered at the highest redshifts, depending on choice of number density.
- The average stellar mass of descendants is overestimated by 15% (70%) at the highest (smallest number densities) by  $z = 0$ , increasing linearly from  $z = 3$ . Furthermore, independent of number density, progenitors' average stellar mass is overestimated by  $\sim 50\%$  at the highest redshift.

Finally, it was investigated whether inferred velocity dispersion could be used as a property with which to trace galaxies over the same redshift range. It is found that a constant number density in velocity dispersion recovers average stellar mass, stellar mass density and average SFR to within  $\pm 50\%$  for both descendants and progenitors. Furthermore, selecting galaxies at a constant velocity dispersion limit recovers the aforementioned properties to within  $\pm 80\%$  of the true values. However, these results are based on inferring velocity dispersion of galaxies which may not be strictly applicable to some SAMs and redshift ranges. The results of this study give weight to the use of velocity dispersion as a ranking indicator, however further study is required to confirm this. This new insight could most likely come from simulations where this property is simulated or calculated directly, e.g. from identified stellar

mass particles in a galaxy, rather than the indirect method used in this work. Such resolution requirements may not be currently achievable.

In conclusion, selecting galaxies at a constant cumulative number density is found to trace the true evolution of average stellar mass and the average SFR of the progenitors and descendants of galaxies in initial selections at  $z = 0$  and  $z = 3$ . However, it does not trace the exact same galaxies but rather galaxies with very similar properties. Furthermore, it is found that selecting galaxies above a constant stellar mass with redshift returns the actual evolution within a larger factor of between two and thirty.

## Chapter 3

# Measuring the Merging Histories of Massive Galaxies

This chapter presents a new method, called **Pyrus**<sup>1</sup>, with which to measure the close-pair fraction of galaxies. The method, built upon the photometric pair fraction method of López-Sanjuan *et al.* (2015), is able to measure the pair fraction for stellar mass selected merger definitions of galaxy samples constructed from flux-limited photometric surveys. Various statistical weights and corrections are defined and its versatility explored in the following Chapter.

### 3.1 A short history of measuring merger histories

The rate at which galaxies merge is one of the fundamental measures of galaxy evolution. While evidence for the  $\Lambda$ CDM paradigm of hierarchical structure assembly is overwhelming (e.g., Komatsu *et al.*, 2011; Planck Collaboration *et al.*, 2015), the role of galaxy mergers or indeed the rate at which they occur remain unsettled and controversial topics at best.

It has long been known that mergers between galaxies — and gravitational interactions in general — imprint signatures on the physical appearance (i.e. morphology) of galaxies. Numerical simulations (e.g., Toomre & Toomre, 1972; Mihos & Hernquist, 1996; Cox *et al.*, 2006) of merging events have demonstrated convincingly that galaxies possessing irregular morphologies are extremely likely the result of mergers. It is therefore no surprise that identifying galaxies with peculiar morphologies has become a fruitful route for the study of mergers. The most commonly used structural measurements used to identify mergers are non-parametric. As such they do not make underlying assumptions about the structure of galaxies, but quan-

---

<sup>1</sup>Pyrus is the genus of tree upon which pears grow.

tify their obvious structural features. Such measurements grew in popularity with the first images of distant galaxies obtained by the Hubble Space Telescope. One particular measure of galaxy structure is the use of concentration (C), asymmetry (A), and clumpiness (S) (e.g., Conselice *et al.*, 2003). Asymmetry is most simply defined as

$$A = \min \left( \frac{\sum |I_0 - I_{180}|}{\sum |I_0|} \right) - \min \left( \frac{\sum |B_0 - B_{180}|}{\sum |B_0|} \right), \quad (3.1)$$

and can be considered the fraction of a galaxy's light contained in non-symmetric components. Here  $I_0$  represents the original image of the galaxy,  $I_{180}$  is the original image rotated about its centre by 180 degrees, and  $B$  is patch of blank sky nearby the galaxy of interest.

Similar in many ways to the Sérsic index (Sérsic, 1963), concentration (C) quantifies the amount of light near to the centre of a galaxy compared to its outer regions. This parameter has been used both qualitatively and quantitatively within the literature for several decades (e.g., Abraham *et al.*, 1994; Bershadsky, Jangren & Conselice, 2000). In general terms, it is usually defined as

$$C \propto \log \left( \frac{r_{\text{out}}}{r_{\text{in}}} \right) \quad (3.2)$$

where  $r_{\text{out}}$  and  $r_{\text{in}}$  are the radii which contain 80% and 20% of a galaxy's total light, respectively (Conselice, 2003).

Finally, the clumpiness quantifies the smoothness of a galaxy's light distribution. It is typically defined in terms of the difference found by subtracting a smoothed image of a galaxy from it's original image, and is usually defined in the following form:

$$S \propto \left( \frac{\sum (I - I^\sigma)}{\sum I} \right) - \left( \frac{\sum (B - B^\sigma)}{\sum B} \right), \quad (3.3)$$

where  $I$  is the original galaxy image,  $I^\sigma$  is the smoothed image (where the smoothing kernel is generally a Gaussian and is a function of the size of a galaxy), and  $B$  represents a patch of nearby blank sky.

Another common set of parameters are the Gini coefficient,  $G$ , and  $M_{20}$  (e.g., Abraham, van denBergh & Nair, 2003; Lotz, Primack & Madau, 2004), which are used in the same way as asymmetry, concentration and clumpiness. Larger values of  $G$  indicate an unequal distribution of light in a galaxy, while  $M_{20}$  is the second-order moment of the largest 20% of fluxes in a galaxy. Though these and other methods (e.g., Freeman *et al.*, 2013; Pawlik *et al.*, 2016) compete, they are all successful in

detecting galaxies at some stage of a merger. However, the need for costly high resolution and high signal-to-noise observations necessarily limits the use of these methods to relatively small sample sizes, especially in the high redshift Universe. It is at these distances that the rest-frame regime in which galaxies are observed becomes ever bluer, and this fact must be accounted for via the use of morphological  $k$ -corrections to ensure comparisons are being made consistently across cosmic time.

Another approach is to perform a search for galaxies with small projected separations on the sky in order to probe the properties and rates of merging galaxies across cosmic time (e.g., Zepf & Koo, 1989; Carlberg, Pritchet & Infante, 1994; Patton *et al.*, 2000; Ellison *et al.*, 2008). The basis of this technique is the simple measurement of the fraction of pairs of galaxies undergoing a merger in a sample. This pair fraction,  $f_{\text{pair}}$ , is assumed — and it is hard to convince oneself otherwise — to be directly proportional to the rate at which galaxies merge. Before the work of Patton *et al.* (1997), various biases caused wildly varying estimates of the merger rate to be found. The worst offender was the bias introduced when comparing low- and high-redshift samples drawn from flux-limited surveys. Such bias would ensure that fewer companions would be found at fixed luminosity for high-redshift galaxies compared to those at low redshift. The result of this would be merger fractions erroneously measured to be lower at high redshift. Other issues, such as line-of-sight projections and small samples sizes, prohibited a consensus from being reached. As such, true comparisons were not being made and evolution incorrectly inferred.

Through the use of computer simulations, it has now been shown that galaxies within some small separation ( $r_p < 100$  kpc) will more than likely coalesce, typically less than 1 Gyr later (e.g., Mihos, 1995; Kitzbichler & White, 2008). Additionally, N-body simulations of individual merger events with varying physical parameters (e.g., stellar mass ratio, inclination, galaxy type) have offered the first estimates of the timescale,  $\langle T_{\text{obs}} \rangle$ , over which galaxy mergers are visible to certain parameter choices (e.g., Lotz *et al.*, 2011). This quantity in particular is of the utmost importance when the conversion from pair fraction to merger rate is performed. As might be expected, the timescale over which a close-pair is observable is correlated with physical separation conditions, and the stellar mass ratio which defines a close-pair of galaxies. For major mergers, defined as a stellar mass ratio of  $\mu > 0.25$ , and a physical separation of  $r_p < 30$  kpc, the timescale is within 0.3–0.6 Gyr (Lotz *et al.*, 2010, 2011).



## 3.2 Counting close-pairs with Pyrus

The ultimate aim of any close-pairs statistics study is to measure the fraction of galaxies undergoing a merger within a defined sample. Spectroscopic studies performed in the local Universe often define a close-pair as two galaxies within some *projected* separation and within some relative velocity offset, typically taken to be  $\Delta v \leq 500 \text{ km s}^{-1}$  (e.g., Bluck *et al.*, 2012; Tasca *et al.*, 2014). Such a definition can then be used to achieve the goal of measuring the pair fraction,  $f_{\text{pair}}$ , defined as

$$f_{\text{pair}} = N_{\text{pairs}}/N_{\text{tot}}, \quad (3.4)$$

where  $N_{\text{pairs}}$  is the number of galaxy close-pairs and  $N_{\text{tot}}$  is the total number of galaxies in the parent sample. The former is the number of close-pairs rather than the number of galaxies in close-pairs — a measure used in other literature studies — which would be a factor of two larger.

The method presented here builds upon that presented in López-Sanjuan *et al.* (2015) to enable measurements of the merger fraction for large flux-limited photometric samples of galaxies across wide redshift ranges. This is achieved using photometric redshift ( $z_{\text{phot}}$ ) probability distribution functions (PDFs) — a necessity in modern wide area, deep surveys — which naturally accounts for the uncertainty in redshift during the close-pair selection procedure.

### 3.2.1 Initial close-pair selection

An initial list of *projected* close-pairs is constructed from the science catalogues in each region described in Section §4.2. This is achieved by selecting pairs of galaxies which exhibit a *projected* separation less than the maximum angular separation of the redshift range probed. As an example, at a redshift of  $z = 0.2$  a separation of 30 kpc (20 kpc) corresponds to a maximum separation of  $9''$  ( $6''$ ) on the sky. Duplicates are removed whereby the galaxy with the larger stellar mass at its respective best-fit photometric redshift is classed as the primary galaxy, and the lower mass system classed as the secondary galaxy within the close-pair.

### 3.2.2 The pair probability function

A redshift probability function,  $\mathcal{Z}(z)$ , is calculated for each close-pair system identified in Section §3.2.1. This quantity encodes the number of close-pairs contributed based solely on the line-of-sight information encoded within each galaxy’s redshift

PDFs. This quantity is defined as

$$\mathcal{Z}(z) = \frac{2 \times P_1(z) \times P_2(z)}{P_1(z) + P_2(z)} = \frac{P_1(z) \times P_2(z)}{N(z)} \quad (3.5)$$

where  $P_1(z)$  and  $P_2(z)$  are the PDFs for the primary and secondary galaxies, respectively. From Equation 3.5 it can be seen that the redshift probability function is normalised such that each pairing can maximally contribute a single pair when integrated over the full redshift range. This can be written as

$$N_{\text{pair},j} = \int_0^\infty \mathcal{Z}_j(z) dz \quad (3.6)$$

and can range between 0 and 1. As each galaxy in the primary sample is allowed to have multiple companions, each *projected* close-pair is considered separately and included in the total pair count.

### 3.2.3 Close-pair constraints

Redshift dependent masks are required to enforce the remaining close-pair selection criteria. These are zero where conditions are not met and unity otherwise. The nomenclature of López-Sanjuan *et al.* (2015) is continued in this work. Therefore the angular separation mask,  $\mathcal{M}^\theta(z)$ , is defined as

$$\mathcal{M}^\theta(z) = \begin{cases} 1, & \text{if } \theta_{\min}(z) \leq \theta_j \leq \theta_{\max}(z), \\ 0, & \text{otherwise.} \end{cases} \quad (3.7)$$

Here the minimum and maximum angular separations are a function of redshift and defined as  $\theta_{\min} = r_p^{\min}/d_A(z)$  and  $\theta_{\max} = r_p^{\max}/d_A(z)$ , respectively, where  $d_A(z)$  is the angular diameter distance. In contrast to López-Sanjuan *et al.* (2015), the close-pairs within this work are selected based on stellar mass rather than luminosity. Therefore the pair selection mask,  $\mathcal{M}^{\text{pair}}$ , is defined as

$$\mathcal{M}^{\text{pair}} = \begin{cases} 1, & \text{if } M_*^{\text{lim},1}(z) \leq M_{*,1}(z) \leq M_{*,\max} \\ & \text{and } M_*^{\text{lim},2}(z) \leq M_{*,2}(z) \\ 0, & \text{otherwise.} \end{cases} \quad (3.8)$$

where  $M_{*,1}(z)$  and  $M_{*,2}(z)$  are the stellar masses as a function of redshift for the primary and secondary galaxies, respectively. The limiting stellar masses in Equation

3.8 are given by

$$M_*^{\text{lim},1}(z) = \max(M_*^{\text{min}}, M_*^{\text{comp}}(z)) \quad (3.9)$$

and

$$M_*^{\text{lim},2}(z) = \max(\mu M_{*,1}(z), M_*^{\text{comp}}(z)). \quad (3.10)$$

Here  $M_*^{\text{comp}}(z)$  represents the redshift-dependent stellar mass completeness limit of each survey region,  $M_*^{\text{min}}$  defines the minimum stellar mass of the primary sample selection, and  $\mu$  represents the choice of stellar mass ratio which is typically  $\mu = 1/4$  for major mergers and  $\mu = 1/10$  for minor mergers. The redshift-dependent stellar mass completeness limits are discussed in Section §4.2. Application of the pair selection mask in Equation 3.8 ensures that (1) the primary galaxy is within the correct stellar mass range, (2) the stellar mass ratio of the primary and secondary galaxies corresponds to either major or minor mergers, and (3) primary and secondary galaxies are both above the stellar mass completeness limit of the survey region they are contained within. With these masks for each *projected* close-pair, the pair probability function,  $\text{PPF}(z)$ , is simply given by

$$\text{PPF}(z) = \mathcal{Z}(z) \times \mathcal{M}^\theta(z) \times \mathcal{M}^{\text{pair}}(z). \quad (3.11)$$

The integral of the PPF provides the *unweighted* number of close-pairs (as defined by the chosen selection criteria) that two galaxies contribute to the measured pair fraction.

### 3.2.4 Selection effect corrections

The flux-limited nature of the photometric surveys used in this study combined with the stellar mass selection of close-pairs requires several selection effects to be appropriately accounted for.

Firstly, a primary galaxy may possess a stellar mass close to the stellar mass completeness limit of the survey region at some redshift. Such a scenario may reduce the stellar mass range in which secondary companions can be found and result in fewer companions found than may exist in reality. In order to address this potential bias, a statistical correction is made involving the galaxy stellar mass function,  $\phi(M_*, z)$ , at the redshift range of interest. Simply, each secondary companion of a

primary galaxy is assigned a weighting defined as

$$\omega_2^{\text{comp}}(z) = \left[ \frac{\int_{M_*^{\text{lim}}(z)}^{M_{*,1}(z)} \phi(M_*, z) dM_*}{\int_{\mu M_{*,1}(z)}^{M_*^1(z)} \phi(M_*, z) dM_*} \right]^{-1}. \quad (3.12)$$

This correction is essentially the inverse of the ratio of galaxy number densities above and below the stellar mass completeness limit. Applying this correction provides close-pair fractions corresponding to a volume-limited study. These secondary weights are the stellar mass analogue of the luminosity weights presented in Patton *et al.* (2000).

A second weighting is applied to the primary galaxies in order to correct for those objects that will have fewer *observed* companions because of their proximity to the completeness limit of the survey region. The primary galaxy completeness weight is defined as

$$\omega_1^{\text{comp}}(z) = \frac{\int_{M_*^{\text{lim}}(z)}^{M_*^{\text{max}}(z)} \phi(M_*, z) dM_*}{\int_{M_*^{\text{min}}(z)}^{M_*^{\text{max}}(z)} \phi(M_*, z) dM_*} \quad (3.13)$$

where  $M_*^{\text{min}}$  and  $M_*^{\text{max}}$  are the minimum and maximum stellar masses of the primary sample for which the merger fraction is being calculated.

Galaxies close to the survey edges or near areas with corrupt photometry (e.g. bright stars, cross-talk) may possess a reduced spatial area in which to find companions. As the spatial search area is a function of a fixed physical search radius, the correction is necessarily a function of redshift. This is achieved by producing a mask image which is 1 where good photometry exists and 0 elsewhere. For each galaxy within the primary sample ‘photometry’ is performed on this mask image over the spatial search area. An area weight is assigned, defined as

$$\omega_{\text{area}}(z) = \frac{1}{f_{\text{area}}(z)}, \quad (3.14)$$

where  $f_{\text{area}}(z)$  is the fraction of the mask image with good photometry within the search annulus. As the search area is a function of redshift, so too are the area weights.

The final weighting applied is based on the photometric redshift quality, encoded by the Odds sampling rate. The Odds parameter,  $\mathcal{O}$ , is defined by Benitez (2000)

and Molino *et al.* (2014) as

$$\mathcal{O}_j = \int_{-K(1+z_p)}^{+K(1+z_p)} P_j(z) \quad (3.15)$$

for each galaxy  $j$ , where  $z_p$  is the galaxy's best-fit photometric redshift and  $P_j(z)$  is the redshift PDF of the galaxy. The value of  $K$  is chosen to represent the typical photometric redshift accuracy of the data in question. In Molino *et al.* (2014)  $K = 0.0125$  due to the use of 20 medium-band ( $\sim 300\text{\AA}$  in width) filters, however the surveys used in this work typically make use of broad-band filters. For the measurements in Chapter 4 and Chapter 5 a larger value of  $K = 0.05$  is chosen as a result of comparing photometric and spectroscopic redshifts in the used surveys.

Therefore the Odds sampling rate (OSR) is defined as the fraction of galaxies with an Odds parameter above this election normalised by the total number of galaxies as a function of apparent magnitude,  $m$ . This is written as

$$\text{OSR}(m) = \frac{\sum N(\mathcal{O} \geq 0.3)}{\sum N(\mathcal{O} \geq 0)}, \quad (3.16)$$

which can be used to compute the weight for a particular galaxy,  $j$ , with magnitude  $m_j$  as

$$\omega_j^{\text{OSR}} = \frac{1}{\text{OSR}(m_j)}. \quad (3.17)$$

Combining these weights, the primary and secondary galaxy weights can be consolidated and defined. Each secondary galaxy around a primary galaxy is assigned a weight given by

$$\omega_2(z) = \omega_1^{\text{area}}(z) \times \omega_1^{\text{comp}}(z) \times \omega_2^{\text{comp}}(z) \times \omega_1^{\text{OSR}} \times \omega_2^{\text{OSR}} \quad (3.18)$$

and each primary galaxy is weighted by

$$\omega_1(z) = \omega_1^{\text{comp}}(z) \times \omega_1^{\text{OSR}}. \quad (3.19)$$

### 3.2.5 The close-pair fraction

Classically, the close-pair fraction is defined as the number of galaxy close-pairs divided by the total number of galaxies in the primary sample. This can be written as  $f_{\text{pair}} = N_{\text{pair}}/N_{\text{tot}}$ . In the prescription presented here, the number of close-pairs associated with galaxy  $i$  in the primary sample, over the redshift range  $z_{\text{min}} < z <$

$z_{\max}$ , is given by

$$N_{\text{pair}}^i = \sum_j \int_{z_{\min}}^{z_{\max}} \omega_2^j(z) \times \text{PPF}_{i,j}(z) \, dz \quad (3.20)$$

where  $j$  indexes the potential secondary galaxies around the primary galaxy and  $\text{PPF}_{i,j}(z)$  the pairs' pair probability function. Accordingly, the contribution from the primary galaxy over the same redshift range is given by

$$N_1^i = \sum_i \int_{z_{\min}}^{z_{\max}} \omega_1^i(z) \times P_i(z) \times \mathcal{S}_1^i(z) \, dz \quad (3.21)$$

where  $\omega_1^i(z)$  is its weighting,  $\mathcal{S}_1^i(z)$  is the primary galaxy selection function and  $P_i(z)$  its normalised redshift probability density function. If a primary galaxy with a stellar mass within the correct range and its redshift PDF entirely contained within the redshift range of interest,  $N_1^i = \omega_1^i$  and is always equal to or greater than unity.

The close-pair fraction can then be estimated by summing Equations 3.20 and 3.21 over all primary galaxies. In the redshift range  $z_{\min} < z < z_{\max}$  the close-pair fraction is then simply given by

$$f_{\text{pair}} = \frac{\sum_i N_{\text{pair}}^i}{\sum_i N_1^i}. \quad (3.22)$$

# Chapter 4

## The major merger histories of massive galaxies

This Chapter describes the efforts made to measure the major merger histories of massive galaxies ( $> 10^{10} M_{\odot}$ ) at  $0.005 < z < 3.5$ , achieved using a large sample of  $\sim 350,000$  galaxies and the method described in Chapter 3. Pair fractions are measured over an area of 144 sq. deg. at  $z < 0.2$ , and over 3.25 sq. deg. at  $0.2 < z < 3.5$ , for samples of galaxies selected at a constant stellar mass as well as galaxies selected at a constant cumulative number density. The latter selection is used in order to better probe the direct progenitors of low-redshift massive galaxies. This analysis utilises modern wide-area, deep near-IR observations of the cosmos, combined, in part, with a complimentary analysis performed in the CANDELS regions. This Chapter, therefore, presents the best constraints on the merger history of massive galaxies at  $z < 3.5$  yet.

### 4.1 Introduction

The hierarchical growth of matter in the Universe naturally emerges from cold dark matter (CDM) dominated paradigms whereby systems observed today are produced through the repeated merging of smaller systems across cosmic time. While such models make clear predictions on the evolution of dark matter halos (e.g., Jenkins *et al.*, 1997; Maller *et al.*, 2006), the consequences for galaxy formation and evolution are not trivial to infer. Observing galaxies in the process of merging therefore represents a probe of these models and of galaxy formation and evolution, and allows constraints to be placed on evolutionary models of massive galaxies as well as cosmology and the nature of dark matter (e.g., Bertone & Conselice, 2009; Conselice *et al.*, 2014).

Both major and minor galaxy mergers have been observationally and theoretically implicated in various aspects of galaxy formation and evolution. Mergers were first employed to explain the observed morphological transformations of galaxies over time. For example, galaxy mergers are most likely an important process in the evolution of massive elliptical galaxies (Toomre & Toomre, 1972; Barnes & Hernquist, 1996; Bell *et al.*, 2006). Furthermore, massive quiescent galaxies selected at fixed stellar mass are observed to be a factor of 3–6 times smaller at  $z \sim 2$  than in the local Universe (Daddi *et al.*, 2005; Trujillo *et al.*, 2007; Buitrago *et al.*, 2008), while massive galaxies have increased their stellar mass by a factor of 2–3 over the same time period (Ilbert *et al.*, 2010, 2013; van der Wel *et al.*, 2014; Mortlock *et al.*, 2015; Ownsworth *et al.*, 2016). Major mergers have been invoked as a possible mechanism responsible for this drastic evolution, and their role has been increasingly constrained over time (e.g., Conselice *et al.*, 2003; Conselice, 2006; Bluck *et al.*, 2012; López-Sanjuan *et al.*, 2011, 2012, 2013; Man *et al.*, 2012; Man, Zirm & Toft, 2014), albeit with merger histories often derived from relatively small samples, especially at high redshift. While some works suggest major mergers do play a significant role in the evolution of massive galaxies, other studies exclude major mergers as the main driver and instead suggest that minor mergers are responsible, at least at high redshift (e.g., McLure *et al.*, 2013). Thus, our understanding of merging is currently incomplete and controversial at best.

One of the most direct measurements one can perform in order to infer how galaxies form and evolve through mergers is to measure the fraction of galaxies undergoing such an event. This provides a path to derive the integrated effect of mergers for specific populations of galaxies. This has previously been achieved at many redshift regimes using two main methodologies. Where high resolution, high signal-to-noise (S/N) imaging exists, selecting mergers through some combination of morphological indicators is popular (e.g., concentration, asymmetry and clumpiness (CAS): Conselice *et al.* 2003; Jogee *et al.* 2009; López-Sanjuan *et al.* 2009; Conselice *et al.* 2014; or Gini and  $M_{20}$ : Lotz, Primack & Madau 2004; Lotz *et al.* 2008). These selections are confirmed to almost always probe *ongoing* merging events (Conselice *et al.*, 2003; Conselice, Rajgor & Myers, 2008). Such analysis has even been used to select galaxies at specific stages after coalescence has occurred (Pawlik *et al.*, 2016). However, the requirement for high resolution and high S/N necessarily means that expensive space-based observations are the only route to performing morphological analysis at  $z > 1$ . The small volumes and thus number densities of galaxies supplied by such campaigns represent a significant source of uncertainty in the robust study of merger histories. The second approach is to select galaxies with small projected



separations — close-pairs — on the sky (e.g., Carlberg, Pritchet & Infante, 1994; Patton *et al.*, 1997, 2000; Kartaltepe *et al.*, 2007).

While much progress has been made in the literature, various complications exist when attempting to compare measures of merger fractions from different studies. Indeed many studies also find an increasing merger fraction with redshift (Le Fevre *et al.*, 2000; Bluck *et al.*, 2009), while others find a relatively flat slope or a plateau at high redshift (Williams, Quadri & Franx, 2011; Newman *et al.*, 2012). At low redshift ( $z < 0.2$ ) studies generally agree on a merger fraction of the order of less than a few percent (e.g., De Propriis *et al.*, 2007). On the other hand, agreement is generally not reached at high redshift ( $z > 1$ ), where merger fractions up to one third (e.g., Le Fevre *et al.*, 2000; Bluck *et al.*, 2009) have been measured. It has been comprehensively shown that measurements made using stellar mass or luminosity selected samples result in stark differences between the normalisation and measured slopes of the merger fraction (Man, Zirm & Toft, 2014). These differences go some but not all the way to reconciling the results from different studies. What is clear is that a consistent picture of galaxy mergers has not been painted over the majority of the history of the Universe.

Deep near-IR imagery combined with complimentary multi-wavelength observations is required to accurately probe the stellar populations at high redshift  $z > 1$ . Such data allow for photometric redshifts reaching precisions of  $\sim 0.01(1+z)$  (e.g., Ilbert *et al.*, 2009; Hartley *et al.*, 2013; Mortlock *et al.*, 2013; Muzzin *et al.*, 2013a), and stellar population parameters including stellar mass to be estimated out to the furthest redshifts (e.g., Duncan *et al.*, 2014). Modern wide-area, deep surveys represent the only way to observe the merger histories of massive galaxies with any statistical significance across cosmic time. To this end, this work, in combination with Duncan *et al.* (*in prep*), who study objects at  $z > 2$  within the CANDELS fields, presents a new method to measure stellar mass selected merger fractions across a large redshift range, exploiting the statistical power of large multi-wavelength datasets. For the first time, the major and minor merger fractions at  $0.005 < z < 5$  can be measured consistently using a combination of ground- and space-based observations, providing the first consistent picture of galaxy mergers to within the first Gyr of cosmic time. This Chapter presents merger fractions and derived merger rates of massive galaxies ( $\log(\mathcal{M}_*/M_\odot) > 10$ ) at  $z < 3.5$  using a combination of three square-degree-sized, deep near-IR surveys (totalling 3.5 square degrees), the publicly available Galaxy And Mass Assembly (GAMA) second data release (DR2) (totalling 144 square degrees), and multiple CANDELS regions (totalling 0.26 square degrees) at  $z < 3.5$ .

This Chapter is organised as follows: Section §4.2 describes the various data used in this work; Section §4.4 explores the measured major merger *fractions*; Section §4.5 details the derivation and comparison of merger *rates* and discusses the results throughout; Section §4.6 discusses results and the tests applied to them; and Section §4.7 summarises the results and implications of this work. Throughout, magnitudes are quoted in the AB system (Oke & Gunn, 1983) unless otherwise stated, stellar masses are calculated using a Chabrier (2003) initial mass function (IMF) and a  $\Lambda$ CDM cosmology with  $\Omega_{m,0} = 0.3$ ,  $H_0 = 70 \text{ km s}^{-1} \text{ Mpc}^{-1}$  and  $\Omega_\Lambda = 1 - \Omega_m$  is assumed.

## 4.2 Data

This Chapter employs the deepest and widest surveys of the low and high redshift Universe available today: a combination of Galaxy And Mass Assembly (GAMA), the UKIDSS Ultra Deep Survey (UDS), VIDEO and UltraVISTA provides 144 square degrees at  $z < 0.2$  and 3.25 square degrees at  $0.2 < z < 3.5$ . The depth and wavelength coverage of the surveys used in this work allows for the study of the distant Universe with fewer biases against red and dusty galaxies, which could otherwise be completely missed in ultraviolet (UV) and optically selected surveys. While details on how photometric redshift and stellar masses are estimated are given in Section §4.3.1 and Section §4.3.2, the following section discusses the survey fields used in this work.

### 4.2.1 UKIDSS Ultra Deep Survey (UDS)

This work employs the eighth data release (DR8) of the UKIDSS UDS (Almaini et al. *in prep*). The UDS is the deepest of the UKIRT (United Kingdom Infra-Red Telescope) Infra-Red Deep Sky Survey (UKIDSS; Lawrence *et al.*, 2007) projects, covering 0.77 square degrees. Deep photometry is obtained in  $J$ ,  $H$  and  $K$  to limiting  $5\sigma$  AB magnitudes of 24.9, 24.2 and 24.6 in  $2''$  apertures. It is currently the deepest near-IR survey ever undertaken over such an area. Complementary multi-wavelength observations exist in the form of  $u$ -band data obtained from CFHT Megacam;  $B$ ,  $V$ ,  $R$ ,  $i$  and  $z$ -band data from the Subaru-XMM Deep Survey (Furusawa *et al.*, 2008);  $Y$ -band data from the ESO VISTA Survey Telescope; and IR photometry from the Spitzer Legacy Program (SpUDS, PI: Dunlop). Typical uncertainties on  $K$ -band photometry are found to be  $f_\lambda/\delta f_\lambda \approx 500$  ( $\approx 5$ ) at  $K = 19$  (24). These observations over the wavelength range  $0.3\mu\text{m} < \lambda < 4.6\mu\text{m}$  are vital

for the computation of accurate photometric redshifts, stellar masses and rest-frame magnitudes out to the highest redshifts probed in this work. A galaxy catalogue selected in the  $K$ -band containing approximately 90,000 galaxies out to  $z \sim 3.5$ , reaching a 99% completeness depth of  $K = 24.3$  with an effective area of 0.63 square degrees, is used. This field provides a combination of spectroscopic redshifts from archival sources as well as the UDSz (Curtis-Lake *et al.*, 2012; Bradshaw *et al.*, 2013), which provide 2292 high quality spectroscopic redshifts at  $0 < z < 4.5$  (90% at  $z < 2$ ) in the UDS region.

### 4.2.2 UltraVISTA

The publicly available  $K_s$ -band selected UltraVISTA catalogue produced by Muzzin *et al.* (2013b) is used in this work. The UltraVISTA survey observes the COSMOS field (Scoville *et al.*, 2007) with the ESO Visible and Infrared Survey Telescope for Astronomy (VISTA) survey telescope, covering an effective area of 1.62 square degrees. The catalogue provides PSF-matched  $2.1''$  aperture photometry across 30 bands covering the wavelength range  $0.15\mu\text{m} < \lambda < 24\mu\text{m}$  down to a limiting 90% completeness magnitude of  $K_s = 23.4$ . Only sources above this detection limit with reliable photometry are used in this work. Typical uncertainties on the  $K_s$ -band photometry are  $f_\lambda/\delta f_\lambda \approx 200$  ( $\approx 10$ ) at  $K_s = 19$  (23). MIPS photometry is not used at any stage going forward as it is uncertain how well models reproduce this regime of a galaxy spectrum. Furthermore, independent photometric redshifts and stellar masses are calculated, as described in §4.3.1 and §4.3.2. The catalogue includes GALEX (Martin *et al.*, 2005), CFHT/Subaru (Capak *et al.*, 2007), S-COSMOS (Sanders *et al.*, 2007) and UltraVISTA (McCracken *et al.*, 2012) photometry as well as the zCOSMOS Bright (Lilly *et al.*, 2007) spectroscopic dataset, providing 5467 high quality spectroscopic redshifts at  $z < 2.5$ . The vast majority (99%) of these spectroscopic redshifts are at  $z < 1$  and 50% are at  $z < 0.5$ .

### 4.2.3 VIDEO

The VISTA Deep Extragalactic Observations (VIDEO) survey (Jarvis *et al.*, 2012) is a  $\sim 12$  square degree survey in the near-infrared  $Z$ ,  $Y$ ,  $J$ ,  $H$  and  $K_s$  bands, specifically designed to enable the evolution of galaxies and large structures to be traced as a function of both epoch and environment from the present day out to  $z = 4$ , and active galactic nuclei (AGNs) and the most massive galaxies up to and into the epoch of reionization. This work uses VISTA observations matched to those of the Canada-France-Hawaii Telescope Legacy Survey Deep-1 field (CFHTLS-D1),

providing multi-wavelength ( $0.3\mu\text{m} < \lambda < 2.1\mu\text{m}$ ) coverage over a total of 1 square degree down to a 90% completeness magnitude of  $K_s = 22.5$ . Comprehensive simulations are performed to calculate the completeness level as a function of total  $K$ -band magnitude which are described in Appendix A. Typical  $K_s$ -band uncertainties are  $f_\lambda/\delta f_\lambda \approx 200$  ( $\approx 15$ ) at  $K_s = 19$  (22).

For the purpose of this work, a  $K_s$ -selected catalogue (released in June 2015) is used containing 54,373 sources after star/galaxy separation using a  $uJK$  colour selection, magnitude cuts, star masking, and selecting only sources with a detection signal-to-noise  $> 2$ . Bright stars and areas visibly contaminated with starlight are manually masked out using the VIDEO  $K_s$ -band image. Objects within these masked regions are flagged and discarded from the sample. A spectroscopic sample of galaxies is constructed from the latest VIMOS VLT Deep Survey (VVDS; Fevre *et al.*, 2004) and the VIMOS Public Extragalactic Redshift Survey (VIPERS; Garilli *et al.*, 2014) data releases. Only the most secure redshifts (quality flags 3 and 4) are matched within one arcsecond of the  $K_s$ -band sources, providing 4,382 high-quality spectroscopic redshifts over the range  $0 < z < 4.5$ . However, the vast majority (90%) of this sample is below  $z < 1.5$ .

#### 4.2.4 GAMA

In order to obtain a measurement of the merger fraction at redshifts which are restricted by volume in other fields, the second data release (DR2) of the Galaxy And Mass Assembly (GAMA) campaign (Driver *et al.*, 2009; Liske *et al.*, 2015) is used. This release provides multi-wavelength photometry in 9 filters over three fields totalling 144 square degrees. Complimenting this data, 98% of the detections are provided with secure spectroscopic redshifts. GAMA therefore represents a large and unique dataset with which to probe galaxy evolution at low redshift.

This work utilises combined data from all three GAMA fields (G09, G12 and G15), herein collectively referred to as the GAMA region, included in the DR2 release. When calculating stellar masses in this region, the recommended photometric zero-point offsets<sup>1</sup> and stellar mass scaling factors (Taylor *et al.*, 2011) provided with the release documentation are applied. What differentiates this dataset from the others used in this work is the unprecedented spectroscopic coverage. Combining the three aforementioned GAMA regions yields 55,199 objects with good quality spectroscopic redshift (quality flag  $nQ > 2$  which provides spectroscopic redshifts at  $> 90\%$  confidence Driver *et al.* 2011) and  $z_{\text{spec}} > 0.005$ , which minimises contami-

---

<sup>1</sup><http://www.gama-survey.org/dr2/schema/table.php?id=168>

nation from stars (visual inspection of a  $u - J$  vs  $J - K$  plot reveals this cut removes the stellar locus), representing 97 per cent of the total number of objects down to a limiting Petrosian  $r$ -band magnitude of  $m_r = 19$ . This allows the analysis to be performed in two ways: photometrically and spectroscopically, which is discussed in Section §4.4.3. Typical uncertainties on  $r$ -band photometry are  $f_\lambda/\delta f_\lambda \approx 700$  ( $\approx 200$ ) at  $r = 17$  (19).

### 4.2.5 Simulated Data

Models of galaxy formation and evolution have advanced dramatically over the last few decades. Semi-analytic models (SAMs) aim to reproduce and predict the statistical properties of galaxy populations, historically at low redshift. This work explores the latest development in the Munich ‘family’ of models (e.g., Croton *et al.*, 2006; De Lucia & Blaizot, 2006; Guo *et al.*, 2011), as described in Henriques *et al.* (2015), herein H15, to provide predictions of the pair fraction. This model is applied to the output of The Millennium Simulation (Springel *et al.*, 2005), scaled to a Planck cosmology (Planck Collaboration (XVI), 2014). All 24 mock lightcones from the German Astrophysical Virtual Observatory (GAVO; Lemson & Consortium, 2006) are downloaded, which are reduced in size from a circular aperture of two degrees diameter to a square field-of-view with an area of one square degree. Doing so permits one to quantify the expected variance between surveys similar in size to those used in this study. Furthermore, the results of the merger fractions obtained using the H15 model are explored and compared in Section §4.6.1. Finally, predictions of the merger rate within the Illustris simulation (Vogelsberger *et al.*, 2014a,b; Rodriguez-Gomez *et al.*, 2015) are compared to observational measurements in Section §4.5.

## 4.3 Data Products

In this section the photometric redshifts and stellar masses derived from the data sets described in Section §4.2 are explained.

### 4.3.1 Photometric redshifts

Photometric redshift probability distributions are calculated for all sources using the EAZY photometric redshift code (Brammer, vanDokkum & Coppi, 2008). EAZY determines the  $z_{\text{phot}}$  for a galaxy by fitting a spectral energy distribution (SED) produced by a linear combination of templates to a set of photometric measure-

ments. It has been shown that the default set of six templates, derived from the PEGASE models (Fioc & Rocca-Volmerange, 1999), in combination with an additional red template from the Maraston (2005) models, and a 1 Gyr-old single-burst Bruzual & Charlot (2003) template are required to provide robust SED fits to the zoo of observed galaxies in modern surveys (e.g., Onodera *et al.*, 2012; Muzzin *et al.*, 2013b).

As such, this set of templates is used to calculate photometric redshifts and photometric redshift probability distributions (PDFs). The PDF is constructed for each galaxy from its  $\chi^2(z)$  distribution following  $P(z) \propto \exp(-\chi^2(z)/2)$ , after convolution with a photometric prior. The following paragraphs discuss the use of a photometric prior in these calculations and the ability of the resulting PDFs to accurately reproduce photometric redshift confidence intervals.

In calculating galaxy PDFs and best-fit photometric redshifts, many studies make use of a luminosity or colour dependent redshift prior. The use of such priors have been shown to improve best-fit solutions when compared to spectroscopic redshift measurements (e.g., Benitez, 2000; Brammer, vanDokkum & Coppi, 2008). However the use of such priors may introduce bias into the measurement of close pairs. As an example, let us consider two galaxies at the same redshift with identical properties except for stellar mass (luminosity). A luminosity based prior will influence the probability distribution of each galaxy and, in the example, the higher mass system will have its PDF biased towards lower redshifts, and vice-versa for the second galaxy. Furthermore, priors are necessarily based on simulations. At higher redshifts ( $z > 2$ ) these may deviate from the true distribution of galaxies, however at lower redshift they are much more constrained and in agreement with observations.

To this end, a luminosity prior,  $P(z|m)$ , is constructed which denotes the probability of a galaxy with apparent  $K$ -band magnitude  $m$  being found at redshift  $z$ , by extracting galaxy number counts from the H15 semi-analytic model using 24 independent light cones. This model has been shown to accurately reproduce the observed number densities of galaxies out to  $z \sim 3$ , and thus is perfect to construct a prior from. This is achieved in the same manner as Brammer, vanDokkum & Coppi (2008) and Benitez (2000), parametrising each magnitude bin  $i$  as

$$P(z|m_{K,i}) \propto z^{\gamma_i} \times \exp(-(z/z_i)^{\gamma_i}), \quad (4.1)$$

where  $\gamma_i$  and  $z_i$  are fit to the redshift distribution in each magnitude bin. This is done to ensure that the prior is smooth over the redshift range of interest. We

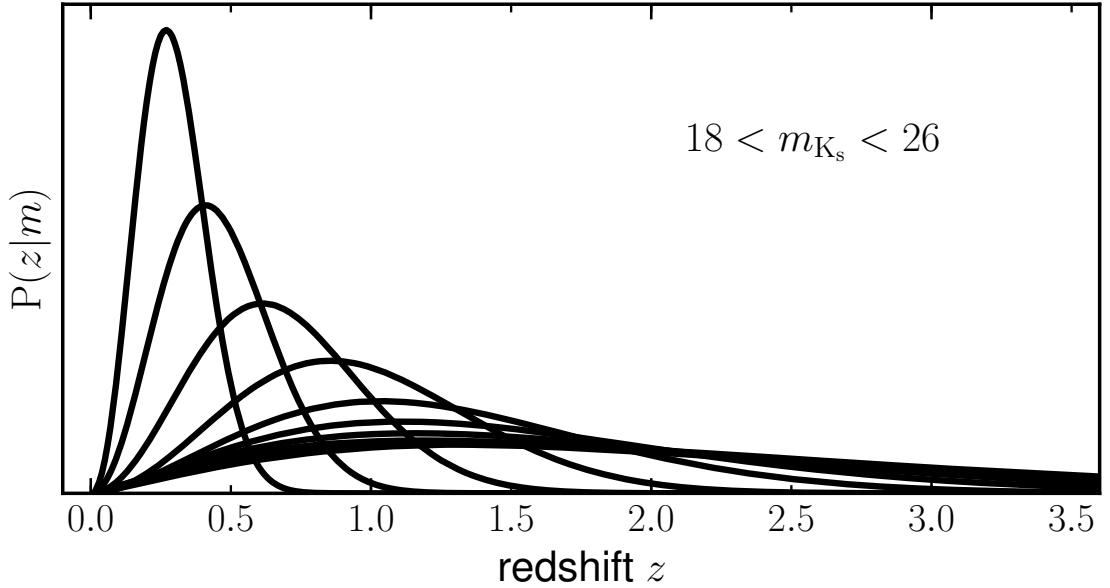


**Figure 4.1:** Relative prior probabilities,  $P(z|m_K)$ , as a function of apparent  $K_s$ -band magnitude extracted from semi-analytic light cones (Henriques *et al.*, 2015). Plotted probability densities in steps of  $\Delta m_K = 1$  over the magnitude range  $18 < m_K < 26$ , normalised such that  $\int P(z|m_K) dz = 1$ , with  $P(z|m_K)$  given by Equation 4.1.

calculate these distributions over the redshift range  $0 < z < 7$  and apparent magnitude range  $17 < m_K < 27$ . Calculated fitting parameters are displayed in Figure 4.1 which shows the calculated prior probabilities as a function of apparent magnitude. Although it is found that pair fractions obtained using photometric redshifts calculated with and without a prior are indistinguishable within the calculated uncertainties, the prior is used in this work as it improves the best-fit  $z_{\text{phot}}$  estimates and reduces the number of catastrophic outliers (see Section §4.3.1.2).

#### 4.3.1.1 Photometric redshift confidence intervals

Redshift probability distributions output by photometric redshift codes are often unable to accurately represent photometric redshift confidence intervals (e.g., Hildebrandt, Wolf & Benítez, 2008; Dahlen *et al.*, 2013). The causes include, but are not limited to, inaccurate photometry errors or the choice of template set. Although average agreement between best-fit  $z_{\text{phot}}$  and  $z_{\text{spec}}$  can be excellent,  $1\sigma$  and  $2\sigma$  confidence intervals can be significantly over- or under-estimated.

Analysing the photometric redshift probability distributions output by **EAZY**, discussed in Section §4.3.1, it is observed that the confidence intervals are indeed incorrect. Using high quality spectroscopically obtained redshifts for a subset of galaxies in each field, it is found that 72%, 71%, 81% and 50% of  $z_{\text{spec}}$  are found within the

$1\sigma$  photometric PDF interval for the UDS, VIDEO, COSMOS and GAMA regions, respectively. In order to address this, PDFs that overestimate the confidence intervals are sharpened. This is done as in Dahlen *et al.* (2013), however the method is briefly outlined here.

To sharpen, the PDFs are replaced with  $P(z_i) = P(z_i)_0^{1/\alpha}$  until the value of  $\alpha$  gives the correct fraction of 68.3%. To smooth, the PDFs are convolved with a kernel of  $[0.25, 0.5, 0.25]$  until the correct fraction of 68.3% is recovered. The same process is then applied to the entire sample. In doing so, values of  $\alpha = 0.850, 0.840, 0.510$  are obtained for the UDS, VIDEO and COSMOS fields, respectively. However, the PDFs within the GAMA region are not smoothed (as opposed to sharpened) as such a process inevitably leads to a high probability at the lowest redshifts which artificially boosts the measured merger fraction in the lowest redshift bin used. This is likely an artefact of using a linear redshift grid, however it is not expected to significantly affect the results of this work, as using unsharpened redshift PDFs in other fields results in no significant changes to measured pair fractions.

#### 4.3.1.2 Best-fit solutions

While the main interest of this work lies in the PDFs associated with each galaxy, it is useful to compare best-fit photometric redshift solutions with spectroscopically obtained values. Various measures exist to quantify the agreement between photometric and spectroscopic redshifts. This work presents the normalised median absolute deviation (NMAD), mean  $|\Delta z|/(1 + z_{\text{spec}})$ , where  $\Delta z = (z_{\text{spec}} - z_{\text{phot}})$ , and outlier fraction, defined in two ways. These measures of photometric redshift quality are provided in Table 4.1, and a visual comparison between spectroscopic and photometric redshifts within all regions is shown in Figure 4.2. All fields except for GAMA possess averages biases of  $z_{\text{spec}} - z_{\text{phot}} \approx 0$ . As is apparent in Figure 4.2, there exists a relatively large apparent bias in our photometric redshifts within the GAMA region whereby our photometric redshifts tend to be larger than the spectroscopic redshift by  $\Delta z = 0.02$  on average. This is the largest bias found in the datasets used. If the brightest 10% (25%) of objects in the GAMA region are analysed, this bias is reduced by a factor of  $\sim 3$  ( $\sim 2$ ), suggesting that fainter ( $r > 18$ ) objects are more affected by this bias. Such an effect would not be seen in the other regions as their spectroscopic samples are typically biased towards the brightest objects in the field. However, as no suggestion of stellar mass dependence (see Section §4.4) of the pair fraction is observed, this issue is not expected to affect the results presented herein.

Use of a photometric prior typically reduces the difference between photometric



**Table 4.1:** Best-fit photometric redshift (with and without prior) comparison with high quality spectroscopic sample outlined in Section §4.2. For each field we list the number of secure spectroscopic redshifts available ( $N_s$ ), the normalised median absolute deviation ( $\sigma_{\text{NMAD}}$ ), mean  $|\Delta z|/(1 + z_s)$ , average bias  $\Delta z = z_{\text{spec}} - z_{\text{phot}}$ , and fraction of catastrophic outliers ( $\eta_1$  and  $\eta_2$ ) defined in two ways.

Field	$N_s$	$\sigma_{\text{NMAD}}$	$\frac{ \Delta z }{(1+z_s)}$	$\Delta z$	$\eta_1^a$	$\eta_2^b$
WITH MAGNITUDE PRIOR						
UDS	2648	0.053	0.045	0.01	5.3%	5.0%
VIDEO	4382	0.044	0.038	0.01	2.9%	3.3%
COSMOS	5467	0.013	0.010	0.00	0.5%	2.5%
GAMA	55199	0.049	0.044	-0.02	2.4%	2.5%
WITHOUT MAGNITUDE PRIOR						
UDS	2648	0.051	0.045	0.01	5.3%	5.3%
VIDEO	4382	0.048	0.042	0.02	3.4%	3.5%
COSMOS	5467	0.013	0.011	0.00	0.5%	3.2%
GAMA	55199	0.060	0.052	-0.03	3.4%	1.7%

<sup>a</sup>Catastrophic outliers determined as  $|\Delta z|/(1 + z_{\text{spec}}) > 0.15$ .

<sup>b</sup>Catastrophic outliers determined as  $|\Delta z|/(1 + z_{\text{spec}}) > 3 \times \sigma_{\text{NMAD}}$ .

and spectroscopic redshifts, whilst also reducing the fraction of catastrophic failures. Furthermore, the COSMOS region provides the most accurate photometric redshifts when compared to a subset of spectroscopic redshifts. However, spectroscopic redshift samples that are co-spatial with deep, wide near-IR surveys like UltraVISTA/COSMOS are often heavily biased towards the nearest and brightest systems. With a 97% completeness fraction the spectroscopic sample in the GAMA region is undoubtedly unbiased and is arguably a better indicator of photometric redshift efficacy. Here the prior reduces the NMAD and the mean offset by 18% and 15%, respectively.

Applying the corrections described in Section §4.3.1.1, results in PDFs which accurately represent the probability of every galaxy at every redshift over the range  $0 < z < 6$ . The integral of the PDF over some redshift range measures the probability of the galaxy being found within said redshift range.

### 4.3.2 Stellar mass estimates

Stellar masses are calculated using `smphy`, a custom spectral energy distribution (SED) fitting code, first introduced in Duncan *et al.* (2014) and available online<sup>2</sup>.

<sup>2</sup><https://www.github.com/dunkenj/smphy/>

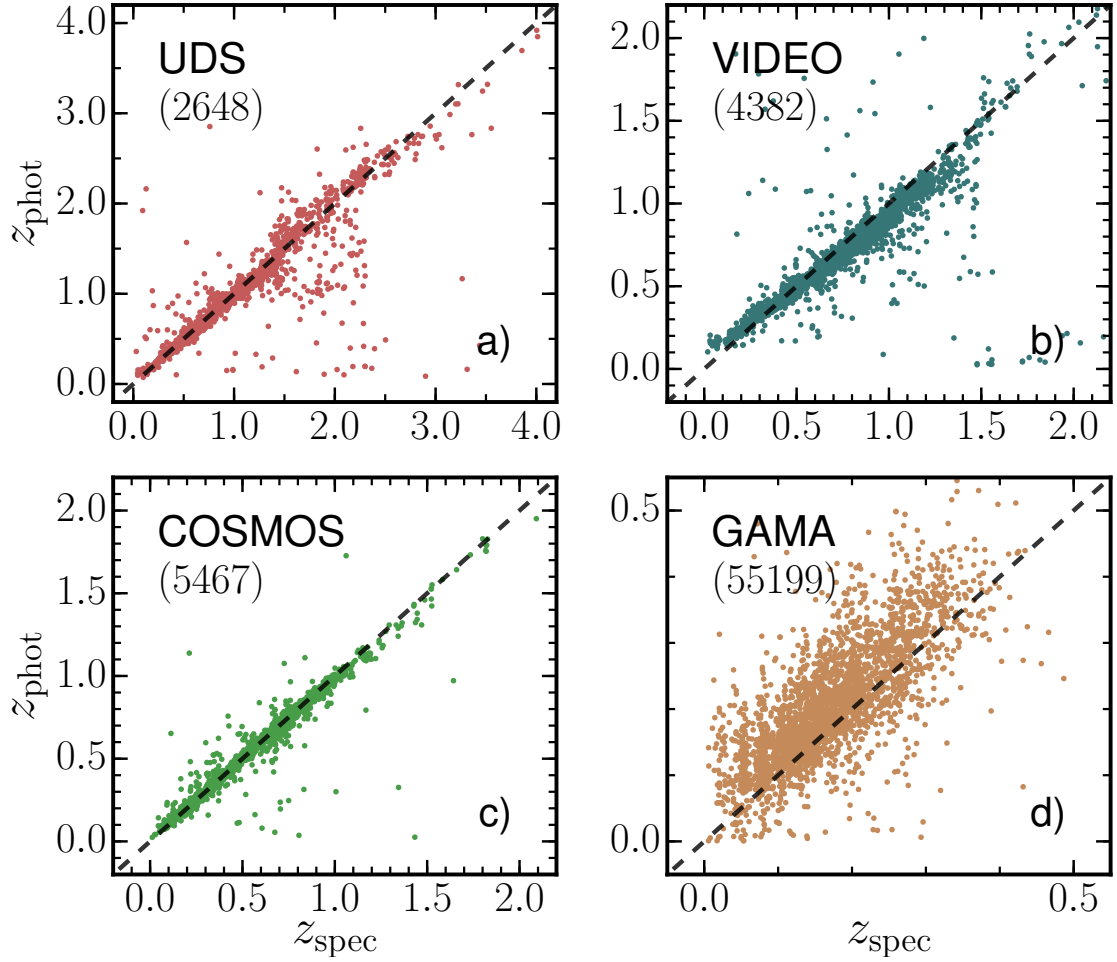


**Figure 4.2:** Comparison between best-fit photometrically derived redshifts,  $z_{\text{phot}}$ , and spectroscopically measured redshifts,  $z_{\text{spec}}$ , in the a) UDS, b) VIDEO, c) COSMOS, and d) GAMA regions. Numbers within parenthesis denote the number of science-quality spectroscopic redshifts within each field. Due to the extremely large number of sources within the GAMA region, a randomly selected sample of 5% is displayed for this field only. The normalised median absolute deviation, average offset and outlier fraction of our photometric redshifts are listed in Table 4.1 for each region.

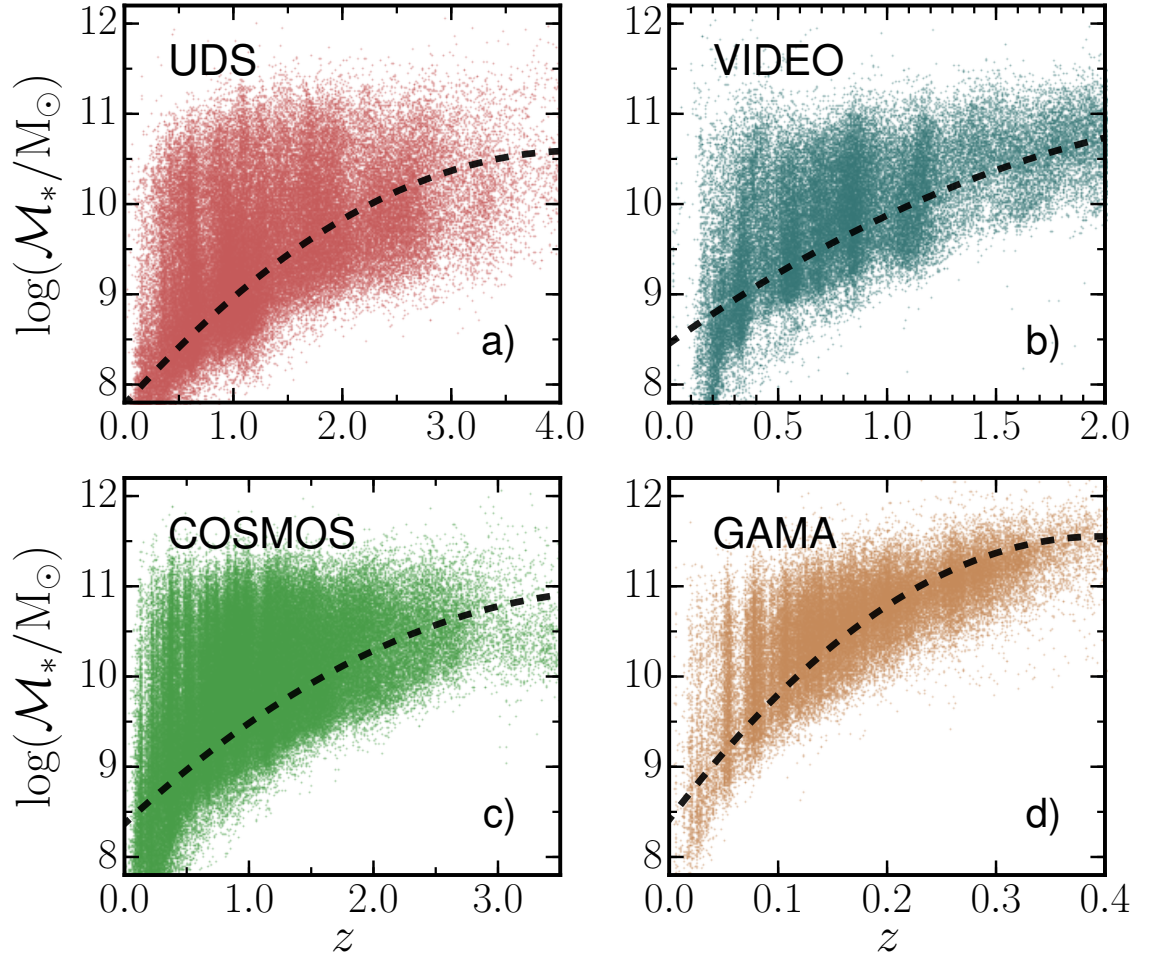


**Figure 4.3:** Redshift versus stellar mass distributions in the in the a) UDS, b) VIDEO, c) COSMOS, and d) GAMA regions. Redshifts presented in the GAMA region are spectroscopic ( $z_{\text{spec}}$ ) while those displayed in other regions are photometric ( $z_{\text{phot}}$ ). 90% stellar mass completeness limits,  $\mathcal{M}_*^{90}(z)$ , within each region, determined using magnitude limits of  $r = 19$  and  $K = 24.3, 22.5, 23.4$ , respectively, are given by the dashed black lines.

The Bruzual & Charlot (2003, BC03) stellar population synthesis models are used in conjunction with a Chabrier (2003) IMF. Model ages are allowed to vary between 0.01–13.7 Gyr. Star-formation histories are described by a simple  $\tau$ -model and are allowed to be exponentially increasing or decreasing, or constant with values of  $|\tau|$  allowed between 0.01–13.7 Gyr, plus an option for a constant star-formation history. The effects of dust are parametrised as in Calzetti *et al.* (2000), with an extinction ( $A_V$ ) allowed to vary between 0 – 4 magnitudes. Stellar metallicity is allowed in the range  $0.005 < Z/Z_\odot < 2.5$ . Rather than estimating the best-fit mass for a fixed input photometric or spectroscopic redshift, the stellar mass is instead estimated at all redshifts in the photometric redshift fitting range simultaneously. Specifically, the likelihood-weighted mean is assumed, defined as

$$\mathcal{M}_*(z) = \frac{\sum_t w_t(z) \mathcal{M}_{*,t}(z)}{\sum_t w_t(z)} \quad (4.2)$$

where the sum is performed over all galaxy template types,  $t$ , with ages less than the age of the Universe at the redshift  $z$  and  $\mathcal{M}_{*,t}$  is the best-fit stellar mass for each galaxy template. The likelihood,  $w_t(z)$ , is determined by

$$w_t(z) = \exp(-\chi_t^2(z)/2) \quad (4.3)$$

where  $\chi_t^2(z)$  is given by

$$\chi_t^2(z) = \sum_j \frac{(F_{j,t}(z) - F_j^{\text{obs}})^2}{\sigma_j^2}. \quad (4.4)$$

Here the sum is over  $j$  available filters for each particular galaxy, its observed photometric fluxes,  $F_j^{\text{obs}}$ , and photometric flux error,  $\sigma_j$ . All available photometry are fit to a library of 34,803 synthetic SEDs simultaneously to achieve this. Stellar mass as a function of redshift within each region is shown in Figure 4.3.

The method described in Chapter 3 is applied to the data described previously. Figure 4.4 displays a collection of identified close-pairs at  $0.3 < z < 3.0$  in the COSMOS field. Finally, an example of the stellar mass and redshift information used in this work for a typical close-pair of galaxies in the COSMOS region is shown in Figure 4.5. In the next Section, the results of measuring the galaxy close-pair fraction are presented and discussed. Section §4.4 presents the raw measured pair fractions for various sample selections, Section §4.5 presents derived merger rates, Section §4.6 discusses the results, and Section §4.7 summarises the main results and implications.

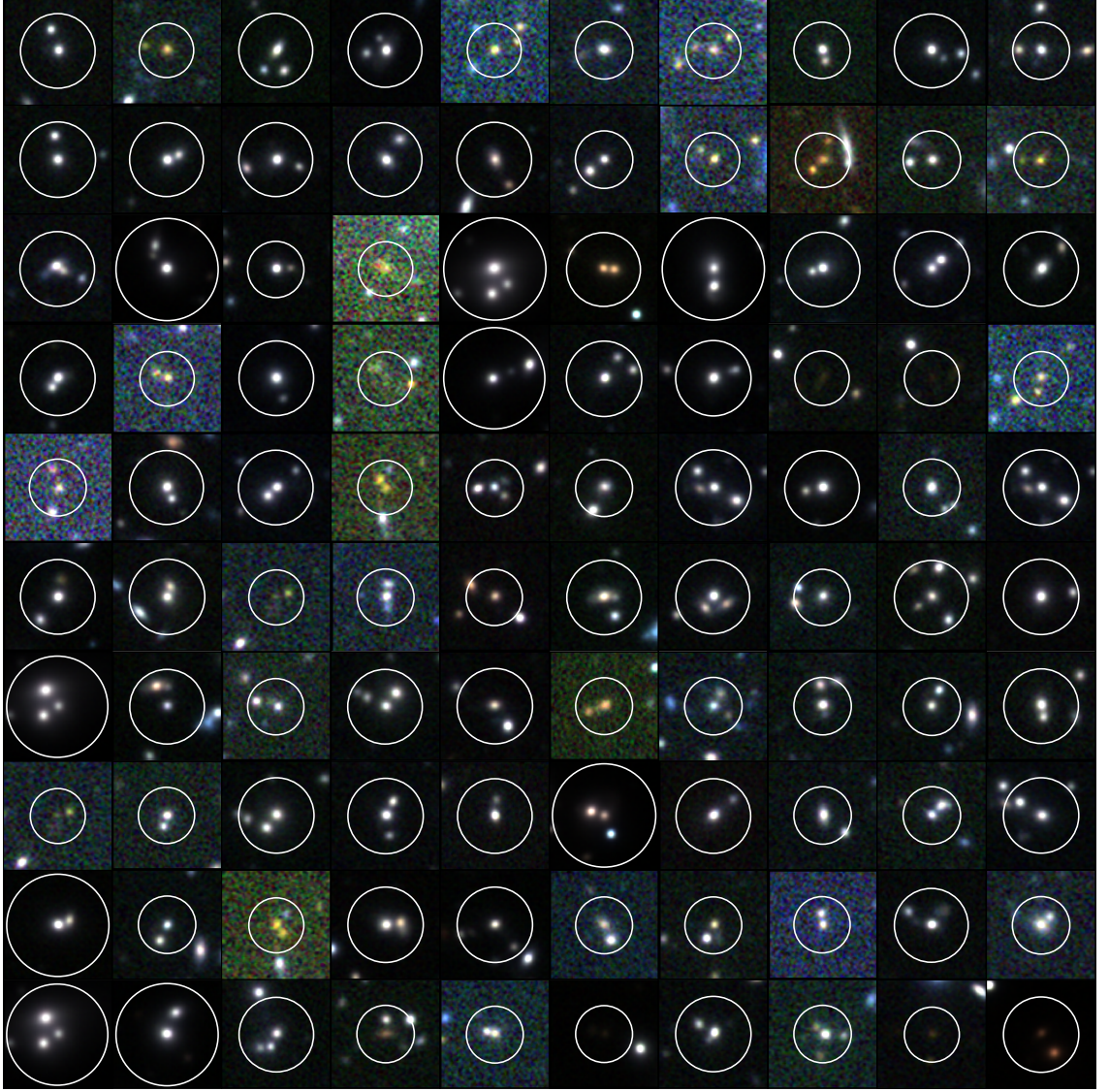


**Figure 4.4:** Three-colour image using the UltraVISTA DR1  $J$ ,  $H$ , and  $K_s$ -band images of close-pairs at  $0.3 < z < 3.0$  that contribute  $N_{\text{pair}} > 0.7$  after weightings are applied. Each postage stamp is centred on the primary (most massive) galaxy and the outer white circles represent a physical search radius of 30 kpc around each centred primary galaxy. Colour scaling is done automatically to highlight the often faint galaxies of interest. A range of morphologies, colours and galaxy sizes are apparent. Pairs with the same primary galaxy (but different secondary galaxy) result in the same postage stamp being shown multiple times within the above image.



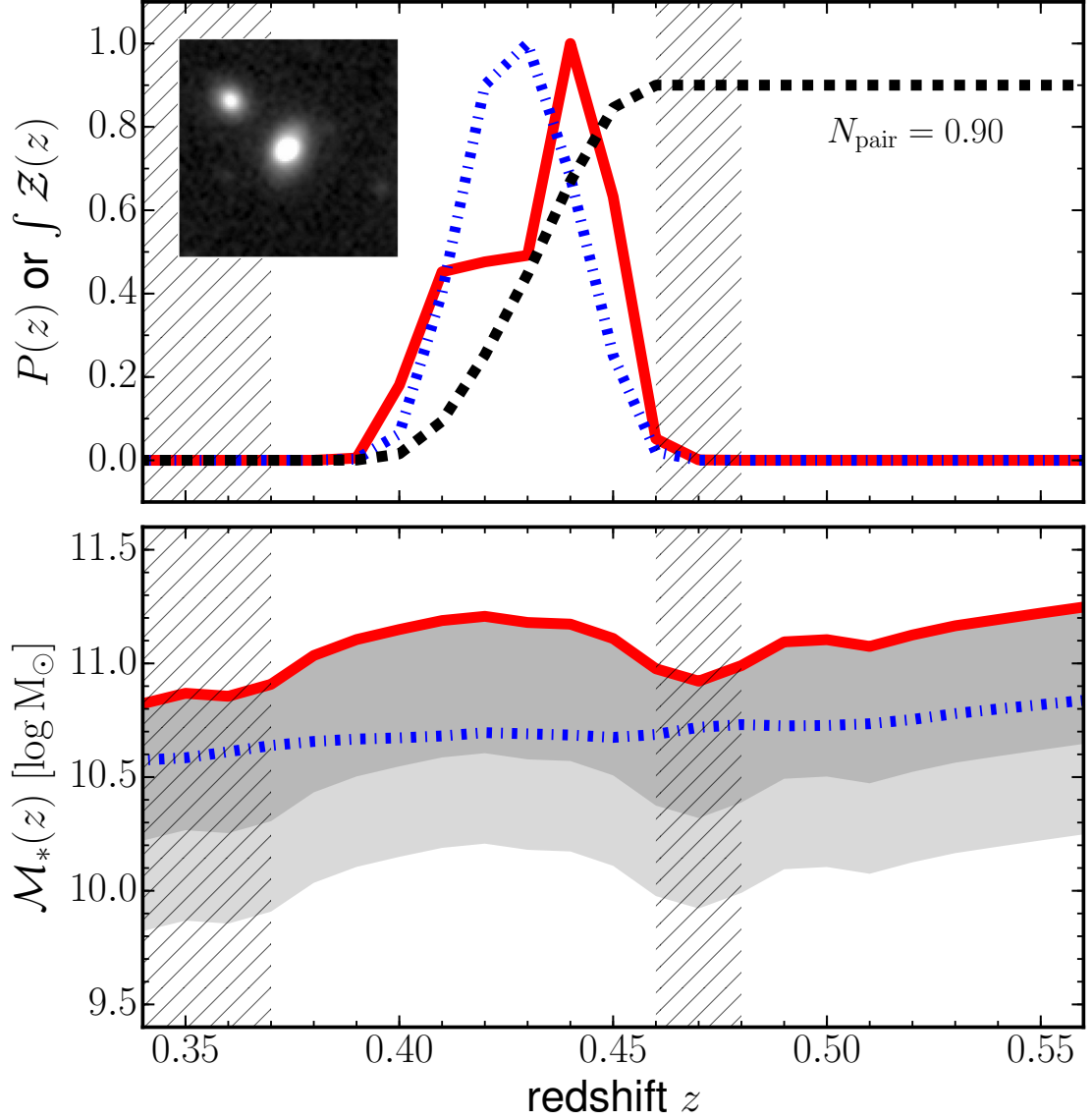


**Figure 4.5:** *Top:* Computed redshift probability distributions,  $P(z)$ , for an identified close-pair system with a primary galaxy (solid red line) at best-fit redshift  $z_{\text{peak}} = 0.44$  and secondary galaxy (dashed dotted blue line) at best-fit redshift  $z_{\text{peak}} = 0.43$ . A greyscale  $K_s$ -band image of the pair, of side length  $20''$ , is shown inset. The integrated cumulative probability function (Equation 3.5) of the system is given by the dashed black line. *Bottom:* The stellar mass as a function of redshift, via SED-fitting, for the primary and secondary galaxies. At their best-fit  $z_{\text{peak}}$ , the primary and secondary galaxies possess stellar masses of  $\log(\mathcal{M}_*/M_\odot) = 11.2$  and  $10.7$ , respectively. The major merger mass ratio (1:4) is given by the dark shaded region while the minor merger mass ratio (1:10) is given by the light shaded region. The hatched regions represent redshift ranges where the close-pair system is not considered as the primary galaxy does not meet the criteria of  $\log(\mathcal{M}_*/M_\odot) > 11$ .

## 4.4 The major merger fraction at $z < 3.5$

This section presents the measured pair fractions obtained for various primary samples. The primary samples are chosen in order to enable comparison of their derived merger rates with previous works touched upon in Section §4.1. As previously mentioned, the close-pair analysis is performed in the GAMA region in two ways: photometrically and spectroscopically. For the latter, conditions are enforced whereby the *projected* close-pairs must be within  $\Delta v < 500$  km/s ( $\Delta z = 0.0017$ ) of each other. A combination of mass (in)completeness and the potential to miss a large population of massive galaxies at faint magnitudes (Caputi *et al.*, 2015) limit our study to  $z < 3.5$  in the deepest near-IR survey region. Section §4.4.1 describes pair fractions obtained for constant stellar mass selected samples, while Section §4.4.2 reports pair fractions for samples of galaxies selected at a constant cumulative co-moving number density.

Firstly our choice of parameters are justified. The minimum physical separation of a close-pair is defined as 5 kpc in order to minimise the influence of objects whose photometry has become blended and to ensure the host galaxy is not counted as its own companion. This physical separation translates into angular separations between 0.7–1.5 arcseconds at the redshift ranges probed in this study. The pixel scales in the UDS (0.27"/pix), VIDEO (0.19"/pix) and COSMOS (0.15"/pix) images, from which the catalogues were produced, represent minimum centroid separations of 3, 3 and 5 pixels, respectively.

### 4.4.1 Constant stellar mass selected samples

The volume afforded by square degree-sized surveys allows the most massive galaxies ( $\mathcal{M}_* > 10^{11} M_\odot$ ) to be probed across cosmic time. Major merger fractions are obtained for two stellar mass selections at two physical separations purely for comparison with previous literature works. These fractions are tabulated for reference in Table 4.2 and Section §4.5 presents derived major merger rates for these selections.

#### 4.4.1.1 Massive galaxies ( $\mathcal{M}_* > 10^{11} M_\odot$ )

The pair fraction for a sample of galaxies defined by the limit  $\mathcal{M}_* > 10^{11} M_\odot$  are measured at maximum physical separations of 20 kpc and 30 kpc to enable comparison with previous works. Obtained fractions and estimated errors at both separations are given in Table 4.2, however only results at a separation of  $< 30$  kpc are discussed in the text due to the larger sample sizes obtained using this larger separation. Results of  $f_{\text{pair}}$  at this separation in the GAMA, UDS, VIDEO and

**Table 4.2:** Major merger ( $\mu > 1/4$ ) pair fractions,  $f_{\text{pair}}$ , and associated errors calculated using *Pyrus* for constant stellar mass selected samples. Fractions are listed by each survey region, separated by stellar mass and physical search radius parameters. Errors include contributions from cosmic variance, bootstrap error analysis and Poisson errors.

$z$	GAMA	UDS	VIDEO	COSMOS
$\mathcal{M}_* > 10^{10} \text{M}_\odot$ (5 – 20kpc)				
0.0 – 0.1	0.020 $\pm$ 0.005	-	-	-
0.1 – 0.2	0.014 $\pm$ 0.002	-	-	-
0.2 – 0.5	-	0.016 $\pm$ 0.006	0.017 $\pm$ 0.005	0.015 $\pm$ 0.004
0.5 – 1.0	-	0.042 $\pm$ 0.007	$\leq 0.031$	0.021 $\pm$ 0.003
1.0 – 1.5	-	0.057 $\pm$ 0.008	-	$\leq 0.031$
1.5 – 2.0	-	$\leq 0.099$	-	-
$\mathcal{M}_* > 10^{10} \text{M}_\odot$ (5 – 30kpc)				
0.0 – 0.1	0.034 $\pm$ 0.008	-	-	-
0.1 – 0.2	0.025 $\pm$ 0.003	-	-	-
0.2 – 0.5	-	0.041 $\pm$ 0.012	0.038 $\pm$ 0.009	0.028 $\pm$ 0.006
0.5 – 1.0	-	0.076 $\pm$ 0.012	$\leq 0.075$	0.052 $\pm$ 0.006
1.0 – 1.5	-	0.101 $\pm$ 0.014	-	$\leq 0.077$
1.5 – 2.0	-	$\leq 0.178$	-	-
$\mathcal{M}_* > 10^{11} \text{M}_\odot$ (5 – 20kpc)				
0.0 – 0.1	0.034 $\pm$ 0.024	-	-	-
0.1 – 0.2	0.017 $\pm$ 0.005	-	-	-
0.2 – 0.5	-	0.017 $\pm$ 0.030	0.004 $\pm$ 0.005	0.023 $\pm$ 0.011
0.5 – 1.0	-	0.035 $\pm$ 0.016	0.034 $\pm$ 0.012	0.016 $\pm$ 0.004
1.0 – 1.5	-	0.053 $\pm$ 0.019	0.027 $\pm$ 0.010	0.018 $\pm$ 0.005
1.5 – 2.0	-	0.097 $\pm$ 0.056	-	0.023 $\pm$ 0.007
2.0 – 2.5	-	0.061 $\pm$ 0.028	-	0.027 $\pm$ 0.010
2.5 – 3.0	-	0.051 $\pm$ 0.029	-	$\leq 0.051$
3.0 – 3.5	-	0.033 $\pm$ 0.026	-	-
$\mathcal{M}_* > 10^{11} \text{M}_\odot$ (5 – 30kpc)				
0.0 – 0.1	0.046 $\pm$ 0.031	-	-	-
0.1 – 0.2	0.025 $\pm$ 0.007	-	-	-
0.2 – 0.5	-	0.067 $\pm$ 0.051	0.014 $\pm$ 0.009	0.038 $\pm$ 0.016
0.5 – 1.0	-	0.061 $\pm$ 0.023	0.060 $\pm$ 0.017	0.040 $\pm$ 0.009
1.0 – 1.5	-	0.084 $\pm$ 0.025	0.076 $\pm$ 0.031	0.041 $\pm$ 0.009
1.5 – 2.0	-	0.084 $\pm$ 0.029	-	0.048 $\pm$ 0.012
2.0 – 2.5	-	0.086 $\pm$ 0.037	-	0.047 $\pm$ 0.015
2.5 – 3.0	-	0.075 $\pm$ 0.039	-	$\leq 0.085$
3.0 – 3.5	-	0.042 $\pm$ 0.031	-	-



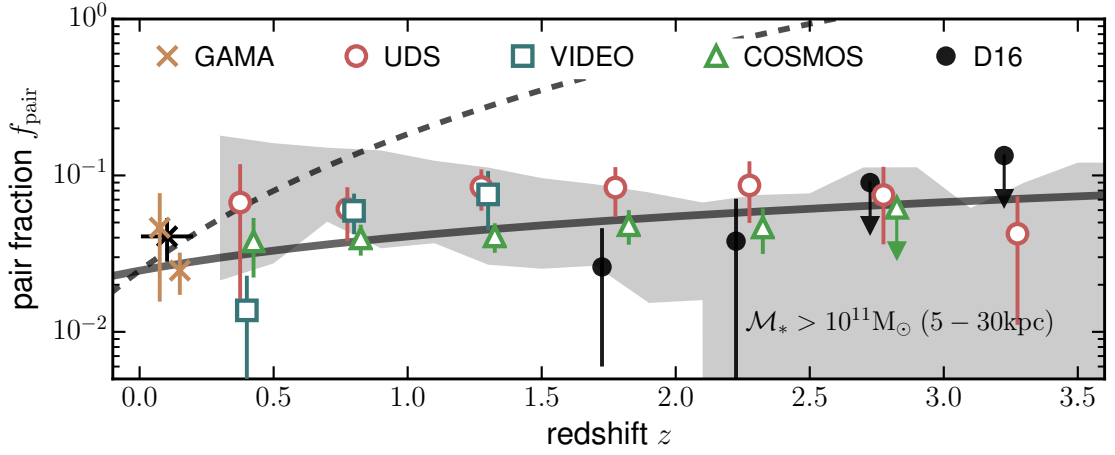


**Figure 4.6:** The measured major merger ( $\mu > 1/4$ ) pair fraction,  $f_{\text{pair}}$ , for galaxies with  $\log(\mathcal{M}_*/M_\odot) > 11$  at physical separations of 5–30 kpc as a function of redshift in the GAMA (gold and black crosses), UDS (red circles), COSMOS (green triangles) and VIDEO (blue squares) fields. The black crosses with horizontal error bars are points measured using the GAMA spectroscopic sample, including Poisson errors and cosmic variance estimates. Results from a complimentary study within the CANDELS fields (Duncan et al., *in prep*) are presented as solid black circles. Upper limits on the pair fraction are given by points with solid filled arrows. The best-fit to all the data, as provided in Table 4.3, is shown as a solid grey line. The grey shaded area represents the  $1\sigma$  variation in the pair fraction as measured using 24 light cones based on the H15 semi-analytic model. The dashed black line is a power law fit of the form  $\sim (1+z)^3$ , as in Bluck *et al.* (2012).

COSMOS regions are shown in Figure 4.6 as gold and black crosses, red circles, blue squares and green triangles, respectively. Results from a complimentary study within the CANDELS fields (Duncan et al., *in prep*) are shown as filled black circles. Where the primary sample is complete (in stellar mass) but the companion search area is  $> 50\%$  complete, one sigma upper limits on  $f_{\text{pair}}$  are denoted by symbols with a filled arrow of the same colour. Errors include contributions from cosmic variance estimates (Moster *et al.*, 2011), Poisson statistics and a bootstrap error analysis. These contributions are summed in quadrature.

Towards higher redshift the UDS, VIDEO and COSMOS fields provide an insight into the evolution of the pair fraction to within the first 2 Gyr of cosmic time. Pair fractions measured in the lowest redshift bin ( $0.2 < z < 0.5$ ) exhibit a large scatter between fields and possess large uncertainties. This is attributed to the relatively small volumes in this redshift bin which translates into a small sample of massive galaxies. However, all three fields report values of  $f_{\text{pair}}$  that agree to within the errors. At  $z > 0.5$  a consensus exists that  $f_{\text{pair}}$  evolves very little at  $z < 3.5$ . The measurements within the VIDEO region are found to be consistent with those obtained in the UDS region, however stellar mass completeness limits our comparison to  $z < 1.5$  in this region.

As in previous works, the pair fraction results are fit via a least-squares fitting routine with a simple power law of the form  $f_{\text{pair}} = f_0(1+z)^m$  (e.g., Patton *et al.*, 2002; Conselice *et al.*, 2003; Bridge *et al.*, 2007), which describes the pair fraction at  $z = 0$  and the slope of the pair fraction with redshift. Generally a weakly increasing pair fraction with redshift is found. A similar evolution is found by López-Sanjuan *et al.* (2009, see their Fig. 5) at  $0.2 < z < 1$ , López-Sanjuan *et al.* (2015, see their Fig. 11) at  $0 < z < 1$ , and Conselice *et al.* (2003, see their Fig. 14) at  $1.4 < z < 3.4$ , albeit with slightly varying selections and methodologies.

Performing the fitting procedure to the data from all *observationally* determined pair fractions shown in Figure 4.6 reveals an evolution in the pair fraction of

$$f_{\text{pair}}(z) = 0.025^{+0.005}_{-0.004} \times (1+z)^{0.62 \pm 0.22}$$

for close-pairs selected at 5–30 kpc. This is plotted as a solid black line. Fitting parameters for close-pairs selected at 5–20 kpc, at lower stellar masses, and using different combinations of data are presented in Table 4.3. Our data are complimented by pair fraction measurements within the CANDELS fields at  $z > 1.5$  presented in Duncan et al. (*in prep*). The relative scarcity of high mass galaxies combined with the small volumes probed by the CANDELS fields result in upper

limits (solid black circles with a downward pointing solid black arrow) of the pair fraction at  $z > 2.5$  although they are consistent with measurements in the UDS and COSMOS regions of this work. If just the GAMA, UDS, VIDEO and COSMOS data are considered, a very similar evolution in the pair fraction is found of

$$f_{\text{pair}}(z) = 0.025^{+0.005}_{-0.004} \times (1+z)^{0.73^{+0.21}_{-0.22}},$$

which is found to be in excellent agreement with the fit obtained when considering the CANDELS data at high redshift.

The fitting procedure consists of the following steps. Firstly, each measurement of the merger fraction is modelled as a Gaussian distribution and a value is selected at random from the distribution. Doing this at every measurement redshift gives a 'realisation' of the merger fraction. This 'realisation' is fitted with the power law using a least squares fitting routine. This process is repeated many times to produce a distribution of each fitting parameter. It is from these distributions that the 16, 50, and 84-th percentiles are selected giving the lower limit, average and upper limit of each fitting parameter. This procedure allows for Poisson uncertainties, cosmic variance estimates (Moster *et al.*, 2011), and uncertainties from the merger fraction bootstrap analysis to be included in the fitting procedure. In the following Sections, this leads to often large uncertainties on the fitting parameters however it is suggested these uncertainties are more realistic compared to previous studies on the subject.

As mentioned previously, it is difficult to compare merger fractions measured between different studies. However, for completeness, the results of this work are compared with previous studies of the major merger pair fraction. This work's value of  $m = 0.62 \pm 0.22$  is in agreement with that found by Conselice *et al.* (2003) for a primary sample of  $M_B > -20$  over a similar redshift range. On the other hand, the major merger fraction slope of  $m = 2.9 \pm 0.4$  found for galaxies with  $\log(\mathcal{M}_*/M_\odot) > 11$  in Bluck *et al.* (2009) is seemingly at odds with the measurement presented in this work. However, their fit is anchored by the  $z = 0$  point of De Propris *et al.* (2007) which was measured using different selection criteria to the  $z > 0.5$  data. Re-fitting to just the high redshift data presented in Fig. 1 of Bluck *et al.* (2009) results in a significantly shallower slope of  $m = 0.48 \pm 0.41$ , in agreement with our result. Xu *et al.* (2012) used close-pair analysis to determine the pair fraction of galaxies with  $11 < \log(\mathcal{M}_*/M_\odot) < 11.4$ , finding  $f_{\text{pair}} = 0.011 \pm 0.002$  at  $z = 0$  and  $f_{\text{pair}} = 0.061 \pm 0.015$  at  $z \sim 0.9$ . These results are in good agreement with the pair fractions obtained in this work. Ferreras *et al.* (2013) performed a similar analysis

**Table 4.3:** Major merger ( $\mu > 1/4$ ) fraction fitting parameters for combinations of survey regions, for a parametrisation of the form  $f_{\text{pair}}(z) = f_0(1+z)^m$ . Fitting is performed on  $f_{\text{pair}}$  measurements up to the redshifts reported in Table 4.2. Errors are determined using a bootstrap analysis and the resulting parameter distributions of 10,000 realisations. The number of merging events,  $N_{\text{merg}}$ , a galaxy undergoes at  $0 < z < 3.5$ , given by the integral in Equation 4.7, is provided in the far right column.

Survey Region	$f_0$	$m$	$N_{\text{merg}}^{z < 3.5}$	$N_{\text{merg}}^{z < 2}$	$N_{\text{merg}}^{z < 1}$
$\mathcal{M}_* > 10^{10} \text{M}_\odot$ (5 – 20kpc)					
UDS	$0.011^{+0.004}_{-0.003}$	$2.04^{+0.39}_{-0.36}$	$1.08^{+0.94}_{-0.52}$	$0.65^{+0.46}_{-0.26}$	$0.33^{+0.21}_{-0.13}$
COSMOS	$0.010^{+0.006}_{-0.005}$	$1.40^{+1.20}_{-1.02}$	$0.57^{+1.27}_{-0.38}$	$0.39^{+0.56}_{-0.23}$	$0.23^{+0.25}_{-0.13}$
All	$0.006^{+0.002}_{-0.001}$	$2.60^{+0.32}_{-0.35}$	$1.00^{+0.83}_{-0.45}$	$0.52^{+0.33}_{-0.19}$	$0.22^{+0.13}_{-0.08}$
All + GAMA	$0.009^{+0.002}_{-0.001}$	$2.07^{+0.29}_{-0.29}$	$0.91^{+0.61}_{-0.34}$	$0.55^{+0.31}_{-0.17}$	$0.27^{+0.14}_{-0.08}$
$\mathcal{M}_* > 10^{10} \text{M}_\odot$ (5 – 30kpc)					
UDS	$0.026^{+0.009}_{-0.007}$	$1.73^{+0.39}_{-0.38}$	$1.03^{+0.88}_{-0.46}$	$0.68^{+0.48}_{-0.28}$	$0.37^{+0.25}_{-0.14}$
COSMOS	$0.014^{+0.008}_{-0.006}$	$2.36^{+1.05}_{-0.93}$	$0.99^{+2.29}_{-0.68}$	$0.57^{+0.83}_{-0.35}$	$0.26^{+0.29}_{-0.14}$
All	$0.017^{+0.003}_{-0.003}$	$2.21^{+0.27}_{-0.28}$	$1.03^{+0.70}_{-0.36}$	$0.60^{+0.36}_{-0.19}$	$0.29^{+0.16}_{-0.09}$
All + GAMA	$0.019^{+0.002}_{-0.002}$	$2.03^{+0.20}_{-0.20}$	$0.98^{+0.58}_{-0.31}$	$0.60^{+0.33}_{-0.17}$	$0.30^{+0.16}_{-0.08}$
All + GAMA + D16	$0.026^{+0.002}_{-0.002}$	$0.89^{+0.16}_{-0.16}$	$0.54^{+0.29}_{-0.15}$	$0.43^{+0.21}_{-0.11}$	$0.27^{+0.14}_{-0.07}$
$\mathcal{M}_* > 10^{11} \text{M}_\odot$ (5 – 20kpc)					
UDS	$0.032^{+0.018}_{-0.013}$	$0.36^{+0.47}_{-0.46}$	$0.88^{+0.76}_{-0.45}$	$0.75^{+0.62}_{-0.38}$	$0.53^{+0.40}_{-0.26}$
VIDEO	$0.003^{+0.003}_{-0.002}$	$2.48^{+1.03}_{-1.22}$	$0.52^{+1.57}_{-0.39}$	$0.27^{+0.49}_{-0.19}$	$0.12^{+0.15}_{-0.08}$
COSMOS	$0.013^{+0.010}_{-0.006}$	$0.52^{+0.71}_{-0.71}$	$0.40^{+0.49}_{-0.24}$	$0.33^{+0.25}_{-0.13}$	$0.22^{+0.14}_{-0.08}$
All	$0.009^{+0.003}_{-0.002}$	$1.11^{+0.36}_{-0.35}$	$0.40^{+0.32}_{-0.17}$	$0.30^{+0.18}_{-0.11}$	$0.19^{+0.11}_{-0.07}$
All + GAMA	$0.011^{+0.003}_{-0.003}$	$0.89^{+0.34}_{-0.35}$	$0.43^{+0.30}_{-0.17}$	$0.33^{+0.21}_{-0.12}$	$0.21^{+0.13}_{-0.08}$
$\mathcal{M}_* > 10^{11} \text{M}_\odot$ (5 – 30kpc)					
UDS	$0.076^{+0.036}_{-0.027}$	$-0.06^{+0.41}_{-0.42}$	$0.87^{+0.69}_{-0.40}$	$0.75^{+0.57}_{-0.34}$	$0.58^{+0.42}_{-0.26}$
VIDEO	$0.008^{+0.006}_{-0.004}$	$2.97^{+0.94}_{-0.98}$	$1.08^{+2.88}_{-0.79}$	$0.48^{+0.80}_{-0.32}$	$0.19^{+0.22}_{-0.11}$
COSMOS	$0.034^{+0.015}_{-0.011}$	$0.30^{+0.48}_{-0.47}$	$0.48^{+0.42}_{-0.23}$	$0.41^{+0.32}_{-0.18}$	$0.28^{+0.22}_{-0.13}$
All	$0.026^{+0.006}_{-0.005}$	$0.69^{+0.25}_{-0.25}$	$0.47^{+0.30}_{-0.16}$	$0.37^{+0.22}_{-0.12}$	$0.25^{+0.14}_{-0.08}$
All + GAMA	$0.025^{+0.005}_{-0.004}$	$0.73^{+0.21}_{-0.22}$	$0.46^{+0.28}_{-0.15}$	$0.37^{+0.20}_{-0.11}$	$0.24^{+0.13}_{-0.07}$
All + GAMA + D16	$0.025^{+0.005}_{-0.004}$	$0.62^{+0.22}_{-0.22}$	$0.43^{+0.25}_{-0.14}$	$0.34^{+0.20}_{-0.10}$	$0.24^{+0.13}_{-0.07}$
$n(> \mathcal{M}_*) = 1 \times 10^{-4} \text{ Mpc}^{-3}$ (5 – 30kpc)					
All	$0.024^{+0.017}_{-0.011}$	$0.85^{+0.69}_{-0.66}$	$0.49^{+0.62}_{-0.28}$	$0.38^{+0.40}_{-0.22}$	$0.26^{+0.24}_{-0.14}$
All + GAMA	$0.021^{+0.008}_{-0.007}$	$0.97^{+0.45}_{-0.40}$	$0.46^{+0.37}_{-0.20}$	$0.35^{+0.27}_{-0.15}$	$0.23^{+0.15}_{-0.10}$
$n(> \mathcal{M}_*) = 5 \times 10^{-4} \text{ Mpc}^{-3}$ (5 – 30kpc)					
All	$0.030^{+0.014}_{-0.011}$	$0.78^{+0.61}_{-0.56}$	$0.58^{+0.59}_{-0.29}$	$0.44^{+0.40}_{-0.20}$	$0.30^{+0.24}_{-0.14}$
All + GAMA	$0.024^{+0.005}_{-0.005}$	$1.06^{+0.31}_{-0.31}$	$0.56^{+0.37}_{-0.20}$	$0.42^{+0.26}_{-0.14}$	$0.27^{+0.15}_{-0.09}$

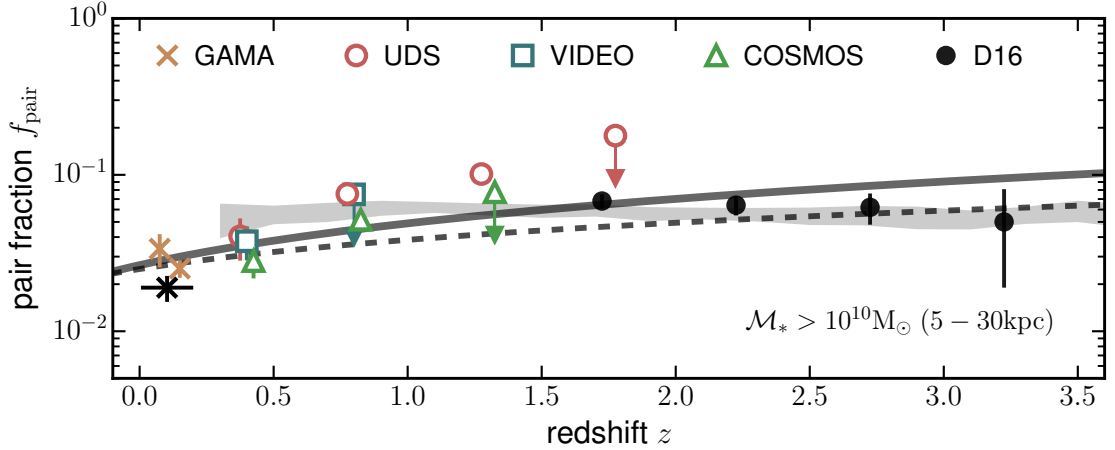


**Figure 4.7:** The measured major merger ( $\mu > 1/4$ ) pair fraction  $f_{\text{pair}}$  for galaxies with  $\log(\mathcal{M}_*/M_\odot) > 10$  at physical separations of 5–30 kpc as a function of redshift in the GAMA (gold and black crosses), UDS (red circles), COSMOS (green triangles) and VIDEO (blue squares) fields. The black crosses with horizontal error bars are points measured using the GAMA spectroscopic sample, including Poisson errors and cosmic variance estimates. Results from a complimentary study within the CANDELS fields (Duncan et al., *in prep*) are presented as solid black circles. Upper limits on the merger fraction are given by points with solid filled arrows. The best-fit  $f_{\text{pair}}(z)$  for galaxies with  $\log(\mathcal{M}_*/M_\odot) > 11$  (Figure 4.6) is shown as a dashed grey line for comparison. The grey shaded area represents the  $1\sigma$  variation in the merger fraction as measured using 24 light cones based on the H15 semi-analytic model.

towards higher redshift finding pair fractions of 10–15% at  $0.5 < z < 1.3$  for galaxies with  $> 10^{11} M_\odot$ . At the lowest of these redshifts, these fractions are much larger than found in this work, however the fractions at the higher redshift end agree well with this work. The work of Ferreras *et al.* (2013) is however based on the small volume of the GOODS-N fields which may introduce large cosmic variance issues at the lowest redshifts.

#### 4.4.1.2 Intermediate mass galaxies ( $\mathcal{M}_* > 10^{10} M_\odot$ )

The same measurement is performed for a sample of lower stellar mass systems with  $\log(\mathcal{M}_*/M_\odot) > 10$ . Stellar mass completeness considerations limit our measurements to  $z < 1.5$ . As displayed in Figure 4.7, an increase in the pair fraction is found from  $f_{\text{pair}} \sim 0.03$  at  $z \sim 0.1$  to  $f_{\text{pair}} \sim 0.1$  at  $z \sim 1.25$ . If the results of Duncan et al. (*in prep*) are considered at  $1.5 < z < 3.5$  in addition to those at  $z < 1.5$ , the pair fraction is found to remain roughly constant ( $f_{\text{pair}} = 0.06$ ) to high redshift. Fitting these data, as in Section §4.4.1.1, gives

$$f_{\text{pair}} = (0.026 \pm 0.002) \times (1 + z)^{0.89 \pm 0.16}.$$

When the calculated uncertainties are considered, the evolution of the pair fraction for intermediate mass galaxies is entirely consistent with that measured for the most massive galaxies in Section §4.4.1.1. The fit for this higher mass selection is illustrated in Figure 4.7 as the dashed black line.

Additionally, the H15 semi-analytic model light cones predict pair fractions (solid grey shaded region in Figure 4.7) in excellent agreement with all observations at  $z > 0.3$ . As with more massive samples, the cosmic variance between the light cones also appears to be reproduced. This agreement also extends to pair fractions measured at the smaller separation of 5–20 kpc.

#### 4.4.2 Constant number density selected samples

Selecting samples of galaxies at a constant cumulative comoving number density has been used to connect samples of galaxies across time (e.g., Papovich *et al.*, 2011; Conselice *et al.*, 2013; Ownsworth *et al.*, 2014; Torrey *et al.*, 2015; Ownsworth *et al.*, 2016), and has been shown to be more successful at tracing galaxy populations than a selection above a constant stellar mass with redshift (See Chapter 2; Behroozi *et al.*, 2013; Leja, van Dokkum & Franx, 2013; Jaacks, Finkelstein & Nagamine, 2016).

To provide the best estimate of the evolution of the merger histories of the progenitors of today’s most massive galaxies, the pair fraction is measured for a sample of galaxies selected at a constant cumulative comoving number density of  $n = 5 \times 10^{-4} \text{ Mpc}^{-3}$  which provides a sample of galaxies with  $\mathcal{M}_* > 10^{11} \text{ M}_\odot$  at  $z \approx 0$ , and galaxies with  $> 10^{9.5} \text{ M}_\odot$  at  $z \sim 3.25$ . The corresponding stellar mass limit is calculated at every redshift using the galaxy stellar mass function, described further in Section §4.6.3.1. Figure 4.8 and Figure 4.9 display the integrated galaxy stellar mass functions at each redshift bin, denoting the calculated stellar mass limits and associated errors. Making this selection directly probes the progenitors of these galaxies at higher redshift (see Chapter 2). The choice of number density is a trade off between satisfactory sample sizes at low redshift and avoiding mass completeness issues at high redshift.

The pair fraction evolution from this number density selection, measured at a separation of 5–30 kpc, is found to have a similar  $z = 0$  normalisation compared to the pair fractions measured for constant stellar mass selected samples. However, the measured slope is a factor of  $\sim 2$  larger compared to galaxies at  $> 10^{11} \text{ M}_\odot$ , and a factor of  $\sim 1.5$  compared to galaxies at  $> 10^{10} \text{ M}_\odot$ . The fitting procedure

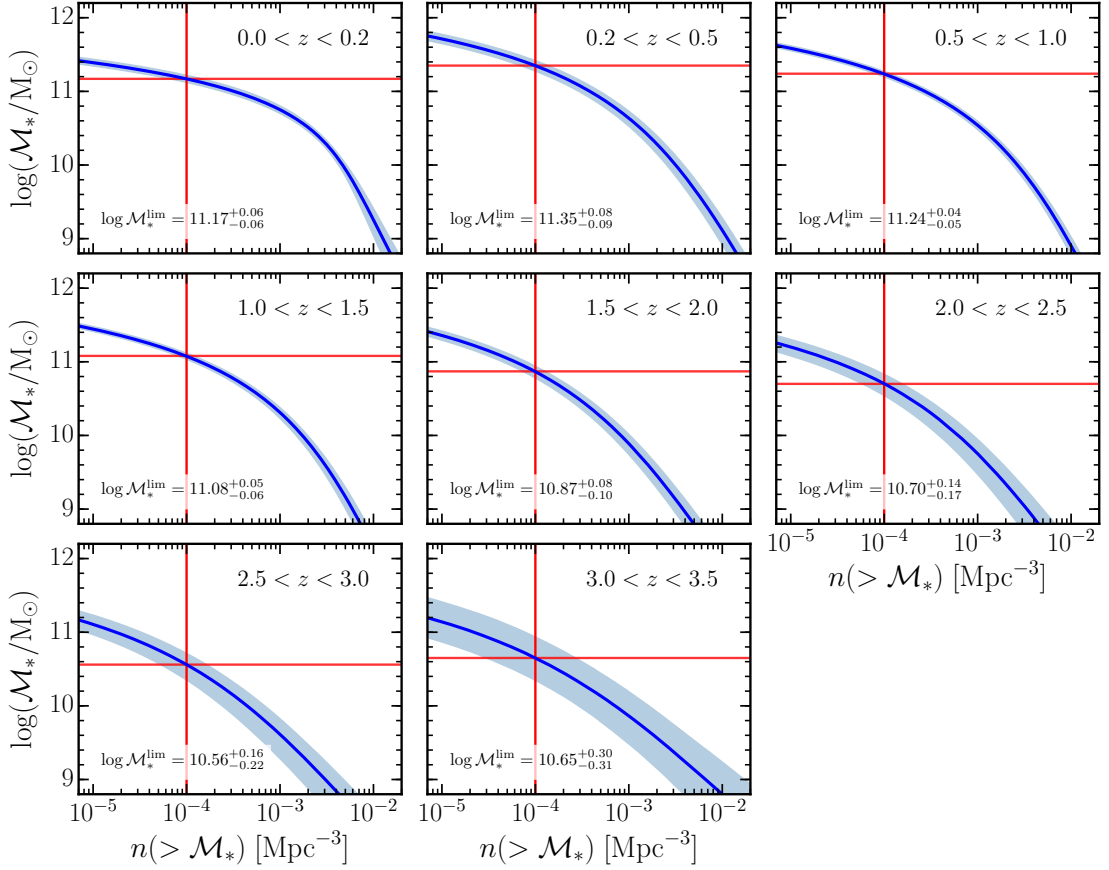


**Figure 4.8:** Integrated galaxy stellar mass functions (solid blue line) at  $0 < z < 3.5$ , with stellar mass limits at a constant cumulative number density of  $1 \times 10^{-4} \text{ Mpc}^{-3}$  indicated by the intersection of the horizontal and vertical red lines. Uncertainties on the integrated values are denoted by the shaded blue regions. Due to the various GSMF parametrisations used — and thus the various surveys used to calculate them — the horizontal red line does not smoothly decrease towards higher redshift as expected. However, where this is the case the calculated stellar mass limits are in good agreement and generally within 0.1 dex.

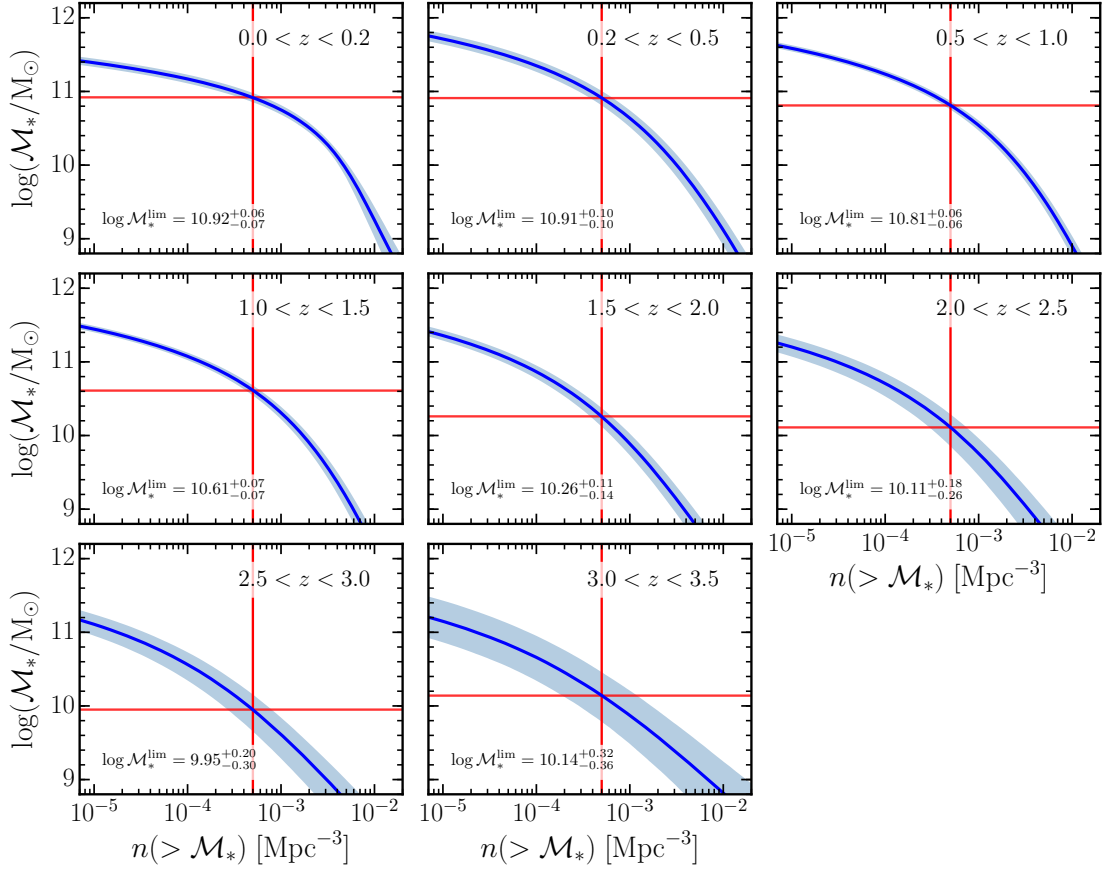


**Figure 4.9:** Integrated galaxy stellar mass functions (solid blue line) at  $0 < z < 3.5$ , with stellar mass limits at a constant cumulative number density of  $5 \times 10^{-4} \text{ Mpc}^{-3}$  indicated by the intersection of the horizontal and vertical red lines. Uncertainties on the integrated values are denoted by the shaded blue regions.



parametrises the pair fraction for this selection as

$$f_{\text{pair}}(z) = (0.021 \pm 0.005) \times (1 + z)^{1.23^{+0.33}_{-0.32}}.$$

This fit is obtained using the pair fraction measurements in the GAMA, UDS, VIDEO and COSMOS fields at  $z < 1.5$ . The pair fraction has been measured on a finer redshift grid in the VIDEO field to constrain the slope of the pair fraction over this small redshift range. Measured pair fractions for this selection are listed in Table 4.4.

Probing a smaller number density selection of  $n = 1 \times 10^{-4} \text{ Mpc}^{-3}$  provides a sample of galaxies at  $0 < z < 0.2$  with stellar mass  $\log(\mathcal{M}_*/\text{M}_\odot) > 11.2$  and allows us to probe the progenitors of such galaxies out to a higher redshift of  $z = 2.5$ . Here, exactly the same  $f(z=0)$  is found as the larger number density, but a slightly shallower evolution with redshift becoming only slightly steeper (but agreeing within the errors) than  $f_{\text{pair}}$  measured for constant stellar mass selections at  $> 10^{10} \text{ M}_\odot$ . Fitting the data finds

$$f_{\text{pair}}(z) = (0.021^{+0.008}_{-0.007}) \times (1 + z)^{0.97^{+0.45}_{-0.40}}.$$

While the best-fit parameters predict a steeper evolution with increasing redshift, once the uncertainties are considered the evolution is consistent with that found for the larger number density of  $n = 5 \times 10^{-4} \text{ Mpc}^{-3}$ . Therefore no significant change in the pair fraction evolution is detected between these two selections. Additionally, there is no significant difference between the evolution of the pair fraction in these selections with those of a constant mass selection when the same redshift range and datasets are considered. Further exploration at higher redshift is needed to constrain this evolution and make a comparison at higher redshift.

#### 4.4.3 Comparison between spectroscopically and photometrically determined merger fractions

The extraordinarily high spectroscopic completeness ( $> 97\%$ ) of the GAMA region (see Baldry *et al.* (2010, 2014), Robotham *et al.* (2010) and Hopkins *et al.* (2013) for details on the spectroscopic targeting campaign and subsequent analysis) allows several tests to be performed. Measured merger fractions are compared in the GAMA region at  $z < 0.2$  in two ways: spectroscopically and photometrically. To perform the measurement spectroscopically some tolerance in redshift must be chosen, translating to a cut in relative velocities between the galaxies in a close-pair

**Table 4.4:** Calculated major merger ( $\mu > 1/4$ ) pair fractions,  $f_{\text{pair}}$ , and associated errors for a constant cumulative comoving number density,  $n$ , selected sample of galaxies. The stellar mass limit,  $\mathcal{M}_*^{\text{lim}}$ , at the corresponding number density and redshift is calculated by integrating the appropriate galaxy stellar mass function. Errors include contributions from cosmic variance, bootstrap error analysis and Poisson errors.

$z$	$\log \mathcal{M}_*^{\text{lim}}$	GAMA	UDS	VIDEO	COSMOS
$n = 5 \times 10^{-4} \text{ Mpc}^{-3} (5 - 30\text{kpc})$					
0.0 – 0.1	10.8	0.045±0.021	-	-	-
0.1 – 0.2	10.8	0.025±0.006	-	-	-
0.2 – 0.5	10.9	-	0.058±0.043	0.015±0.010	0.035±0.013
0.5 – 0.7	10.9	-	-	0.066±0.026	-
0.7 – 0.9	10.9	-	-	0.070±0.023	-
0.5 – 1.0	10.9	-	0.069±0.021	-	0.040±0.008
0.9 – 1.1	10.9	-	-	0.070±0.019	-
1.1 – 1.3	10.8	-	-	<= 0.084	-
1.0 – 1.5	10.8	-	0.094±0.023	-	0.044±0.008
1.5 – 2.0	10.6	-	<= 0.142	-	<= 0.076
$n = 1 \times 10^{-4} \text{ Mpc}^{-3} (5 - 30\text{kpc})$					
0.0 – 0.1	11.2	0.046±0.036	-	-	-
0.1 – 0.2	11.2	0.021±0.009	-	-	-
0.2 – 0.5	11.3	-	0.018±0.053	0.004±0.008	0.081±0.050
0.5 – 0.7	11.2	-	-	0.041±0.034	-
0.7 – 0.9	11.2	-	-	0.068±0.039	-
0.5 – 1.0	11.2	-	0.031±0.025	-	0.038±0.011
0.9 – 1.1	11.2	-	-	0.068±0.034	-
1.1 – 1.3	11.1	-	-	0.029±0.016	-
1.0 – 1.5	11.1	-	0.081±0.025	-	0.042±0.010
1.5 – 1.7	10.9	-	-	<= 0.121	-
1.5 – 2.0	10.9	-	0.082±0.030	-	0.049±0.012
2.0 – 2.5	10.7	-	0.092±0.034	-	<= 0.073
2.5 – 3.0	10.6	-	<= 0.129	-	-

system. Previous studies have chosen a relative velocity offset of  $|\Delta v| < 500$  km/s (e.g., Patton *et al.*, 2000; Lin *et al.*, 2004, 2008; de Ravel *et al.*, 2009; López-Sanjuan *et al.*, 2012) in order to select close-pairs with a high probability of coalescence. This work therefore enforces this condition when measuring the spectroscopic pair fraction in the GAMA region (see black crosses with horizontal error bars in Figures 4.6 and 4.7).

Pair fractions measured with photometric and spectroscopic redshifts for massive galaxies ( $\mathcal{M}_* > 10^{11} M_\odot$ ; Section §4.4.1.1) are found to be in excellent agreement. Using the calculated GAMA photometric redshifts result in pair fraction of  $f_{\text{pair}} = 0.046 \pm 0.031$  at  $0.005 < z < 0.1$ , and  $f_{\text{pair}} = 0.025 \pm 0.007$  at  $0.1 < z < 0.2$ . Performing the analysis at  $0.005 < z < 0.2$  using the available spectroscopic redshifts instead results in  $f_{\text{pair}} = 0.041 \pm 0.013$ , in good agreement with the photometric analysis. Intermediate mass galaxies ( $\mathcal{M}_* > 10^{10} M_\odot$ ; Section §4.4.1.2) possess photometric pair fractions of  $f_{\text{pair}} = 0.034 \pm 0.008$  and  $f_{\text{pair}} = 0.014 \pm 0.002$  within the same redshift bins. Again performing the analysis spectroscopically, the pair fraction is found to be  $f_{\text{pair}} = 0.011 \pm 0.002$ . This close agreement suggests that the criteria we enforce on the photometric redshift probability distributions of the galaxies is approximately equivalent to enforcing a cut of  $\Delta v < 500$  km/s in relative velocity. Similar agreement is also seen at the smaller separation of 5–20 kpc. The observed consistency between the results of performing the analysis photometrically and spectroscopically suggests that the two methods perform equivalent measurements.

## 4.5 The major merger rate at $z < 3.5$

While the fraction of galaxies undergoing a merger event within a particular sample is a useful quantity, the ultimate goal is to measure the rate at which a typical galaxy (or population of galaxies) undergoes merging events. To achieve this, the merger fraction must be converted to a merger rate. The following section describes the process undertaken.

### 4.5.1 Calculating the merger rate from the pair fraction

Whereas merger fractions obtained via different methods may not necessarily be directly comparable, derived merger rates can be compared if the typical timescale over which each method can observe a galaxy merger is known. The conversion to merger rates is strongly dependent on the method of choice (e.g. close-pairs) and is

sensitive to various parameter choices (e.g. physical separation). The same method as described in Lotz *et al.* (2011) is used to derive merger rates from the merger fractions presented in Section §4.4 and the interested reader is referred to this paper for a concise and thorough introduction to the topic.

Two measures of the merger rate are often used in the literature. These are the volume-averaged galaxy merger rate,  $\Gamma_{\text{merg}}$ , and the fractional galaxy merger rate,  $\mathcal{R}_{\text{merg}}$ . The difference between these two quantities is important:  $\Gamma(z)$  traces the number of merging events per unit comoving volume and time above a mass limit, while  $\mathcal{R}(z)$  encodes the number of mergers per massive galaxy (Lotz *et al.*, 2011) per unit time. The volume-averaged merger rate is defined as

$$\Gamma_{\text{merg}}(z) = \frac{\phi_{\text{merg}}(z)}{\langle T_{\text{obs}} \rangle} = \frac{f_{\text{merg}}(z)n_1(z)}{\langle T_{\text{obs}} \rangle}, \quad [\text{Mpc}^{-3} \text{ Gyr}^{-1}] \quad (4.5)$$

and the fractional merger rate defined as

$$\mathcal{R}_{\text{merg}}(z) = \frac{f_{\text{merg}}(z)}{\langle T_{\text{obs}} \rangle}, \quad [\text{Gyr}^{-1}] \quad (4.6)$$

where  $\langle T_{\text{obs}} \rangle$  is the average timescale during which a merger can be observed given the method used to identify it,  $n_1(z)$  is the volume number density of the primary sample,  $\phi_{\text{merg}}$  is the volume number density of mergers, and  $f_{\text{merg}}$  is the merger fraction. As only *pair* fraction is directly measured, a correction must be made such that  $f_{\text{merg}} = C_{\text{merg}} f_{\text{pair}}$ , where  $C_{\text{merg}}$  is the fraction of pairs that will eventually result in a merger event. This is typically taken to be  $C_{\text{merg}} = 0.6$  (Lotz *et al.*, 2011) and so this convention is continued, however note the large uncertainty on this quantity and its origin going forward. The number density of the primary sample,  $n_1(z)$ , is calculated by integrating the GSMF at the appropriate redshift between the stellar mass limits of  $\mathcal{M}_{*}^{\text{min}}(z) < \mathcal{M}_{*}(z) < \mathcal{M}_{*}^{\text{max}}(z)$ , where the maximum stellar mass considered is  $10^{12} \text{M}_{\odot}$ .

Values of  $\langle T_{\text{obs}} \rangle = 0.60 \text{ Gyr}$  for close-pairs selected at 5–30 kpc, and  $\langle T_{\text{obs}} \rangle = 0.32 \text{ Gyr}$  for close-pairs selected at 5–20 kpc (Lotz *et al.*, 2011) are assumed. Using these values, which are measured using a suite of simulations, remarkable agreement is found between derived merger rates of both 20 kpc and 30 kpc separation. For the sake of brevity, and the advantage of larger number statistics, only merger rates derived from 5–30 kpc pair fractions are reported in the text and figures. The derived merger rate points are fit with either a simple power law of the same form as fitted to the pair fraction, or with a combined power law and exponential (Conselice, 2009). The choice of fitting form is determined using the  $\chi^2$  goodness-of-fit

parameter. Fitted volume-averaged and fractional merger rates at both separations are listed in Table 4.5 and Table 4.6.

Galaxies at  $\log(\mathcal{M}_*/M_\odot) > 11$  exhibit a constant volume-averaged merger rate (top panel in Figure 4.10) of  $\Gamma \sim 10^{-5} \text{ Mpc}^{-3} \text{ Gyr}^{-1}$  at  $z < 1.5$ , which declines steadily by a factor of  $\sim 10$  towards higher redshift such that, at  $z = 3.25$ , it is found that  $\Gamma = 4 \times 10^{-7} \text{ Mpc}^{-3} \text{ Gyr}^{-1}$ . This is attributed to the decrease in the number density of such massive galaxies. Conselice *et al.* (2007) estimate the merger rate of a morphologically selected sample using the same stellar mass criteria at  $0.4 < z < 1.4$  as  $2.0^{+3.0}_{-1.6} \times 10^{-5} \text{ Mpc}^{-3} \text{ Gyr}^{-1}$  which is consistent with our findings. Bluck *et al.* (2009) measure merger rates for a similar sample at high redshift and find a merger rate of  $\Gamma < 1.2 \times 10^{-4} \text{ Mpc}^{-3} \text{ Gyr}^{-1}$  at  $z = 0.5$ , and at  $z = 2.6$  find  $\Gamma < 5 \times 10^{-4} \text{ Mpc}^{-3} \text{ Gyr}^{-1}$ . These upper limits are consistent with the results presented here, with  $\Gamma$  found to be  $\sim 10^{-5} \text{ Mpc}^{-3} \text{ Gyr}^{-1}$  at  $z = 0.5$  and  $\sim 10^{-6} \text{ Mpc}^{-3} \text{ Gyr}^{-1}$  at  $z = 2.6$ . As seen in Figure 4.10 our derived merger rates at  $z < 1.5$  are found to be a factor of  $\sim 2$  smaller than those described in the aforementioned literature sources, although note that this work is typically consistent within  $2\sigma$ . This discrepancy is attributed to a number of factors. Bluck *et al.* (2009) find significantly higher pair fractions than this work; approximately  $\sim 5\%$  at  $0.5 < z < 1.5$ , and  $\sim 30\%$  at  $2 < z < 3$ . These are a factor of  $\sim 2$  and  $\sim 4$  larger, respectively, which, coupled with merger timescales of  $0.4 \pm 0.2 \text{ Gyr}$  (close-pair sample) and  $1.0 \pm 0.2 \text{ Gyr}$  (CAS sample) that Bluck *et al.* adopt, makes their derived merger rates a factor of  $\sim 2$  larger at low redshift, and a significant factor larger at high redshift (see their Section §3.2).

Galaxies with  $\log(\mathcal{M}_*/M_\odot) > 10$  exhibit a qualitatively similar evolution of the volume-averaged merger rate, shown in the top panel of Figure 4.11. However the rate is typically an order of magnitude greater than that derived for the higher stellar mass sample. At  $z < 1.5$  an approximately constant  $\Gamma \sim 2 \times 10^{-4} \text{ Mpc}^{-3} \text{ Gyr}^{-1}$  is found. Considering the derived merger rates using the pair fractions obtained by Duncan *et al.* (*in prep*) in the CANDELS fields extends the measurement at this stellar mass range to  $z = 3.25$ . A steep decline of  $\Gamma$  is found at  $z > 1.5$  such that at  $z = 3.25$ ,  $\Gamma \sim 3 \times 10^{-6} \text{ Mpc}^{-3} \text{ Gyr}^{-1}$ , albeit with an uncertainty of a factor of  $\sim 5$ . These derived merger rates are compared with a selection of literature rates (Lotz *et al.*, 2008; Bluck *et al.*, 2009; Conselice, 2009; de Ravel *et al.*, 2009; López-Sanjuan *et al.*, 2009) compiled in Lotz *et al.* (2011). These are shown in Figure 4.10 as solid grey markers. This work's results are consistent with merger rates derived in Bluck *et al.* (2009), López-Sanjuan *et al.* (2009) and de Ravel *et al.* (2009), however the best-fit rates are consistently a factor of  $\sim 2$

**Table 4.5:** Fitting parameters for the volume-averaged merger rate,  $\Gamma_{\text{merg}}(z)$ , as given in Equation 4.5, for various combinations of surveys used within this work. Fits with two parameters are of the form  $\Gamma_{\text{merg}}(z) = \Gamma_0(1+z)^{m_{\Gamma}}$ , while those with three parameters are of the form  $\Gamma_{\text{merg}}(z) = \Gamma_0(1+z)^{m_{\Gamma}} \exp(-c_{\Gamma}z)$ . Appropriate fitting forms are decided by comparing the goodness of fit using the  $\chi^2$ . Parameters and their associated uncertainties are calculating using a bootstrap technique, accounting for uncertainties on the pair fraction and GSMF.

Survey	$\Gamma_0$ ( $\text{Mpc}^{-3} \text{ Gyr}^{-1}$ )	$m_{\Gamma}$	$c_{\Gamma}$
$\mathcal{M}_* > 10^{10} \text{M}_{\odot} \text{ (5 - 20kpc)}$			
All	$6.47^{+4.53}_{-3.03} \times 10^{-5}$	$1.29^{+1.07}_{-1.12}$	-
All + GAMA	$1.00^{+0.58}_{-0.39} \times 10^{-4}$	$0.50^{+1.00}_{-1.28}$	-
$\mathcal{M}_* > 10^{10} \text{M}_{\odot} \text{ (5 - 30kpc)}$			
All	$8.16^{+4.88}_{-3.46} \times 10^{-5}$	$1.06^{+0.92}_{-0.97}$	-
All + GAMA	$1.06^{+0.44}_{-0.34} \times 10^{-4}$	$0.60^{+0.80}_{-0.93}$	-
All + GAMA + D16	$1.02^{+0.64}_{-0.51} \times 10^{-4}$	$3.10^{+4.99}_{-3.62}$	$2.00^{+1.74}_{-2.53}$
$\mathcal{M}_* > 10^{11} \text{M}_{\odot} \text{ (5 - 20kpc)}$			
All	$2.17^{+4.08}_{-1.76} \times 10^{-5}$	$0.48^{+8.87}_{-5.09}$	$1.34^{+2.36}_{-4.31}$
All + GAMA	$2.98^{+6.61}_{-2.55} \times 10^{-6}$	$6.59^{+12.90}_{-7.03}$	$3.68^{+3.39}_{-6.70}$
$\mathcal{M}_* > 10^{11} \text{M}_{\odot} \text{ (5 - 30kpc)}$			
All	$2.96^{+5.53}_{-2.28} \times 10^{-6}$	$9.22^{+9.37}_{-6.28}$	$5.16^{+3.12}_{-4.85}$
All + GAMA	$4.88^{+5.46}_{-3.32} \times 10^{-6}$	$6.89^{+7.28}_{-5.07}$	$4.07^{+2.52}_{-3.78}$
All + GAMA + D16	$4.59^{+6.60}_{-3.41} \times 10^{-6}$	$7.95^{+9.05}_{-6.75}$	$4.82^{+3.44}_{-4.69}$
$n(> \mathcal{M}_*) = 1 \times 10^{-4} \text{ Mpc}^{-3} \text{ (5 - 30kpc)}$			
All	$2.12^{+2.13}_{-1.23} \times 10^{-6}$	$0.99^{+1.05}_{-1.00}$	-
All + GAMA	$2.14^{+1.29}_{-1.01} \times 10^{-6}$	$0.96^{+0.81}_{-0.71}$	-
$n(> \mathcal{M}_*) = 5 \times 10^{-4} \text{ Mpc}^{-3} \text{ (5 - 30kpc)}$			
All	$1.69^{+1.28}_{-0.87} \times 10^{-5}$	$0.78^{+1.02}_{-0.93}$	-
All + GAMA	$1.38^{+0.56}_{-0.49} \times 10^{-5}$	$1.05^{+0.65}_{-0.61}$	-

**Table 4.6:** Fitting parameters for the fractional merger rate,  $\mathcal{R}_{\text{merg}}(z)$ , as given in Equation 4.6, for various combinations of surveys used within this work. Fits with two parameters are of the form  $\mathcal{R}_{\text{merg}}(z) = \mathcal{R}_0(1+z)^{m_{\mathcal{R}}}$ , while those with three parameters are of the form  $\mathcal{R}_{\text{merg}}(z) = \mathcal{R}_0(1+z)^{m_{\mathcal{R}}} \exp(-c_{\mathcal{R}}z)$ . Appropriate fitting forms are decided by comparing the goodness of fit using the  $\chi^2$ . Parameters and their associated uncertainties are calculating using a bootstrap technique.

Survey	$\mathcal{R}_0$ ( $\text{Gyr}^{-1}$ )	$m_{\mathcal{R}}$	$c_{\mathcal{R}}$
$\mathcal{M}_* > 10^{10} \text{M}_{\odot} \text{ (5 - 20kpc)}$			
All	$1.02^{+0.23}_{-0.20} \times 10^{-2}$	$2.76^{+0.35}_{-0.35}$	-
All + GAMA	$1.83^{+0.21}_{-0.20} \times 10^{-2}$	$1.79^{+0.22}_{-0.22}$	-
$\mathcal{M}_* > 10^{10} \text{M}_{\odot} \text{ (5 - 30kpc)}$			
All	$1.54^{+0.18}_{-0.17} \times 10^{-2}$	$2.29^{+0.19}_{-0.19}$	-
All + GAMA	$1.87^{+0.13}_{-0.12} \times 10^{-2}$	$1.97^{+0.12}_{-0.12}$	-
All + GAMA + D16	$1.73^{+0.15}_{-0.14} \times 10^{-2}$	$3.79^{+0.48}_{-0.44}$	$1.23^{+0.23}_{-0.24}$
$\mathcal{M}_* > 10^{11} \text{M}_{\odot} \text{ (5 - 20kpc)}$			
All	$1.65^{+0.48}_{-0.40} \times 10^{-2}$	$1.08^{+0.29}_{-0.29}$	-
All + GAMA	$2.17^{+0.47}_{-0.44} \times 10^{-2}$	$0.79^{+0.27}_{-0.26}$	-
$\mathcal{M}_* > 10^{11} \text{M}_{\odot} \text{ (5 - 30kpc)}$			
All	$1.63^{+0.68}_{-0.53} \times 10^{-2}$	$2.83^{+1.50}_{-1.33}$	$0.94^{+0.57}_{-0.66}$
All + GAMA	$1.98^{+0.43}_{-0.39} \times 10^{-2}$	$2.17^{+1.01}_{-0.92}$	$0.68^{+0.43}_{-0.48}$
All + GAMA + D16	$2.01^{+0.44}_{-0.40} \times 10^{-2}$	$2.13^{+1.03}_{-0.94}$	$0.68^{+0.44}_{-0.49}$
$n(> \mathcal{M}_*) = 1 \times 10^{-4} \text{ Mpc}^{-3} \text{ (5 - 30kpc)}$			
All	$2.05^{+1.05}_{-0.75} \times 10^{-2}$	$1.03^{+0.50}_{-0.47}$	-
All + GAMA	$2.01^{+0.65}_{-0.57} \times 10^{-2}$	$1.04^{+0.37}_{-0.33}$	-
$n(> \mathcal{M}_*) = 5 \times 10^{-4} \text{ Mpc}^{-3} \text{ (5 - 30kpc)}$			
All	$1.91^{+0.62}_{-0.53} \times 10^{-2}$	$1.37^{+0.42}_{-0.36}$	-
All + GAMA	$2.09^{+0.38}_{-0.35} \times 10^{-2}$	$1.25^{+0.25}_{-0.23}$	-

smaller than the average literature merger rate. The derived fractional merger rate shows a clear evolution to larger values with increasing redshift and is consistent with the results of López-Sanjuan *et al.* (2009) and de Ravel *et al.* (2009), where overlap allows comparison. Additionally, it is found that the discrepancy between COSMOS and the other survey regions is reduced when probing this stellar mass range, suggesting the cause of the discrepancy seen in Figure 4.6 is limited to higher mass galaxies. Cosmic variance likely contributes to the observed discrepancy, as it affects observations of the most massive objects more (Somerville *et al.*, 2004; Driver & Robotham, 2010; Moster *et al.*, 2011). However, it most likely cannot explain the systematic offset of the COSMOS field. This issue and the steps taken to identify the cause are discussed further in Section §4.6.3.

### 4.5.2 Number of major merger events at $z < 3.5$

The number of merger events a typical galaxy within each primary sample goes through between two redshifts can be approximated by integrating over the average time between merger events with respect to time. This typical timescale is given by  $\langle T_{\text{obs}} \rangle / f_{\text{merg}}(z) = \mathcal{R}_{\text{merg}}(z)^{-1}$ , where  $\langle T_{\text{obs}} \rangle$  is the average time during which a merger can be observed, as in Equations 4.5 and 4.6. The number of mergers,  $N_{\text{merg}}$ , between two redshift bins is then simply given by

$$N_{\text{merg}} = \int_{t_1}^{t_2} \mathcal{R}_{\text{merg}}(z) dt = \int_{z_2}^{z_1} \frac{\mathcal{R}_{\text{merg}}(z)}{(1+z)H(z)} dz, \quad (4.7)$$

where the substitution  $dt = dz/(1+z)H(z)$  has been made. Here  $H(z)$  is the Hubble constant at redshift  $z$ , alternatively defined as  $H(z) = H_0(\Omega_M(1+z)^3 + \Omega_\Lambda)^{1/2}$ .

Performing this integration between  $0 < z < 3.5$  and assuming a conservative 33% uncertainty on the value of  $\langle T_{\text{obs}} \rangle$ , a galaxy with  $\log(\mathcal{M}_*/M_\odot) > 11$  undergoes  $0.43^{+0.24}_{-0.14}$  major mergers between these times. Lower stellar mass galaxies, with  $\log(\mathcal{M}_*/M_\odot) > 10$  undergo  $0.54^{+0.29}_{-0.15}$  major mergers, approximately the same as higher mass galaxies. This means that, on average, one out of every two galaxies with  $> 10^{10}M_\odot$  has undergone a single major merger over the last 12 Gyr. For the most massive galaxies, this value is a factor of  $\sim 2$  smaller than that reported in Ownsworth *et al.* (2014), which calculated  $N_{\text{merg}} = 1.2 \pm 0.5$  using a fit to merger fractions from several literature sources (Bluck *et al.*, 2009; Bundy *et al.*, 2009; Xu *et al.*, 2012; Ruiz, Trujillo & Marmol-Queralto, 2014). These works use values of  $C_{\text{merg}} \approx 0.5 - 1.0$ . Fitting parameters are driven by the large merger fractions at high-redshift ( $z > 1.5$ ) from Bluck *et al.* (2009) and the  $z = 0$  point of Xu *et al.* (2012), and are obtained from works with various definitions and sample selections.



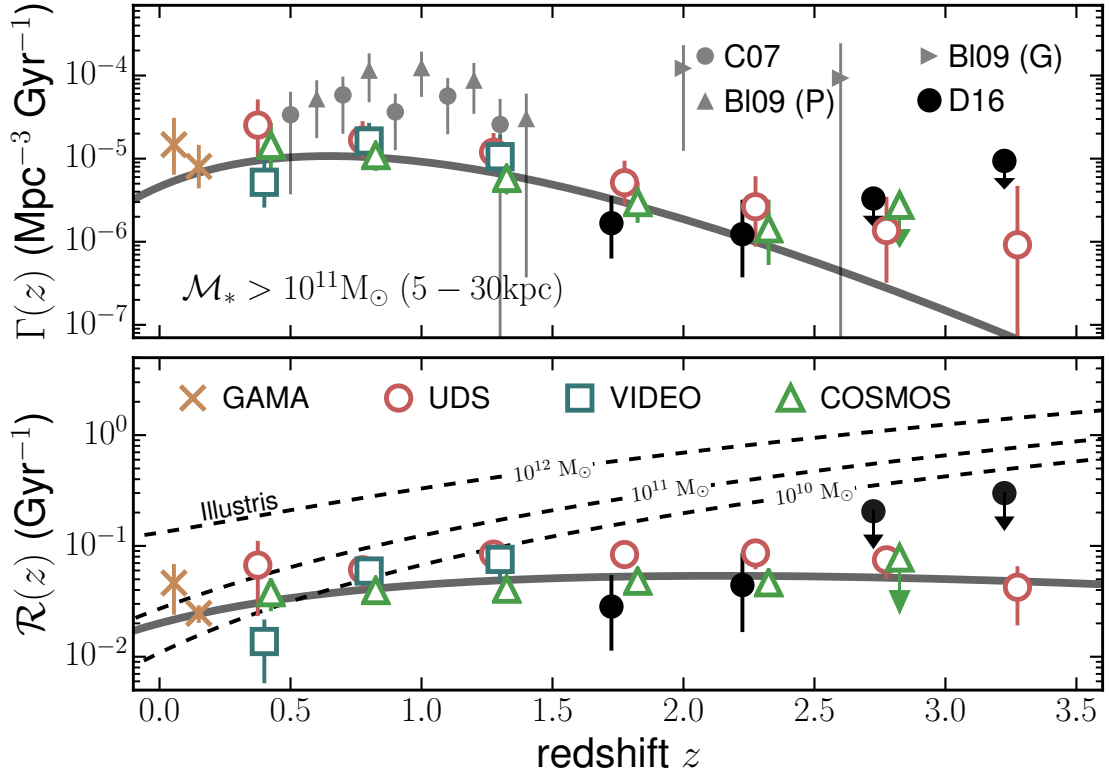


**Figure 4.10:** Derived volume-averaged (top) and fractional (bottom) major merger rates for galaxies at  $\log(\mathcal{M}_*/M_\odot) > 11$  at  $5 < r$  [kpc]  $< 30$  in the GAMA (gold crosses), UDS (red circles), VIDEO (blue squares) and COSMOS (green triangles) regions. Error bars include contributions from a bootstrap error analysis, cosmic variance estimates and Poisson statistics, combined in quadrature. Data points from Conselice *et al.* (2007) and Bluck *et al.* (2009) are shown for comparison. Illustris major merger rates for galaxies with stellar masses of  $10^{10}$ ,  $10^{11}$  and  $10^{12} M_\odot$  are shown as dashed black lines.

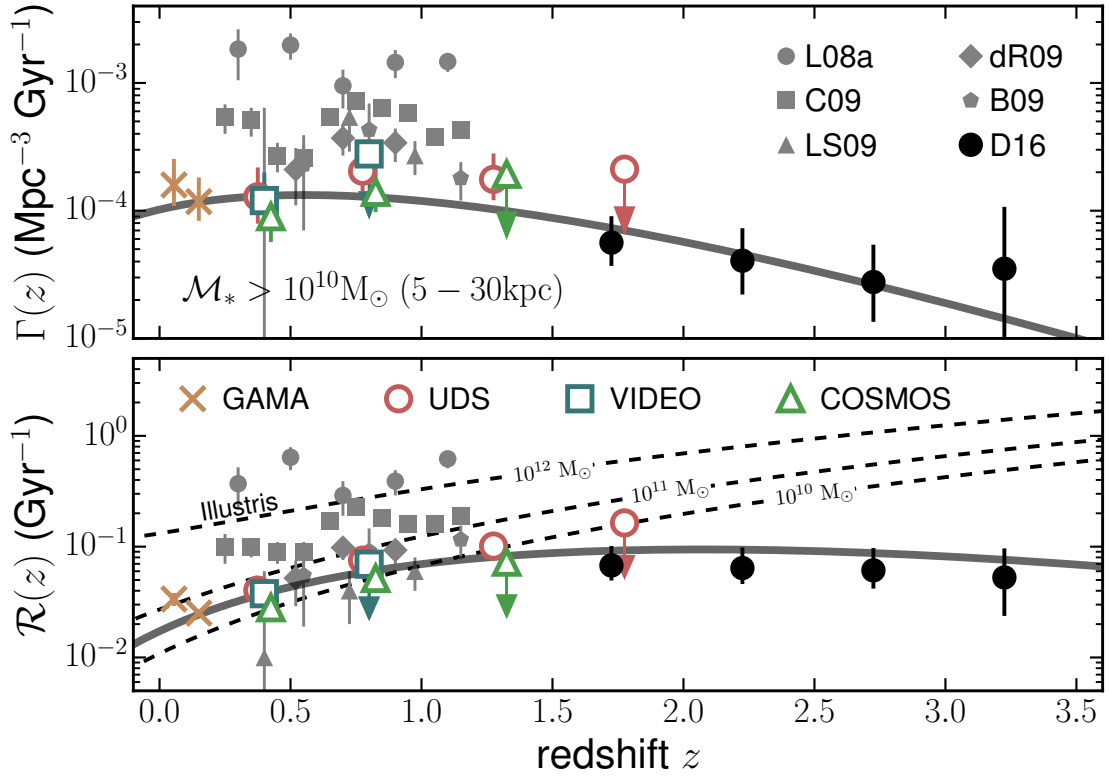


**Figure 4.11:** Derived volume-averaged (top) and fractional (bottom) major merger rates for galaxies at  $\log(\mathcal{M}_*/M_\odot) > 10$  in the GAMA (gold crosses), UDS (red circles), VIDEO (blue squares) and COSMOS (green triangles) regions. Error bars include contributions from a bootstrap error analysis, cosmic variance estimates and Poisson statistics, combined in quadrature. Data points, compiled in Lotz *et al.* (2011), from Lotz *et al.* (2008); Conselice (2009); López-Sanjuan *et al.* (2009); de Ravel *et al.* (2009) and Bundy *et al.* (2009) are shown as grey symbols for comparison. Illustris major merger rates for galaxies with stellar masses of  $10^{10}$ ,  $10^{11}$  and  $10^{12} M_\odot$  are shown as dashed black lines.

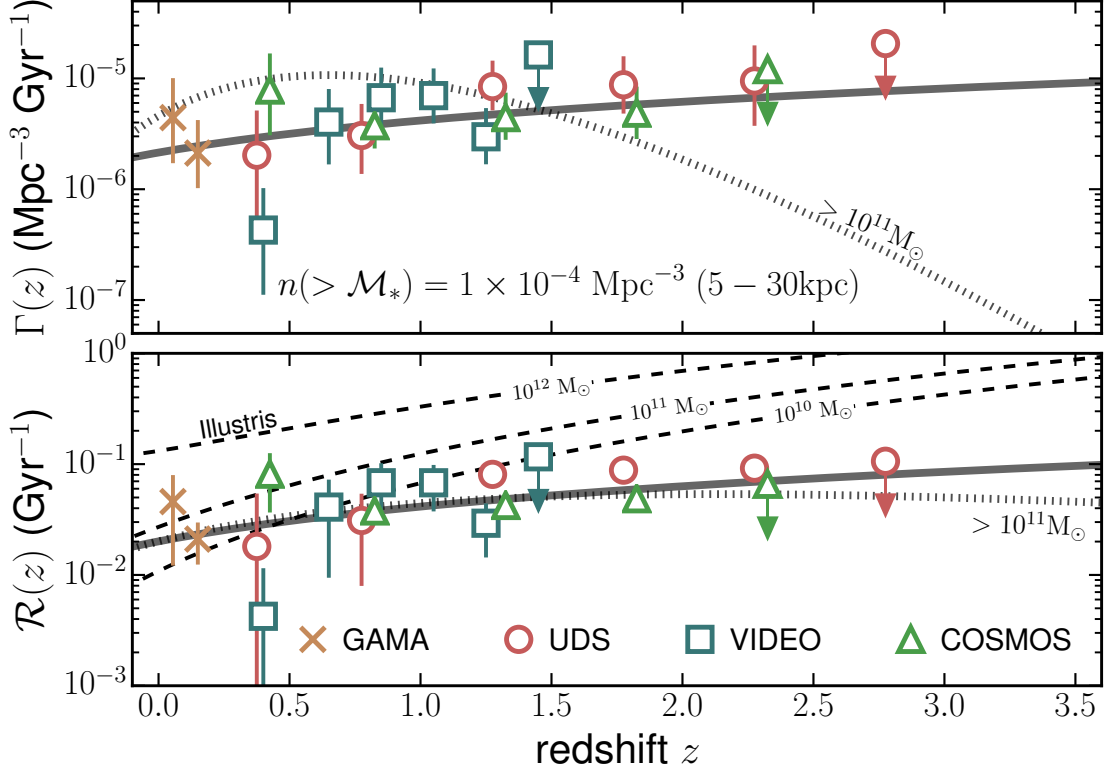


**Figure 4.12:** Derived volume-averaged (top) and fractional (bottom) major merger rates for galaxies at a constant cumulative comoving number density of  $n(> \mathcal{M}_*) = 1 \times 10^{-4} \text{ Mpc}^{-3}$  at 5–30 kpc in the GAMA (gold crosses), UDS (red circles), VIDEO (blue squares) and COSMOS (green triangles) regions. Error bars include contributions from a bootstrap error analysis, cosmic variance estimates and Poisson statistics, combined in quadrature. Illustris major merger rates at  $10^{10}$ ,  $10^{11}$  and  $10^{12} \text{ M}_\odot$  are shown as dashed black lines. These are obtained by integrating the galaxy-galaxy merger rate parametrisation given in Table 1 of Rodriguez-Gomez *et al.* (2015) with respect to the stellar mass merger ratio between  $0.25 < \mu < 1.0$ . Best-fit relations, as described in the text, are shown as solid grey lines. The dotted grey line represents the derived merger gates for galaxies with  $> 10^{11} \text{ M}_\odot$ .

### 4.5.3 Major merger rates at a constant cumulative number density

Merger rates are calculated for the two number density selections first introduced in Section §4.4.2. For a selection at  $n = 5 \times 10^{-4} \text{ Mpc}^{-3}$  it is found that the evolution of the volume-averaged merger rate can be parametrised as

$$\Gamma(z) = (1.4_{-0.5}^{+0.6} \times 10^{-5}) \times (1+z)^{1.1_{-0.6}^{+0.7}},$$

and the fractional merger rate for the same selection is given by

$$\mathcal{R}(z) = (2.1_{-0.4}^{+0.4} \times 10^{-2}) \times (1+z)^{1.3_{-0.2}^{+0.3}}.$$

Similarly, for the smaller choice of number density,  $n = 1 \times 10^{-4} \text{ Mpc}^{-3}$ , it is found

$$\Gamma(z) = (2.1_{-1.0}^{+1.3} \times 10^{-5}) \times (1+z)^{1.0_{-0.7}^{+0.8}},$$

and

$$\mathcal{R}(z) = (2.0_{-0.6}^{+0.7} \times 10^{-2}) \times (1+z)^{1.0_{-0.3}^{+0.4}}.$$

Individual merger rate data points and the best fitting parametrisation for the latter number density choice are shown in Figure 4.12, as this extends further in redshift than the former number density. Our fit is thus better constrained for this number density choice and, as has been mentioned, is not significantly different to the larger number density. Merger rate fits for both number density selections are shown in Table 4.5 and Table 4.6.

In contrast to the derived merger rates of constant stellar mass selections (see Section §4.5.1), no evidence is observed for a turnover in either merger rate, which are consistent with remaining approximately constant at  $z < 2.5$ . These data suggest that the merger rate of galaxies as they evolve over time have remained approximately constant, however further exploration is needed at high redshift to determine this (see Duncan et al. *in prep*).

Assuming these rates, a typical galaxy in a selection at  $n = 5 \times 10^{-4} \text{ Mpc}^{-3}$  and  $n = 1 \times 10^{-4} \text{ Mpc}^{-3}$  is found to undergo  $0.5_{-0.2}^{+0.4}$  and  $0.6_{-0.2}^{+0.4}$  major mergers since  $z = 3.5$ , respectively. These rates represent a total accreted stellar masses of  $\log(\mathcal{M}_*/\text{M}_\odot) = 10.4 \pm 0.2$  and  $10.5 \pm 0.3$ , respectively. Using the average stellar mass of these samples at  $z \sim 0$ , major mergers are found to account for  $20_{-10}^{+12}\%$  and  $20_{-12}^{+16}\%$ , respectively, of the in-situ stellar mass at this redshift. For the smaller number density choice, this is in excellent agreement with Ownsworth *et al.* (2014) who find major mergers responsible for  $17 \pm 15\%$  of the accumulated stellar mass in a typical  $z = 0.3$  massive galaxy.

## 4.6 Discussion

This section discusses the implications of this work's results with respect to galaxy evolution at  $z < 3.5$ , and explores various issues with the methods this work has employed. In Section §4.6.1 the measured pair fractions are compared with the H15 semi-analytic model, and our merger rates with those of the Illustris cosmological hydrodynamical simulation. Section §4.6.2 explores possible explanations for the systematic difference between pair fractions measured in the COSMOS region, and

those measured in the other regions. Finally, Section §4.6.3 describes the tests performed on the data and measurements of the pair fraction which demonstrates their robustness.

A caveat of this work and indeed any close-pair study of merger histories is the inherent uncertainty surrounding the fraction,  $C_{\text{merg}}$ , of close-pair systems that will eventually merge. Throughout this work it has been explicitly assumed this fraction is constant with redshift, stellar mass and physical separation. Although numerical simulations and empirical measurements of close-pairs at  $r < 30$  kpc have determined  $C_{\text{merg}} \approx 0.4 - 1.0$  (Kitzbichler & White, 2008; Patton & Atfield, 2008; Bundy *et al.*, 2009), its dependence on stellar mass and redshift is as yet unexplored in detail. Furthermore the timescale,  $\langle T_{\text{obs}} \rangle$ , over which one can observe a merger event (as defined in this paper) has been explored only at  $z < 1.5$  (Lotz *et al.*, 2011), and its constancy beyond this is unknown. This work assumes that this timescale is fixed at earlier times. If any of these assumptions prove incorrect, the results presented herein will be in doubt. Further investigation of these parameters is required.

It is relatively simple, however, to correct the results presented in this work to other combinations of  $C_{\text{merg}}$  and  $\langle T_{\text{obs}} \rangle$ , as these values are simply constants in any integrations performed. For this purpose, the ratio of these two quantities is defined as

$$\eta_{\text{merg}} = \frac{C_{\text{merg}}}{\langle T_{\text{obs}} \rangle}. \quad [\text{Gyr}^{-1}] \quad (4.8)$$

The  $r_p < 30$  kpc merger *rates* used in this work therefore correspond to  $\eta_{\text{merg}} = 1$ , while the  $r_p < 20$  kpc merger rates assume  $\eta_{\text{merg}} = 1.875$ . If one then wished to correct the merger rates, the estimated number of major mergers undergone by a galaxy, or even the stellar mass accrued through major mergers for a different value of  $\eta$ , simply multiply the values quoted in this paper by a factor of  $\eta_{\text{new}}/\eta_{\text{old}}$ .

#### 4.6.1 Comparison with semi-analytic models and hydrodynamical simulations

Figure 4.6 and Figure 4.7 in Section §4.4 present a comparison between  $f_{\text{pair}}$  measured observationally and from lightcones extracted from the H15 semi-analytic model, illustrated as the grey shaded area in these figures. The model predicts pair fractions in excellent agreement with those found in this work, especially when the higher redshift CANDELS data are considered. Additionally, the (cosmic) variance seen between the lightcones appears to reflect the variance between the ob-

servational measurements in different survey regions. The measured pair fractions depend mainly on the clustering of galaxies (i.e. the cosmology) and the stellar mass of galaxies. As H15 uses the most current cosmological model and is able to reproduce the (total) GSMFs out to at least  $z \sim 3$ , this is welcome agreement. This agreement also extends the argument that **Pyrus** is in fact measuring close-pairs with  $\Delta v < 500$  km/s, as seen at  $z \sim 0$  using GAMA in Section §4.4.3.

Figures 4.10 and 4.11 illustrate the derived fractional merger rates of galaxies at  $> 10^{11} M_{\odot}$  and  $> 10^{10} M_{\odot}$ , respectively. Shown as dashed lines, the merger rates of galaxies within the Illustris cosmological hydrodynamical simulation are also plotted using the equation given in Table 1 of Rodriguez-Gomez *et al.* (2015). This equation estimates the galaxy-galaxy merger rate as a function of stellar mass, stellar mass merger ratio, and redshift. Integrating this equation with respect to stellar mass merger ratio at  $0.25 < \mu < 1$ , results in the cumulative merger rate comparable to our observations. It can be seen clearly that the predictions from Illustris are found to be inconsistent with observational estimates of the fractional merger rates. The predictions made by the simulation evolve strongly with redshift and do not reproduce the observed values of  $\mathcal{R}$  at  $\mathcal{M}_* < 10^{12} M_{\odot}$ . This may well be due to the overproduction of both high ( $\mathcal{M}_* > 10^{10.5} M_{\odot}$ ) and low ( $\mathcal{M}_* < 10^{10} M_{\odot}$ ) stellar mass galaxies within Illustris (Genel *et al.*, 2014; Schaye *et al.*, 2015; Arthur *et al.*, 2016) compared to observed number densities.

#### 4.6.2 Field-to-field variation

Evident in the measured pair fractions (e.g., Figure 4.6) is an apparent systematic offset in the measured merger fractions between the COSMOS region and the UDS and VIDEO regions. At  $z > 1$  the pair fractions measured in the COSMOS region are found to be a factor of  $\sim 2$  lower than those in either the UDS or VIDEO regions. Such a consistent systematic difference over such a large redshift range cannot in all likelihood be attributed to cosmic variance alone. This section describes the efforts undertaken to determine the cause of this systematic difference.

During the course of this work an issue with the IRAC photometry in the UDS catalogue was identified whereby fluxes were found to be underestimated by approximately 20%. This issue was traced to the background estimation process in these bands whereby the background level was overestimated and the resulting fluxes underestimated. As these filters aid in constraining the photometric redshifts and stellar masses of galaxies, the effect of such an underestimate in the flux on photometric redshifts and stellar population parameters is not trivial to predict. To probe this, the sample's IRAC fluxes are increased by a factor of 1.2 whilst conserv-

ing the signal-to-noise ratio. Next the photometric redshifts and stellar masses of galaxies are recalculated and the pair fraction measurement is reapplied on the adjusted photometry. No significant differences are found between the recalculated  $f_{\text{pair}}$  and those tabulated in Table 4.2. A similar issue with IRAC photometry was discovered within the COSMOS catalogue as well. Spatially dependent systematic shifts in IRAC fluxes of up to one magnitude exist which essentially renders the IRAC photometry in this catalogue unusable. The IRAC photometry was excluded, photometric redshifts and stellar masses were recalculated for all galaxies and measurements of the pair fraction were performed once more. A systematic increase of  $\sim 10\%$  is identified in the pair fraction in all redshift bins. This can be attributed to a slight rise of  $\sim 0.1$  dex in the estimated stellar mass calculated without IRAC photometry. While this goes part of the way to reducing the observed offset between COSMOS and the other regions, erroneous IRAC photometry cannot be the primary source of the observed offset and its absence does not significantly affect the results of this work. Further work is needed to pinpoint the cause of this difference.

Another suspected source of the discrepancy is the different pixel scales of the images from which photometry is extracted. Companion galaxies could be missed by our analysis if it was close enough to a primary galaxy to have its photometry blended in with the host galaxy’s light. The minimum separation for two galaxies to be considered a close-pair is doubled to 10 kpc and the pair fraction measurement is rerun. Comparing the remeasured fractions revealed the discrepancy remained and thus is not predominantly due to source extraction/blending issues.

### 4.6.3 Tests on the merger fraction

Several tests and sanity checks are performed on the data and the method to ensure the robustness of the results presented in this work. As *Pyrus* makes use of the GSMF to statistically correct for missing close-pairs if the stellar mass search area is reduced (e.g. if  $\mu\mathcal{M}_{*,1} < \mathcal{M}_*^{\text{comp}}$ ), the dependence on the choice of GSMF used to perform this correction on the measured fractions is important to quantify. Using different published GSMF parameters (described in Section §4.6.3.1) results in no significant change in the measured pair fractions, even at high redshift where incompleteness and errors on the GSMF parameters are large. Furthermore, spatial dependence of the merger fractions is tested for within each survey region by splitting each dataset into four contiguous sub-fields and performing the merger fraction measurement once more. No significant differences are found except in the UDS region. A slight excess in the pair fraction is found, with  $f_{\text{pair}}$  found to be a

factor of  $\sim 1.5$  higher at  $1.5 < z < 2.0$ , in one sub-field. This quadrant contains a known galaxy cluster at  $z = 1.6$  (Papovich *et al.*, 2010), to which the observed excess is attributed. Averaged over the entire region, this excess signal is not found to significantly impact the measured pair fractions.

Where possible, merger fractions are remeasured using redshift PDFs produced by independent works (e.g. Hartley *et al.* (2013) in the UDS region and Muzzin *et al.* (2013a) in the COSMOS region). No significant difference is found when these data are used. Additionally, a measurement of the contribution to the measured pair fraction by the random projected positions of galaxies on the sky is performed. Given these conditions, one would expect a negligible pair fraction extremely close to zero. Pair fractions of  $\sim 10^{-4}$ , approximately two orders of magnitude lower than those tabulated in Table 4.2, are found.

#### 4.6.3.1 Galaxy stellar mass function choice

Various parts of this work make use of the galaxy stellar mass function (GSMF). For example we employ the GSMF to calculate statistical weightings for primary and secondary galaxies if a search in  $\mathcal{M}_*$ -space falls below the completeness limit of a survey. Additionally, in Section §4.5.3 we use the GSMF to calculate stellar mass limits for a constant cumulative comoving number density selected sample.

GSMF parametrisations are sourced from various literature works for this purpose. At  $z < 0.2$  the GSMF of Baldry *et al.* (2012) is used, at  $0.2 < z < 3$  the values presented in Mortlock *et al.* (2015, 2016) are used, and at  $3.0 < z < 3.5$  the results of Santini *et al.* (2012) are assumed. The numerical results presented in this work are based on these GSMF parametrisations, making appropriate conversions to a Chabrier (2003) IMF. To ensure the results presented herein are not dependent on the choice of GSMF, all measurements that depend on the GSMF are performed with other literature parametrisations. At low redshift ( $z < 0.2$ ) GSMF parameters from Pozzetti *et al.* (2010) and Kelvin *et al.* (2014) are substituted. At higher redshifts the values presented in Muzzin *et al.* (2013b) and Duncan *et al.* (2014) are used. No significant change to the results presented in this work are observed using any of these GSMF parametrisations and thus our results are robust to the choice of GSMF. Summarising all aforementioned tests, we conclude that the results presented in this work are robust and not significantly influenced by any of the factors discussed.



## 4.7 Conclusions

This Chapter has presented measurements of the merger fraction for flux-limited, stellar mass selected samples of galaxies using the full photometric redshift probability information afforded by modern multi-wavelength surveys. Using a sample of  $\sim 350,000$  galaxies within the UKIDSS UDS, VIDEO/CFHT-LS, UltraVISTA/COSMOS and GAMA survey regions, merger *fractions* have been measured and derived merger *rates* calculated for constant stellar mass selected galaxies ( $> 10^{10}M_{\odot}$ ) and samples selected at two constant cumulative number densities of  $n(> \mathcal{M}_*) > 1 \times 10^{-4} \text{ Mpc}^{-3}$ . For the first time a consistent picture of the major merger histories of massive galaxies over the vast majority of cosmic time has been painted.

Samples of galaxies selected at a constant stellar mass were probed to enable comparison to previous literature. The main findings for these samples can be summarised as followed. Measured pair fractions are found to be approximately constant over the redshift range probed, and no significant difference between the normalisation or evolution of the pair fraction for galaxies selected above stellar masses of  $10^{10}M_{\odot}$  and  $10^{11}M_{\odot}$  was seen at  $z < 3.5$ . Pair fractions measured photometrically and spectroscopically ( $\Delta v < 500 \text{ kms/s}$ ) using the second data release of GAMA are found to be consistent with each other at both constant stellar mass selection limits.

Major merger rates are derived from major merger fractions for massive galaxies. We subsequently calculated the average number of major merger events and the stellar mass gained through major mergers at  $z < 3.5$  for our samples. The volume-averaged merger rates,  $\Gamma(z)$ , of galaxies selected above stellar masses of  $10^{10}M_{\odot}$  and  $10^{11}M_{\odot}$  is found to be a factor of 2–3 smaller than many previous works. These rates exhibit a strong evolution with redshift and are well fit by a combined power law plus exponential. Due to lower major merger rates, galaxies are expected to undergo fewer major mergers than previously found. Galaxies with  $\mathcal{M}_* > 10^{11}M_{\odot}$  undergo  $0.43^{+0.25}_{-0.14}$  major mergers while galaxies with  $\mathcal{M}_* > 10^{10}M_{\odot}$  undergo  $0.54^{+0.29}_{-0.15}$  major merger events. However, these precise numbers strongly depend on the assumed values of  $C_{\text{merg}}$  and  $\langle T_{\text{obs}} \rangle$ . Galaxies with stellar masses  $> 10^{11}M_{\odot}$  ( $> 10^{10}M_{\odot}$ ) at  $z \approx 3.25$  accumulate additional stellar mass of  $\log(\mathcal{M}_*/M_{\odot}) = 10.5 \pm 0.2$  ( $10.1 \pm 0.2$ ) at  $z < 3.5$  solely via major mergers.

Tracing the direct progenitors of local massive galaxies by sampling at a constant cumulative number density of  $n = 1 \times 10^{-4}$  ( $5 \times 10^{-4}$ )  $\text{Mpc}^{-3}$ , representing  $z = 0$  selections of  $\mathcal{M}_* > 10^{11.2}M_{\odot}$  ( $> 10^{11.0}M_{\odot}$ ), it is found that a stellar mass of

$\log(\mathcal{M}_*/M_\odot) = 10.5 \pm 0.3$  ( $10.4 \pm 0.2$ ) is accrued via major mergers over the same redshift range.

Furthermore, many of the results presented in this work are compared to predictions made by the Henriques *et al.* (2015) semi-analytic model, and the Illustris cosmological hydrodynamical simulation. The main results can be summarised as follows. The Henriques *et al.* (2015) semi-analytic model predicts pair fractions (measured spectroscopically with  $\Delta v < 500$  km/s) in excellent agreement with observations. Furthermore, the model variance between  $1 \text{ deg}^2$  fields-of-view similar to that seen between the observed fields.

Finally, the fractional merger rates,  $\mathcal{R}(z)$ , predicted within Illustris are qualitatively and quantitatively inconsistent with our derived rates at  $z > 0.5$ . This may be due to the inability of the simulation to reproduce the correct number density of galaxies over a wide range of stellar masses at most redshifts. Illustris predictions of the major merger accretion rate density,  $\rho_{1/4}$ , are qualitatively similar to those estimated for galaxies at a constant number density and constant stellar mass. However, the normalisation is typically smaller than that observed by a factor of  $\sim 2$ – $3$ .

# Chapter 5

## The total merger histories of massive galaxies at $z < 3.5$

In this Chapter the ‘total’ ( $\mu > 1/10$ ) merging histories of massive galaxies are explored at  $z < 2.5$ . This is the sum of the major mergers explored in Chapter 4 as well as the signal from minor mergers, typically defined as  $0.1 < \mu < 0.25$ . Pair fractions are measured within the same survey regions described in Chapter 4, and merger rates are derived. From these the number of minor mergers is estimated and the results compared with results from previous chapters and the literature.

### 5.1 Introduction

While many studies have investigated major mergers out to high redshift, the same cannot be said of mergers at even smaller host-to-companion stellar mass ratios — so-called minor mergers. These are typically defined in the literature as galaxy pairings with  $0.25 < \mu < 0.1$ , although variations do occur. The deep imagery, increased sample sizes or high completeness needed for such a study has only become reality in the recent past. It is therefore prudent to investigate minor mergers and accompany the few studies of minor mergers in the high-redshift Universe.

Minor mergers have been increasingly implicated in the observed size evolution of massive elliptical galaxies (e.g., Bluck *et al.*, 2012). An apparent change in size of these galaxies by up to a factor of 5 from  $z \sim 3$  to  $z \sim 0$  can be theoretically explained by several processes. These include adiabatic expansion (‘puffing up’) from stellar mass loss or feedback mechanisms (e.g., Fan *et al.*, 2008; Damjanov *et al.*, 2009), or indeed dry, dissipationless mergers. Simple arguments using the virial theorem suggest that the latter mechanism can produce an increase in size proportional to the square of the change in stellar mass (e.g., Naab, Johansson &

Ostriker, 2009) from a merger event. This suggests that minor mergers are much more efficient at changing the size of a galaxy than mergers at larger stellar mass ratios (Bezanson *et al.*, 2009; Hopkins *et al.*, 2010). Given a high enough rate of minor merger events, they may be a dominant driver in the size evolution of massive galaxies if a large fraction are dry mergers (van der Wel *et al.*, 2009). Indeed it is reasonable to expect that the fraction of galaxies undergoing a minor merger event would be larger than that for major mergers, due in part to the larger dynamical friction timescales between galaxies at these stellar mass regimes, and the shape of the GSMF (i.e. Schechter function; Schechter, 1976). However, some cosmological simulations have indicated that major and minor merger rates are comparable (within a factor of  $\sim 2$ ) at high stellar masses ( $> 10^{11} M_{\odot}$ ) and redshifts of  $z \leq 3$  (e.g., Croton *et al.*, 2006; Maller *et al.*, 2006; Somerville *et al.*, 2008).

The simplest measurement that can be performed to investigate minor mergers is to measure the fraction of galaxies undergoing such events. Recently, Man, Zirm & Toft (2014) used 3DHST/CANDELS and UltraVISTA observations to determine the role of minor mergers out to  $z = 2.5$  for galaxies at  $> 10^{10.8} M_{\odot}$ . Ignoring a selection in flux rather than stellar mass, whereby the former generally selects gas-rich pairings that the latter would otherwise exclude, Man, Zirm & Toft find that minor merger pair fractions are comparable to that of major mergers and exhibit a similar evolution with respect to redshift. Additionally, in their Figure 4, Man, Zirm & Toft find a large scatter of up to a factor of  $\sim 3$  in the measured major and minor merger fractions between the different CANDELS fields. The observed similarity between the major and minor pair fractions is in contrast to the results of Jogee *et al.* (2009), one of the first attempts to study minor mergers at high redshift. They find that the fraction of morphologically selected minor mergers is at least 3 times that of major mergers out to  $z \sim 0.8$ .

Delving deeper into the issue, various investigations have been carried out in order to quantify the impact of minor mergers on galaxy size, as well as other properties such as stellar mass growth. Naab, Johansson & Ostriker (2009) performed analyses on cosmological N-body and SPH simulations. They found that minor mergers increased the size of massive ellipticals on average by a factor of 3.4 from  $z = 3$  to  $z = 0$ . Newman *et al.* (2012) used observations in the CANDELS fields to explore the role of minor mergers. They found that minor mergers could account for most of the observed size evolution at  $z < 1$  if the merger timescale was sufficiently short at  $\leq 1$  Gyr. Using morphological selections, Bluck *et al.* (2012) inferred that minor mergers could be responsible for, at most, a factor of two increase in the sizes

of massive galaxies from  $z = 3$  to the present. Ownsworth *et al.* (2014) compared selections at a constant number density in order to infer the role of minor mergers in the stellar mass growth of the direct progenitors of  $z \sim 0.4$  massive galaxies, finding that minor mergers contribute approximately twice the stellar mass content compared to major mergers since  $z \sim 3$ . A more direct measurement for more massive galaxies (selected at constant stellar mass) was made by Man, Zirm & Toft (2014) using standard conversions from pair fractions to merger rates, who find that minor mergers supply approximately one quarter of the stellar mass compared to major mergers over a similar redshift regime.

The results of previous studies highlight the need for studies that combine wide-area, deep independent fields in the robust determination of the minor merger histories of galaxies. To this end, this Chapter presents measurements of the total and minor merger histories of massive galaxies.

## 5.2 Data overview

The work in this Chapter utilises several datasets to achieve a measurement of the total and minor merger histories of massive galaxies. They are described in detail in Section §4.2, however a brief description follows.

At low redshift, multi-wavelength photometry and spectroscopic observations from the second data release (DR2) of the GAMA survey are used. This dataset provides a flux-limited sample of galaxies from three independent lines of sight (totalling 144 square degrees) down to a limiting Petrosian  $r$ -band magnitude of  $m_r = 19$ . At  $z > 0.2$ , three independent lines of sight provide an effective area of 3.25 square degrees. The eighth data release (DR8) of the UKIDSS UDS provides galaxies down to a limiting  $K$ -band magnitude of  $m_K = 24.3$  over 0.6 square degrees. The UKIDSS UDS remains the deepest  $K$ -selected square-degree sized survey to date. The VIDEO survey, combined with CFHT observations in the CFHT-LS D1 field, provides multi-wavelength observations over a 1 square degree field. Finally, UltraVISTA observations in the COSMOS field are combined with archival observations. The publicly available catalogue provided in Muzzin *et al.* (2013a) presents a sample of galaxies down to a limiting magnitude of  $m_K = 23.4$  over an area of 1.6 square degrees. From these datasets photometric redshift probability distributions,  $P(z)$ , are calculated using **EAZY**, and stellar mass-redshift functions,  $\mathcal{M}_*(z)$ , are calculated using a custom spectral energy distribution (SED) fitting routine.

## 5.3 Pair fractions measurements

### 5.3.1 Total merger pair fraction

Total (major plus minor) merger pair fractions are measured using exactly the same method as for the major merger pair fractions in Chapter 4. The only change implemented is to search for close-pairs within a stellar mass ratio of  $\mu > 1/10$ . Pair fractions are presented for the same galaxy selections as previously described, however only those at 5–30kpc are reported herein for the sake of brevity and larger number statistics. Pair fractions measured within each survey region are displayed in Table 5.1, while simple power law fits for various combinations of survey regions are given in Table 5.2.

Total pair fractions are measured for massive galaxies at  $> 10^{11} M_{\odot}$  out to  $z \sim 2.25$ , beyond which measurements of the pair fraction are upper limits due to the stellar mass completeness limit of the UKIDSS UDS field. Results for this sample are plotted in the top panel of Figure 5.1 for the GAMA (gold and black crosses), UKIDSS UDS (open red circles), VIDEO (open blue squares), and COSMOS (open green triangles) regions. Generally,  $f_{\text{pair}}$  is observed to increase steadily from  $\sim 4\%$  at  $z = 0$  to  $\sim 14\%$  at  $z = 2.25$ , however large differences are seen between fields. Fractions within the UKIDSS UDS region remain approximately constant at  $0.35 < z < 2.25$ , with  $f_{\text{pair}} \approx 0.13$ , while measurements in the VIDEO region rise sharply from 4% to 12% at  $z \sim 0.35$  and  $z \sim 1$ , respectively. A similar evolution is seen in the COSMOS region where  $f_{\text{pair}} \approx 0.07$  at  $z < 1.5$ .

Once again the pair fractions are calculated in the GAMA region using both the photometric and spectroscopic redshifts (assuming  $\Delta v < 500$  km/s for the spectroscopic sample). These are given in all panels of Figure 5.1 as gold and black crosses, respectively. Similarly to when probing major mergers, excellent agreement is found between pair fractions measured these ways. A spectroscopic pair fraction at  $0.005 < z < 0.2$  of  $0.061 \pm 0.013$  is in agreement with the fractions measured photometrically at  $\sim 4\%$ . Following the same procedure adopted in Chapter 4, pair fractions are also measured within 24 light cones extracted from the Henriques *et al.* (2015) semi-analytic model. The model is treated as a complete spectroscopic sample, maintaining the same velocity difference criteria as used within the GAMA region. The  $1\sigma$  uncertainty region from the model is shown as the grey shaded area in Figure 5.1. The model predicts pair fractions that remain approximately constant at  $\sim 20\%$  with redshift. This qualitative evolution is consistent with the UKIDSS UDS and COSMOS regions, albeit systematically larger by a factor of 2–3 relative to the observations. However, when all the observational data is considered, the

**Table 5.1:** Total merger ( $\mu > 1/10$ ) pair fractions,  $f_{\text{pair}}$ , and associated errors calculated using **Pyrus** for constant stellar mass selected samples. Fractions are listed by each survey region, separated by stellar mass and physical search radius parameters. Errors include contributions from cosmic variance, bootstrap error analysis and Poisson errors.

$z$	GAMA	UDS	VIDEO	COSMOS
$\mathcal{M}_* > 10^{10} \text{M}_\odot$ (5 – 30kpc)				
0.0 – 0.1	0.042 $\pm$ 0.010	-	-	-
0.2 – 0.5	-	0.065 $\pm$ 0.018	0.077 $\pm$ 0.018	0.046 $\pm$ 0.010
0.5 – 0.7	-	-	$\leq 0.111$	-
0.5 – 1.0	-	0.115 $\pm$ 0.018	-	$\leq 0.087$
1.0 – 1.5	-	$\leq 0.163$	-	-
$\mathcal{M}_* > 10^{11} \text{M}_\odot$ (5 – 30kpc)				
0.0 – 0.1	0.052 $\pm$ 0.032	-	-	-
0.1 – 0.2	0.036 $\pm$ 0.013	-	-	-
0.2 – 0.5	-	0.125 $\pm$ 0.075	0.038 $\pm$ 0.022	0.066 $\pm$ 0.023
0.5 – 0.7	-	-	0.063 $\pm$ 0.030	-
0.7 – 0.9	-	-	0.106 $\pm$ 0.042	-
0.9 – 1.1	-	-	0.115 $\pm$ 0.034	-
0.5 – 1.0	-	0.144 $\pm$ 0.053	-	0.072 $\pm$ 0.015
1.1 – 1.3	-	-	$\leq 0.121$	-
1.3 – 1.5	-	-	$\leq 0.159$	-
1.0 – 1.5	-	0.137 $\pm$ 0.037	-	0.065 $\pm$ 0.015
1.5 – 2.0	-	0.127 $\pm$ 0.041	-	$\leq 0.096$
2.0 – 2.5	-	0.143 $\pm$ 0.055	-	$\leq 0.111$
2.5 – 3.0	-	$\leq 0.157$	-	-

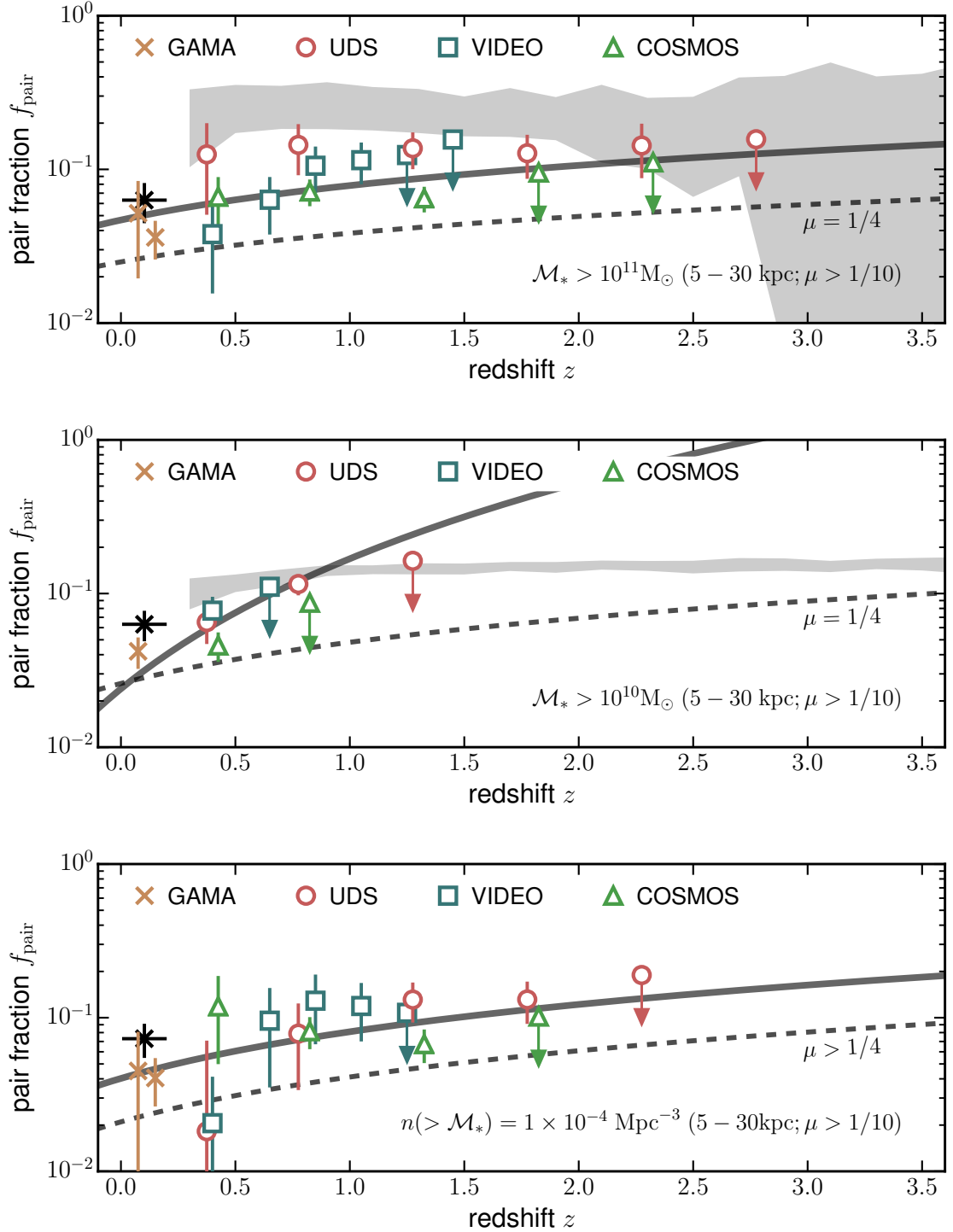


**Figure 5.1:** Total (minor + major) merger pair fractions for galaxies selected at  $> 10^{11} M_{\odot}$  (top panel),  $> 10^{10} M_{\odot}$  (middle panel), and  $n(> M_*) = 1 \times 10^{-4} \text{ Mpc}^{-3}$  (bottom panel) with physical separations of 5–30 kpc. Measurements are presented from the GAMA (gold and black crosses at  $z < 0.2$ ), UDS (red circles), COSMOS (green triangles) and VIDEO (blue squares) regions. The black crosses with horizontal error bars are points measured using the GAMA spectroscopic sample, including Poisson errors and cosmic variance estimates. Upper limits on the pair fraction are given by points with solid, down-pointing arrows. The best-fit to all the data, as provided in Table 5.2, is shown as a solid grey line. The grey shaded areas represent the  $1\sigma$  variation in the pair fraction as measured using 24 light cones based on the H15 semi-analytic model.



**Table 5.2:** Total merger ( $\mu > 1/10$ ) fraction fitting parameters for combinations of survey regions, for a parametrisation of the form  $f_{\text{pair}}(z) = f_0(1+z)^m$ . Fitting is performed on  $f_{\text{pair}}$  measurements up to the redshifts reported in Table 5.1. Errors are determined using a bootstrap analysis and the resulting parameter distributions of 10,000 realisations. The number of merging events,  $N_{\text{merg}}$ , a galaxy undergoes at  $0 < z < 3.5$ , given by the integral in Equation 4.7, is provided in the far right column.

Survey Region	$f_0$	$m$	$N_{\text{merg}}^{z<3.5}$	$N_{\text{merg}}^{z<1}$	$N_{\text{merg}}^{z<2}$
$\mathcal{M}_* > 10^{10} \text{M}_\odot$ (5 – 30kpc)					
All	$0.024^{+0.010}_{-0.007}$	$2.81^{+0.82}_{-0.81}$	$1.7^{+3.4}_{-1.1}$	$0.3^{+0.4}_{-0.2}$	$0.8^{+1.1}_{-0.5}$
All + GAMA	$0.030^{+0.008}_{-0.007}$	$2.29^{+0.68}_{-0.66}$	$1.3^{+2.0}_{-0.7}$	$0.3^{+0.3}_{-0.2}$	$0.7^{+0.8}_{-0.4}$
$\mathcal{M}_* > 10^{11} \text{M}_\odot$ (5 – 30kpc)					
All	$0.047^{+0.017}_{-0.013}$	$0.75 \pm 0.45$	$0.6^{+0.6}_{-0.3}$	$0.3^{+0.3}_{-0.1}$	$0.4^{+0.4}_{-0.2}$
All + GAMA	$0.038^{+0.009}_{-0.008}$	$1.07^{+0.32}_{-0.33}$	$0.6^{+0.5}_{-0.2}$	$0.3^{+0.2}_{-0.1}$	$0.4^{+0.4}_{-0.2}$
$n(> \mathcal{M}_*) = 1 \times 10^{-4} \text{Mpc}^{-3}$ (5 – 30kpc)					
All	$0.031^{+0.015}_{-0.012}$	$1.32^{+0.60}_{-0.56}$	$0.6^{+0.7}_{-0.3}$	$0.2^{+0.2}_{-0.1}$	$0.4^{+0.4}_{-0.2}$
All + GAMA	$0.040^{+0.012}_{-0.011}$	$1.01^{+0.42}_{-0.39}$	$0.6^{+0.5}_{-0.3}$	$0.3^{+0.2}_{-0.1}$	$0.4^{+0.4}_{-0.2}$

model predictions do not predict consistent pair fractions until the highest redshifts probed at  $z > 1.5$ .

As in Chapter 4, pair fractions are fitted with a power law of the form  $f_{\text{pair}}(z) = f_0(1+z)^m$ . The optimal fitting parameters and their uncertainties are given in Table 5.2. Uncertainties on these parameters are estimated by sampling individual data points from a normal distribution, centred on  $f_{\text{pair}}$  with standard deviation given by the errors quoted in Table 5.1, and building a distribution of parameters by performing a least-squares fitting routine  $10^4$  times. The best-fit parameters for massive galaxies are shown in the top panel of Figure 5.1 as a solid grey curve, and is best fit by

$$f_{\text{pair}}(z) = 0.038^{+0.009}_{-0.008} \times (1+z)^{1.06^{+0.32}_{-0.33}}.$$

Shown in the top panel of Figure 5.1 is the best-fit major merger parametrisation for the same massive sample of galaxies, given by the dashed grey curve. It is apparent that the evolution of major and total mergers share a common slope over the redshift range, and that the total merger pair fraction is consistently a factor of  $\sim 2$  larger than the major merger pair fraction. It is trivial to deduce from this Figure that close-pairs of galaxies with  $\mathcal{M}_* > 10^{11} \text{M}_\odot$ , therefore, are observed to be in equal amounts of major ( $\mu > 1/4$ ) and minor ( $1/4 > \mu > 1/10$ ) mergers at

the redshifts probed.

The total merger pair fractions for a lower stellar mass ( $\mathcal{M}_* > 10^{10} \text{ M}_\odot$ ) sample of galaxies is also probed. These measurements are presented in the middle panel of Figure 5.1. A steep rise in the total merger pair fraction is observed over the redshift range probed, rising from 4% at  $z \sim 0$  to 10% at  $z \sim 1$ . The fractions are fit with a simple power law, and is best described by

$$f_{\text{pair}}(z) = 0.030_{-0.007}^{+0.008} \times (1+z)^{2.29_{-0.66}^{+0.68}},$$

which is given in the Figure as a solid grey curve. The major merger pair fraction for this sample is given as the dashed grey curve in the same Figure. Although comparison between these lines is only possible at  $z < 1$ , as this is the regime where observations constrain both measurements, it can be inferred that the total merger pair fraction is approximately a factor of  $\sim 2$ – $3$  larger than the major merger pair fraction. As with more massive galaxies this suggests at least an equal number of intermediate stellar mass close-pairs in major and minor mergers over these times. Additionally, comparing the total merger pair fractions of intermediate mass and massive galaxies reveals extremely similar fractions with a suggestion that fractions may be slightly higher for the lower mass galaxies. As found with major mergers, there does not therefore appear to be a significant dependence on stellar mass for the measured total merger pair fractions.

Predictions on the total merger pair fraction from the H15 semi-analytic model are shown as the grey shaded region. An approximately constant pair fraction of 10% is predicted at  $0.5 < z < 3.5$ , with little variation between the lightcones used to measure it. It is difficult to compare these predictions due to the limited overlap, however they are in agreement with the single UKIDSS UDS data point at  $z = 0.75$ , but are 1.5 times larger than the best-fit parametrisation at  $z = 0.35$ .

The bottom panel of Figure 5.1 displays the measured total pair fractions for a sample of galaxies selected at a constant cumulative number density of  $n(> \mathcal{M}_*) = 10^{-4} \text{ Mpc}^{-3}$ . The smaller number density probed in Chapter 4 is not probed here due to stellar mass completeness issues. For this sample the pair fraction is observed to evolve mildly with redshift, from 4% at  $z = 0$  to 11% at  $z = 1.75$ . As given by the solid grey curve in the figure, this evolution is described as

$$f_{\text{pair}}(z) = (0.04 \pm 0.01) \times (1+z)^{1.0 \pm 0.4}.$$

This evolution is consistent with that found for galaxies at  $> 10^{11} \text{ M}_\odot$ . Also plotted in the bottom panel of Figure 5.1 is the major merger pair fraction, represented by

the dashed grey curve. As the measured pair fraction slopes are in agreement, the difference between the major and minor pair fraction for this sample is consistently a factor of 2 across the entire redshift range probed. Similar to that found for the previous samples, it therefore suggests that the progenitors of local massive galaxies are found to reside in approximately equal numbers of major and minor mergers at every epoch probed.

### 5.3.2 The minor merger pair fraction

With measurements of the major merger and ‘total’ merger pair fraction in hand, the signal from minor mergers can be extracted. The fraction of minor merger pairs can be considered the residual of subtracting the number of major mergers from the total number of mergers measured. This can be achieved in two ways: using the raw counts of primary galaxies and close pairs in each redshift bin, or taking the pair fraction fits and subtracting the major from total pair fraction fits. The latter is the simplest method of achieving this, and as the simple power law fits describe the observations exceptionally well, this is the method used henceforth. For completeness, total, major, and minor pair fractions are presented in their raw form in Appendix B. Firstly, many realisations of the total and major pair fractions are made using the best-fit parametrisations and associated uncertainties given in Table 5.2 and Table 4.3. This includes taking asymmetric error distributions into account. Within each realisation, the major merger pair fraction is subtracted from the total pair fraction at  $0 < z < 3.5$ , and the residual fitted with the same power law as used previously. Visual inspection of all residuals confirms they are well fit by this power law parametrisation. Collecting the distributions of fitting parameters from the realisations allows for the 50th, 16th and 84th percentiles to be calculated on each parameter. These best-fit parameters and the  $1\sigma$  uncertainties of the minor merger pair fraction are given in Table 5.3.

Figure 5.2 displays the evolution of the total (major + minor), major and minor pair fractions for all three galaxy selections probed in this Chapter. Massive galaxies are shown in the top panel, intermediate mass ( $\mathcal{M}_* > 10^{10} \text{ M}_\odot$ ) galaxies in the middle panel, and the number density selection in the bottom panel. The shaded areas highlight the 68% confidence region for the different stellar mass merger ratio choices. For the most massive galaxies, the minor merger pair fraction rises from 1% at  $z = 0$  to 6% at  $z = 2$ , beyond which only the major merger pair fraction is constrained. Averaged over  $z < 2$ , the major and minor pair fractions are therefore found to be approximately equal. If the minor merger pair fraction evolves as predicted beyond  $z = 2$ , the minor merger pair fraction is predicted to become a

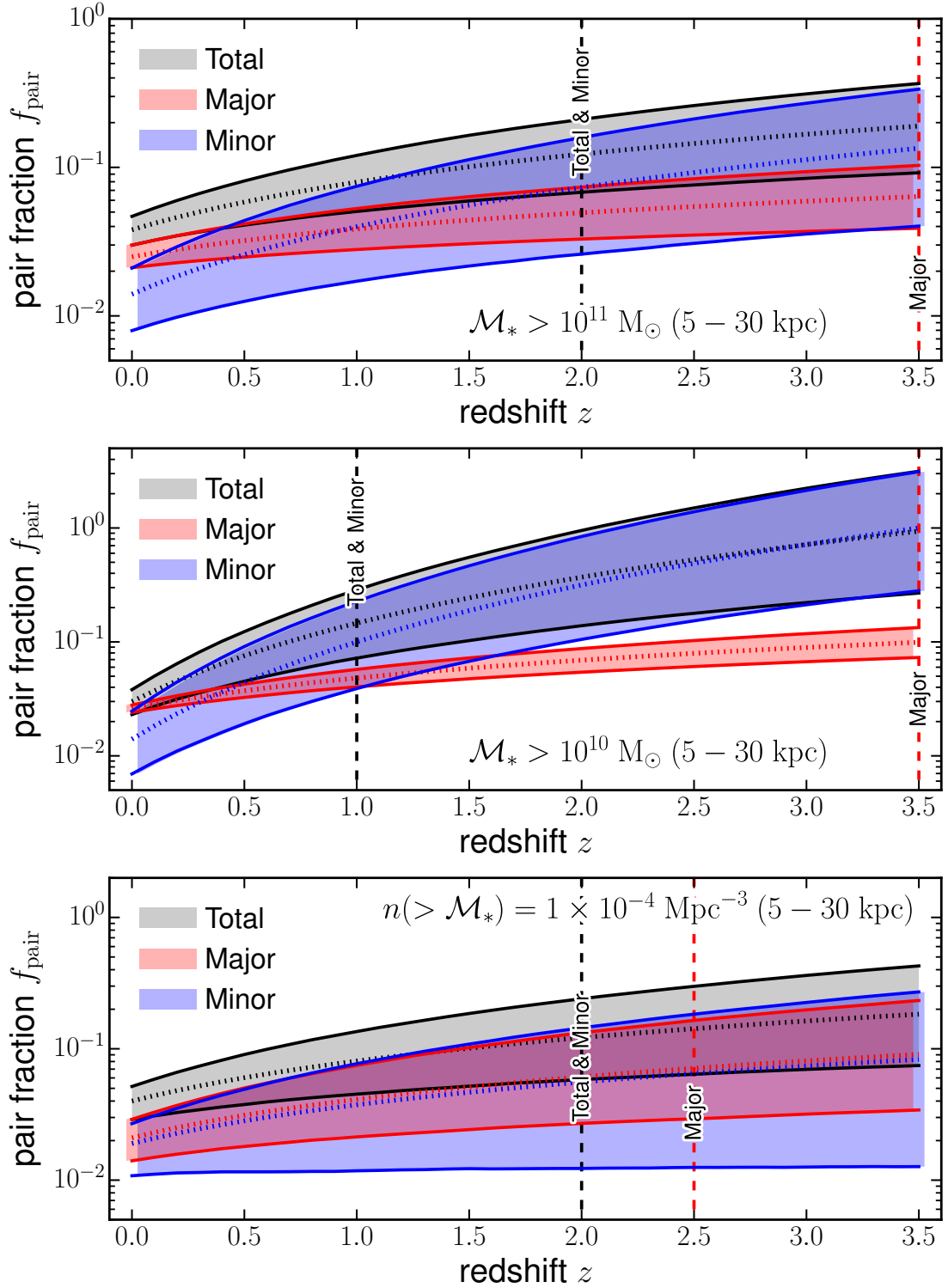


**Figure 5.2:** Evolution of the fitted total (major + minor), major, and minor pair fractions as a function of redshift for galaxies at  $> 10^{11} M_{\odot}$  (top panel),  $> 10^{10} M_{\odot}$  (middle panel), and  $n(> \mathcal{M}_*) = 1 \times 10^{-4} \text{ Mpc}^{-3}$  (bottom panel). The 68% confidence regions for the total, major and minor pair fractions are given by the grey, red and blue shaded areas, respectively. The most likely evolution is given by the dashed curves of their respective colours, while the vertical dashed lines denote the lowest redshift where observational data constrain the fits for the different merger ratio selections.

**Table 5.3:** Minor merger ( $1/10 < \mu < 1/4$ ) fraction fitting parameters for combinations of survey regions, for a parametrisation of the form  $f_{\text{pair}}(z) = f_0(1+z)^m$ . Fitting is performed on the residual of subtracting the major merger pair fraction from the total merger pair fraction. Errors are determined using a bootstrap analysis and the resulting parameter distributions of 10,000 realisations. The number of merging events,  $N_{\text{merg}}$ , a galaxy undergoes at  $z < 3.5$ ,  $z < 2$ , and  $z < 1$  are given in the far right columns.

Survey Region	$f_0$	$m$	$N_{\text{merg}}^{z<3.5}$	$N_{\text{merg}}^{z<2}$	$N_{\text{merg}}^{z<1}$
$\mathcal{M}_* > 10^{10} \text{M}_\odot$ (5 – 30kpc)					
All	$0.011^{+0.011}_{-0.007}$	$3.22^{+0.69}_{-1.03}$	$1.3^{+3.2}_{-0.9}$	$0.5^{+1.0}_{-0.4}$	$0.2^{+0.3}_{-0.1}$
All + GAMA	$0.014^{+0.011}_{-0.009}$	$2.84^{+0.43}_{-0.39}$	$1.1^{+1.4}_{-0.7}$	$0.5^{+0.6}_{-0.3}$	$0.2^{+0.2}_{-0.1}$
$\mathcal{M}_* > 10^{11} \text{M}_\odot$ (5 – 30kpc)					
All	$0.038^{+0.015}_{-0.011}$	$0.60^{+0.53}_{-0.60}$	$0.4^{+0.5}_{-0.2}$	$0.3^{+0.3}_{-0.2}$	$0.2^{+0.2}_{-0.1}$
All + GAMA	$0.014^{+0.007}_{-0.006}$	$1.50^{+0.38}_{-0.42}$	$0.3^{+0.3}_{-0.2}$	$0.2^{+0.2}_{-0.1}$	$0.1^{+0.1}_{-0.1}$
$n(> \mathcal{M}_*) = 1 \times 10^{-4} \text{Mpc}^{-3}$ (5 – 30kpc)					
All	$0.009^{+0.010}_{-0.009}$	$1.73^{+0.98}_{-1.20}$	$0.3^{+0.7}_{-0.2}$	$0.2^{+0.4}_{-0.1}$	$0.1^{+0.1}_{-0.1}$
All + GAMA	$0.019^{+0.008}_{-0.008}$	$0.98^{+0.60}_{-0.87}$	$0.3^{+0.4}_{-0.2}$	$0.2^{+0.3}_{-0.1}$	$0.1^{+0.1}_{-0.1}$

factor of 2 larger than the major merger pair fraction at  $z = 3.5$ .

Intermediate mass ( $\mathcal{M}_* > 10^{10} \text{M}_\odot$ ) galaxies are found to have a strong evolution in the minor merger pair fraction, however it is likely this is due to the relatively strict redshift range ( $z < 1$ ) in which this quantity is measured. As found for major mergers when considering the high redshift data of Duncan et al. (*in prep*), higher redshift observations may reduce the measured slope of the pair fraction, bringing it into line with the major merger pair fraction. As such the total, major and minor pair fractions from this work can only be fruitfully compared at  $z < 1$ . As with the larger mass selection, the major and minor merger pair fractions are approximately comparable at this redshift regime.

Finally, tracing the progenitors of local massive galaxies with a constant number density selection reveals an equal fraction of galaxies in both major and minor mergers out to  $z \sim 2.25$ , where the fits become unconstrained by observational measurements. This evolution is shown in the bottom panel of Figure 5.2. The major and minor pair fraction is found to increase mildly from 2% at low redshift to 6% at  $z = 2$ .

## 5.4 Total Merger rate estimations

Merger *rates* are derived from the total merger pair fractions presented in Section §5.3.1. As previously shown, a timescale over which a merger event (as defined in this work) can be observed must be assumed. For close-pairs of galaxies selected at 5-30kpc and a stellar mass ratio of  $\mu > 1/10^1$ , an observability timescale of  $\langle T_{\text{obs}} \rangle = 0.95$  Gyr (Lotz *et al.*, 2010, see their Table 5) and an associated 50% error (Hopkins *et al.*, 2010) is assumed. As with the major merger results presented in Chapter 4, a constant fraction of 60% of close-pairs are assumed to eventually merge, i.e.  $C_{\text{merg}} = 0.6$ .

### 5.4.1 Massive galaxies ( $> 10^{11} M_{\odot}$ )

Total merger pair fractions for massive ( $> 10^{11} M_{\odot}$ ) galaxies are converted to total merger rates using Equations 4.5 and 4.6, inserting the new value of  $\langle T_{\text{obs}} \rangle$  mentioned above. Uncertainties on the merger rates are estimated using a bootstrap approach, incorporating uncertainties on the galaxy stellar mass function (where applicable), the measured pair fractions, cosmic variance estimates, and Poisson noise. Figure 5.3 displays the derived volume-averaged ( $\Gamma(z)$ ; top panel) and fractional ( $\mathcal{R}(z)$ ; bottom panel) merger rates for this sample of massive galaxies in the survey regions described in Section §4.2. The same marker styles as in previous figures are continued.

The volume-averaged merger rate for massive galaxies is found to remain approximately constant at  $z < 1$ , maintaining  $\Gamma \approx 10^{-5} \text{ Mpc}^{-3} \text{ Gyr}^{-1}$  at this redshift regime. At higher redshift,  $\Gamma$  is observed to decline out to  $z \sim 2.25$  beyond which an upper limit constrains the merger rate to  $\Gamma < 3 \times 10^{-6} \text{ Mpc}^{-3} \text{ Gyr}^{-1}$ . The variation in estimates of the merger rates between fields is approximately a factor of  $\sim 2$  and this ratio remains the same across the redshift range where multiple observations are made. The data are found to be best described by a power law plus exponential parametrisation which can be written as

$$\Gamma(z) = (0.95_{-0.8}^{+1.8} \times 10^{-5}) \times (1 + z)^{4.11_{-6.00}^{+11.90}} \times \exp(-2.74_{-6.62}^{+2.94} \times z).$$

This is given as the solid grey curve in the upper panel of Figure 5.3. This parametrisation better describes the observed evolution of the merger rate compared to a simple power law used to describe the pair fraction.

---

<sup>1</sup>Lotz *et al.* calculate the observability timescale of 9:1 stellar mass ratio selected mergers at 10-30kpc.

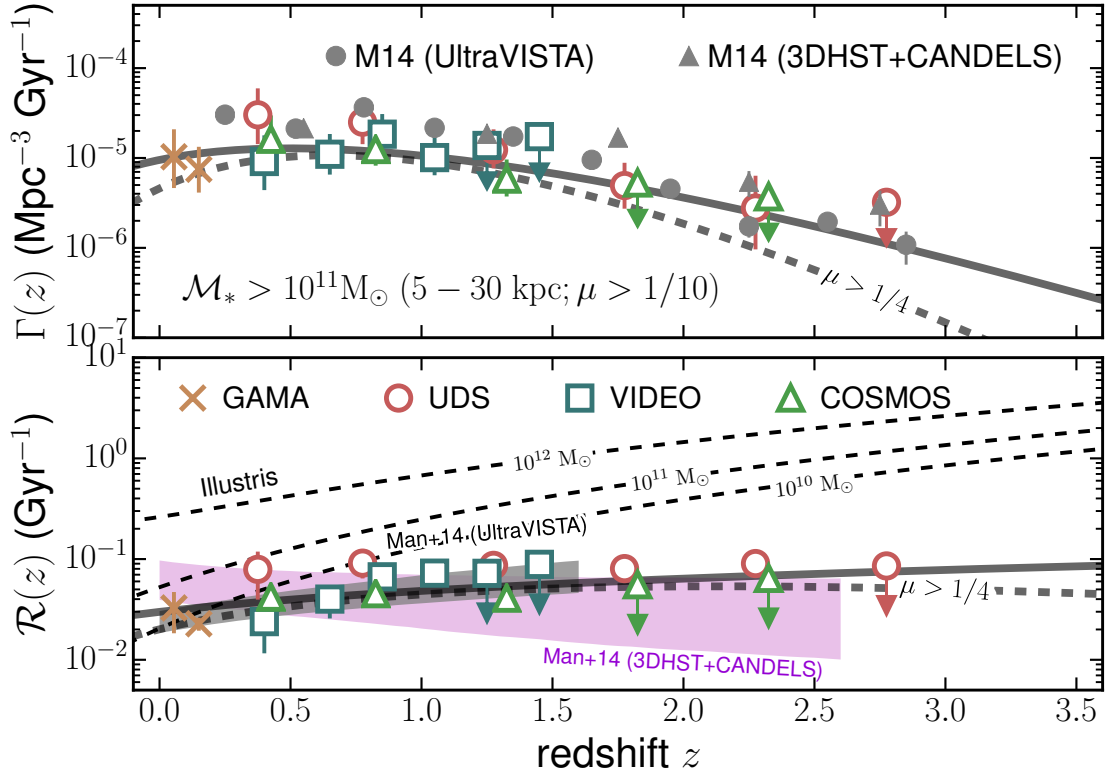


**Figure 5.3:** Derived volume-averaged (top panel) and fractional (bottom panel) minor merger rates for galaxies at  $> 10^{11} M_{\odot}$ . Estimates derived for data in the GAMA (gold crosses), UKIDSS UDS (red open circles), VIDEO (blue open squares), and COSMOS (green open triangles) regions for close-pairs selected at 5–30 kpc. Illustris minor merger rate predictions for galaxies with stellar masses of  $10^{10}$ ,  $10^{11}$ , and  $10^{12} M_{\odot}$  are shown as dashed black lines, while results from Man, Zirm & Toft (2014) are given by grey symbols (top panel), and grey and pink shaded regions (bottom panel).

Also plotted is the major ( $\mu > 1/4$ ) merger volume averaged merger rate, given by the dashed grey curve. As one would expect the total merger rate best-fit line is consistently higher than the major merger, however the ratio of major and minor merger rates evolves with redshift. At  $z < 0.5$ , the total merger rate is a factor of 1.5–2 larger than the major merger rate, while at  $z > 2$ , the ratio of total to major merger rate rises steadily to  $\sim 2.5$  at  $z \sim 3$ .

Minor merger studies are much less bountiful than major mergers. However, estimates of the volume averaged total merger rate from Man, Zirm & Toft (2014, see their Table 4) are also plotted. Points using UltraVISTA/COSMOS data given by filled grey circles while points derived using a combination of 3DHST and CANDELS data are given by filled grey triangles. After their data has been converted to use  $C_{\text{merg}} = 0.6$  and  $\langle T_{\text{obs}} \rangle = 0.95$  Gyr (where necessary), their derived merger rates are found to be in agreement with those presented in this work. At  $z < 1.5$  the rates of Man, Zirm & Toft are typically a 1.5–2 times larger, while at  $z > 1.5$  their points are in excellent agreement with this work.

Estimates of the fractional merger rate,  $\mathcal{R}(z)$ , are shown in the bottom panel of Figure 5.3. As this work divides by a constant observability timescale it is unsurprising that the evolution of the merger rate evolves in a similar fashion to the pair fraction. It is found to remain relatively constant at  $\sim 0.05$  Gyr $^{-1}$  and increasing by only a factor of  $\sim 2$  over the redshift range probed. A simple power law best describes its evolution, with

$$\mathcal{R}(z) = (3.0^{+0.8}_{-0.7} \times 10^{-2}) \times (1 + z)^{0.69^{+0.34}_{-0.32}}$$

giving the best fitting parameters and their uncertainties. This fit is given by the solid grey curve in the bottom panel of Figure 5.3. Plotted as the dashed grey curve is the major merger fractional merger rate. The two curves are extremely similar and diverge significantly only at high redshift ( $z > 2.5$ ) where the fits are unconstrained by observational data. This suggests that the rate of minor mergers per galaxy per unit time is relatively low compared to major mergers.

Also shown are total merger rate estimates from the Illustris hydrodynamical simulation, given by the dashed black lines, for stellar masses of  $10^{10}$ – $10^{12}$   $M_{\odot}$ . These are calculated in exactly the same way as described in Section §4.6.1. It is apparent the predictions from the simulation evolve strongly with redshift, increasing from  $3 \times 10^{-2}$  Gyr $^{-1}$  at  $z = 0$  to  $\sim 1$  Gyr $^{-1}$  at  $z = 3$ . These predictions are therefore qualitatively and quantitatively inconsistent with the derived merger rates of this work at  $z > 0.5$ . Further estimates of the merger rate from Man, Zirm



& Toft (2014, see their Table 1) are shown as the grey and pink shaded regions in Figure 5.3. These represent the  $1\sigma$  uncertainty of their fractional merger rates, derived using pair fractions measured with data from the UltraVISTA region, and the 3DHST and CANDELS combination, respectively. This work’s merger rates are seen to be in excellent agreement with those of Man, Zirm & Toft, even out to high redshift.

### 5.4.2 Intermediate mass galaxies ( $> 10^{10} M_{\odot}$ )

Total merger rates are also estimated for intermediate mass galaxies, however stellar mass incompleteness limits all estimates to  $z < 1$ . The derived volume-averaged (top panel) and fractional (bottom panel) total merger rates, as well as upper limits on these quantities, are presented in Figure 5.4 for the GAMA, UKIDSS UDS, VIDEO and COSMOS regions. At  $z < 1$ , the volume-averaged minor merger rate is consistent with a constant value of  $\sim 10^{-4} \text{ Mpc}^{-3} \text{ Gyr}^{-1}$ , while the fractional merger rate evolves mildly from  $0.03 \text{ Gyr}^{-1}$  at  $z = 0$  to  $0.07 \text{ Gyr}^{-1}$  at  $z = 0.75$ . Given the small redshift range and limited coverage, both these rates are fitted with simple power laws. For the volume-averaged merger rate,

$$\Gamma(z) = (6.40_{-3.96}^{+9.04} \times 10^{-5}) \times (1+z)^{2.07_{-2.49}^{+2.07}}$$

best describes the data, while

$$\mathcal{R}(z) = (1.51_{-0.22}^{+0.25} \times 10^{-2}) \times (1+z)^{2.81_{-0.35}^{+0.36}}$$

best describes the derived fractional merger rates for galaxies at  $> 10^{10} M_{\odot}$ . These fits are only valid at  $z < 1.5$ , however.

Also plotted are estimates of the volume-averaged and fractional merger rates from Lotz *et al.* (2008, filled grey circles) and López-Sanjuan *et al.* (2009, filled grey squares), which are morphological and close-pair studies, respectively. Lotz *et al.* use the Gini and  $M_{20}$  parameters to derive ‘total’ merger rates. As this method is able to detect merging events down to baryonic mass ratios of  $> 1/10 - > 1/30$ , it is unsurprising that the derived rates are many times larger (typically a factor of 4–10 larger) than those calculated in this work, however this difference could also be due in part to the uncertainties on the timescales used between the contrasting methodologies (Lotz *et al.*, 2011). López-Sanjuan *et al.* derive minor merger rates from a spectroscopic sample of close-pair galaxies at  $z < 1$  in the VVDS survey. These galaxies are luminosity selected ( $L_B > L_B^*$ ) which generally

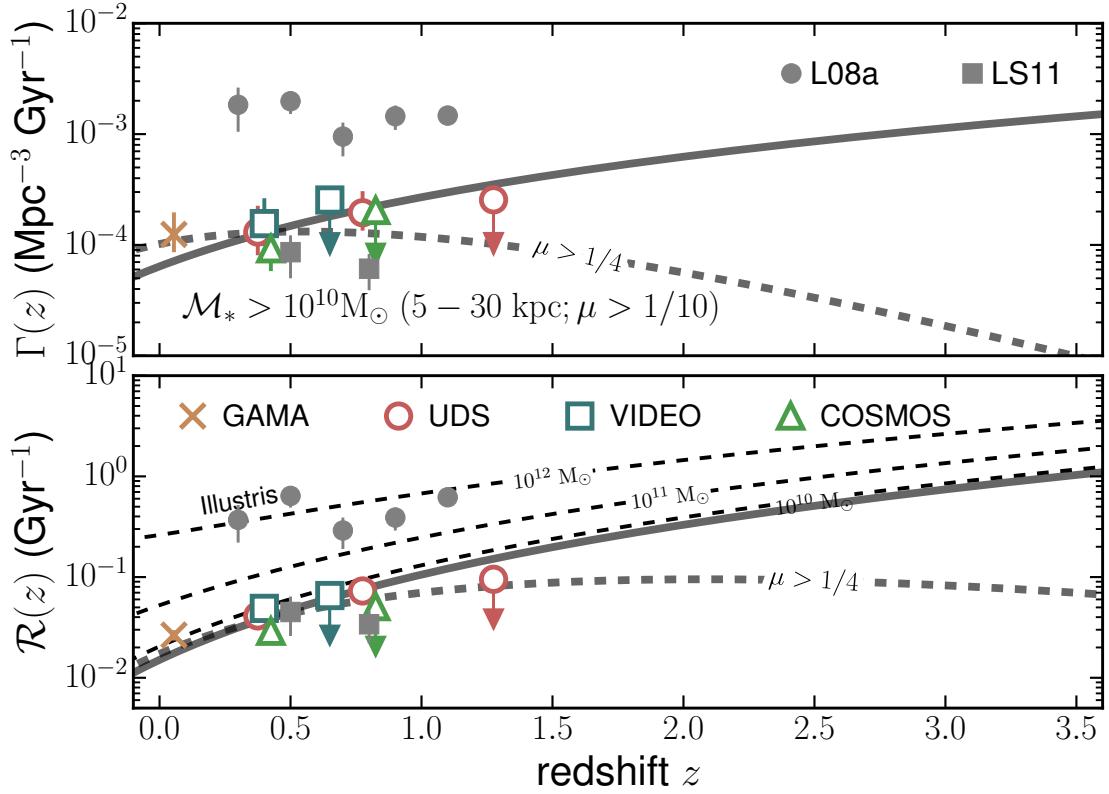


**Figure 5.4:** Derived volume-averaged (top panel) and fractional (bottom panel) total merger rates for galaxies at  $> 10^{10} M_{\odot}$ . Estimates derived for data in the GAMA (gold crosses), UKIDSS UDS (red open circles), VIDEO (blue open squares), and COSMOS (green open triangles) regions for close-pairs selected at 5–30 kpc. Illustris total merger rate predictions for galaxies with stellar masses of  $10^{10}$ ,  $10^{11}$ , and  $10^{12} M_{\odot}$  are shown as dashed black lines, while merger rates from Lotz *et al.* (2008) and López-Sanjuan *et al.* (2009) are shown as the filled grey circles and filled grey squares, respectively.

**Table 5.4:** Total merger ( $\mu > 1/10$ ) fitting parameters for derived volume-averaged and fractional merger rates, as presented in Figures 5.3, 5.4, and 5.5 for different combinations of data points. ‘All’ indicates fits derived from the data points of UKIDSS UDS, VIDEO and COSMOS. Fits using two parameters are of the form  $\chi(z) = \chi_0(1+z)^{m_\chi}$  while those using three parameters are of the form  $\chi(z) = \chi_0(1+z)^{m_\chi} \exp(-c_\chi z)$ , where  $\chi$  is either the volume-averaged merger rate,  $\Gamma$ , or the fractional merger rate,  $\mathcal{R}$ . Uncertainties are estimated by performing a bootstrap analysis.

Survey	$\Gamma_0$ ( $\text{Mpc}^{-3} \text{ Gyr}^{-1}$ )	$m_\Gamma$	$c_\Gamma$	$\mathcal{R}_0$ ( $\text{Gyr}^{-1}$ )	$m_\mathcal{R}$
$\mathcal{M}_* > 10^{10} \text{ M}_\odot$ (5 – 30kpc)					
All	$6.24^{+9.35}_{-3.81} \times 10^{-5}$	$2.12^{+2.04}_{-2.53}$	-	$1.51^{+0.25}_{-0.22} \times 10^{-2}$	$2.82^{+0.35}_{-0.36}$
All + GAMA	$1.00^{+0.78}_{-0.54} \times 10^{-4}$	$0.96^{+2.04}_{-2.14}$	-	$1.86^{+0.24}_{-0.23} \times 10^{-2}$	$2.36 \pm 0.32$
$\mathcal{M}_* > 10^{11} \text{ M}_\odot$ (5 – 30kpc)					
All	$0.88^{+1.72}_{-0.74} \times 10^{-5}$	$4.53^{+8.75}_{-6.25}$	$2.97^{+3.12}_{-7.20}$	$3.00^{+0.79}_{-0.68} \times 10^{-2}$	$0.69^{+0.35}_{-0.33}$
All + GAMA	$6.73^{+5.21}_{-4.01} \times 10^{-6}$	$6.16^{+8.92}_{-4.66}$	$3.79^{+2.60}_{-5.37}$	$2.26^{+0.29}_{-0.28} \times 10^{-2}$	$1.05^{+0.19}_{-0.18}$
$n(> \mathcal{M}_*) = 1 \times 10^{-4} \text{ Mpc}^{-3}$ (5 – 30kpc)					
All	$1.40^{+1.07}_{-0.70} \times 10^{-6}$	$1.83^{+0.89}_{-0.82}$	-	$3.62^{+2.14}_{-1.53} \times 10^{-2}$	$0.47^{+0.70}_{-0.61}$
All + GAMA	$2.85^{+1.48}_{-1.24} \times 10^{-6}$	$0.99^{+0.78}_{-0.69}$	-	$2.68^{+0.70}_{-0.66} \times 10^{-2}$	$0.85^{+0.36}_{-0.33}$

translates to stellar masses of  $> 10^{10} \text{ M}_\odot$  at these redshifts. Their low-redshift point is in agreement with this work, however their high-redshift point is smaller by a factor of 2–3. This could be due in part to the different selection criteria (luminosity rather than stellar mass) and the use of spectroscopic redshifts rather than photometric. It is reassuring, however, that two close-pair studies are found to agree within a factor of  $\sim 2$ .

### 5.4.3 Galaxies at a constant number density

Selecting galaxies at a constant cumulative number density enables the total merger histories of the direct progenitors of local massive galaxies to be probed (see Chapter 2; Mundy, Conselice & Ownsworth, 2015). The larger number density choice explored in Section §4.4.2 is again used to measure the minor merger fractions. Figure 5.5 presents the derived minor merger rates for this sample, following the same structure as previous figures on this topic. Derived values are given by the open symbols for the UKIDSS UDS, VIDEO and COSMOS regions at  $z > 0.2$ , while gold crosses denote values derived in the GAMA region at low redshift.

The volume-averaged merger rate, displayed in the top panel of Figure 5.5, is observed to increase with redshift from  $\sim 10^{-6} \text{ Mpc}^{-3} \text{ Gyr}^{-1}$  in the lowest red-

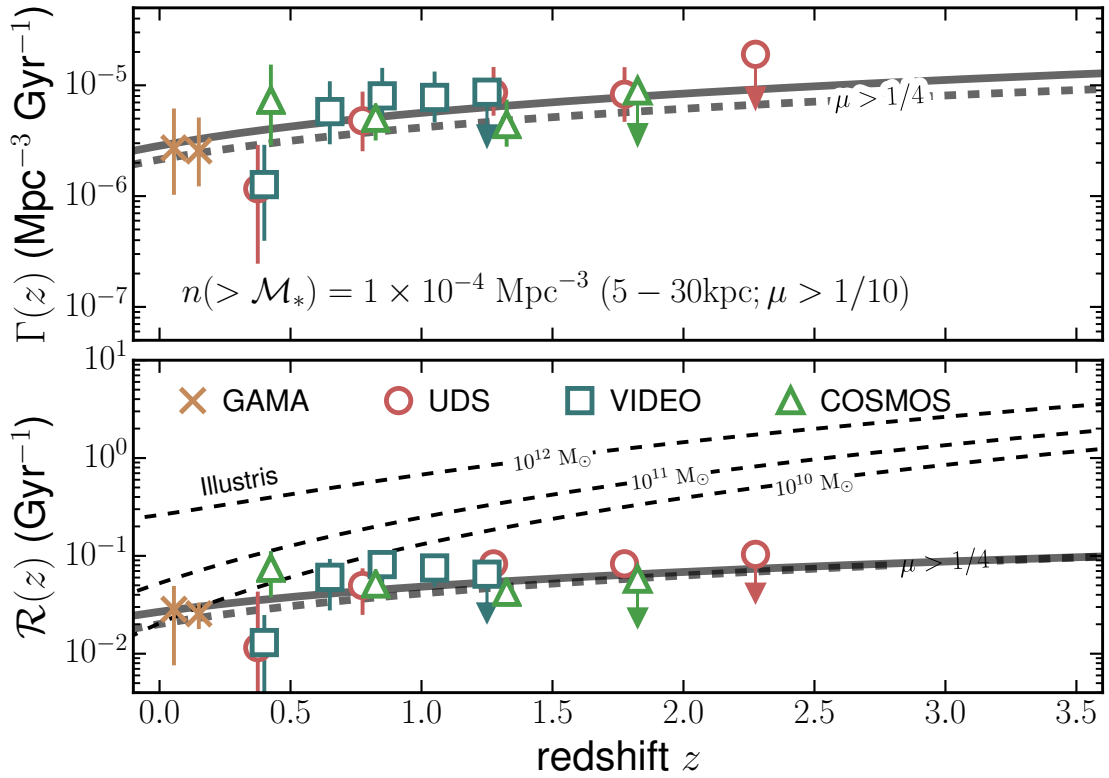


**Figure 5.5:** Derived volume-averaged (top panel) and fractional (bottom panel) minor merger rates for galaxies at  $n(> \mathcal{M}_*) = 1 \times 10^{-4} \text{ Mpc}^{-3}$ . Estimates derived for data in the GAMA (gold crosses), UKIDSS UDS (red open circles), VIDEO (blue open squares), and COSMOS (green open triangles) regions for close-pairs selected at 5–30 kpc. Illustris minor merger rate predictions for galaxies with stellar masses of  $10^{10}$ ,  $10^{11}$ , and  $10^{12} \text{ M}_\odot$  are shown as dashed black lines.

shift bin to  $\sim 10^{-5} \text{ Mpc}^{-3} \text{ Gyr}^{-1}$  in the highest redshift bin which is stellar mass complete. The evolution of this merger rate is best parametrised by

$$\Gamma(z) = (2.9_{-1.2}^{+1.5} \times 10^{-6}) \times (1+z)^{1.0 \pm 0.8},$$

and is shown in the figure as the solid grey curve. Comparing this to the major merger rate, given as the dashed grey curve, similar slopes are found but a normalisation approximately a factor of 1.5 larger. Put another way, minor mergers contribute approximately one third of the total merger rate. This is observed to be constant at redshifts where the fit is constrained by observational data.

The bottom panel of Figure 5.5 displays the evolution of the fractional merger rate with redshift. It is found to increase by just a factor of  $\sim 2$  from  $z = 0$  to  $z = 2$ , from  $0.03 \text{ Gyr}^{-1}$  to  $0.07 \text{ Gyr}^{-1}$ , and is best parametrised as

$$\mathcal{R}(z) = (2.7 \pm 0.7 \times 10^{-2}) \times (1+z)^{0.9_{-0.3}^{+0.4}}.$$

Compared to the fit to the major merger rate for this selection (dashed grey curve), minor mergers add no more than 50% towards the total merger rate at  $z < 1$ , and less so at higher redshifts.

## 5.5 Discussion

The total merger pair fractions ( $\mu > 1/10$ ) have been measured and found to be approximately a factor of 1.5–2 larger than the major merger ( $\mu > 1/4$ ) pair fractions, depending on sample selection. Due to the larger observability timescale expected for minor mergers ( $\sim 1.6$  times larger) these pair fractions transform into merger rates comparable to the derived major merger rates. This result is in agreement with several cosmological simulations that predict extremely similar major and minor merger rates at the redshifts and stellar masses probed in this work (e.g., Croton *et al.*, 2006; Somerville *et al.*, 2008).

It can be seen from the previous figures and the fitting parameters presented in Table 5.2 that there is no significant dependence of the pair fraction on stellar mass at the mass and redshift regimes probed. This is similar to the results for major mergers discussed in Chapter 4, however it is at odds with the merger rates within the Illustris cosmological hydrodynamical model, which finds a dependence of the merger rate on stellar mass, especially at high masses (Rodríguez-Gomez *et al.*, 2015, see their Fig. 7). This is highlighted in previous figures where Illustris fails to reproduce the derived merger rates of galaxies sampled in this work.

**Table 5.5:** Estimates of the number of major, minor and total merging events experienced by a typical galaxy at  $z < 3.5$ ,  $z < 2$ , and  $z < 1$ . Estimates of the number of major and total merging events are calculated by integrating Equation 4.7 with the appropriate fitting function, while the number of minor mergers is estimated by subtracting distributions of these quantities. The distributions are generated using a bootstrap approach, encompassing uncertainties on the pair fraction fitting parameters and observability timescale.

$N_{\text{merg}}(z < 3.5)$			$N_{\text{merg}}(z < 2)$			$N_{\text{merg}}(z < 1)$		
Major	Minor	Total	Major	Minor	Total	Major	Minor	Total
$\mathcal{M}_* > 10^{11} \text{ M}_\odot$ (5–30 kpc)								
$0.4^{+0.3}_{-0.1}$	$0.2^{+0.3}_{-0.1}$	$0.6^{+0.5}_{-0.2}$	$0.3^{+0.2}_{-0.2}$	$0.2^{+0.3}_{-0.1}$	$0.4^{+0.4}_{-0.2}$	$0.2^{+0.1}_{-0.1}$	$0.1^{+0.1}_{-0.1}$	$0.3^{+0.2}_{-0.1}$
$\mathcal{M}_* > 10^{10} \text{ M}_\odot$ (5–30 kpc)								
$0.5^{+0.3}_{-0.2}$	$0.9^{+1.8}_{-0.5}$	$1.3^{+2.0}_{-0.7}$	$0.4^{+0.2}_{-0.1}$	$0.4^{+0.7}_{-0.2}$	$0.7^{+0.8}_{-0.4}$	$0.3^{+0.1}_{-0.1}$	$0.1^{+0.1}_{-0.1}$	$0.3^{+0.3}_{-0.2}$
$n(> \mathcal{M}_*) = 1 \times 10^{-4} \text{ Mpc}^{-3}$ (5–30 kpc)								
$0.5^{+0.4}_{-0.2}$	$0.2^{+0.3}_{-0.1}$	$0.6^{+0.5}_{-0.3}$	$0.4^{+0.3}_{-0.2}$	$0.1^{+0.2}_{-0.1}$	$0.4^{+0.4}_{-0.2}$	$0.2^{+0.2}_{-0.1}$	$0.1^{+0.1}_{-0.1}$	$0.3^{+0.2}_{-0.1}$

### 5.5.1 Number of merger events at $z < 3.5$

The total number of merging events from major and minor mergers are estimated using the same procedure as in Section §4.5.2. This quantity,  $N_{\text{merg}}$ , is given in Table 5.2 for different redshift ranges and survey region combinations. From these quantities it is trivial to estimate the contributions from major and minor mergers towards the total number of merging events over the past 11 Gyr.

Comparing the calculated total number of merger events at  $z < 3.5$  to the major merger events presented in Table 4.3, it is found that a typical galaxy at  $> 10^{11} \text{ M}_\odot$  experiences  $0.4^{+0.3}_{-0.1}$  major mergers and  $0.2^{+0.3}_{-0.1}$  minor mergers over this time. Within this population, approximately every other galaxy would experience a major merger and one in five galaxies would experience a minor merger. Intermediate mass galaxies are found to experience  $0.5^{+0.3}_{-0.2}$  major mergers and  $0.9^{+1.8}_{-0.5}$  minor mergers, on average. Finally, the constant number density sample of galaxies undergoes  $0.5^{+0.4}_{-0.2}$  major mergers and  $0.2^{+0.3}_{-0.1}$  minor mergers per galaxy at  $z < 3.5$ . A compilation of the number of minor, major and total merging events at various redshift ranges is given in Table 5.5.

These values are calculated using the fits to the pair fraction which may be unconstrained by observational measurements at certain redshift and stellar mass regimes. It is therefore prudent to compare these quantities between sample selections at redshifts where the fits are constrained. This is the impetus for calculating the number of merger events at various redshift regimes: The number of mergers a typical galaxy experiences at  $z < 2$  and  $z < 1$  is also calculated and given in Table

4.3 and Table 5.2. At  $z < 1$  approximately one in ten massive and intermediate mass galaxies undergo a minor merger compared to one in 4 which undergo a major merger. Similar numbers are seen for the constant number density selection, where 0.1 minor mergers and 0.3 major mergers are experienced by each galaxy on average. At  $z < 2$  these numbers typically double suggesting that approximately equal numbers of merging events occur at  $z < 1$  and  $1 < z < 2$  for these samples of galaxies.

Man, Zirm & Toft calculate the expected number of minor mergers for galaxies at  $> 10^{10.8} M_{\odot}$  selected by stellar mass ratio. Converting the estimated number of mergers (see their Table 5) to  $C_{\text{merg}} = 0.6$ , Man, Zirm & Toft find massive galaxies undergo  $0.4 \pm 0.1$  minor mergers at  $0.1 < z < 2.5$ . This is larger than the value of  $0.2^{+0.3}_{-0.1}$  merging events found in this work by a factor of 2, however these values do agree within the  $1\sigma$  uncertainty ranges. The discrepancy surrounding the most likely value can be attributed to cosmic variance, but there is also the case of using a different observability timescale. However, this cannot be the ultimate cause as Man, Zirm & Toft use a minor merger observability timescale of  $0.96 \pm 0.47$  Gyr.

## 5.6 Conclusions

In this Chapter the minor merger ( $1/10 < \mu < 1/4$ ) histories of massive galaxies have been probed by measuring the total merger ( $\mu > 1/10$ ) pair fractions of massive galaxies at  $z < 2.5$  using the same technique presented in Chapter 4 for major mergers. By extracting the signal from major mergers, the minor merger histories of galaxies at  $> 10^{10} M_{\odot}$  and at a constant cumulative number density of  $n(> \mathcal{M}_*) = 10^{-4} \text{ Mpc}^{-3}$  have been constrained.

Firstly, the total merger pair fractions were measured at  $z < 0.2$  in the GAMA region, and at  $0.2 < z < 2.5$  using a combination of the UKIDSS UDS, VIDEO and COSMOS survey regions. This provided an area of 144 sq. deg. at  $z < 0.2$  and an area of 3.25 sq. deg. at  $0.2 < z < 3.5$  in which to probe the pair fractions of massive galaxies. Measured total pair fractions for galaxies at  $> 10^{11} M_{\odot}$  are found to be twice that observed for major mergers across the entire redshift range probed. Furthermore, an approximately constant pair fraction of  $\sim 20\%$  predicted by the Henriques *et al.* (2015) SAM is not consistent with observed pair fractions at  $z < 1.5$  and not qualitatively consistent with the observed weak slope found for this sample. Similar differences are found with the intermediate stellar mass sample ( $> 10^{10} M_{\odot}$ ) which exhibit total pair fractions a factor of 2–4 times larger than the major merger pair fractions. However, no comparisons can be made beyond  $z = 1.5$

unless more observations are made.

Total merger rates were derived for the three galaxy selections, however stellar mass incompleteness limited the observational constraints to  $z < 1$  at the lowest masses probed in this work. The derived total merger rates for massive galaxies imply that minor mergers occur half as frequently as major mergers over the evolutionary history of a typical galaxy over the last 11 Gyr. A similar result is found for less massive galaxies, however more observations at  $z > 1$  are needed to constrain this figure over the same redshift range in which major mergers are constrained.

It is clear from the results presented in this Chapter that high-redshift measurements are desperately needed to constrain the minor merger histories of massive galaxies at these regimes. This requirement will be met in part by the results of Duncan et al. (*in prep*) who probe mergers at a range of stellar mass ratios at  $2 < z < 5$  using the full set of CANDELS fields. However, larger fields are required to minimise interference from the observed cosmic variance identified in this work, as well as other works (e.g., Man, Zirm & Toft, 2014). Therefore the most recent and final data release (DR11) of the UKIDSS UDS, which provides  $K$ -band photometry almost a magnitude deeper than the DR8 used in this work, presents an exciting dataset to push the limits of this study. Additionally, continuing Ultra-VISTA observations mean that further overlap at high redshift is possible — two data releases have emerged since the work in this Chapter was undertaken.



# Chapter 6

## The build-up of stellar mass in massive galaxies at $z < 3.5$

This Chapter explores the relative roles of major ( $\mu > 0.25$ ) and minor ( $0.1 < \mu < 0.25$ ) galaxy mergers and star-formation in the build-up of stellar mass in massive galaxies at  $z < 3.5$ . The observational measurements of massive galaxies' merger histories from Chapter 4 and Chapter 5 are combined with a new approach to measuring the star-formation properties of stellar mass selected samples of galaxies.

### 6.1 Introduction

A wealth of observations have shown that the stellar mass budgets of galaxies increases by several factors over the past  $\sim 10$  Gyr (e.g., Daddi *et al.*, 2005; Ownsworth *et al.*, 2016). This is most obvious in the evolution of the number density of galaxies by a factor of  $\sim 10$  for the most massive galaxies, and a factor of  $\sim 6$  for the intermediate mass galaxies, at  $z < 3$  (Mortlock *et al.*, 2015). There are two main pathways through which a galaxy increases its stellar mass with time: the process of star-formation and the consumption of other galaxies. It is therefore imperative to disentangle the relative contribution from each of these sources in the build-up of stellar mass of massive galaxies.

Various studies have investigated whether the observed star-formation rates of galaxies across a range of redshifts can explain the stellar mass growth of massive galaxies. At extreme redshifts ( $3 < z < 8$ ) Papovich *et al.* (2010) used a number density selection of  $2 \times 10^{-4} \text{ Mpc}^{-3}$  to show that the observed star-formation histories of galaxies at  $3 < z < 8$  are consistent with the factor of  $\sim 10$  increase in stellar mass (see their Fig. 3). Marchesini *et al.* (2009) used the same number density selection at  $z < 4$  to suggest that the star-formation history of massive galaxies

could not fully account for the observed stellar mass growth at  $z < 1$ .

Probing the galaxy merger pathway in a more direct manner, Ownsworth *et al.* (2014) used selections at a constant number density of  $10^{-4} \text{ Mpc}^{-3}$  combined with SED fitting SFR estimates and the known merger histories of massive galaxies to determine the relative roles of star-formation and mergers in the build-up of stellar mass from  $z = 3$  to  $z = 0.3$  in massive galaxies. They found that minor mergers were the dominant source of stellar mass growth in the progenitors of  $z \sim 0.3$  galaxies with  $> 10^{10.2} \text{ M}_{\odot}$ , responsible for  $34 \pm 14\%$  of the stellar mass during this time. However, this particular study used a compilation of literature merger fractions that included both morphological and close-pair studies that result in a steep increase of the merger fraction with redshift.

This Chapter presents a study into the relative roles of star-formation and galaxy mergers which addresses the issues identified in previous works. Section §6.2 details the calculation of the stellar mass accreted through mergers, Section §6.3 details the calculation of the stellar mass accrued through the process of star-formation, and Section §6.6 summarises and concludes the results of this Chapter.

## 6.2 Stellar mass added by mergers

Ultimately, this work aims to uncover the role of galaxy mergers in the grander picture of galaxy formation. The stellar mass accrued through major mergers is an important quantity that allows comparisons to be made between other pathways of stellar mass growth such as star-formation, however knowing the rate at which a merger event occurs for a given sample of galaxies is not enough to calculate this quantity between two redshifts. The average stellar mass of a companion galaxy must be known as well. With this information, the additional stellar mass from mergers,  $\mathcal{M}_{*}^{+}$ , for a typical primary sample galaxy between two redshifts can be estimated as

$$\mathcal{M}_{*}^{+} = \int_{t_1}^{t_2} \mathcal{R}_{\text{merg}}(z) \mathcal{M}_{*,2}(z) dt, \quad (6.1)$$

where  $\mathcal{R}_{\text{merg}}$  is the fractional merger rate, defined in Equation 4.6 in terms of the pair fraction, and  $\mathcal{M}_{*,2}(z)$  is the average stellar mass of a close-pair companion at redshift  $z$ .

Within any redshift bin the GSMF,  $\phi(z, \mathcal{M}_{*})$ , can be used to calculate the

average stellar mass of a galaxy within the primary sample, and is defined as

$$\mathcal{M}_{*,1}(z) = \frac{\int_{\mathcal{M}_{*,1}^{\min}}^{\mathcal{M}_{*,1}^{\max}} \phi(z, \mathcal{M}_*) \mathcal{M}_* d\mathcal{M}_*}{\int_{\mathcal{M}_{*,1}^{\min}}^{\mathcal{M}_{*,1}^{\max}} \phi(z, \mathcal{M}_*) d\mathcal{M}_*}, \quad (6.2)$$

where  $\mathcal{M}_{*,1}^{\max}$  and  $\mathcal{M}_{*,1}^{\min}$  are the maximum and minimum stellar masses of the primary galaxy sample, respectively. A similar integration is performed to calculate the average stellar mass of a companion galaxy,  $\mathcal{M}_{*,2}(z)$ , whereby the integration in Equation 6.2 is instead performed between the stellar mass limits of  $\mathcal{M}_{*,1}$  and  $\mu\mathcal{M}_{*,1}$ . Armed with this information, the quantity of stellar mass added through major mergers alone is calculated. Uncertainties are estimated using a bootstrap approach, accounting for errors on the galaxy stellar mass function parameters and the uncertainty in the fit of  $f_{\text{pair}}$  given in Chapter 4 or Chapter 5.

### 6.2.1 Major merger stellar mass accretion rate density

It is then trivial to calculate the major merger stellar mass accretion rate density,  $\rho_{1/4}$ , for each of the selected samples presented in previous chapters. This quantity is defined as

$$\rho_{1/4} = \frac{\mathcal{M}_*^+(z) n_1(z)}{dt}, \quad (6.3)$$

where  $n_1(z)$  represents the number density of the primary sample, obtainable by integration of the GSMF,  $\mathcal{M}_*^+(z)$  is defined in Equation 6.1, and  $dt$  is the time between the two redshifts of interest. The quantity  $\rho_{1/4}$  represents the stellar mass gained through major mergers per unit time and per unit volume for a particular stellar mass (or constant number density) selected population of galaxies, and can be considered the major merger analogue of the well-studied star-formation rate density (see Section §1.2).

The top panel of Figure 6.1 displays this quantity for galaxies selected at  $\mathcal{M}_* > 10^{10} M_{\odot}$  (blue dashed line and shaded area) and  $\mathcal{M}_* > 10^{11} M_{\odot}$  (red solid line and shaded area), while the bottom panel displays results for galaxies selected at  $n(> \mathcal{M}_*) = 1 \times 10^{-4} \text{ Mpc}^{-3}$  (blue solid line and shaded area) and  $n(> \mathcal{M}_*) = 5 \times 10^{-4} \text{ Mpc}^{-3}$  (gold dashed line and shaded area). Derived major merger accretion rate densities change significantly within the redshift range probed. From  $z = 3.25$  to  $z = 0.1$ , an increase in  $\rho_{1/4}$  is observed at  $z < 3.5$  by a factor of  $6_{-5}^{+45}$  ( $3_{-2}^{+8}$ ) for the high (low) stellar mass selected samples, respectively.

Using the fitted pair fractions (see Table 4.3) using data points from GAMA,

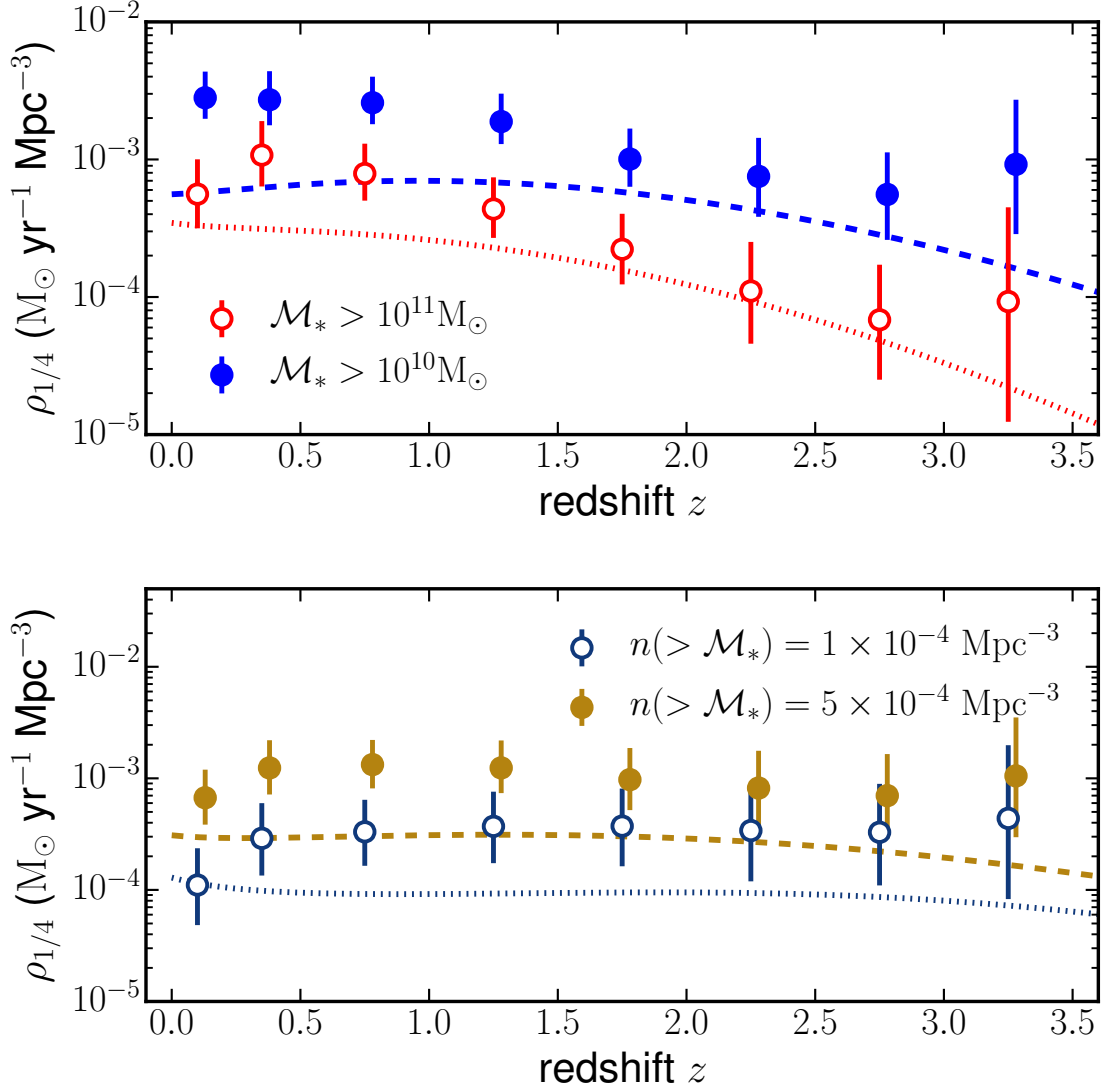


**Figure 6.1:** The major merger accretion rate density,  $\rho_{1/4}$ , for galaxies selected at  $\mathcal{M}_* > 10^{10} M_\odot$  and  $\mathcal{M}_* > 10^{11} M_\odot$  (blue filled circles and red open circles in the top panel), and galaxies selected at  $n(> \mathcal{M}_*) = 1 \times 10^{-4} \text{ Mpc}^{-3}$  and  $n(> \mathcal{M}_*) = 5 \times 10^{-4} \text{ Mpc}^{-3}$  (blue open circles and gold filled circles in the bottom panel). Error bars represent the  $1\sigma$  uncertainty on this quantity, including errors from GSMF parameters, errors from fits on the pair fraction, and a 33% uncertainty on the observability timescale. Dashed and dotted lines indicate the derived  $\rho_{1/4}$  values from Illustris using Equation 6.4.

UDS, VIDEO, COSMOS and D16, it is found that galaxies with  $\mathcal{M}_* > 10^{11} \text{M}_\odot$  are estimated to accrete an average stellar mass of  $\log(\mathcal{M}_*^+/\text{M}_\odot) = 10.5 \pm 0.2$  at  $0 < z < 3.5$ . Similarly, over the same redshift range, galaxies with  $\mathcal{M}_* > 10^{10} \text{M}_\odot$  are expected to accrete  $\log(\mathcal{M}_*^+/\text{M}_\odot) = 10.0 \pm 0.2$  from major mergers. As the typical galaxy in each of these samples at  $z \sim 3.25$  is  $\log(\mathcal{M}_*/\text{M}_\odot) = 11.2 \pm 0.1$  and  $\log(\mathcal{M}_*/\text{M}_\odot) = 10.5 \pm 0.1$ , respectively, this represents an average increase in stellar mass of  $20_{-12}^{+15}\%$ , and  $32_{-18}^{+23}\%$ , respectively, due solely to major mergers. Furthermore, the constant number density selection of  $10^{-4} \text{Mpc}^{-3}$  gains  $\log(\text{M}_\odot) = 10.5 \pm 0.3$  from major mergers over the same redshift range, while the larger number density of  $5 \times 10^{-4} \text{Mpc}^{-3}$  gains  $\log(\text{M}_\odot) = 10.4 \pm 0.2$ . As the average stellar mass of a galaxy in these selections at  $z = 3 - 3.5$  is  $\log(\text{M}_\odot) = 10.9 \pm 0.1$  and  $10.5 \pm 0.1$ , this suggests that major mergers increase the stellar mass of the average galaxy by  $40_{-20}^{+30}\%$  and  $79_{-22}^{+30}\%$ , respectively. The average stellar mass of primary and secondary samples and the stellar mass gained through major mergers are tabulated in Table 6.1.

The derived stellar mass growth estimates agree well with previous studies that have probed the major merger histories of stellar mass selected samples of galaxies. Man, Zirm & Toft (2014) estimate the stellar mass accrued by galaxies with  $> 10^{11} \text{M}_\odot$  via major mergers during  $z = 0.1 - 2.5$  as  $\log(\text{M}_\odot) = 10.4$  (after conversion to  $C_{\text{merg}} = 0.6$ ). Ferreras *et al.* (2013) find major mergers contribute approximately  $\log(\text{M}_\odot) = 10.2$  during  $z = 0.3 - 1.3$  to a typical galaxy with  $> 10^{11} \text{M}_\odot$ . Similarly, the results presented in this Chapter suggest that major mergers account for 80%, 60% and 80% of the total accreted stellar mass from mergers for massive, intermediate mass and a selection at a constant number density of  $10^{-4} \text{Mpc}^{-3}$ . This agrees with previous studies of major mergers at  $> 10^{11} \text{M}_\odot$  such as Bluck *et al.* (2012), López-Sanjuan *et al.* (2012) and Ferreras *et al.* (2013) who find major mergers account for 65%, 75%, and 70% of total merger accreted stellar mass, respectively.

### 6.2.2 Minor merger stellar mass accretion rate density

Using the fits to the minor merger pair fraction given in Table 5.3, the minor merger stellar mass accretion rate density is calculated. This is done in exactly the same way as described in Section §6.2.1, however the average stellar mass of a companion is calculated over the stellar mass range of  $0.1\mathcal{M}_{*,1} < \mathcal{M}_* < 0.25\mathcal{M}_{*,1}$ . This represents the number density weighted average stellar mass of a minor merger companion galaxy.

Figure 6.2 displays the derived minor merger accretion rate densities for the three

**Table 6.1:** The estimated number density of the primary sample,  $n_1$ , stellar masses of a typical primary sample galaxy,  $\mathcal{M}_{*,1}$ , secondary sample galaxy,  $\mathcal{M}_{*,2}$ , and estimated stellar mass,  $\mathcal{M}_*^+$ , accreted through major and minor mergers as a function of redshift for three samples of galaxies:  $> 10^{11} \text{ M}_\odot$ ,  $> 10^{10} \text{ M}_\odot$ , and  $n(> \mathcal{M}_*) = 10^{-4} \text{ Mpc}^{-3}$ .

$z$	$n_1$ ( $10^{-4} \text{ Mpc}^{-3}$ )	$\log \mathcal{M}_{*,1}$ ( $\log \text{M}_\odot$ )	Major Mergers		Minor Mergers	
			$\log \mathcal{M}_{*,2}$ ( $\log \text{M}_\odot$ )	$\log \mathcal{M}_*^+$ ( $\log \text{M}_\odot$ )	$\log \mathcal{M}_{*,2}$ ( $\log \text{M}_\odot$ )	$\log \mathcal{M}_*^+$ ( $\log \text{M}_\odot$ )
$\mathcal{M}_* > 10^{11} \text{ M}_\odot$						
0.0 – 0.2	$3.2^{+1.3}_{-1.0}$	$11.2 \pm 0.1$	$10.8 \pm 0.1$	$9.6 \pm 0.1$	$10.4 \pm 0.1$	$8.8 \pm 0.3$
0.2 – 0.5	$3.8^{+1.3}_{-1.0}$	$11.3 \pm 0.1$	$11.0 \pm 0.1$	$9.9 \pm 0.2$	$10.5 \pm 0.1$	$9.1 \pm 0.3$
0.5 – 1.0	$2.7^{+0.6}_{-0.5}$	$11.3 \pm 0.1$	$10.9 \pm 0.1$	$9.9 \pm 0.2$	$10.5 \pm 0.1$	$9.2 \pm 0.3$
1.0 – 1.5	$1.4 \pm 0.3$	$11.2 \pm 0.1$	$10.9 \pm 0.1$	$9.7 \pm 0.2$	$10.4 \pm 0.1$	$9.1 \pm 0.3$
1.5 – 2.0	$0.6 \pm 0.2$	$11.2 \pm 0.1$	$10.9 \pm 0.1$	$9.6 \pm 0.2$	$10.4 \pm 0.1$	$9.0 \pm 0.3$
2.0 – 2.5	$0.3 \pm 0.2$	$11.2 \pm 0.1$	$10.8 \pm 0.1$	$9.4 \pm 0.2$	$10.4 \pm 0.1$	$8.9 \pm 0.4$
2.5 – 3.0	$0.2^{+0.2}_{-0.1}$	$11.2 \pm 0.1$	$10.8 \pm 0.1$	$9.3 \pm 0.2$	$10.4 \pm 0.1$	$8.9 \pm 0.4$
3.0 – 3.5	$0.2^{+0.6}_{-0.2}$	$11.2 \pm 0.1$	$10.8 \pm 0.1$	$9.2 \pm 0.2$	$10.4 \pm 0.1$	$8.8 \pm 0.4$
				$10.5 \pm 0.2$	$9.9 \pm 0.3$	
$\mathcal{M}_* > 10^{10} \text{ M}_\odot$						
0.0 – 0.2	$46.7^{+6.1}_{-5.5}$	$10.6 \pm 0.1$	$10.3 \pm 0.1$	$9.2 \pm 0.2$	$9.8 \pm 0.1$	$8.3^{+0.4}_{-0.3}$
0.2 – 0.5	$31.9^{+7.5}_{-7.2}$	$10.7 \pm 0.1$	$10.4 \pm 0.1$	$9.4^{+0.1}_{-0.2}$	$9.9 \pm 0.1$	$8.7^{+0.4}_{-0.3}$
0.5 – 1.0	$26.8^{+3.9}_{-3.7}$	$10.7 \pm 0.1$	$10.4 \pm 0.1$	$9.4^{+0.1}_{-0.2}$	$9.9 \pm 0.1$	$8.9^{+0.4}_{-0.3}$
1.0 – 1.5	$17.3^{+3.0}_{-2.8}$	$10.6 \pm 0.1$	$10.3 \pm 0.1$	$9.2^{+0.1}_{-0.2}$	$9.8 \pm 0.1$	$9.0 \pm 0.4$
1.5 – 2.0	$8.3^{+2.3}_{-2.0}$	$10.6 \pm 0.1$	$10.3 \pm 0.1$	$9.1 \pm 0.2$	$9.8 \pm 0.1$	$9.0 \pm 0.4$
2.0 – 2.5	$6.2^{+3.0}_{-2.5}$	$10.5 \pm 0.1$	$10.2 \pm 0.1$	$8.9 \pm 0.2$	$9.7 \pm 0.1$	$9.0 \pm 0.4$
2.5 – 3.0	$4.4^{+2.6}_{-2.1}$	$10.5 \pm 0.1$	$10.2 \pm 0.1$	$8.8 \pm 0.2$	$9.7 \pm 0.1$	$8.9^{+0.5}_{-0.4}$
3.0 – 3.5	$7.0^{+10.0}_{-4.3}$	$10.5 \pm 0.1$	$10.1 \pm 0.1$	$8.6 \pm 0.2$	$9.6 \pm 0.1$	$8.9^{+0.5}_{-0.4}$
				$10.0 \pm 0.2$	$9.8 \pm 0.4$	
$n(> \mathcal{M}_*) = 1 \times 10^{-4} \text{ Mpc}^{-3}$						
0.0 – 0.2	$1.0^{+0.6}_{-0.4}$	$11.3 \pm 0.1$	$10.9 \pm 0.1$	$9.4^{+0.3}_{-0.2}$	$10.5 \pm 0.1$	$9.0 \pm 0.3$
0.2 – 0.5	$1.0^{+0.5}_{-0.3}$	$11.5 \pm 0.1$	$11.2 \pm 0.1$	$9.9^{+0.3}_{-0.2}$	$10.7 \pm 0.1$	$9.4 \pm 0.3$
0.5 – 1.0	$1.0^{+0.3}_{-0.2}$	$11.4 \pm 0.1$	$11.1 \pm 0.1$	$10.0 \pm 0.3$	$10.6 \pm 0.1$	$9.4 \pm 0.3$
1.0 – 1.5	$1.0^{+0.3}_{-0.2}$	$11.3 \pm 0.1$	$10.9 \pm 0.1$	$9.7 \pm 0.3$	$10.5 \pm 0.1$	$9.1 \pm 0.4$
1.5 – 2.0	$1.0 \pm 0.3$	$11.1 \pm 0.1$	$10.8 \pm 0.1$	$9.6^{+0.4}_{-0.3}$	$10.3 \pm 0.1$	$8.9 \pm 0.4$
2.0 – 2.5	$1.0^{+0.6}_{-0.5}$	$11.0 \pm 0.1$	$10.6 \pm 0.1$	$9.4 \pm 0.3$	$10.2 \pm 0.1$	$8.6 \pm 0.5$
2.5 – 3.0	$1.0^{+0.7}_{-0.5}$	$10.9 \pm 0.1$	$10.5 \pm 0.1$	$9.2 \pm 0.4$	$10.1 \pm 0.1$	$8.4 \pm 0.5$
3.0 – 3.5	$1.0^{+1.8}_{-0.7}$	$10.9 \pm 0.1$	$10.6 \pm 0.1$	$9.2 \pm 0.4$	$10.1 \pm 0.1$	$8.4 \pm 0.6$
				$10.5 \pm 0.3$	$9.9 \pm 0.4$	

galaxy samples. Massive galaxies are given by the blue filled circles, intermediate mass galaxies are given by the red open circles, and the number density selection is given by the blue open triangles. The massive and intermediate stellar mass selections exhibit an approximately constant minor merger accretion rate density of  $1 \times 10^{-4} \text{ M}_{\odot} \text{ yr}^{-1} \text{ Mpc}^{-3}$  and  $6 \times 10^{-4} \text{ M}_{\odot} \text{ yr}^{-1} \text{ Mpc}^{-3}$ , respectively.

The approximately constant evolution of  $\rho_{1/10}$  for the constant stellar mass samples is in contrast to that seen for major mergers (see Figure 6.1), which shows a decline in  $\rho_{1/4}$  at high redshift. Caution must be taken when making this comparison however, as the major merger fractions (and thus rates) are better constrained at high redshift than minor mergers. In the major merger case, observations at high redshift generally result in a shallower pair fraction slope which eventually translates to a lower accretion rate density. Therefore it is possible that further observations of minor mergers will do just the same. Considering the constant number density selection,  $\rho_{1/10}$  is found to remain approximately constant with redshift, as found for the major merger equivalent. Taking the data points where the pair fraction fits are observationally constrained,  $\rho_{1/10}$  is a factor of  $\sim 5$  smaller than  $\rho_{1/4}$  on average. This is found for all of the sample selections given in Figure 6.2.

In the calculation of this quantity, is it trivial to calculate the expected stellar mass added to a typical galaxy from minor mergers over  $z = 0 - 3.5$ . Massive, intermediate mass and galaxies at a constant number density are found to gain  $\log(\text{M}_{\odot}) = 9.9 \pm 0.3$ ,  $9.8 \pm 0.4$ , and  $9.9 \pm 0.4$ , respectively. It is also found that approximately 40%, 25% and 34% of this stellar mass is accreted at in the last half of cosmic time ( $z < 1$ ).

These values agree well with other studies of minor merger histories. Though study of close-pairs, Man, Zirm & Toft (2014) expect minor mergers to contribute  $\log(\text{M}_{\odot}) = 9.7$  (after conversion to  $C_{\text{merg}} = 0.6$ ) to galaxies with  $> 10^{11} \text{ M}_{\odot}$  during  $z = 0.1 - 2.5$ , with an approximate  $\pm 80\%$  ( $\sim 0.3$  dex) uncertainty associated with this value. Furthermore Ferreras *et al.* (2013) study close-pairs of galaxies with  $> 10^{11} \text{ M}_{\odot}$  at  $z = 0.3 - 1.3$  in the Survey for High- $z$  Absorption Red and Dead Sources (SHARDS) survey (Pérez-González *et al.*, 2013). For this selection they find that  $(\Delta M/M)/\Delta t \sim 0.08 \text{ Gyr}^{-1}$ , with  $\sim 30\%$  of this mass growth attributed to mergers at mass ratios of 1:3 – 1:100. For a typical galaxy over this  $\sim 5 \text{ Gyr}$  period this equates to an upper limit of  $\log(\text{M}_{\odot}) \approx 10.1$  added through ‘minor’ mergers. Appropriate merger history studies of lower mass galaxies are unfortunately not available to draw comparisons to.

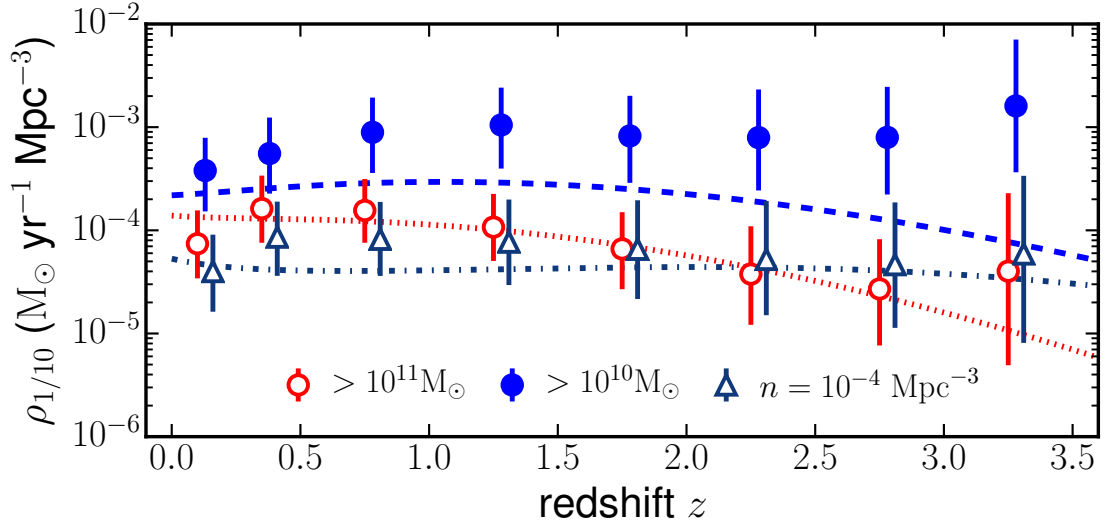


**Figure 6.2:** The minor merger ( $1/10 < \mu < 1/4$ ) accretion rate density,  $\rho_{1/10}$ , for galaxies selected at  $\mathcal{M}_* > 10^{10} M_\odot$  and  $\mathcal{M}_* > 10^{11} M_\odot$  (blue filled circles and red open circles), and galaxies selected at  $n(> \mathcal{M}_*) = 1 \times 10^{-4} \text{ Mpc}^{-3}$  (blue open triangles). Error bars represent the  $1\sigma$  uncertainty on this quantity, including errors from GSMF parameters, errors from fits on the pair fraction, and the uncertainty on the observability timescale. Dashed, dotted, and dashed-dotted lines indicate the derived  $\rho_{1/10}$  values from Illustris using Equation 6.4.

### 6.2.3 Comparison to hydrodynamical simulations

Several literature publications are used to calculate the major and minor merger accretion rate density,  $\rho_{1/4}$ , within the Illustris simulation. This is achieved by using fits to the GSMF within the simulation (Equation 1 of Torrey *et al.* 2015) combined with the fitting function of the specific merger accretion rate,  $\dot{m}_{\text{acc}}(\mathcal{M}_*, \mu, z)$ , in Table 1 of Rodriguez-Gomez *et al.* (2016). It is then trivial to estimate  $\rho$  within Illustris;

$$\rho^{\text{sim}} = \int_{\mathcal{M}_l}^{\mathcal{M}_h} \phi(\mathcal{M}_*, z) \mathcal{M}_* \int_{\mu_l}^{\mu_h} \dot{m}_{\text{acc}}(\mathcal{M}_*, \mu, z) d\mu d\mathcal{M}_*, \quad (6.4)$$

where  $\mathcal{M}_*$  is stellar mass,  $\phi(\mathcal{M}_*, z)$  is the GSMF evaluated at  $\mathcal{M}_*$  and redshift  $z$ , and the specific merger accretion rate is defined as

$$\dot{m}_{\text{acc}}(\mathcal{M}_*, \mu, z) = \frac{1}{\mathcal{M}_*} \frac{d\mathcal{M}_{\text{acc}}}{dt d\mu}. \quad (6.5)$$

For the purposes of this work an integration is performed with respect to the stellar mass merger ratio between  $0.25 < \mu < 1.0$  for major mergers, and  $0.1 < \mu < 0.25$  for minor mergers, in order to attain the accretion mass.

Figure 6.1 displays estimates of the major merger accretion rate density,  $\rho_{1/4}$ ,



within the Illustris simulation for galaxies at  $> 10^{10} M_{\odot}$  (top panel), and galaxies selected at two number densities of  $n > 10^{-4} \text{ Mpc}^{-3}$  (bottom panel). The Illustris estimates are given as the dashed and dotted curves in the respective panels. For the constant stellar mass samples (upper panel), Illustris estimates are typically a factor of  $\sim 2\text{--}3$  smaller than the estimates based on observations at  $z < 1.5$ , but generally in agreement at earlier times although, admittedly, the uncertainties are large. Qualitatively, the evolution of  $\rho$  displays a decreasing value with redshift — typically an order of magnitude at  $z = 0 - 3.5$  — which agrees with the evolution of observational estimates. Predictions of  $\rho_{1/4}$  for constant number density samples (bottom panel) qualitatively agree with the observational estimates, however they are a factor of  $2\text{--}3$  smaller over the entire redshift range probed.

Figure 6.2 displays predictions of the minor merger accretion rate density within Illustris. Similar evolutions of the quantity are seen for the constant stellar mass samples, whereby  $\rho_{1/10}$  decreases with redshift. Simulation predictions are roughly a factor of  $\sim 2$  smaller than observational estimates for the lower mass ( $> 10^{10} M_{\odot}$ ) sample, however they agree for the most massive ( $> 10^{11} M_{\odot}$ ) galaxies. As before, a similarly flat evolution is found for the constant number density sample, remaining at  $\approx 5 \times 10^{-5} M_{\odot} \text{ yr}^{-1} \text{ Mpc}^{-3}$  across the redshift range probed.

The differences between the simulation predictions and observational estimates could be due to a number of factors. The ability of the simulation to predict the observed number densities of massive galaxies will affect not only the primary sample, but the average stellar mass of an accreted secondary sample companion. At  $z < 4$  it has been shown that Illustris matches observations of the GSMF at masses of  $10 < \log(\mathcal{M}_*/M_{\odot}) < 11$  however it typically *over*-predicts the number densities of galaxies with  $> 10^{11} M_{\odot}$  by  $0.3\text{--}0.5$  dex (Genel *et al.*, 2014, see their Fig. 3). With more massive galaxies to merge with it would be expected that the major merger accretion rate might be *over*-estimated within the simulation. As this is not the case it suggests that the rate at which galaxies merge in the simulation is smaller than derived from observational measurements of the merger fraction. From Figure 4.10 and Figure 4.11 it can be seen that the merger rates within Illustris are actually *higher* than those derived from observational measurements of the merger fraction. This suggests that companion galaxies are much less massive than would be expected from an average of the masses of galaxies between the  $\mu$  limits (i.e. companion galaxies are at the very low end of the  $\mu$  distribution).

### 6.3 Stellar mass added by star-formation

In order to compare the stellar mass accreted through major mergers with that produced via the process of star-formation, the star-formation rate density,  $\rho_\Psi$ , must be calculated for the same stellar mass selected samples of galaxies used to calculate the merger fractions and subsequent merger rates in the previous chapter. This section describes the steps taken to achieve this.

Estimated stellar masses and total (UV + IR) star-formation rates are taken from Muzzin *et al.* (2013a, see their Section §5.5) and the distribution of star-formation rates,  $\Psi$ , are observed within discrete bins of stellar mass and redshift. This work and the SFR estimates in Muzzin *et al.* (2013a) both use a Chabrier (2003) IMF. Sources brighter than the 90% completeness  $K$ -band magnitude of 23.4 with reliable photometry are used. Stellar mass bins over the range  $9.5 < \log \mathcal{M}_* < 11.5$  with a width of 0.25 dex are used, while redshift bins are chosen to be the same as the redshift bins probed in Figure 4.6. The resulting distributions of  $\log \Psi$  are fit with a combination of two Gaussian functions, representing a ‘red’ and a ‘blue’ population, respectively. It is important only that the total SFR distribution is well reproduced at every stellar mass and redshift bin and a combination of two Gaussian function achieves this. These fitted distributions are normalised such that a galaxy with a particular  $(\mathcal{M}_*, z)$  must have a star-formation rate in the range  $-3 < \log \Psi [\text{M}_\odot \text{ yr}^{-1}] < 5$ . This range encompasses the range of SFRs within this particular catalogue. The fitted star-formation rate distributions are presented in Figure 6.3 as a function of stellar mass (columns) and redshift bin (rows).

In order to estimate  $\rho_\Psi$ , stellar mass is substituted for star-formation rate in the GSMF, effectively transforming the GSMF into a star-formation rate function (SFRF),  $\phi_\Psi$ . As the GSMF is defined as

$$\phi_*(\mathcal{M}_*, z) = \frac{dN}{dV d\log \mathcal{M}_*}, \quad (6.6)$$

it is trivial to define the SFRF,  $\phi_\Psi$ , as

$$\phi_\Psi(\mathcal{M}_*, z) = \frac{dN}{dV d\log \Psi}, \quad (6.7)$$

where  $\Psi$  is the star-formation rate. The SFRF evaluates the number density of objects with a particular star-formation rate at a particular redshift. At fixed redshift this substitute is performed by sampling a star-formation rate from the appropriate distribution at every stellar mass. The star-formation rate density can then be estimated by integrating the sampled  $\phi_\Psi$  with respect to star-formation

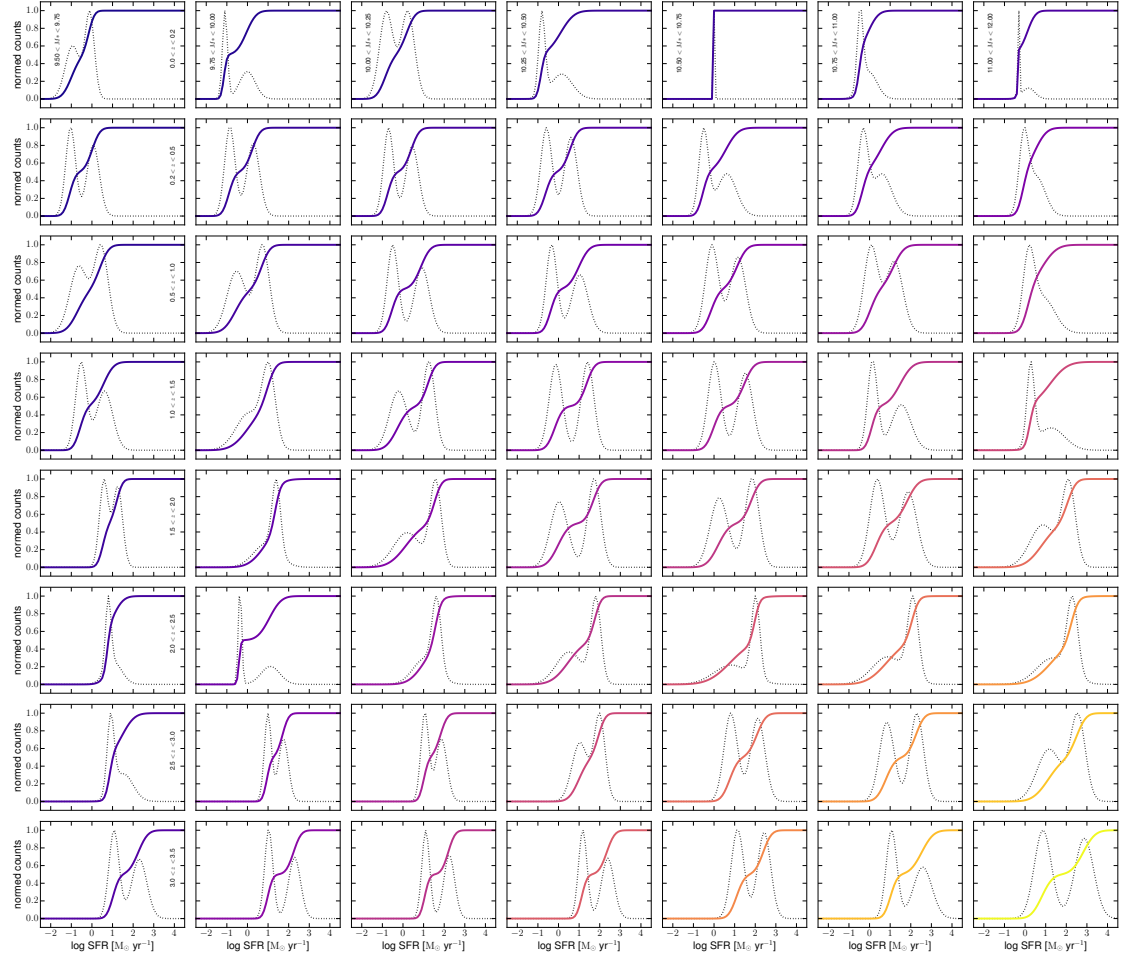


**Figure 6.3:** Star-formation rate distributions as a function of redshift (rows) and stellar mass (columns) bins. Dashed grey lines represent the sum of a double Gaussian fit to the SFR distributions of Muzzin *et al.* (2013a), while the coloured solid curves represent the cumulative counts as a function of star-formation rate.

rate. This can be written as

$$\rho_{\Psi} = \int_{\Psi(\mathcal{M}_{*,1})}^{\Psi(\mathcal{M}_{*,2})} \phi_{\Psi} \times \Psi \, d\Psi. \quad (6.8)$$

Performing a large number of these  $\rho_{\Psi}$  ‘realisations’ obtains a distribution of values for the star-formation rate density for a mass selected sample of galaxies from which the most likely value and associated uncertainties are extracted as the 50th, 16th and 84th percentiles, respectively.

As the star-formation rate distributions are constructed from the flux-limited catalogue of Muzzin *et al.* (2013a), care is taken to only use  $\rho_{\Psi}$  estimates at redshifts where  $\mathcal{M}_{*,1} > \mathcal{M}_{*}^{90}(z)$ , i.e. where distributions of  $\log \Psi$  are complete. Not accounting for this would result in values of  $\rho_{\Psi}$  which are likely to be *over*-estimated, as it would assume that lower mass galaxies have the same star-formation rate distribution as higher mass systems. At these redshifts where this is the case, lower limits on  $\rho_{\Psi}$  are estimated by integrating down to the appropriate stellar mass completeness limit. Nonetheless, as one incrementally integrates down to stellar masses of  $10^8 \, \text{M}_{\odot}$  estimations of  $\rho_{\Psi}$  are achieved that are in excellent agreement with the cosmic star-formation rate density given in Equation 15 of Madau & Dickinson (2014). Although taking SFR distributions from deeper survey data (e.g., Laigle *et al.*, 2016) would permit extending comparisons to higher redshifts, these SFR estimates would most likely be based on SED fitting techniques which can provide substantially inaccurate SFR estimates if the assumed star-formation history is not correct (Maraston *et al.*, 2010; Papovich *et al.*, 2011). For completeness, results are presented using other SFR estimates in the text while figures are provided in Appendix C. One caveat of this work is that it explicitly assumes the SFR of a galaxy is dependent only on stellar mass and redshift. However, it is known that other galaxy properties (e.g., rest-frame UVJ colour) correlate with SFR and could be used to provide better constraints on  $\rho_{\Psi}$  in the future.

The estimated SFR densities,  $\rho_{\Psi}$ , for the constant stellar mass samples, shown in the top panel of Figure 6.4, evolve strongly with both redshift and stellar mass. The calculated  $\rho_{\Psi}$  for galaxies at  $> 10^{10} \, \text{M}_{\odot}$  is found to be at least an order of magnitude larger than that calculated for more massive galaxies at  $> 10^{11} \, \text{M}_{\odot}$ . The more massive galaxies evolve from  $\log(\rho_{\Psi}) = -3.4$  at  $z = 0$  to  $\log(\rho_{\Psi}) = -2.0$  at  $z = 3.5$ , indicating a factor of  $\sim 25$  difference. The lower mass sample evolves from  $\log(\rho_{\Psi}) = -2.5$  at  $z = 0$  to  $\log(\rho_{\Psi}) = -1.3$  at  $z = 1.5$ . This represents a change by a factor of  $\sim 16$  over this time (compared to a factor of  $\sim 5$  for the more massive sample by  $z = 1.5$ ). Similar trends are seen the constant number

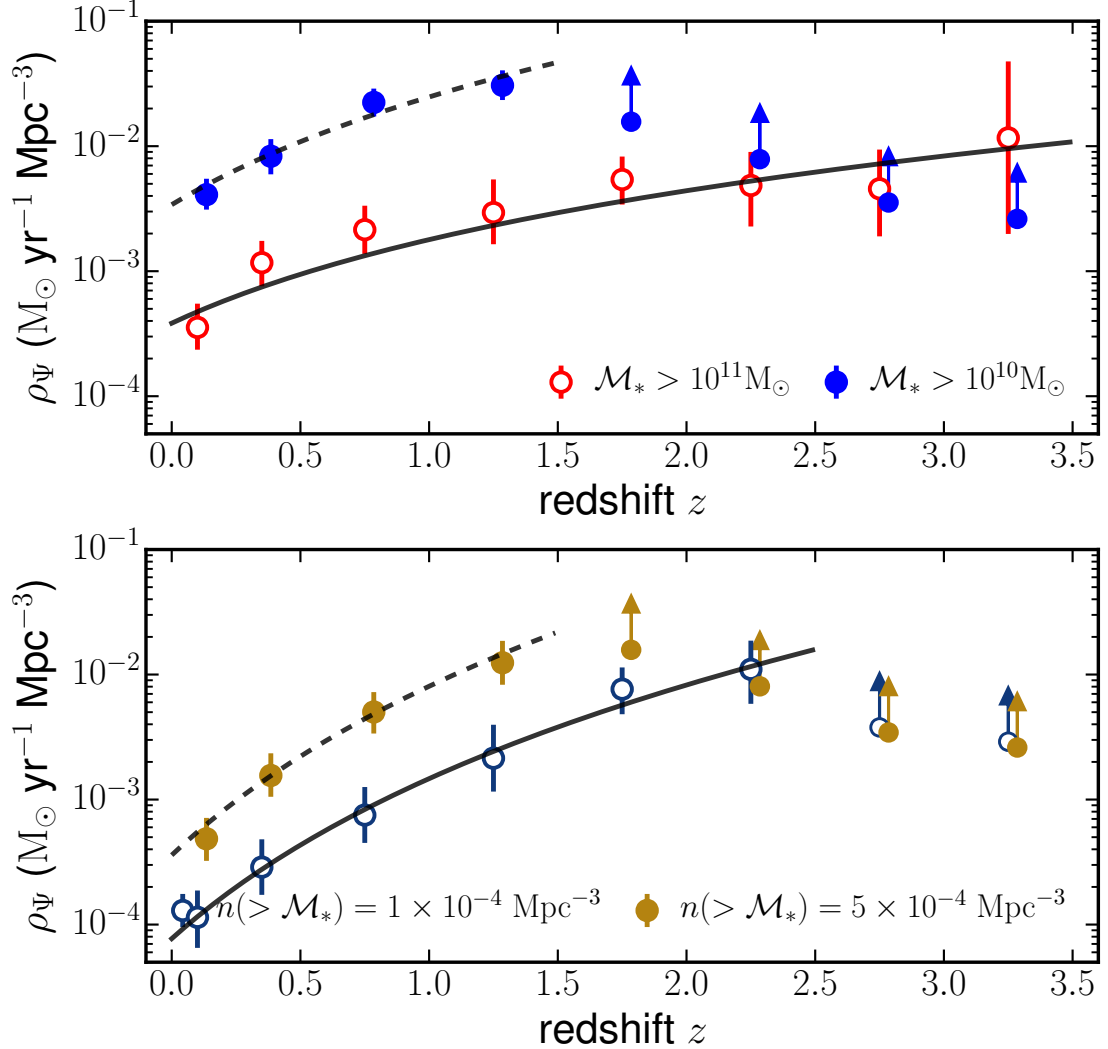


**Figure 6.4:** The estimated star-formation rate densities,  $\rho_\Psi$ , for galaxies selected at  $> 10^{11} M_\odot$  and  $> 10^{10} M_\odot$  (red open circles and blue filled circles in the top panel), and galaxies selected at two different constant cumulative number density of  $1 \times 10^{-4}$  and  $5 \times 10^{-4} \text{ Mpc}^{-3}$  (gold filled circles and blue open circles in the bottom panel). See the text for details on how these are calculated. Dashed and solid lines represent the best fitting power law parametrisation of  $\rho_\Psi$ . Arrows represent lower limits on  $\rho_\Psi$ , estimated by integrating down to the stellar mass completeness limit of the catalogue from which the SFR distributions are constructed. Fitting parameters for these samples are presented in Table 6.2.

**Table 6.2:** Star-formation rate density fitting parameters for galaxies with  $> 10^{11} M_{\odot}$ ,  $> 10^{10} M_{\odot}$ , and at  $n(> \mathcal{M}_*) = 10^{-4} \text{ Mpc}^{-3}$ . The data in Figure 6.4 is fit with a simple power law of the form  $\rho_{\Psi}(z) = \rho_0(1+z)^{m_{\Psi}}$ , where  $\rho_0$  represents the star-formation rate density at  $z = 0$  and  $m_{\Psi}$  represents the slope towards higher redshift.

Selection	$\rho_{\Psi}(z = 0)$	$m_{\Psi}$	Fit range
$\mathcal{M}_* > 10^{11} M_{\odot}$	$3.8^{+1.2}_{-1.1} \times 10^{-4}$	$2.2^{+0.4}_{-0.4}$	$z < 3.5$
$\mathcal{M}_* > 10^{10} M_{\odot}$	$3.5^{+0.9}_{-0.8} \times 10^{-3}$	$2.9^{+0.5}_{-0.5}$	$z < 1.5$
$n(> \mathcal{M}_*) = 1 \times 10^{-4} \text{ Mpc}^{-3}$	$7.5^{+3.9}_{-3.4} \times 10^{-5}$	$4.3^{+0.6}_{-0.7}$	$z < 2.5$
$n(> \mathcal{M}_*) = 5 \times 10^{-4} \text{ Mpc}^{-3}$	$3.6^{+1.3}_{-1.1} \times 10^{-4}$	$4.5^{+0.6}_{-0.7}$	$z < 1.5$

density samples (bottom panel of Figure 6.4), however the slopes are visibly steeper than for the constant mass samples. For the constant number density sample at  $n = 1 \times 10^{-4} \text{ Mpc}^{-3}$ , an increase by a factor of  $\sim 100$  in star-formation rate is seen from  $z = 0$  to  $z = 2$ .

## 6.4 Comparing star-formation to major and minor mergers in the build up of stellar mass

The star-formation rate densities of the different samples can be compared to the merger accretion rate densities in order to ascertain the relative roles of mergers and star-formation in the build-up of stellar mass in massive galaxies at  $z < 3.5$ . The ratio of star-formation rate density to major (or minor) merger accretion rate density quantifies the relative roles of star-formation and mergers as a function of redshift for a specific stellar mass selected sample of galaxies. Fits of this ratio, parametrised as  $p(z) = p_0(1+z)^m$ , are given for major and minor mergers in Table 6.3.

To this end, the ratio  $\rho_{\Psi}/\rho_{1/4}$  is shown in the top panel of Figure 6.5. Points for intermediate mass galaxies are given by the filled blue circles, while massive galaxies are shown as the open red circles, and the constant number density sample is shown as open blue triangles. Given the dependence of  $\rho_{\Psi}$  on stellar mass, it is no surprise that a dependence of  $\rho_{\Psi}/\rho_{1/4}$  is also found. The combination of a lower  $\rho_{\Psi}$  and weak dependence of  $\rho_{1/4}$  on stellar mass allows for major mergers to become a comparable (within a factor of  $\sim 2$ ) source of stellar mass growth compared to star-formation at  $z < 1$  for this sample. Intermediate mass galaxies experience this duality at later times ( $z < 0.5$ ) than massive galaxies while the constant number density sample has ratios similar to the more massive sample across the entire redshift range probed.

**Table 6.3:** Best fitting parameters and uncertainties, derived from a bootstrap analysis, of the ratio of star-formation rate density and major merger accretion rate density,  $\rho_\Psi/\rho_{1/4}$ . This quantity is parametrised as  $\rho_\Psi/\rho_{1/4} = p_0(1+z)^m$ . Parameters shown for the two constant stellar mass selections and two constant number density selections probed in this work. Fits are shown in Figure 6.5 as dashed and solid black curves.

Major Mergers ( $\rho_\Psi/\rho_{1/4}$ )			Minor Mergers ( $\rho_\Psi/\rho_{1/10}$ )		
$p_0$	$m$	redshift range	$p_0$	$m$	redshift range
$\mathcal{M}_* > 10^{10} \text{M}_\odot$					
$1.07^{+0.56}_{-0.46}$	$3.49^{+0.87}_{-0.88}$	$z < 1.5$	$11.96^{+14.20}_{-8.71}$	$1.32^{+1.91}_{-2.65}$	$z < 1.5$
$\mathcal{M}_* > 10^{11} \text{M}_\odot$					
$0.37^{+0.39}_{-0.23}$	$3.89^{+1.17}_{-1.46}$	$z < 3.5$	$3.30^{+4.86}_{-2.40}$	$2.88^{+1.52}_{-2.16}$	$z < 3.5$
$n(> \mathcal{M}_*) = 1 \times 10^{-4} \text{Mpc}^{-3}$					
$0.49^{+1.33}_{-0.39}$	$3.35^{+1.96}_{-3.76}$	$z < 2.5$	$1.57^{+5.38}_{-1.31}$	$1.32^{+1.91}_{-2.65}$	$z < 2.5$
$n(> \mathcal{M}_*) = 5 \times 10^{-4} \text{Mpc}^{-3}$					
$0.49^{+0.46}_{-0.31}$	$3.74^{+1.52}_{-1.70}$	$z < 1.5$	-	-	-

Similar trends are seen for minor mergers, shown in the bottom panel of Figure 6.5. It is clear that minor mergers have not yet become a comparable source of stellar mass relative to star-formation for any of the galaxy selections. Massive galaxies and galaxies selected at a constant number density evolve from a ratio of  $\sim 100$  at  $z \sim 2.5$  to a ratio of  $\sim 3\text{--}5$  at  $z = 0$ . The ratio for intermediate mass galaxies evolves weakly with redshift from a ratio of  $\sim 40$  at  $z \sim 1.5$  to a ratio of  $\sim 10$  at  $z = 0$ . The uncertainties are however large, owing to the larger uncertainties on the minor merger rates compared to major mergers.

It is clear then that the process of star-formation remains the dominant source of stellar mass growth in massive galaxies at  $z < 3.5$ , with the exception of the most massive galaxies where major mergers become comparable to and possibly larger since the last 5 Gyr.

## 6.5 Role of major and minor mergers in the size evolution of massive galaxies

Studies have shown that massive galaxies have grown in size by a factor of 2–4 since  $z \sim 2$  (Daddi *et al.*, 2005; Trujillo *et al.*, 2006, 2007; Buitrago *et al.*, 2008; Lani *et al.*, 2013). Sizes of galaxies selected at a constant number density have been shown to evolve by a factor of  $\sim 1.5\text{--}4$  since  $z \sim 3$  (Ownsworth *et al.*, 2014; van Dokkum

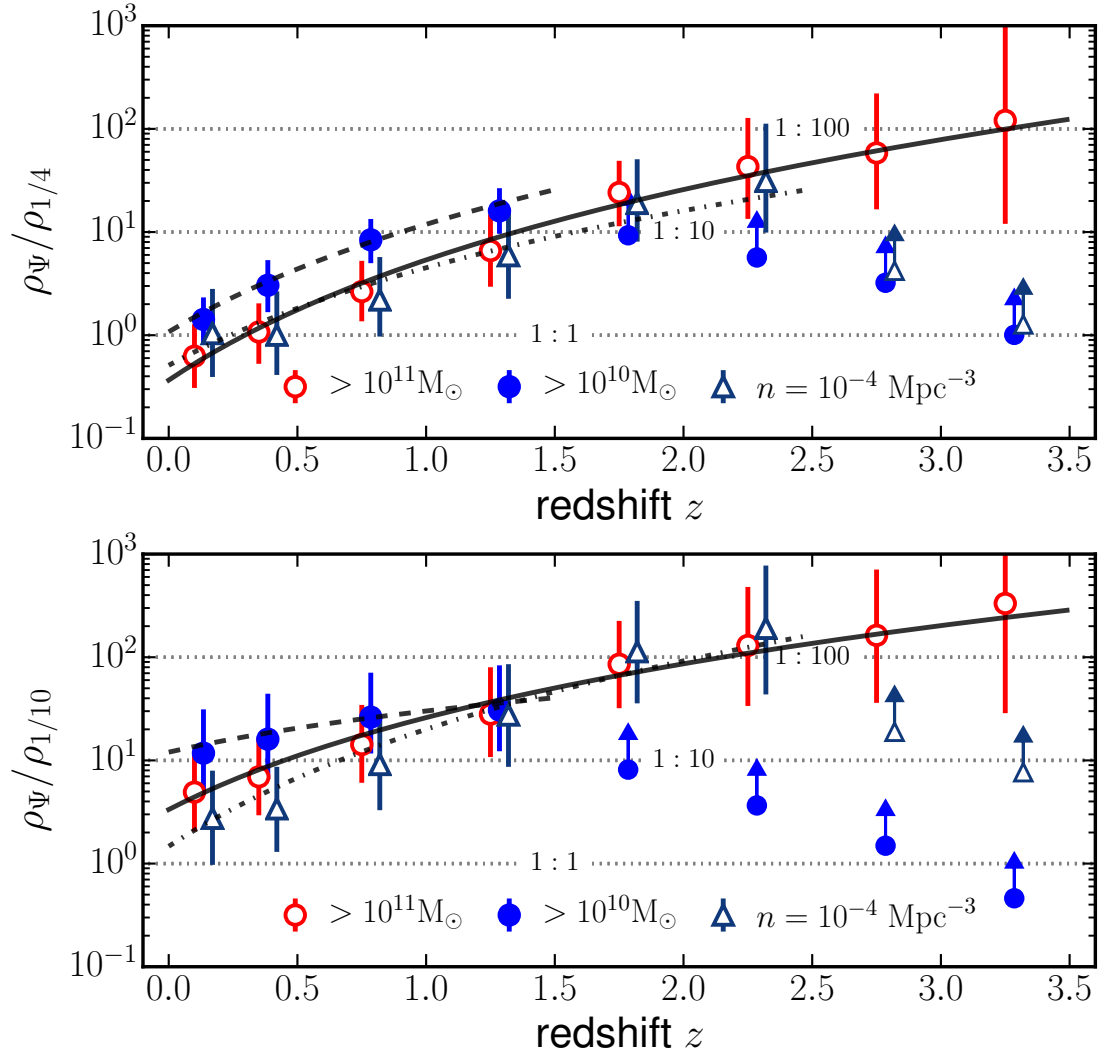


**Figure 6.5:** The ratio of star-formation rate density to major (top panel) and minor (bottom panel) merger accretion rate density as a function of redshift for galaxies at  $> 10^{11} M_\odot$  (open red circles),  $> 10^{10} M_\odot$  (filled blue circles), and a constant number density of  $1 \times 10^{-4} \text{ Mpc}^{-3}$  (open blue triangles). Arrows represent lower limits on these quantities. Dotted horizontal lines indicate ratio values of 1, 10, and 100. Solid, dashed, and dashed-dotted curves represent fits of a simple power law to the data for the samples mentioned above, respectively.



*et al.*, 2010). Recent works have shown that mergers between galaxies with low gas content — so-called dry mergers — allow galaxies to increase in size by a few times from  $z > 2$  to  $z \sim 0$  (e.g., Bezanson *et al.*, 2009; Oser *et al.*, 2012). Virial theorem arguments and galaxy merger simulations indicate that the size evolution due to dry mergers can be parametrised as  $R \propto \mathcal{M}_*^\alpha$ , where  $\alpha \approx 1$  for major mergers and  $\alpha \approx 2$  for minor mergers (e.g., Bezanson *et al.*, 2009; Hilz *et al.*, 2012; Hilz, Naab & Ostriker, 2013).

In order to explore the role of mergers in this observed size evolution, the change in radius of a typical galaxy in each of the selections is estimated. Going forward in time (towards lower redshift) over each redshift bin, the stellar mass accreted through major or minor mergers has been estimated in the previous section. As the typical stellar mass of a galaxy at each selection is known in the highest redshift bin, the change in radius of a typical galaxy can be estimated. Using the arguments given above, the ratio between initial and final radius can be written as

$$\frac{R(z)}{R(z=3.5)} = \left( \frac{\mathcal{M}_0 + \mathcal{M}_*^+}{\mathcal{M}_0} \right)^\alpha = \left( 1 + \frac{\mathcal{M}_*^+}{\mathcal{M}_0} \right)^\alpha, \quad (6.9)$$

where  $\mathcal{M}_0$  is the initial  $z = 3.5$  stellar mass of a primary sample galaxy, and  $\mathcal{M}_*^+$  is the stellar mass added via mergers from  $z = 3.5$  to  $z = z_2$  where  $z_2 < 3.5$ . Normalising the left hand side of the equation by the initial radius removes any assumption of the initial size of the galaxy and instead focuses on the evolution rather than absolute values. The results in this work assume  $\alpha = 1$  for major mergers and  $\alpha = 2$  for minor mergers.

Estimated size evolution,  $R(z)/R(z=3.5)$ , is shown in Figure 6.6 for major (top panel) and minor (bottom panel) mergers. Major mergers are found to increase the size of galaxies selected at  $> 10^{11} M_\odot$  and  $> 10^{10} M_\odot$  by 20% and 40%, respectively, while minor mergers contribute an increase of 10% and 50% for the same samples. The progenitors of local massive galaxies, selected at a constant number density of  $10^{-4} \text{ Mpc}^{-3}$ , are expected to increase in size by 40% and 20% from major and minor mergers, respectively. There are, however, large uncertainties on these estimates owing to the uncertainty on the minor merger rate. Although minor merger rates are lower and the mass accreted from them is small, the value of  $\alpha \approx 2$  predicts minor mergers are much more efficient in increasing galaxy size. Summing the contributions from major and minor mergers suggests that galaxy mergers are responsible for an increase in size by a factor of 1.3, 1.9 and 1.6 for the selections mentioned above. These estimates are upper limits as the assumption of all mergers being dry mergers may not always be correct (especially as lower stellar masses are

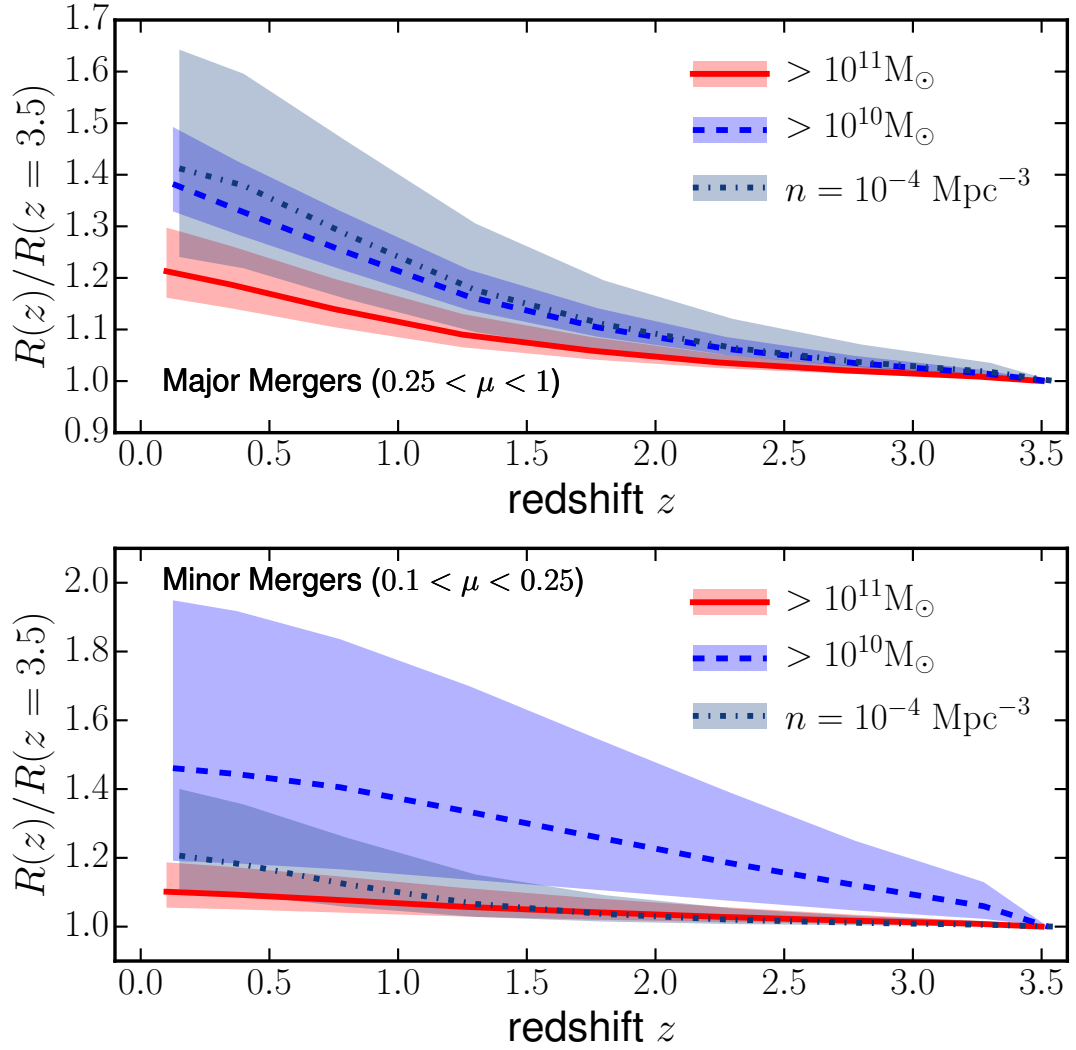


**Figure 6.6:** Estimated size increase due to major (top panel) and minor (bottom panel) mergers at  $z < 3.5$  for galaxies selected at  $> 10^{11} M_{\odot}$  (red solid line and shaded area) and  $> 10^{10} M_{\odot}$  (blue dashed line and shaded area) and at a constant number density of  $10^{-4} \text{ Mpc}^{-3}$  (blue dashed dotted line and shaded area).

probed) and the assumption that all mergers are dissipationless will not always be true either.

The derived size evolution for the most massive galaxies ( $\sim 1.3\times$ ) is similar although smaller than the factor of  $\sim 1.7$  found for galaxies at  $> 10^{10.8} M_{\odot}$  at  $z < 2.5$  using data from UltraVISTA and 3DHST+CANDELS. However, if the value of  $C_{\text{merg}}$  is normalised to that used in this work, Man, Zirm & Toft find size growth on the order of a factor of  $\sim 1.1$ , only 20% away from the value derived in this work. The predicted factor of  $\sim 1.6\times$  size growth for the constant number density selected sample is smaller than the evolution in size (effective radius) observed by Ownsworth *et al.* (2014, see their Table 5) for a sample of galaxies selected at  $z < 3$  and  $10^{-4} \text{ Mpc}^{-3}$ . They find an average size increase of  $\sim 2.7$  over this redshift

range, suggesting that merging can only account for at most  $\sim 70\%$  of the observed size evolution of massive galaxy progenitors. As with all the results presented in this Chapter, this depends heavily on the assumed value of  $C_{\text{merg}}$ , and using a value of unity instead of 0.6 allows for merging to account for the vast majority of the observed size evolution.

As more massive galaxies are found to evolve in size by a smaller (relative) amount compared to lower mass galaxies, these results support the idea of 'down-sizing' (Cowie *et al.*, 1996) whereby the most massive galaxies formed first and being to evolve passively first.

The assumptions made in this work reveal that in most cases, therefore, mergers cannot fully account for the observed size evolution of galaxies at  $z < 3.5$ . Other sources of size evolution may come from AGN feedback (e.g., Fan *et al.*, 2008), or the process of star-formation (e.g., Dekel, Sari & Ceverino, 2009; Ownsworth *et al.*, 2012). However, the relative roles of these processes in the size evolution of massive galaxies has not yet been explored in as much detail as galaxy mergers.

## 6.6 Conclusions

The relative roles of star-formation and mergers in the build up of stellar mass in massive galaxies has been probed at  $z < 3.5$ . The best constraints on the major and minor merger histories of massive galaxies have been used to estimate the stellar mass accreted by a typical galaxy at  $> 10^{10} M_{\odot}$  through merging events. From this the major and minor merger accretion rate densities are estimated, providing a quantity which can be compared to the star-formation properties of a population of galaxies. This was achieved by calculating the well known star-formation rate density for the stellar mass selected populations of galaxies probed throughout this thesis. The main conclusions from this comparison are as follows. Star-formation remains the dominant source of stellar mass growth for massive galaxies for the majority of cosmic time, only being comparable to growth from major mergers at  $z < 1$ , and possibly surpassed by major mergers at  $z < 0.5$ . Stellar mass growth from minor mergers are found to be 2–3 times smaller than star-formation in the local Universe ( $z \sim 0$ ) but has not yet surpassed star-formation like major mergers.

The results from this work and the results of Chapter 5 indicate that although minor mergers contribute less stellar mass to intermediate mass galaxies relative to major mergers, they play a greater role in the size evolution of intermediate mass galaxies at  $z < 3$ . This is in contrast to more massive galaxies which are less affected by minor mergers. It is therefore imperative that merger histories are studied at

lower stellar mass and merger ratio regimes in the future.

Finally, the role of mergers in driving the observed size evolution of massive galaxies are explored. Upper limits are placed on the expected size increase from high to low redshift. Major mergers are found to be the dominant contribution to the size increase, with galaxies at  $> 10^{10} M_{\odot}$  expected to increase in size by 30–90% at  $z < 3.5$ , while the direct progenitors of local massive galaxies are expected to increase in size by 60% in this same time period. However, these growth factors scale as  $\sim (C_{\text{merg}})^{\alpha}$ , and so the considerable uncertainty on this quantity could allow for mergers to account for the vast majority of the size evolution if the value is significantly different to that chosen here. This uncertainty is much more pronounced for minor mergers due to the larger value of  $\alpha$ .

# Chapter 7

## Conclusions

This Thesis has presented work relating to the history of the most massive galaxies at  $z < 3.5$ . Specifically, it has described work that investigated methods which aim to connect populations of galaxies across cosmic time (Chapter 2); described modifications to a method which allows for the measurement of close-pair fractions for stellar mass-selected, flux-limited samples of galaxies (Chapter 3); and investigated the role of major and minor mergers in the stellar mass and size evolution of massive galaxies using the best constraints on the merger fractions and merger rates at  $z < 3.5$  (Chapter 4, Chapter 5 and Chapter 6). The main conclusions from the work presented in this Thesis are described below.

1. *The best method to trace the properties of galaxies forwards and backwards in time is through a selection at a constant cumulative number density in stellar mass.* Selecting galaxies above a constant stellar mass limit results in large (up to a factor of  $\sim 20$ ) systematics in estimations of the average stellar mass, star-formation rate and stellar mass density. Furthermore, the contamination of the sample increases exponentially with redshift. This is in stark contrast to a selection at a constant cumulative number density which recovers the same properties within a more acceptable factor of 2–3. Therefore, if one wishes to trace the true evolution of local (or high-redshift) galaxies backwards (forwards) in time, the best method is to use a selection at a constant number density. Additionally, velocity dispersion may be a better ranking indicator than stellar mass for future surveys. However this conclusion depends entirely on how true inferred simulation velocity dispersions are.
2. *Mergers occur much less frequently than previously thought resulting in a diminished capacity to drive the observed stellar mass and size evolution of massive galaxies.* Using the full redshift probability distributions afforded by

multi-wavelength SED fitting techniques, pair fractions are measured for three samples of galaxies at  $z < 3.5$ . Galaxies with masses  $> 10^{10} M_{\odot}$  are expected to undergo  $< 1$  merging event over the past 11 Gyr. Probing major and minor mergers separately reveals a suggestion of a mild dependence of the merger fraction on stellar mass. Major and minor merger pair fractions are similar for primary samples of  $> 10^{11} M_{\odot}$ , however the major merger pair fraction is a factor of  $\sim 2$  larger than the minor merger pair fraction for galaxies with  $> 10^{10} M_{\odot}$ .

3. *Star-formation remained the dominant source of stellar mass growth in massive galaxies up until the last 5 Gyr.* Comparison of sample-specific merger accretion rate density with the star-formation rate density revealed that the most massive galaxies have comparable stellar mass growth from the two channels at  $z < 0.5$ , while less massive galaxies have achieved similar ratios in the last  $\sim 2$  Gyr ( $z < 0.2$ ). Furthermore, major mergers provide  $10\times$  more stellar mass than minor mergers.
4. *Major and minor mergers are (probably) not the dominant source of the observed size evolution of massive elliptical galaxies.* Using simple virial theorem arguments it is found that mergers can increase the size of a typical massive early-type galaxy by, at most, a factor of 1.3, assuming dry mergers and no inefficiency due to dissipational processes.

## 7.1 Future work

The work presented in this Thesis results in further questions that require investigation, most of which could be achieved with the dataset in hand. These potential future avenues are discussed below.

Firstly, the method presented in Chapter 3 could be improved in several ways. Currently the method uses a single estimated stellar mass at every redshift. Modern SED-fitting techniques can provide the probability distribution of stellar mass through the conversion of  $\chi^2$  which could, in theory, provide  $P(\mathcal{M}_*|z)$ . Given sufficient computing power this information could be folded in to provide a more probabilistic measurement of the pair fraction, folding in the intrinsic uncertainty of the stellar mass estimation process. Additionally, further investigation is warranted into choice of certain parameters, e.g. Odds, which are assumed. As an example, the Odds parameter,  $\mathcal{O}$ , is assumed to be the same for each region however it is supposed to represent the typical uncertainty in photometric redshifts. While the

regions used in Chapter 4 and Chapter 5 have similar photometric redshift uncertainties, it would be prudent to explore this in more detail and ensure that the values do not significantly change.

Next, the data itself could be improved. Use of the latest data releases (e.g., UKIDSS UDS DR11 and UltraVISTA DR3) would allow smaller stellar mass regimes and higher redshift regimes to be probed. Further investigation into the possible systematic shift seen in the COSMOS region in Chapter 4 should be a priority. It may well be that the unprecedented multi-wavelength coverage (29 bands) results in systematically larger or smaller stellar mass estimates compared to surveys like the UKIDSS UDS (11 bands) which sample a smaller portion of a galaxy’s SED. This can be investigated by simply comparing estimated stellar masses using the whole filter set in COSMOS and a filter set similar to that used in the UDS and VIDEO regions.

Recent works have attempted to probe the connection between AGN and galaxy mergers. Some works conclude that AGN are primarily fuelled by merging events (e.g., Chiaberge *et al.*, 2015; Kaviraj *et al.*, 2015), while others do not (e.g., Ellison, Patton & Hickox, 2015). All of the surveys used in this work possess co-spatial X-ray and/or radio observations which can be used to identify AGN candidates. While extra SED templates would likely have to be added into the mix when estimating stellar masses and photometric redshifts for these objects (as they are likely not well fit using ‘normal’ galaxy SED templates), it would be possible to investigate the AGN fraction as a function of physical separation.

Another open question related to mergers between galaxies is whether and how mergers impact star formation in the host galaxy. Several works have investigated whether an excess in the star-formation rate of galaxies exists in close-pairs compared to field galaxies (e.g., Barton, Geller & Kenyon, 2000; Lin *et al.*, 2007; Ellison *et al.*, 2008), however these studies are confined to low redshift ( $z < 1$ ) and/or small sample sizes. Infra-red star-formation rate estimates, or those calculated through SED fitting, in the fields used in this thesis could allow for a more comprehensive probe into this matter.

As mentioned in Chapter 4, a shadow on any study of merger histories is the conversion of fractions to rates. The two parameters required to do so — the probability of a close-pair merging,  $C_{\text{merg}}$  and the observability time scale,  $T_{\text{obs}}$  — are still not well constrained. The most recent and arguably most complex simulations from which these parameters have been estimated (Lotz *et al.*, 2010) consider only a handful of simulated events due to their cost in terms of computing time and analysis. Furthermore, Lotz *et al.* explore these parameters only at  $z < 1.5$ . It

is therefore imperative for the entire field of mergers that further simulations are performed with larger sample sizes and at a wider range of redshifts. Until this is achieved, these two parameters will remain the dominant source of uncertainty in merger rate measurements.

Finally, the next two decades will revolutionise the study of galaxy formation and evolution. New telescopes, such as the James Webb Space Telescope (JWST), the new class of ground-based Extremely Large Telescopes (ELTs), and the Large Synoptic Survey Telescope (LSST), will provide an unprecedented window on the Universe. Not only will samples of galaxies increase by orders of magnitude or more, but study of the Universe's formative years ( $z \geq 3$ ) will be transformed. While each of these datasets — unimaginable by even the best astronomers a century ago — will be revolutionary in their own right, combining them will forever change the study of galaxy formation and evolution.



# Appendix A

## VIDEO completeness simulations

Comprehensive completeness simulations were performed on the VIDEO data in order to determine the completeness limit of the data. The VIDEO region provided exactly 1 square degree with pixel scale-matched photometry in the VIDEO near-IR ( $ZYJHK_s$ ) and CFHT-LS optical ( $ugriz$ ) filters. In order to calculate the completeness (i.e., the ability to recover sources) as a function of total  $K_s$ -band magnitude, areas of background were identified and stitched together in order to create a ‘noise’ image of the same dimensions as the image from which the catalogue is extracted. The image was then populated with realistic galaxy light profiles at random<sup>1</sup> positions, ensuring that the number density of sources is comparable to the real image. Galaxy properties from which the light profiles are derived are taken from those observed in the UKIDSS UDS DR8 data release, also used in this work. This provided complete distributions of galaxy structural parameters from which to sample. Profiles were generated using the *IRAF* `mkobjects` routine and are given total magnitudes within  $17 < m_{K_s} < 27$ , Sérsic (Sérsic, 1963) indices of  $0.5 < n < 8$  and sizes taken from the distribution seen in the UKIDSS UDS. SExtractor then analysed the image using the same parameters as used to construct the source catalogue. Comparing the input and extracted parameters, a source was considered ‘recovered’ if it is found within  $1''$  of its true position and 0.5 magnitudes of its input magnitude. This results in 95, 90, 80 and 50 per cent completeness limits of  $m_{K_s} = 21.5, 22.5, 23.1, 23.7$  AB, as seen in Figure A.1.

---

<sup>1</sup>This process used the `numpy.random` Python module which employs the Mersenne Twister algorithm for generating random numbers. Therefore these positions are strictly pseudo-random in nature.

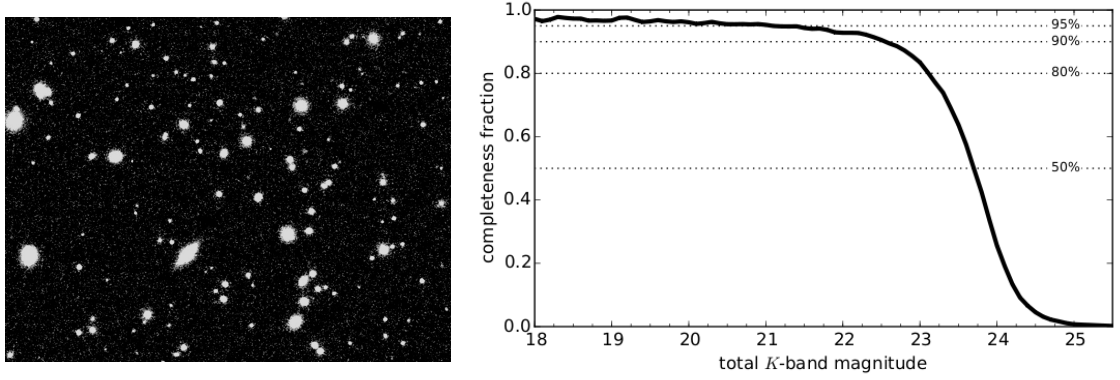


**Figure A.1:** *Left:* A typical simulated image (zoom in on a created in the comprehensive completeness simulations of the VIDEO  $K_s$ -band image using the method described in the text. *Right:* Completeness fraction as a function of total  $K_s$ -band magnitude. Horizontal dashed lines indicate the 95%, 90%, 80% and 50% completeness levels.

# Appendix B

## Supplementary minor merger pair fraction estimations

In this supplementary material, measurements of the total ( $\mu > 0.1$ ) and major ( $\mu > 0.25$ ) merger fractions are used to determine the minor ( $0.1 < \mu < 0.25$ ) major pair fraction using raw ‘counts’ of galaxies. As the pair fraction for a particular primary sample is defined as

$$f_{\text{pair}} = \frac{N_{\text{pair}}}{N_{\text{pri}}},$$

where  $N_{\text{pair}}$  is the number of close-pairs of galaxies and  $N_{\text{pri}}$  is the number of galaxies in the primary sample, it is trivial to show that the minor merger pair fraction can be written in terms of the total and major merger pair fractions as

$$f_{\text{minor}} = f_{\text{total}} - f_{\text{major}} = \frac{N_{\text{total}} - N_{\text{major}}}{N_{\text{pri}}}.$$

Using the values of  $N_{\text{total}}$  and  $N_{\text{major}}$  obtained in the measurements of the pair fraction (with **Pyrus**), the minor merger pair fraction is estimated along with its uncertainty.

Figure B.1 displays the total ( $\mu > 0.1$ ; upper panel) and major ( $\mu > 0.25$ ; middle panel), and derived minor ( $0.1 < \mu < 0.25$ ; bottom panel) pair fractions,  $f_{\text{pair}}$ , for galaxies with  $\mathcal{M}_* > 10^{11} \text{ M}_{\odot}$  and selected at separations of 5–30 kpc. The top two panels show the pair fractions calculated using the counts of pairs and counts of primary sample galaxies as discussed in Chapter 4. The bottom panel displays the inferred minor merger pair fraction as a function of redshift. The average value and uncertainties are estimated using distributions of  $N_{\text{pair}}$  and  $N_{\text{pri}}$  for total and major mergers. The total merger pair fraction is best fit as  $\propto (1 + z)^{1.0}$ , while the major

merger pair fraction is best fit as  $\propto (1+z)^{0.8}$ . The best-fit parameters are shown as a dashed grey curve. Additionally, the middle panel includes a dotted black curve which is the best fit parameters using data points over the same redshift regime as for the total and minor mergers. It can be seen that fitting of  $f_{\text{major}}(z)$  is not strongly dependent on the redshift range used, with  $f_0$  changing by 5% and the exponent,  $m$ , changing by 14%. Fitting the inferred minor merger pair fraction finds it  $\propto (1+z)^{1.1}$ . This is similar to the best fit exponent for  $f_{\text{total}}(z)$ . For this galaxy selection, the average ratio of  $f_{\text{major}}/f_{\text{minor}}$  is  $\sim 1.3$  at  $z < 2.5$ .

Pair fractions for intermediate mass ( $\mathcal{M}_* > 10^{10} \text{ M}_\odot$ ) galaxies are shown in Figure B.2. The total merger pair fraction is found to be best fit as  $\propto (1+z)^{2.1}$ , using measurements at  $z < 1$ . At  $z < 1.5$  the major merger pair fraction is best fit as  $\propto (1+z)^{2.1}$ , however if the data at  $z < 1$  is fit an 18% shallower slope and 11% larger  $f_0$  is found. These parameters are consistent with each other when their uncertainties are taken into account, something which is visually obvious in the middle panel of Figure B.2. Inferred  $f_{\text{minor}}$  values are best fit  $\propto (1+z)^{2.6}$ . The uncertainties on all these fitting parameters are large, however, due to the small redshift range available to fit over. At  $z < 1$ , the the major merger pair fraction is found to be  $\sim 2$  times larger than the minor merger pair fraction.

Figure B.3 displays the total, major and minor merger pair fractions for galaxies selected at a constant number density of  $10^{-4} \text{ Mpc}^{-3}$ . The total merger pair fraction is best fit as  $\propto (1+z)^{1.0}$ , rising from a pair fraction of 0.04 at  $z = 0$ . The major merger pair fraction is best fit as  $\propto (1+z)^{1.1}$  using the full set of available data, however the exponent decreases slightly to  $m = 0.9$  while  $f_0$  increases by 10% if the same redshift range as the total and minor merger pair fraction is used in fitting. Whichever fitting is used, the major merger pair fraction rises from a fraction of 0.02 at  $z = 0$ . The bottom panel of the Figure displays the inferred minor merger pair fraction which is found to rise from 0.02 at  $z = 0$  as  $\propto (1+z)^{0.7}$ . Comparing major and minor pair fractions from this sample, it is found that the major merger pair fraction is a factor of  $\sim 2$  larger than the minor merger pair fraction across the redshift range probed.

The method described here is an alternative way of estimating the minor merger pair fraction to that used in Chapter 5. No significant difference is found whether the power-law fits or the raw pair counts are used to estimate  $f_{\text{minor}}$  and these results are provided for completeness. It can be seen from these results, as in the main text, that matching redshift regimes during the fitting process results in power-law fitting parameters in agreement with each other, changing less than 20% depending on the galaxy selection. Generally, reducing the redshift range used for fitting results in a

larger  $f_0$  and a shallower slope, however all fitting parameters are consistent with each other. Finally, these results suggest there may be a slight mass dependence of the inferred minor merger pair fraction, with galaxies at smaller stellar masses possessing a steeper minor merger fraction.

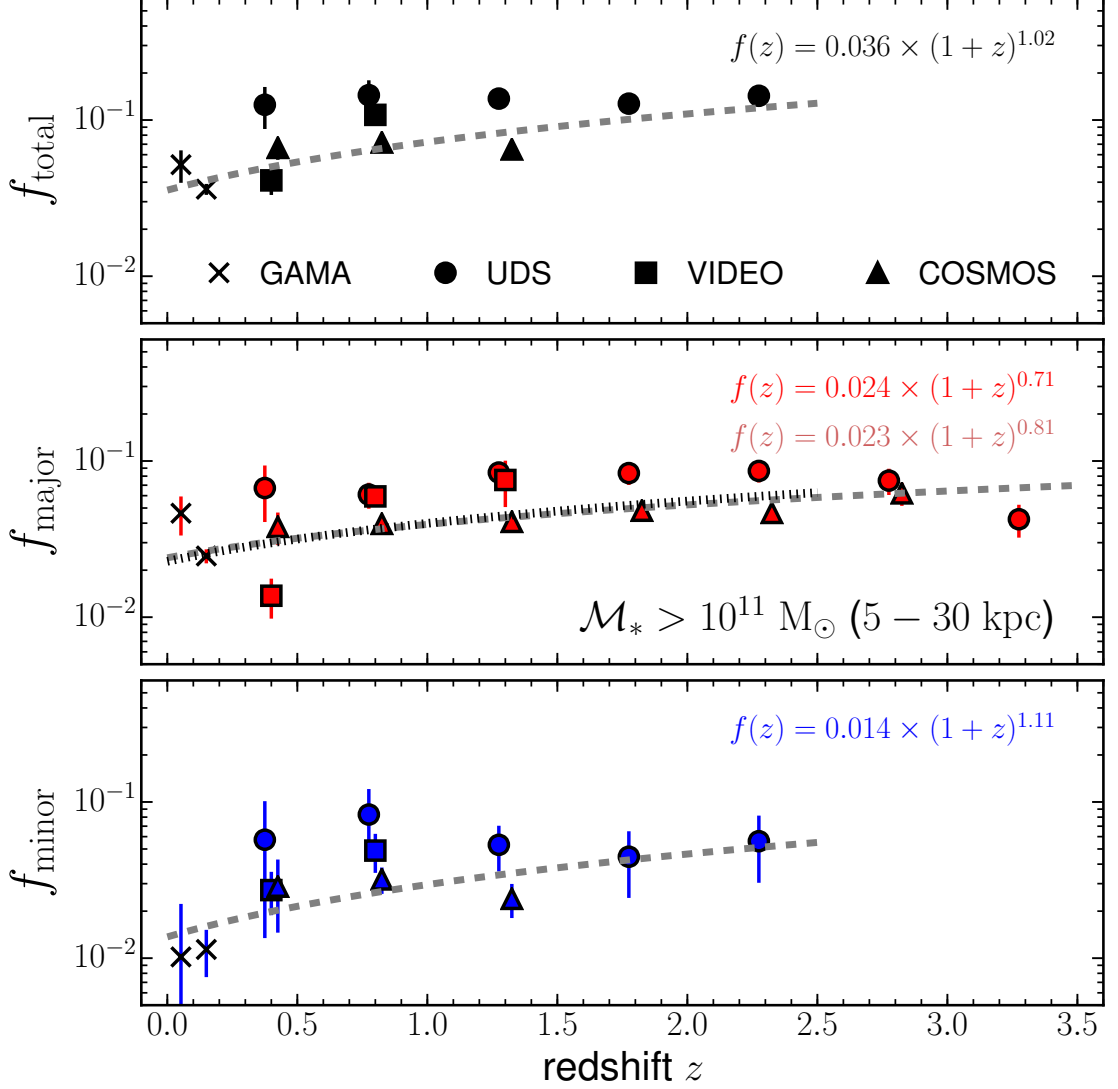


**Figure B.1:** Measured total ( $\mu > 0.1$ ; upper panel) and major ( $\mu > 0.25$ ; middle panel), and derived minor ( $0.1 < \mu < 0.25$ ; bottom panel) merger pair fractions,  $f_{\text{pair}}$ , for galaxies with  $\mathcal{M}_* > 10^{11} \text{ M}_\odot$  and selected at separations of 5–30 kpc. Points from the GAMA, UDS, VIDEO and COSMOS regions are given by crosses, circles, squares and triangles, respectively, in each panel. Dashed grey curves represent the best fitting power law fitting parameters, stated in the upper right of each panel. The dark grey fitting parameters and black dotted curve represent a fit of the major merger pair fraction at the same redshift range as the total and minor merger pair fraction.

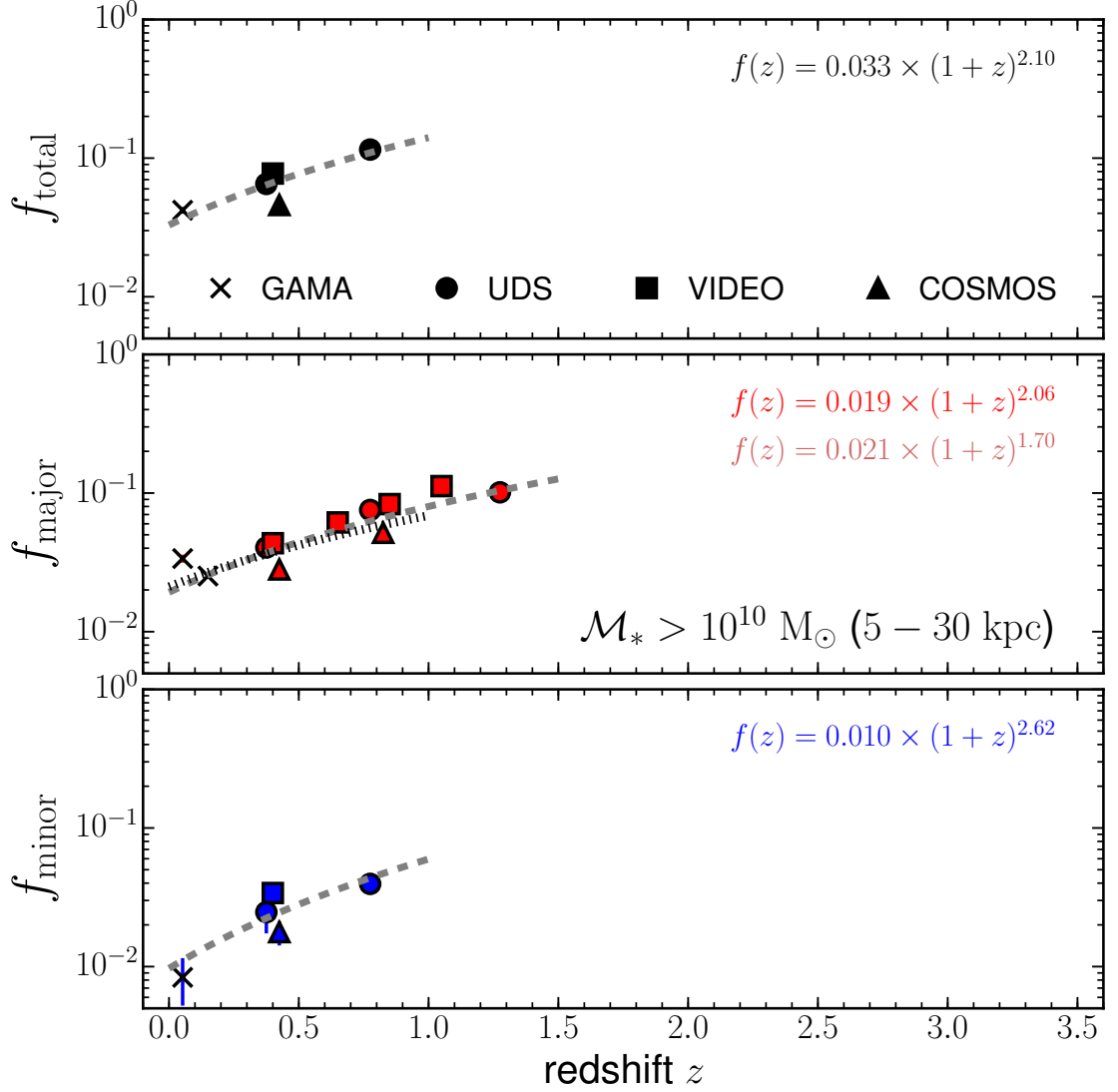


**Figure B.2:** Measured total ( $\mu > 0.1$ ; upper panel) and major ( $\mu > 0.25$ ; middle panel), and derived minor ( $0.1 < \mu < 0.25$ ; bottom panel) merger pair fractions,  $f_{\text{pair}}$ , for galaxies with  $\mathcal{M}_* > 10^{10} \text{ M}_\odot$  and selected at separations of 5–30 kpc. Points from the GAMA, UDS, VIDEO and COSMOS regions are given by crosses, circles, squares and triangles, respectively, in each panel. Dashed grey curves represent the best fitting power law fitting parameters, stated in the upper right of each panel. The dark grey fitting parameters and black dotted curve represent a fit of the major merger pair fraction at the same redshift range as the total and minor merger pair fraction.

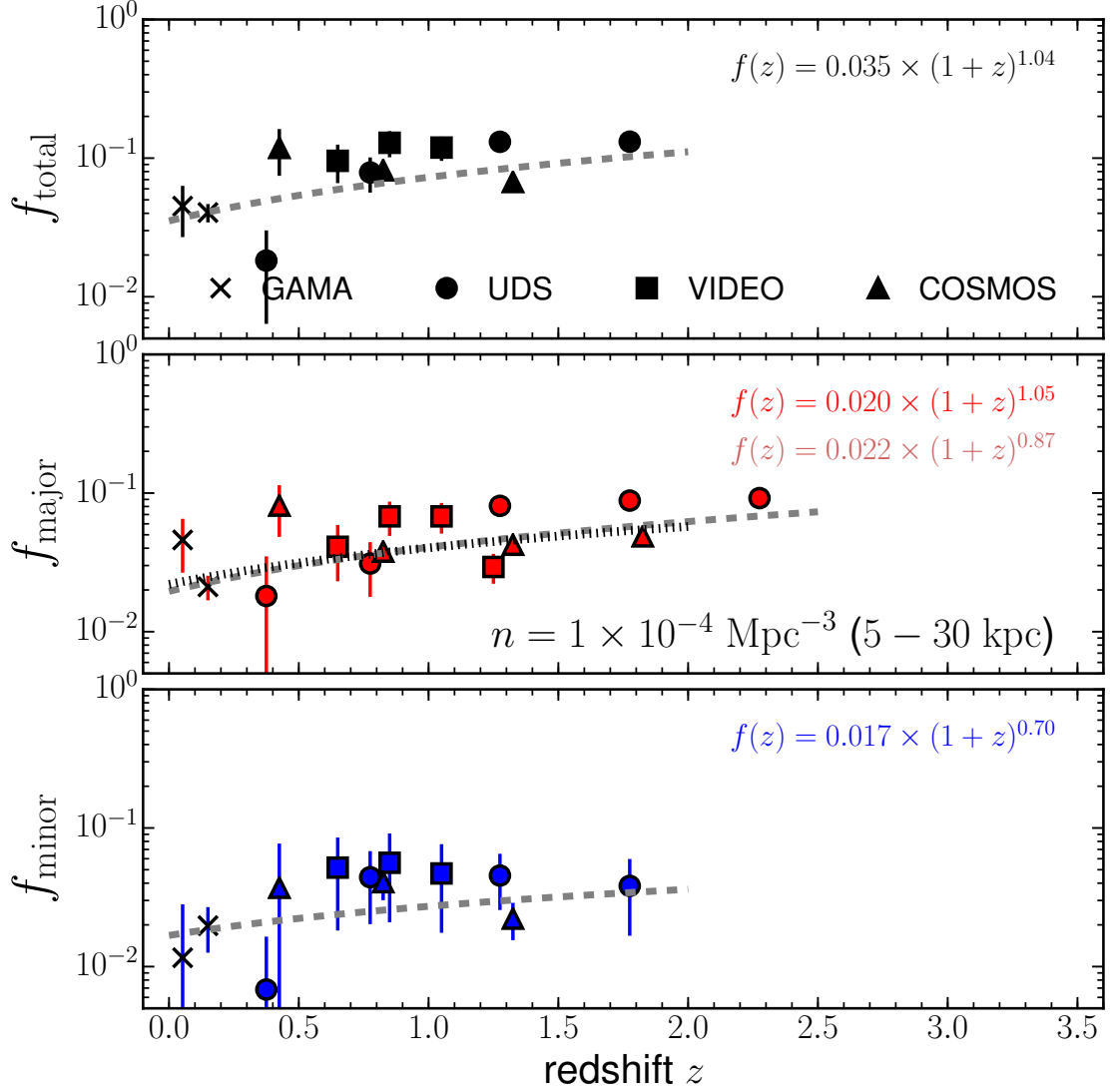


**Figure B.3:** Measured total ( $\mu > 0.1$ ; upper panel) and major ( $\mu > 0.25$ ; middle panel), and derived minor ( $0.1 < \mu < 0.25$ ; bottom panel) merger pair fractions,  $f_{\text{pair}}$ , for galaxies selected at  $n = 1 \times 10^{-4} \text{ Mpc}^{-3}$  and selected at separations of 5–30 kpc. Points from the GAMA, UDS, VIDEO and COSMOS regions are given by crosses, circles, squares and triangles, respectively, in each panel. Dashed grey curves represent the best fitting power law fitting parameters, stated in the upper right of each panel. The dark grey fitting parameters and black dotted curve represent a fit of the major merger pair fraction at the same redshift range as the total and minor merger pair fraction.



# Appendix C

## Additional SFR density estimates

The star-formation rate density estimates presented in Chapter 6 use the star-formation rate estimates of Muzzin *et al.* (2013a). These (UV + IR) star-formation rates are calculated by converting  $L_{2800}$  and  $L_{\text{IR}}$  which are estimated using template fitting techniques. This section presents alternative star-formation rate density estimates that use the catalogue presented in Laigle *et al.* (2016). The star-formation rates provided by this work are based on multi-wavelength SED fitting estimates from the COSMOS field, whereby galaxies are selected using deeper  $K$ -band photometry than used Chapter 6.

Figure presents estimates of the star-formation rate density,  $\rho_{\Psi}$ , the ratio between the star-formation rate density and the major merger accretion rate density, and the ratio between the star-formation rate density and the minor merger accretion rate density in the top, middle and bottom panels, respectively. Compared to the results in Chapter 6, the evolution of  $\rho_{\Psi}$  is much milder for the constant mass selections and are found to be approximately constant over the redshift range probed, however the typical normalisations are consistent. The evolution for the number density selection is much shallower than found in Chapter 6, however the average value is very similar.

Although the milder evolution of these quantities results in a milder evolution in the ratio between  $\rho_{\Psi}$  and the major and minor merger accretion rate density, the general conclusions drawn in Chapter 6 remain the same: Major mergers become comparable to star-formation in the build up of stellar mass at  $z < 0.5$ , while minor mergers are still approximately an order of magnitude smaller than star-formation at all redshifts probed.

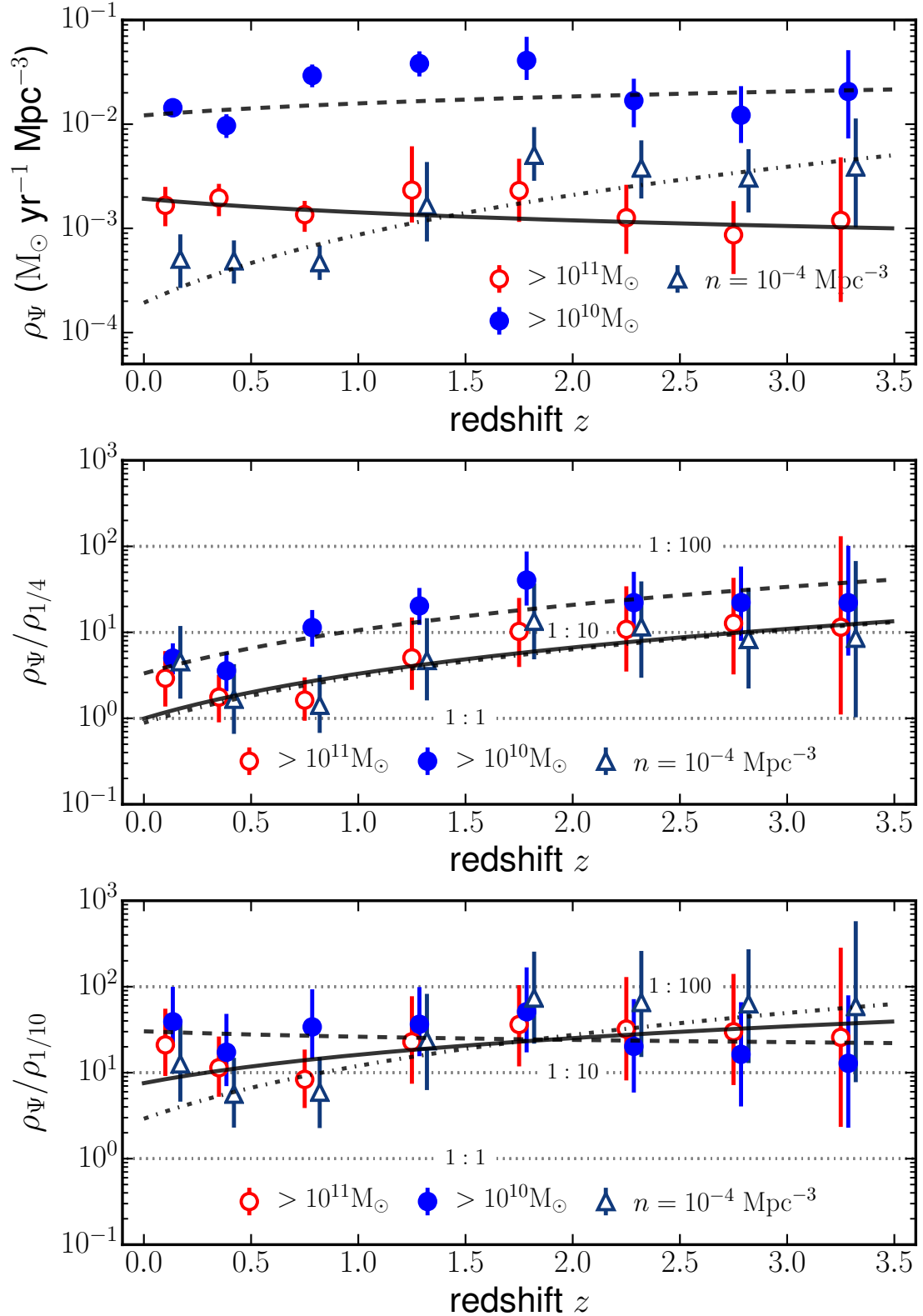


**Figure C.1:** Estimations of the star-formation rate density ( $\rho_\Psi$ ; top panel), the ratio of  $\rho_\Psi$  to the major merger accretion rate density ( $\rho_\Psi/\rho_{1/4}$ ; middle panel), and the ratio of  $\rho_\Psi$  to the minor merger accretion rate density ( $\rho_\Psi/\rho_{1/10}$ ; bottom panel) for galaxies with  $> 10^{11} M_\odot$  (red open circles),  $> 10^{10} M_\odot$  (blue filled circles), and at a constant cumulative number density of  $10^{-4} \text{ Mpc}^{-3}$  (blue open triangles). Fits to each of these are given by the solid, dashed and dashed-dotted lines in each panel, respectively. Horizontal dotted lines in the bottom panel indicate ratios of 100, 10 and 1.

# Bibliography

- Abraham R. G., Valdes F., Yee H. K. C., van den Bergh S., 1994. *The Astrophysical Journal*, **432**, 75.
- Abraham R. G., van den Bergh S., Nair P., 2003. *The Astrophysical Journal*, **588**(1), 218.
- Abramson L. E., Gladders M. D., Dressler A., Oemler A., Poggianti B., Vulcani B., 2015. *The Astrophysical Journal*, **801**(1), L12.
- Ade P. A. R., Aghanim N., Armitage-Caplan C., Arnaud M., Ashdown M., Atrio-Barandela F., Aumont J., Baccigalupi C., Banday A. J., Barreiro R. B., Bartlett J. G., Battaner E., Benabed K., Benoît A., Benoit-Lévy A., Bernard J.-P., Bersanelli M., Bielewicz P., Bobin J., Bock J. J., Bonaldi A., Bond J. R., Borrill J., Bouchet F. R., Bridges M., Bucher M., Burigana C., Butler R. C., Calabrese E., Cappellini B., Cardoso J.-F., Catalano A., Challinor A., Chamballu A., Chary R.-R., Chen X., Chiang H. C., Chiang L.-Y., Christensen P. R., Church S., Clements D. L., Colombi S., Colombo L. P. L., Couchot F., Coulais A., Crill B. P., Curto A., Cuttaia F., Danese L., Davies R. D., Davis R. J., de Bernardis P., de Rosa A., de Zotti G., Delabrouille J., Delouis J.-M., Désert F.-X., Dickinson C., Diego J. M., Dolag K., Dole H., Donzelli S., Doré O., Douspis M., Dunkley J., Dupac X., Efstathiou G., Elsner F., Enßlin T. A., Eriksen H. K., Finelli F., Forni O., Frailis M., Fraisse A. A., Franceschi E., Gaier T. C., Galeotta S., Galli S., Ganga K., Giard M., Giardino G., Giraud-Héraud Y., Gjerløw E., González-Nuevo J., Górski K. M., Gratton S., Gregorio A., Gruppuso A., Gudmundsson J. E., Haissinski J., Hamann J., Hansen F. K., Hanson D., Harrison D., Henrot-Versillé S., Hernández-Monteagudo C., Herranz D., Hildebrandt S. R., Hivon E., Hobson M., Holmes W. A., Hornstrup A., Hou Z., Hovest W., Hufenberger K. M., Jaffe A. H., Jaffe T. R., Jewell J., Jones W. C., Juvela M., Keihänen E., Keskitalo R., Kisner T. S., Kneissl R., Knoche J., Knox L., Kunz M., Kurki-Suonio H., Lagache G., Lähteenmäki A., Lamarre J.-M., Lasenby A., Lattanzi M., Laureijs R. J., Lawrence C. R., Leach S., Leahy J. P., Leonardi R.,

- León-Tavares J., Lesgourgues J., Lewis A., Liguori M., Lilje P. B., Linden-Vørnle M., López-Caniego M., Lubin P. M., Macías-Pérez J. F., Maffei B., Maino D., Mandolesi N., Maris M., Marshall D. J., Martin P. G., Martínez-González E., Masi S., Massardi M., Matarrese S., Matthai F., Mazzotta P., Meinhold P. R., Melchiorri A., Melin J.-B., Mendes L., Menegoni E., Mennella A., Migliaccio M., Millea M., Mitra S., Miville-Deschênes M.-A., Moneti A., Montier L., Morgante G., Mortlock D., Moss A., Munshi D., Murphy J. A., Naselsky P., Nati F., Natoli P., Netterfield C. B., Nørgaard-Nielsen H. U., Noviello F., Novikov D., Novikov I., ODwyer I. J., Osborne S., Oxborrow C. A., Paci F., Pagano L., Pajot F., Paladini R., Paoletti D., Partridge B., Pasian F., Patanchon G., Pearson D., Pearson T. J., Peiris H. V., Perdureau O., Perotto L., Perrotta F., Pettorino V., Piacentini F., Piat M., Pierpaoli E., Pietrobon D., Plaszczynski S., Platania P., Pointecouteau E., Polenta G., Ponthieu N., Popa L., Poutanen T., Pratt G. W., Prézeau G., Prunet S., Puget J.-L., Rachen J. P., Reach W. T., Rebolo R., Reinecke M., Remazeilles M., Renault C., Ricciardi S., Riller T., Ristorcelli I., Rocha G., Rosset C., Roudier G., Rowan-Robinson M., Rubiño-Martín J. A., Rusholme B., Sandri M., Santos D., Savelainen M., Savini G., Scott D., Seiffert M. D., Sheldard E. P. S., Spencer L. D., Starck J.-L., Stolyarov V., Stompor R., Sudiwala R., Sunyaev R., Sureau F., Sutton D., Suur-Uski A.-S., Sygnet J.-F., Tauber J. A., Tavagnacco D., Terenzi L., Toffolatti L., Tomasi M., Tristram M., Tucci M., Tuovinen J., Türlér M., Umama G., Valenziano L., Valiviita J., Van Tent B., Vielva P., Villa F., Vittorio N., Wade L. A., Wandelt B. D., Wehus I. K., White M., White S. D. M., Wilkinson A., Yvon D., Zacchei A., Zonca A., 2014. *Astronomy & Astrophysics*, **571**, A16.
- Arthur J., Pearce F. R., Gray M. E., Elahi P. J., Knebe A., Beck A. M., Cui W., Cunname D., Davé R., February S., Huang S., Katz N., Kay S. T., McCarthy I. G., Murante G., Perret V., Power C., Puchwein E., Saro A., Sembolini F., Teyssier R., Yepes G., 2016. *Monthly Notices of the Royal Astronomical Society*.
- Baldry I. K., Glazebrook K., Brinkmann J., Ivezić ., Lupton R. H., Nichol R. C., Szalay A. S., 2004. *The Astrophysical Journal*, **600(2)**, 681.
- Baldry I. K., Robotham A. S. G., Hill D. T., Driver S. P., Liske J., Norberg P., Bamford S. P., Hopkins A. M., Loveday J., Peacock J. A., Cameron E., Croom S. M., Cross N. J. G., Doyle I. F., Dye S., Frenk C. S., Jones D. H., van Kampen E., Kelvin L. S., Nichol R. C., Parkinson H. R., Popescu C. C., Prescott M., Sharp R. G., Sutherland W. J., Thomas D., Tuffs R. J., 2010. *Monthly Notices of the Royal Astronomical Society*, **404(1)**, 86.

- Baldry I. K., Driver S. P., Loveday J., Taylor E. N., Kelvin L. S., Liske J., Norberg P., Robotham A. S. G., Brough S., Hopkins A. M., Bamford S. P., Peacock J. A., Bland-Hawthorn J., Conselice C. J., Croom S. M., Jones D. H., Parkinson H. R., Popescu C. C., Prescott M., Sharp R. G., Tuffs R. J., 2012. *Monthly Notices of the Royal Astronomical Society*, **421**, no.
- Baldry I. K., Alpaslan M., Bauer A. E., Bland-Hawthorn J., Brough S., Cluver M. E., Croom S. M., Davies L. J. M., Driver S. P., Gunawardhana M. L. P., Holwerda B. W., Hopkins A. M., Kelvin L. S., Liske J., Lopez-Sanchez A. R., Loveday J., Norberg P., Peacock J., Robotham A. S. G., Taylor E. N., 2014. *Monthly Notices of the Royal Astronomical Society*, **441(3)**, 2440.
- Barnes J. E., Hernquist L., 1996. *The Astrophysical Journal*, **471(1)**, 115.
- Barton E. J., Geller M. J., Kenyon S. J., 2000. *The Astrophysical Journal*, **530(2)**, 660.
- Behroozi P. S., Marchesini D., Wechsler R. H., Muzzin A., Papovich C., Stefanon M., 2013. *The Astrophysical Journal*, **777(1)**, L10.
- Bell E. F., McIntosh D. H., Katz N., Weinberg M. D., 2003. *The Astrophysical Journal Supplement Series*, **149(2)**, 289.
- Bell E. F., Naab T., McIntosh D. H., Somerville R. S., Caldwell J. A. R., Barden M., Wolf C., Rix H.-W., Beckwith S. V., Borch A., Haussler B., Heymans C., Jahnke K., Jogee S., Koposov S., Meisenheimer K., Peng C. Y., Sanchez S. F., Wisotzki L., 2006. *The Astrophysical Journal*, **640(1)**, 241.
- Benitez N., 2000. *The Astrophysical Journal*, **536(2)**, 571.
- Bernardi M., Shankar F., Hyde J. B., Mei S., Marulli F., Sheth R. K., 2010. *Monthly Notices of the Royal Astronomical Society*, **404(4)**, 2087.
- Bershady M. A., Jangren A., Conselice C. J., 2000. *The Astronomical Journal*, **119(6)**, 2645.
- Bertone S., Conselice C. J., 2009. *Monthly Notices of the Royal Astronomical Society*, **396(4)**, 2345.
- Bezanson R., van Dokkum P. G., Tal T., Marchesini D., Kriek M., Franx M., Coppi P., 2009. *The Astrophysical Journal*, **697(2)**, 1290.

- Bezanson R., van Dokkum P., Franx M., 2012. *The Astrophysical Journal*, **760**(1), 62.
- Bluck A. F. L., Conselice C. J., Bouwens R. J., Daddi E., Dickinson M., Papovich C., Yan H., 2009. *Monthly Notices of the Royal Astronomical Society: Letters*, **394**(1), L51.
- Bluck A. F. L., Conselice C. J., Buitrago F., Grützbauch R., Hoyos C., Mortlock A., Bauer A. E., 2012. *The Astrophysical Journal*, **747**(1), 34.
- Bluck A. F. L., Mendel J. T., Ellison S. L., Moreno J., Simard L., Patton D. R., Starkenburg E., 2014. *Monthly Notices of the Royal Astronomical Society*, **441**(1), 599.
- Bouwens R. J., Illingworth G. D., Oesch P. A., Trenti M., Labbé I., Franx M., Stiavelli M., Carollo C. M., van Dokkum P., Magee D., 2012. *The Astrophysical Journal*, **752**(1), L5.
- Bower R. G., Benson A. J., Malbon R., Helly J. C., Frenk C. S., Baugh C. M., Cole S., Lacey C. G., 2006. *Monthly Notices of the Royal Astronomical Society*, **370**(2), 645.
- Bradshaw E. J., Almaini O., Hartley W. G., Smith K. T., Conselice C. J., Dunlop J. S., Simpson C., Chuter R. W., Cirasuolo M., Foucaud S., McLure R. J., Mortlock A., Pearce H., 2013. *Monthly Notices of the Royal Astronomical Society*, **433**(1), 194.
- Brammer G. B., van Dokkum P. G., Coppi P., 2008. *The Astrophysical Journal*, **686**(2), 1503.
- Bridge C. R., Appleton P. N., Conselice C. J., Choi P. I., Armus L., Fadda D., Laine S., Marleau F. R., Carlberg R. G., Helou G., Yan L., 2007. *The Astrophysical Journal*, **659**(2), 931.
- Bromm V., 2013. *Reports on Progress in Physics*, **76**(11), 112901.
- Bruce V. A., Dunlop J. S., McLure R. J., Cirasuolo M., Buitrago F., Bowler R. A. A., Targett T. A., Bell E. F., McIntosh D. H., Dekel A., Faber S. M., Ferguson H. C., Grogin N. A., Hartley W., Kocevski D. D., Koekemoer A. M., Koo D. C., McGrath E. J., 2014. *Monthly Notices of the Royal Astronomical Society*, **444**(2), 1001.

- Bruzual G., Charlot S., 2003. *Monthly Notices of the Royal Astronomical Society*, **344**(4), 1000.
- Buitrago F., Trujillo I., Conselice C. J., Bouwens R. J., Dickinson M., Yan H., 2008. *The Astrophysical Journal*, **687**(2), L61.
- Bundy K., Ellis R. S., Conselice C. J., Taylor J. E., Cooper M. C., Willmer C. N. A., Weiner B. J., Coil A. L., Noeske K. G., Eisenhardt P. R. M., 2006. *The Astrophysical Journal*, **651**(1), 120.
- Bundy K., Fukugita M., Ellis R. S., Targett T. A., Belli S., Kodama T., 2009. *The Astrophysical Journal*, **697**(2), 1369.
- Calzetti D., Armus L., Bohlin R. C., Kinney A. L., Koornneef J., StorchiBergmann T., 2000. *The Astrophysical Journal*, **533**(2), 682.
- Capak P., Aussel H., Ajiki M., McCracken H. J., Mobasher B., Scoville N., Shopbell P., Taniguchi Y., Thompson D., Tribiano S., Sasaki S., Blain A. W., Brusa M., Carilli C., Comastri A., Carollo C. M., Cassata P., Colbert J., Ellis R. S., Elvis M., Giavalisco M., Green W., Guzzo L., Hasinger G., Ilbert O., Impey C., Jahnke K., Kartaltepe J., Kneib J., Koda J., Koekemoer A., Komiyama Y., Leauthaud A., Lefevre O., Lilly S., Liu C., Massey R., Miyazaki S., Murayama T., Nagao T., Peacock J. A., Pickles A., Porciani C., Renzini A., Rhodes J., Rich M., Salvato M., Sanders D. B., Scarlata C., Schiminovich D., Schinnerer E., Scodeggio M., Sheth K., Shioya Y., Tasca L. A. M., Taylor J. E., Yan L., Zamorani G., 2007. *The Astrophysical Journal Supplement Series*, **172**(1), 99.
- Cappellari M., Bacon R., Bureau M., Damen M. C., Davies R. L., de Zeeuw P. T., Emsellem E., Falcon-Barroso J., Krajnovic D., Kuntschner H., McDermid R. M., Peletier R. F., Sarzi M., van den Bosch R. C. E., van de Ven G., 2006. *Monthly Notices of the Royal Astronomical Society*, **366**(4), 1126.
- Caputi K. I., Ilbert O., Laigle C., McCracken H. J., Le Fèvre O., Fynbo J., Milvang-Jensen B., Capak P., Salvato M., Taniguchi Y., 2015. *The Astrophysical Journal*, **810**(1), 73.
- Carlberg R. G., Pritchett C. J., Infante L., 1994. *The Astrophysical Journal*, **435**, 540.
- Chabrier G., 2003. *Publications of the Astronomical Society of the Pacific*, **115**(809), 763.

- Chiaberge M., Gilli R., Lotz J., Norman C., 2015. *The Astrophysical Journal*, **806(2)**, 147.
- Clowe D., Gonzalez A., Markevitch M., 2004. *The Astrophysical Journal*, **604(2)**, 596.
- Cole S., Aragon-Salamanca A., Frenk C. S., Navarro J. F., Zepf S. E., 1994. *Monthly Notices of the Royal Astronomical Society*, **271(4)**, 781.
- Cole S., Lacey C. G., Baugh C. M., Frenk C. S., 2002. *Monthly Notices of the Royal Astronomical Society*, **319(1)**, 168.
- Colless M., Dalton G., Maddox S., Sutherland W., Norberg P., Cole S., Bland-Hawthorn J., Bridges T., Cannon R., Collins C., Couch W., Cross N., Deeley K., De Propriis R., Driver S. P., Efsthathiou G., Ellis R. S., Frenk C. S., Glazebrook K., Jackson C., Lahav O., Lewis I., Lumsden S., Madgwick D., Peacock J. A., Peterson B. A., Price I., Seaborne M., Taylor K., 2001. *Monthly Notices of the Royal Astronomical Society*, **328(4)**, 1039.
- Conroy C., 2013. *Annual Review of Astronomy and Astrophysics*, **51(1)**, 393.
- Conselice C. J., Bershadsky M. A., Dickinson M., Papovich C., 2003. *The Astronomical Journal*, **126(3)**, 1183.
- Conselice C. J., Bundy K., Trujillo I., Coil A., Eisenhardt P., Ellis R. S., Georgakakis A., Huang J., Lotz J., Nandra K., Newman J., Papovich C., Weiner B., Willmer C., 2007. *Monthly Notices of the Royal Astronomical Society*, **381(3)**, 962.
- Conselice C. J., Mortlock A., Bluck A. F. L., Grutzbauch R., Duncan K., 2013. *Monthly Notices of the Royal Astronomical Society*, **430(2)**, 1051.
- Conselice C. J., Bluck A. F. L., Mortlock A., Palamara D., Benson A. J., 2014. *Monthly Notices of the Royal Astronomical Society*, **444(2)**, 1125.
- Conselice C. J., Rajgor S., Myers R., 2008. *Monthly Notices of the Royal Astronomical Society*, **386(2)**, 909.
- Conselice C. J., Yang C., Bluck A. F. L., 2009. *Monthly Notices of the Royal Astronomical Society*, **394(4)**, 1956.
- Conselice C. J., 2003. *The Astrophysical Journal Supplement Series*, **147(1)**, 1.
- Conselice C. J., 2006. *The Astrophysical Journal*, **638(2)**, 686.



- Conselice C. J., 2009. *Monthly Notices of the Royal Astronomical Society: Letters*, **399(1)**, L16.
- Conselice C. J., 2014. *Annual Review of Astronomy and Astrophysics*, **52(1)**, 291.
- Cowie L. L., Songaila A., Hu E. M., Cohen J. G., 1996. *The Astronomical Journal*, **112**, 839.
- Cox T. J., Dutta S. N., Di Matteo T., Hernquist L., Hopkins P. F., Robertson B., Springel V., 2006. *The Astrophysical Journal*, **650(2)**, 791.
- Crichton N. H. M., O'Meara J. M., Murphy M. T., 2016. *Monthly Notices of the Royal Astronomical Society: Letters*, **457(1)**, L44.
- Croton D. J., Springel V., White S. D. M., De Lucia G., Frenk C. S., Gao L., Jenkins A., Kauffmann G., Navarro J. F., Yoshida N., 2006. *Monthly Notices of the Royal Astronomical Society*, **365(1)**, 11.
- Curtis-Lake E., McLure R. J., Pearce H. J., Dunlop J. S., Cirasuolo M., Stark D. P., Almaini O., Bradshaw E. J., Chuter R., Foucaud S., Hartley W. G., 2012. *Monthly Notices of the Royal Astronomical Society*, **422(2)**, 1425.
- Daddi E., Renzini A., Pirzkal N., Cimatti A., Malhotra S., Stiavelli M., Xu C., Pasquali A., Rhoads J. E., Brusa M., di Serego Alighieri S., Ferguson H. C., Koekemoer A. M., Moustakas L. A., Panagia N., Windhorst R. A., 2005. *The Astrophysical Journal*, **626(2)**, 680.
- Dahlen T., Mobasher B., Faber S. M., Ferguson H. C., Barro G., Finkelstein S. L., Finlator K., Fontana A., Gruetzbauch R., Johnson S., Pforr J., Salvato M., Wiklind T., Wuyts S., Acquaviva V., Dickinson M. E., Guo Y., Huang J., Huang K.-H., Newman J. A., Bell E. F., Conselice C. J., Galametz A., Gawiser E., Gialaisco M., Grogin N. A., Hathi N., Kocevski D., Koekemoer A. M., Koo D. C., Lee K.-S., McGrath E. J., Papovich C., Peth M., Ryan R., Somerville R., Weiner B., Wilson G., 2013. *The Astrophysical Journal*, **775(2)**, 93.
- Damjanov I., McCarthy P. J., Abraham R. G., Glazebrook K., Yan H., Mentuch E., Le Borgne D., Savaglio S., Crampton D., Murowinski R., Juneau S., Carlberg R. G., Jørgensen I., Roth K., Chen H.-W., Marzke R. O., 2009. *The Astrophysical Journal*, **695(1)**, 101.
- De Lucia G., Blaizot J., 2006. *Monthly Notices of the Royal Astronomical Society*, **375(1)**, 2.

- De Propriis R., Conselice C. J., Liske J., Driver S. P., Patton D. R., Graham A. W., Allen P. D., 2007. *The Astrophysical Journal*, **666**(1), 212.
- de Ravel L., Le Fèvre O., Tresse L., Bottini D., Garilli B., Le Brun V., Maccagni D., Scaramella R., Scodeggio M., Vettolani G., Zanichelli A., Adami C., Arnouts S., Bardelli S., Bolzonella M., Cappi A., Charlot S., Ciliegi P., Contini T., Foucaud S., Franzetti P., Gavignaud I., Guzzo L., Ilbert O., Iovino A., Lamareille F., McCracken H. J., Marano B., Marinoni C., Mazure A., Meneux B., Merighi R., Paltani S., Pellò R., Pollo A., Pozzetti L., Radovich M., Vergani D., Zamorani G., Zucca E., Bondi M., Bongiorno A., Brinchmann J., Cucciati O., de la Torre S., Gregorini L., Memeo P., Perez-Montero E., Mellier Y., Merluzzi P., Tempurin S., 2009. *Astronomy and Astrophysics*, **498**(2), 379.
- Dekel A., Sari R., Ceverino D., 2009. *The Astrophysical Journal, Volume 703, Issue 1, pp. 785-801 (2009).*, **703**, 785.
- Driver S. P., Robotham A. S. G., 2010. *Monthly Notices of the Royal Astronomical Society*, **407**(4), 2131.
- Driver S. P., Norberg P., Baldry I. K., Bamford S. P., Hopkins A. M., Liske J., Loveday J., Peacock J. A., 2009. *Astronomy & Geophysics*, **50**(5), 12.
- Driver S. P., Hill D. T., Kelvin L. S., Robotham A. S. G., Liske J., Norberg P., Baldry I. K., Bamford S. P., Hopkins A. M., Loveday J., Peacock J. A., Andrae E., Bland-Hawthorn J., Brough S., Brown M. J. I., Cameron E., Ching J. H. Y., Colless M., Conselice C. J., Croom S. M., Cross N. J. G., De Propriis R., Dye S., Drinkwater M. J., Ellis S., Graham A. W., Grootes M. W., Gunawardhana M., Jones D. H., van Kampen E., Maraston C., Nichol R. C., Parkinson H. R., Phillipps S., Pimbblet K., Popescu C. C., Prescott M., Roseboom I. G., Sadler E. M., Sansom A. E., Sharp R. G., Smith D. J. B., Taylor E., Thomas D., Tuffs R. J., Wijesinghe D., Dunne L., Frenk C. S., Jarvis M. J., Madore B. F., Meyer M. J., Seibert M., Staveley-Smith L., Sutherland W. J., Warren S. J., 2011. *Monthly Notices of the Royal Astronomical Society*, **413**(2), 971.
- Duncan K., Conselice C. J., Mortlock A., Hartley W. G., Guo Y., Ferguson H. C., Dave R., Lu Y., Ownsworth J., Ashby M. L. N., Dekel A., Dickinson M., Faber S., Giavalisco M., Grogin N., Kocevski D., Koekemoer A., Somerville R. S., White C. E., 2014. *Monthly Notices of the Royal Astronomical Society*, **444**(3), 2960.
- Ellis R. S., Abraham R. G., Dickinson M., 2001. *The Astrophysical Journal*, **551**(1), 111.

- Ellison S. L., Patton D. R., Simard L., McConnachie A. W., 2008. *The Astronomical Journal*, **135(5)**, 1877.
- Ellison S. L., Patton D. R., Hickox R. C., 2015. *Monthly Notices of the Royal Astronomical Society: Letters*, **451(1)**, L35.
- Faber S. M., Jackson R. E., 1976. *The Astrophysical Journal*, **204**, 668.
- Fan L., Lapi A., De Zotti G., Danese L., 2008. *The Astrophysical Journal*, **689(2)**, L101.
- Ferreras I., Trujillo I., Mármol-Queraltó E., Pérez-González P., Cava A., Barro G., Cenarro J., Hernán-Caballero A., Cardiel N., Rodríguez-Zaurín J., Cebrián M., 2013. *Monthly Notices of the Royal Astronomical Society*, **444(1)**, 906.
- Fevre O. L., Vettolani G., Garilli B., Tresse L., Brun D. B. V. L., Maccagni D., Picat J. P., Scaramella R., Scodeggio M., Zanichelli A., Adami C., Bardelli S., Bolzonella M., Cappi A., Charlot S., Contini T., Foucaud S., Franzetti P., Gavi-gnaud I., Guzzo L., Ilbert O., Iovino A., McCracken H. J., Marano B., Marinoni C., Mathez G., Mazure A., Meneux B., Merighi R., Paltani S., Pellò R., Pollo A., Pozzetti L., Radovich M., Zamorani G., Zucca E., Bondi M., Bongiorno A., Busarello G., Ciliegi P., Mellier Y., Merluzzi P., Ripepi V., Rizzo D., 2004. *Astronomy and Astrophysics*, **439(3)**, 30.
- Fioc M., Rocca-Volmerange B., 1999. *eprint arXiv:astro-ph/9912179*.
- Freeman P. E., Izbicki R., Lee A. B., Newman J. A., Conselice C. J., Koekemoer A. M., Lotz J. M., Mozena M., 2013. *Monthly Notices of the Royal Astronomical Society*, **434(1)**, 282.
- Frenk C. S., White S. D. M., Davis M., Efstathiou G., 1988. *The Astrophysical Journal*, **327**, 507.
- Fumagalli M., Patel S. G., Franx M., Brammer G., van Dokkum P., da Cunha E., Kriek M., Lundgren B., Momcheva I., Rix H.-W., Schmidt K. B., Skelton R. E., Whitaker K. E., Labbe I., Nelson E., 2012. *The Astrophysical Journal*, **757(2)**, L22.
- Furlong M., Bower R. G., Theuns T., Schaye J., Crain R. A., Schaller M., Dalla Vecchia C., Frenk C. S., McCarthy I. G., Helly J., Jenkins A., Rosas-Guevara Y. M., 2015. *Monthly Notices of the Royal Astronomical Society*, **450(4)**, 4486.

- Furusawa H., Kosugi G., Akiyama M., Takata T., Sekiguchi K., Tanaka I., Iwata I., Kajisawa M., Yasuda N., Doi M., Ouchi M., Simpson C., Shimasaku K., Yamada T., Furusawa J., Morokuma T., Ishida C. M., Aoki K., Fuse T., Imanishi M., Iye M., Karoji H., Kobayashi N., Kodama T., Komiyama Y., Maeda Y., Miyazaki S., Mizumoto Y., Nakata F., Noumaru J., Ogasawara R., Okamura S., Saito T., Sasaki T., Ueda Y., Yoshida M., 2008. *The Astrophysical Journal Supplement Series*, **176(1)**, 1.
- Garilli B., Guzzo L., Scodeggio M., Bolzonella M., Abbas U., Adami C., Arnouts S., Bel J., Bottini D., Branchini E., Cappi A., Coupon J., Cucciati O., Davidzon I., De Lucia G., de la Torre S., Franzetti P., Fritz A., Fumana M., Granett B. R., Ilbert O., Iovino A., Krywult J., Le Brun V., Le Fèvre O., Maccagni D., Malek K., Marulli F., McCracken H. J., Paiono L., Polletta M., Pollo A., Schlagenhauser H., Tasca L. A. M., Tojeiro R., Vergani D., Zamorani G., Zanichelli A., Burden A., Di Porto C., Marchetti A., Marinoni C., Mellier Y., Moscardini L., Nichol R. C., Peacock J. A., Percival W. J., Phleps S., Wolk M., 2014. *Astronomy & Astrophysics*, **562**, A23.
- Genel S., Vogelsberger M., Springel V., Sijacki D., Nelson D., Snyder G., Rodriguez-Gomez V., Torrey P., Hernquist L., 2014. *Monthly Notices of the Royal Astronomical Society*, **445(1)**, 175.
- Graham A. W., Driver S. P., 2005. *Publications of the Astronomical Society of Australia*, **22(02)**, 118.
- Guo Q., White S., Boylan-Kolchin M., De Lucia G., Kauffmann G., Lemson G., Li C., Springel V., Weinmann S., 2011. *Monthly Notices of the Royal Astronomical Society*, **413(1)**, 101.
- Guo Q., White S., Angulo R. E., Henriques B., Lemson G., Boylan-Kolchin M., Thomas P., Short C., 2013. *Monthly Notices of the Royal Astronomical Society*, **428(2)**, 1351.
- Harker G., Cole S., Helly J., Frenk C., Jenkins A., 2006. *Monthly Notices of the Royal Astronomical Society*, **367(3)**, 1039.
- Hartley W. G., Almaini O., Mortlock A., Conselice C. J., Grutzbauch R., Simpson C., Bradshaw E. J., Chuter R. W., Foucaud S., Cirasuolo M., Dunlop J. S., McLure R. J., Pearce H. J., 2013. *Monthly Notices of the Royal Astronomical Society*, **431(4)**, 3045.

- Henriques B. M. B., White S. D. M., Thomas P. A., Angulo R., Guo Q., Lemson G., Springel V., Overzier R., 2015. *Monthly Notices of the Royal Astronomical Society*, **451**(3), 2663.
- Hildebrandt H., Wolf C., Benítez N., 2008. *Astronomy and Astrophysics*, **480**(3), 703.
- Hilz M., Naab T., Ostriker J. P., Thomas J., Burkert A., Jesseit R., 2012. *Monthly Notices of the Royal Astronomical Society*, **425**(4), 3119.
- Hilz M., Naab T., Ostriker J. P., 2013. *Monthly Notices of the Royal Astronomical Society*, **429**(4), 2924.
- Hopkins P. F., Croton D., Bundy K., Khochfar S., van den Bosch F., Somerville R. S., Wetzel A., Keres D., Hernquist L., Stewart K., Younger J. D., Genel S., Ma C.-P., 2010. *The Astrophysical Journal*, **724**(2), 915.
- Hopkins A. M., Driver S. P., Brough S., Owers M. S., Bauer A. E., Gunawardhana M. L. P., Cluver M. E., Colless M., Foster C., Lara-Lopez M. A., Roseboom I., Sharp R., Steele O., Thomas D., Baldry I. K., Brown M. J. I., Liske J., Norberg P., Robotham A. S. G., Bamford S., Bland-Hawthorn J., Drinkwater M. J., Loveday J., Meyer M., Peacock J. A., Tuffs R., Agius N., Alpaslan M., Andrae E., Cameron E., Cole S., Ching J. H. Y., Christodoulou L., Conselice C., Croom S., Cross N. J. G., De Propriis R., Delhaize J., Dunne L., Eales S., Ellis S., Frenk C. S., Graham A. W., Grootes M. W., Haussler B., Heymans C., Hill D., Hoyle B., Hudson M., Jarvis M., Johansson J., Jones D. H., van Kampen E., Kelvin L., Kuijken K., Lopez-Sanchez A., Maddox S., Madore B., Maraston C., McNaught-Roberts T., Nichol R. C., Oliver S., Parkinson H., Penny S., Phillipps S., Pimblet K. A., Ponman T., Popescu C. C., Prescott M., Proctor R., Sadler E. M., Sansom A. E., Seibert M., Staveley-Smith L., Sutherland W., Taylor E., Van Waerbeke L., Vazquez-Mata J. A., Warren S., Wijesinghe D. B., Wild V., Wilkins S., 2013. *Monthly Notices of the Royal Astronomical Society*, **430**(3), 2047.
- Hubble E. P., 1926. *The Astrophysical Journal*, **64**, 321.
- Ilbert O., Capak P., Salvato M., Aussel H., McCracken H. J., Sanders D. B., Scoville N., Kartaltepe J., Arnouts S., Flocc'h E. L., Mobasher B., Taniguchi Y., Lamareille F., Leauthaud A., Sasaki S., Thompson D., Zamojski M., Zamorani G., Bardelli S., Bolzonella M., Bongiorno A., Brusa M., Caputi K. I., Carollo C. M., Contini T., Cook R., Coppa G., Cucciati O., de la Torre S., de Ravel L., Franzetti P.,

- Garilli B., Hasinger G., Iovino A., Kampczyk P., Kneib J.-P., Knobel C., Kovac K., Le Borgne J. F., Le Brun V., Fèvre O. L., Lilly S., Looper D., Maier C., Mainieri V., Mellier Y., Mignoli M., Murayama T., Pellò R., Peng Y., Pérez-Montero E., Renzini A., Ricciardelli E., Schiminovich D., Scodeggio M., Shioya Y., Silverman J., Surace J., Tanaka M., Tasca L., Tresse L., Vergani D., Zucca E., 2009. *The Astrophysical Journal*, **690**(2), 1236.
- Ilbert O., Salvato M., Le Floch E., Aussel H., Capak P., McCracken H. J., Mobasher B., Kartaltepe J., Scoville N., Sanders D. B., Arnouts S., Bundy K., Cassata P., Kneib J.-P., Koekemoer A., Le Fèvre O., Lilly S., Surace J., Taniguchi Y., Tasca L., Thompson D., Tresse L., Zamojski M., Zamorani G., Zucca E., 2010. *The Astrophysical Journal*, **709**(2), 644.
- Ilbert O., McCracken H. J., Le Fèvre O., Capak P., Dunlop J., Karim A., Renzini M. A., Caputi K., Boissier S., Arnouts S., Aussel H., Comparat J., Guo Q., Hudelot P., Kartaltepe J., Kneib J. P., Krogager J. K., Le Floch E., Lilly S., Mellier Y., Milvang-Jensen B., Moutard T., Onodera M., Richard J., Salvato M., Sanders D. B., Scoville N., Silverman J. D., Taniguchi Y., Tasca L., Thomas R., Toft S., Tresse L., Vergani D., Wolk M., Zirm A., 2013. *Astronomy & Astrophysics*, **556**, A55.
- Jaacks J., Finkelstein S. L., Nagamine K., 2016. *The Astrophysical Journal*, **817**(2), 174.
- Jarvis M. J., Bonfield D. G., Bruce V. A., Geach J. E., McAlpine K., McLure R. J., Gonzalez-Solares E., Irwin M., Lewis J., Yoldas A. K., Andreon S., Cross N. J. G., Emerson J. P., Dalton G., Dunlop J. S., Hodgkin S. T., Le F. O., Karouzos M., Meisenheimer K., Oliver S., Rawlings S., Simpson C., Smail I., Smith D. J. B., Sullivan M., Sutherland W., White S. V., Zwart J. T. L., 2012. *Monthly Notices of the Royal Astronomical Society*, **428**(2), 1281.
- Javier Cenarro A., Trujillo I., 2009. *The Astrophysical Journal*, **696**(1), L43.
- Jenkins A., Frenk C. S., Pearce F. R., Thomas P. A., Colberg J. M., White S. D. M., Couchman H. M. P., Peacock J. A., Efstathiou G., Nelson A. H., 1997. *The Astrophysical Journal*, **499**, 20.
- Jogee S., Miller S. H., Penner K., Skelton R. E., Conselice C. J., Somerville R. S., Bell E. F., Zheng X. Z., Rix H.-W., Robaina A. R., Barazza F. D., Barden M., Borch A., Beckwith S. V. W., Caldwell J. A. R., Peng C. Y., Heymans C.,

- McIntosh D. H., Häußler B., Jahnke K., Meisenheimer K., Sanchez S. F., Wisotzki L., Wolf C., Papovich C., 2009. *The Astrophysical Journal*, **697(2)**, 1971.
- Karman W., Macciò A. V., Kannan R., Moster B. P., Somerville R. S., 2015. *Monthly Notices of the Royal Astronomical Society*, **452(3)**, 2984.
- Kartaltepe J. S., Sanders D. B., Scoville N. Z., Calzetti D., Capak P., Koekemoer A., Mobasher B., Murayama T., Salvato M., Sasaki S. S., Taniguchi Y., 2007. *The Astrophysical Journal Supplement Series*, **172(1)**, 320.
- Kauffmann G., Heckman T. M., Simon White D. M., Charlot S., Tremonti C., Brinchmann J., Bruzual G., Peng E. W., Seibert M., Bernardi M., Blanton M., Brinkmann J., Castander F., Csábai I., Fukugita M., Ivezić Z., Munn J. A., Nichol R. C., Padmanabhan N., Thakar A. R., Weinberg D. H., York D., 2003. *Monthly Notices of the Royal Astronomical Society*, **341(1)**, 33.
- Kauffmann G., White S. D. M., Guiderdoni B., 1993. *Monthly Notices of the Royal Astronomical Society*, **264(1)**, 201.
- Kaviraj S., Shabala S. S., Deller A. T., Middelberg E., 2015. *Monthly Notices of the Royal Astronomical Society*, **452(1)**, 774.
- Kelvin L. S., Driver S. P., Robotham A. S. G., Taylor E. N., Graham A. W., Alpaslan M., Baldry I., Bamford S. P., Bauer A. E., Bland-Hawthorn J., Brown M. J. I., Colless M., Conselice C. J., Holwerda B. W., Hopkins A. M., Lara-Lopez M. A., Liske J., Lopez-Sanchez A. R., Loveday J., Norberg P., Phillipps S., Popescu C. C., Prescott M., Sansom A. E., Tuffs R. J., 2014. *Monthly Notices of the Royal Astronomical Society*, **444(2)**, 1647.
- Kitzbichler M. G., White S. D. M., 2008. *Monthly Notices of the Royal Astronomical Society*, **391(4)**, 1489.
- Komatsu E., Smith K. M., Dunkley J., Bennett C. L., Gold B., Hinshaw G., Jarosik N., Larson D., Nolte M. R., Page L., Spergel D. N., Halpern M., Hill R. S., Kogut A., Limon M., Meyer S. S., Odegard N., Tucker G. S., Weiland J. L., Wollack E., Wright E. L., 2011. *The Astrophysical Journal Supplement Series*, **192(2)**, 18.
- Labbé I., Huang J., Franx M., Rudnick G., Barmby P., Daddi E., van Dokkum P. G., Fazio G. G., Schreiber N. M. F., Moorwood A. F. M., Rix H.-W., Röttgering H., Trujillo I., van der Werf P., 2005. *The Astrophysical Journal*, **624(2)**, L81.

- Lagos C. d. P., Lacey C. G., Baugh C. M., 2013. *Monthly Notices of the Royal Astronomical Society*, **436**(2), 1787.
- Laigle C., McCracken H. J., Ilbert O., Hsieh B. C., Davidzon I., Capak P., Hasinger G., Silverman J. D., Pichon C., Coupon J., Aussel H., Borgne D. L., Caputi K., Cassata P., Chang Y. Y., Civano F., Dunlop J., Fynbo J., kartaltepe J. S., Koekemoer A., Fevre O. L., Floc'h E. L., Leauthaud A., Lilly S., Lin L., Marchesi S., Milvang-Jensen B., Salvato M., Sanders D. B., Scoville N., Smolcic V., Stockmann M., Taniguchi Y., Tasca L., Toft S., Vaccari M., Zabl J., 2016.
- Lani C., Almaini O., Hartley W. G., Mortlock A., Haussler B., Chuter R. W., Simpson C., van der Wel A., Grutzbauch R., Conselice C. J., Bradshaw E. J., Cooper M. C., Faber S. M., Grogin N. A., Kocevski D. D., Koekemoer A. M., Lai K., 2013. *Monthly Notices of the Royal Astronomical Society*, **435**(1), 207.
- Lawrence A., Warren S. J., Almaini O., Edge A. C., Hambly N. C., Jameson R. F., Lucas P., Casali M., Adamson A., Dye S., Emerson J. P., Foucaud S., Hewett P., Hirst P., Hodgkin S. T., Irwin M. J., Lodieu N., McMahon R. G., Simpson C., Smail I., Mortlock D., Folger M., 2007. *Monthly Notices of the Royal Astronomical Society*, **379**(4), 1599.
- Le Fevre O., Abraham R., Lilly S. J., Ellis R. S., Brinchmann J., Schade D., Tresse L., Colless M., Crampton D., Glazebrook K., Hammer F., Broadhurst T., 2000. *Monthly Notices of the Royal Astronomical Society*, **311**(3), 565.
- Leja J., van Dokkum P., Franx M., 2013. *The Astrophysical Journal*, **766**(1), 33.
- Lemson G., Consortium t. V., 2006. *eprint arXiv:astro-ph/0608019*, **1**, 1.
- Lilly S. J., Fevre O. L., Renzini A., Zamorani G., Scodeggio M., Contini T., Carollo C. M., Hasinger G., Kneib J., Iovino A., Le Brun V., Maier C., Mainieri V., Mignoli M., Silverman J., Tasca L. A. M., Bolzonella M., Bongiorno A., Bottini D., Capak P., Caputi K., Cimatti A., Cucciati O., Daddi E., Feldmann R., Franzetti P., Garilli B., Guzzo L., Ilbert O., Kampczyk P., Kovac K., Lamareille F., Leauthaud A., Borgne J. L., McCracken H. J., Marinoni C., Pello R., Ricciardelli E., Scarlata C., Vergani D., Sanders D. B., Schinnerer E., Scoville N., Taniguchi Y., Arnouts S., Aussel H., Bardelli S., Brusa M., Cappi A., Ciliegi P., Finoguenov A., Foucaud S., Franceschini R., Halliday C., Impey C., Knobel C., Koekemoer A., Kurk J., Maccagni D., Maddox S., Marano B., Marconi G., Meneux B., Mobasher B., Moreau C., Peacock J. A., Porciani C., Pozzetti L., Scaramella R., Schiminovich D., Shopbell P., Smail I., Thompson D., Tresse L.,



- Vettolani G., Zanichelli A., Zucca E., 2007. *The Astrophysical Journal Supplement Series*, **172(1)**, 70.
- Lin L., Koo D. C., Willmer C. N. A., Patton D. R., Conselice C. J., Yan R., Coil A. L., Cooper M. C., Davis M., Faber S. M., Gerke B. F., Guhathakurta P., Newman J. A., 2004. *The Astrophysical Journal*, **617(1)**, L9.
- Lin L., Koo D. C., Weiner B. J., Chiueh T., Coil A. L., Lotz J., Conselice C. J., Willner S. P., Smith H. A., Guhathakurta P., Huang J.-S., Le Flo'c'h E., Noeske K. G., Willmer C. N. A., Cooper M. C., Phillips A. C., 2007. *The Astrophysical Journal*, **660(1)**, L51.
- Lin L., Patton D. R., Koo D. C., Casteels K., Conselice C. J., Faber S. M., Lotz J., Willmer C. N. A., Hsieh B. C., Chiueh T., Newman J. A., Novak G. S., Weiner B. J., Cooper M. C., 2008. *The Astrophysical Journal*, **681(1)**, 232.
- Lin Y.-T., Brodwin M., Gonzalez A. H., Bode P., Eisenhardt P. R. M., Stanford S. A., Vikhlinin A., 2013. *Astrophysical Journal*, **771(1)**, 6.
- Liske J., Baldry I. K., Driver S. P., Tuffs R. J., Alpaslan M., Andrae E., Brough S., Cluver M. E., Grootes M. W., Gunawardhana M. L. P., Kelvin L. S., Loveday J., Robotham A. S. G., Taylor E. N., Bamford S. P., Bland-Hawthorn J., Brown M. J. I., Drinkwater M. J., Hopkins A. M., Meyer M. J., Norberg P., Peacock J. A., Agius N. K., Andrews S. K., Bauer A. E., Ching J. H. Y., Colless M., Conselice C. J., Croom S. M., Davies L. J. M., De Propriis R., Dunne L., Eardley E. M., Ellis S., Foster C., Frenk C. S., Häußler B., Holwerda B. W., Howlett C., Ibarra H., Jarvis M. J., Jones D. H., Kafle P. R., Lacey C. G., Lange R., Lara-López M. A., López-Sánchez . R., Maddox S., Madore B. F., McNaught-Roberts T., Moffett A. J., Nichol R. C., Owers M. S., Palamara D., Penny S. J., Philipps S., Pimblet K. A., Popescu C. C., Prescott M., Proctor R., Sadler E. M., Sansom A. E., Seibert M., Sharp R., Sutherland W., Vázquez-Mata J. A., van Kampen E., Wilkins S. M., Williams R., Wright A. H., 2015. *Monthly Notices of the Royal Astronomical Society*, **452(2)**, 2087.
- López-Sanjuan C., Balcells M., Pérez-González P. G., Barro G., García-Dabó C. E., Gallego J., Zamorano J., 2009. *Astronomy and Astrophysics*, **501(2)**, 505.
- López-Sanjuan C., Le Fèvre O., de Ravel L., Cucciati O., Ilbert O., Tresse L., Bardelli S., Bolzonella M., Contini T., Garilli B., Guzzo L., Maccagni D., McCracken H. J., Mellier Y., Pollo A., Vergani D., Zucca E., 2011. *Astronomy & Astrophysics*, **530**, A20.

- López-Sanjuan C., Le Fèvre O., Ilbert O., Tasca L. A. M., Bridge C., Cucciati O., Kampezyk P., Pozzetti L., Xu C. K., Carollo C. M., Contini T., Kneib J.-P., Lilly S. J., Mainieri V., Renzini A., Sanders D., Scodeggio M., Scoville N. Z., Taniguchi Y., Zamorani G., Aussel H., Bardelli S., Bolzonella M., Bongiorno A., Capak P., Caputi K., de la Torre S., de Ravel L., Franzetti P., Garilli B., Iovino A., Knobel C., Kovač K., Lamareille F., Le Borgne J.-F., Le Brun V., Le Floch E., Maier C., McCracken H. J., Mignoli M., Pelló R., Peng Y., Pérez-Montero E., Presotto V., Ricciardelli E., Salvato M., Silverman J. D., Tanaka M., Tresse L., Vergani D., Zucca E., Barnes L., Bordoloi R., Cappi A., Cimatti A., Coppa G., Koekemoer A., Liu C. T., Moresco M., Nair P., Oesch P., Schawinski K., Welikala N., 2012. *Astronomy & Astrophysics*, **548**, A7.
- López-Sanjuan C., Le Fèvre O., Tasca L. A. M., Epinat B., Amram P., Contini T., Garilli B., Kissler-Patig M., Moutaka J., Paoro L., Perret V., Queyrel J., Tresse L., Vergani D., Divoy C., 2013. *Astronomy & Astrophysics*, **553**, A78.
- López-Sanjuan C., Cenarro A. J., Varela J., Viironen K., Molino A., Benítez N., Arnalte-Mur P., Ascaso B., Díaz-García L. A., Fernández-Soto A., Jiménez-Teja Y., Márquez I., Masegosa J., Moles M., Pović M., Aguerri J. A. L., Alfaro E., Aparicio-Villegas T., Broadhurst T., Cabrera-Caño J., Castander F. J., Cepa J., Cerviño M., Cristóbal-Hornillos D., Del Olmo A., González Delgado R. M., Husillos C., Infante L., Martínez V. J., Perea J., Prada F., Quintana J. M., 2015. *Astronomy & Astrophysics*, **576**, A53.
- Lotz J. M., Davis M., Faber S. M., Guhathakurta P., Gwyn S., Huang J., Koo D. C., Le Floch E., Lin L., Newman J., Noeske K., Papovich C., Willmer C. N. A., Coil A., Conselice C. J., Cooper M., Hopkins A. M., Metevier A., Primack J., Rieke G., Weiner B. J., 2008. *The Astrophysical Journal*, **672(1)**, 177.
- Lotz J. M., Jonsson P., Cox T. J., Primack J. R., 2010. *Monthly Notices of the Royal Astronomical Society*, **404(2)**, 575.
- Lotz J. M., Jonsson P., Cox T. J., Croton D., Primack J. R., Somerville R. S., Stewart K., 2011. *The Astrophysical Journal*, **742(2)**, 103.
- Lotz J. M., Primack J., Madau P., 2004. *The Astronomical Journal*, **128(1)**, 163.
- Lu Y., Wechsler R. H., Somerville R. S., Croton D., Porter L., Primack J., Behroozi P. S., Ferguson H. C., Koo D. C., Guo Y., Safarzadeh M., Finlator K., Castellano M., White C. E., Sommariva V., Moody C., 2014. *The Astrophysical Journal*, **795(2)**, 123.

- Madau P., Dickinson M., 2014. *Annual Review of Astronomy and Astrophysics*, **52(1)**, 415.
- Magnelli B., Popesso P., Berta S., Pozzi F., Elbaz D., Lutz D., Dickinson M., Altieri B., Andreani P., Aussel H., Béthermin M., Bongiovanni A., Cepa J., Charmandaris V., Chary R.-R., Cimatti A., Daddi E., Förster Schreiber N. M., Genzel R., Gruppioni C., Harwit M., Hwang H. S., Ivison R. J., Magdis G., Maiolino R., Murphy E., Nordon R., Pannella M., Pérez García A., Poglitsch A., Rosario D., Sanchez-Portal M., Santini P., Scott D., Sturm E., Tacconi L. J., Valtchanov I., 2013. *Astronomy & Astrophysics*, **553**, A132.
- Maller A. H., Katz N., Kereš D., Dave R., Weinberg D. H., 2006. *The Astrophysical Journal*, **647(2)**, 763.
- Man A. W. S., Toft S., Zirm A. W., Wuyts S., van der Wel A., 2012. *The Astrophysical Journal*, **744(2)**, 85.
- Man A. W. S., Zirm A. W., Toft S., 2014. *eprint arXiv:1410.3479*.
- Maraston C., Pforr J., Renzini A., Daddi E., Dickinson M., Cimatti A., Tonini C., 2010. *Monthly Notices of the Royal Astronomical Society*, **407(2)**, 830.
- Maraston C., 2005. *Monthly Notices of the Royal Astronomical Society*, **362(3)**, 799.
- Marchesini D., van Dokkum P. G., Förster Schreiber N. M., Franx M., Labbé I., Wuyts S., 2009. *The Astrophysical Journal*, **701(2)**, 1765.
- Marchesini D., Muzzin A., Stefanon M., Franx M., Brammer G. G., Marsan C. Z., Vulcani B., Fynbo J. P. U., Milvang-Jensen B., Dunlop J. S., Buitrago F., 2014. *The Astrophysical Journal*, **794(1)**, 65.
- Markevitch M., Gonzalez A. H., Clowe D., Vikhlinin A., Forman W., Jones C., Murray S., Tucker W., 2004. *The Astrophysical Journal*, **606(2)**, 819.
- Martin D. C., Fanson J., Schiminovich D., Morrissey P., Friedman P. G., Barlow T. A., Conrow T., Grange R., Jelinsky P. N., Milliard B., Siegmund O. H. W., Bianchi L., Byun Y.-I., Donas J., Forster K., Heckman T. M., Lee Y.-W., Madore B. F., Malina R. F., Neff S. G., Rich R. M., Small T., Surber F., Szalay A. S., Welsh B., Wyder T. K., 2005. *The Astrophysical Journal*, **619(1)**, L1.

- Martinez-Manso J., Guzman R., Barro G., Cenarro J., Perez-Gonzalez P., Sanchez-Blazquez P., Trujillo I., Balcells M., Cardiel N., Gallego J., Hempel A., Prieto M., 2011. *The Astrophysical Journal*, **738**(2), L22.
- McCracken H. J., Milvang-Jensen B., Dunlop J., Franx M., Fynbo J. P. U., Le Fèvre O., Holt J., Caputi K. I., Goranova Y., Buitrago F., Emerson J. P., Freudling W., Hudelot P., López-Sanjuan C., Magnard F., Mellier Y., Møller P., Nilsson K. K., Sutherland W., Tasca L., Zabl J., 2012. *Astronomy & Astrophysics*, **544**, A156.
- McLure R. J., Pearce H. J., Dunlop J. S., Cirasuolo M., Curtis-Lake E., Bruce V. A., Caputi K. I., Almaini O., Bonfield D. G., Bradshaw E. J., Buitrago F., Chuter R., Foucaud S., Hartley W. G., Jarvis M. J., 2013. *Monthly Notices of the Royal Astronomical Society*, **428**(2), 1088.
- Mihos J. C., Hernquist L., 1996. *The Astrophysical Journal*, **464**, 641.
- Mihos J. C., 1995. *The Astrophysical Journal*, **438**, L75.
- Molino A., Benitez N., Moles M., Fernandez-Soto A., Cristobal-Hornillos D., Ascaso B., Jimenez-Teja Y., Schoenell W., Arnalte-Mur P., Povi M., Coe D., Lopez-Sanjuan C., Diaz-Garcia L. A., Varela J., Stefanon M., Cenarro J., Matute I., Masegosa J., Marquez I., Perea J., Del Olmo A., Husillos C., Alfaro E., Aparicio-Villegas T., Cervino M., Huertas-Company M., Aguerri J. A. L., Broadhurst T., Cabrera-Cano J., Cepa J., Gonzalez R. M., Infante L., Martinez V. J., Prada F., Quintana J. M., 2014. *Monthly Notices of the Royal Astronomical Society*, **441**(4), 2891.
- Mortlock A., Conselice C. J., Bluck A. F. L., Bauer A. E., Grützbauch R., Buitrago F., Ownsworth J., 2011. *Monthly Notices of the Royal Astronomical Society*, **413**(4), 2845.
- Mortlock A., Conselice C. J., Hartley W. G., Ownsworth J. R., Lani C., Bluck A. F. L., Almaini O., Duncan K., Wel A. v. d., Koekemoer A. M., Dekel A., Dave R., Ferguson H. C., de Mello D. F., Newman J. A., Faber S. M., Grogin N. A., Kocevski D. D., Lai K., 2013. *Monthly Notices of the Royal Astronomical Society*, **433**(2), 1185.
- Mortlock A., Conselice C. J., Hartley W. G., Duncan K., Lani C., Ownsworth J. R., Almaini O., Wel A. v. d., Huang K.-H., Ashby M. L. N., Willner S. P., Fontana A., Dekel A., Koekemoer A. M., Ferguson H. C., Faber S. M., Grogin

- N. A., Kocevski D. D., 2015. *Monthly Notices of the Royal Astronomical Society*, **447(1)**, 2.
- Mortlock A., Conselice C. J., Hartley W. G., Duncan K., Lani C., Ownsworth J. R., Almaini O., van der Wel A., Huang K.-H., Ashby M. L. N., Willner S. P., Fontana A., Dekel A., Koekemoer A. M., Ferguson H. C., Faber S. M., Grogin N. A., Kocevski D. D., 2016. *Monthly Notices of the Royal Astronomical Society*, **458(4)**, 3478.
- Moster B. P., Somerville R. S., Newman J. A., Rix H.-W., 2011. *The Astrophysical Journal*, **731(2)**, 113.
- Mundy C. J., Conselice C. J., Ownsworth J. R., 2015. *Monthly Notices of the Royal Astronomical Society*, **450(4)**, 3696.
- Muzzin A., Marchesini D., Stefanon M., Franx M., McCracken H. J., Milvang-Jensen B., Dunlop J. S., Fynbo J. P. U., Brammer G., Labbé I., van Dokkum P. G., 2013a. *The Astrophysical Journal*, **777(1)**, 18.
- Muzzin A., Marchesini D., Stefanon M., Franx M., Milvang-Jensen B., Dunlop J. S., Fynbo J. P. U., Brammer G., Labbé I., van Dokkum P., 2013b. *The Astrophysical Journal Supplement Series*, **206(1)**, 8.
- Naab T., Johansson P. H., Ostriker J. P., 2009. *The Astrophysical Journal*, **699(2)**, L178.
- Newman A. B., Ellis R. S., Bundy K., Treu T., 2012. *The Astrophysical Journal*, **746(2)**, 162.
- Oke J. B., Gunn J. E., 1983. *The Astrophysical Journal*, **266**, 713.
- Onodera M., Renzini A., Carollo M., Cappellari M., Mancini C., Strazzullo V., Daddi E., Arimoto N., Gobat R., Yamada Y., McCracken H. J., Ilbert O., Capak P., Cimatti A., Giavalisco M., Koekemoer A. M., Kong X., Lilly S., Motohara K., Ohta K., Sanders D. B., Scoville N., Tamura N., Taniguchi Y., 2012. *The Astrophysical Journal*, **755(1)**, 26.
- Oser L., Naab T., Ostriker J. P., Johansson P. H., 2012. *The Astrophysical Journal*, **744(1)**, 63.
- Ownsworth J. R., Conselice C. J., Mortlock A., Hartley W. G., Buitrago F., 2012. *Monthly Notices of the Royal Astronomical Society, Volume 426, Issue 1, pp. 764-778.*, **426**, 764.

- Owensworth J. R., Conselice C. J., Mortlock A., Hartley W. G., Almaini O., Duncan K., Mundy C. J., 2014. *Monthly Notices of the Royal Astronomical Society*, **445**(3), 2198.
- Owensworth J. R., Conselice C. J., Mundy C. J., Mortlock A., Hartley W. G., Duncan K., Almaini O., 2016. *eprint arXiv:1605.05741*.
- Papovich C., Finkelstein S. L., Ferguson H. C., Lotz J. M., Giavalisco M., 2010. *Monthly Notices of the Royal Astronomical Society*, **412**(2).
- Papovich C., Finkelstein S. L., Ferguson H. C., Lotz J. M., Giavalisco M., 2011. *Monthly Notices of the Royal Astronomical Society*, **412**(2), 1123.
- Patton D. R., Atfield J. E., 2008. *The Astrophysical Journal*, **685**(1), 235.
- Patton D. R., Pritchett C. J., Yee H. K. C., Ellingson E., Carlberg R. G., 1997. *The Astrophysical Journal*, **475**(1), 29.
- Patton D. R., Carlberg R. G., Marzke R. O., Pritchett C. J., da Costa L. N., Pellegrini P. S., 2000. *The Astrophysical Journal*, **536**(1), 153.
- Patton D. R., Pritchett C. J., Carlberg R. G., Marzke R. O., Yee H. K. C., Hall P. B., Lin H., Morris S. L., Sawicki M., Shepherd C. W., Wirth G. D., 2002. *The Astrophysical Journal*, **565**(1), 208.
- Pawlik M. M., Wild V., Walcher C. J., Johansson P. H., Villforth C., Rowlands K., Mendez-Abreu J., Hewlett T., 2016. *Monthly Notices of the Royal Astronomical Society*, **456**(3), 3032.
- Peebles P. J. E., 1970. *The Astronomical Journal*, **75**, 13.
- Peng Y.-j., Lilly S. J., Kovač K., Bolzonella M., Pozzetti L., Renzini A., Zamorani G., Ilbert O., Knobel C., Iovino A., Maier C., Cucciati O., Tasca L., Carollo C. M., Silverman J., Kampeczyk P., de Ravel L., Sanders D., Scoville N., Contini T., Mainieri V., Scodeggio M., Kneib J.-P., Le Fèvre O., Bardelli S., Bongiorno A., Caputi K., Coppa G., de la Torre S., Franzetti P., Garilli B., Lamareille F., Le Borgne J.-F., Le Brun V., Mignoli M., Montero E. P., Pello R., Ricciardelli E., Tanaka M., Tresse L., Vergani D., Welikala N., Zucca E., Oesch P., Abbas U., Barnes L., Bordoloi R., Bottini D., Cappi A., Cassata P., Cimatti A., Fumana M., Hasinger G., Koekemoer A., Leauthaud A., Maccagni D., Marinoni C., McCracken H., Memeo P., Meneux B., Nair P., Porciani C., Presotto V., Scaramella R., 2010. *The Astrophysical Journal*, **721**(1), 193.

Penzias A. A., Wilson R. W., 1965. *The Astrophysical Journal*, **142**, 419.

Pérez-González P. G., Cava A., Barro G., Villar V., Cardiel N., Ferreras I., Rodríguez-Espinosa J. M., Alonso-Herrero A., Balcells M., Cenarro J., Cepa J., Charlot S., Cimatti A., Conselice C. J., Daddi E., Donley J., Elbaz D., Espino N., Gallego J., Gobat R., González-Martín O., Guzmán R., Hernán-Caballero A., Muñoz-Tuñón C., Renzini A., Rodríguez-Zaurín J., Tresse L., Trujillo I., Zamorano J., 2013. *The Astrophysical Journal*, **762**(1), 46.

Perlmutter S., Aldering G., Valle M. D., Deustua S., Ellis R. S., Fabbro S., Fruchter A., Goldhaber G., Groom D. E., Hook I. M., Kim A. G., Kim M. Y., Knop R. A., Lidman C., McMahon R. G., Nugent P., Pain R., Panagia N., Pennypacker C. R., Ruiz-Lapuente P., Schaefer B., Walton N., 1998. *Nature*, **391**(6662), 51.

Planck Collaboration, Ade P. A. R., Aghanim N., Arnaud M., Ashdown M., Aumont J., Baccigalupi C., Banday A. J., Barreiro R. B., Bartlett J. G., Bartolo N., Battaner E., Battye R., Benabed K., Benoit A., Benoit-Levy A., Bernard J.-P., Bersanelli M., Bielewicz P., Bonaldi A., Bonavera L., Bond J. R., Borrill J., Bouchet F. R., Boulanger F., Bucher M., Burigana C., Butler R. C., Calabrese E., Cardoso J.-F., Catalano A., Challinor A., Chamballu A., Chary R.-R., Chiang H. C., Chluba J., Christensen P. R., Church S., Clements D. L., Colombi S., Colombo L. P. L., Combet C., Coulais A., Crill B. P., Curto A., Cuttaia F., Danese L., Davies R. D., Davis R. J., de Bernardis P., de Rosa A., de Zotti G., Delabrouille J., Desert F.-X., Di Valentino E., Dickinson C., Diego J. M., Dolag K., Dole H., Donzelli S., Dore O., Douspis M., Ducout A., Dunkley J., Dupac X., Efstathiou G., Elsner F., Ensslin T. A., Eriksen H. K., Farhang M., Fergusson J., Finelli F., Forni O., Frailis M., Fraisse A. A., Franceschi E., Frejsel A., Galeotta S., Galli S., Ganga K., Gauthier C., Gerbino M., Ghosh T., Giard M., Giraud-Heraud Y., Giusarma E., Gjerlow E., Gonzalez-Nuevo J., Gorski K. M., Gratton S., Gregorio A., Gruppuso A., Gudmundsson J. E., Hamann J., Hansen F. K., Hanson D., Harrison D. L., Helou G., Henrot-Versille S., Hernandez-Monteagudo C., Herranz D., Hildebrandt S. R., Hivon E., Hobson M., Holmes W. A., Hornstrup A., Hovest W., Huang Z., Huppenberger K. M., Hurier G., Jaffe A. H., Jaffe T. R., Jones W. C., Juvela M., Keihänen E., Keskitalo R., Kisner T. S., Kneissl R., Knoch J., Knox L., Kunz M., Kurki-Suonio H., Lagache G., Lahteenmaki A., Lamarre J.-M., Lasenby A., Lattanzi M., Lawrence C. R., Leahy J. P., Leonardi R., Lesgourgues J., Levrier F., Lewis A., Liguori M., Lilje P. B., Linden-Vornle M., Lopez-Caniego M., Lubin P. M., Macias-Perez J. F., Maggio G., Maino D., Mandolesi N., Mangilli A., Marchini A., Martin P. G., Martinelli M., Martinez-

Gonzalez E., Masi S., Matarrese S., Mazzotta P., McGehee P., Meinhold P. R., Melchiorri A., Melin J.-B., Mendes L., Mennella A., Migliaccio M., Millea M., Mitra S., Miville-Deschenes M.-A., Moneti A., Montier L., Morgante G., Mortlock D., Moss A., Munshi D., Murphy J. A., Naselsky P., Nati F., Natoli P., Netterfield C. B., Norgaard-Nielsen H. U., Noviello F., Novikov D., Novikov I., Oxborrow C. A., Paci F., Pagano L., Pajot F., Paladini R., Paoletti D., Partridge B., Pasian F., Patanchon G., Pearson T. J., Perdureau O., Perotto L., Perrotta F., Pettorino V., Piacentini F., Piat M., Pierpaoli E., Pietrobon D., Plaszczyński S., Pointecouteau E., Polenta G., Popa L., Pratt G. W., Prezeau G., Prunet S., Puget J.-L., Rachen J. P., Reach W. T., Rebolo R., Reinecke M., Remazeilles M., Renault C., Renzi A., Ristorcelli I., Rocha G., Rosset C., Rossetti M., Roudier G., Rouille d'Orfeuil B., Rowan-Robinson M., Rubino-Martin J. A., Rusholme B., Said N., Salvatelli V., Salvati L., Sandri M., Santos D., Savelainen M., Savini G., Scott D., Seiffert M. D., Serra P., Shellard E. P. S., Spencer L. D., Spinelli M., Stolyarov V., Stompor R., Sudiwala R., Sunyaev R., Sutton D., Suur-Uski A.-S., Sygnet J.-F., Tauber J. A., Terenzi L., Toffolatti L., Tomasi M., Tristram M., Trombetti T., Tucci M., Tuovinen J., Turler M., Umana G., Valenziano L., Valiviita J., Van Tent B., Vielva P., Villa F., Wade L. A., Wandelt B. D., Wehus I. K., White M., White S. D. M., Wilkinson A., Yvon D., Zacchei A., Zonca A., 2015. *eprint arXiv:1502.01589*.

Planck Collaboration (XVI), 2014. *Astronomy & Astrophysics*, **571**, A16.

Pozzetti L., Bolzonella M., Zucca E., Zamorani G., Lilly S., Renzini A., Moresco M., Mignoli M., Cassata P., Tasca L., Lamareille F., Maier C., Meneux B., Halliday C., Oesch P., Vergani D., Caputi K., Kovač K., Cimatti A., Cucciati O., Iovino A., Peng Y., Carollo M., Contini T., Kneib J.-P., Le Fèvre O., Mainieri V., Scodeggio M., Bardelli S., Bongiorno A., Coppia G., de la Torre S., de Ravel L., Franzetti P., Garilli B., Kampczyk P., Knobel C., Le Borgne J.-F., Le Brun V., Pellò R., Perez Montero E., Ricciardelli E., Silverman J. D., Tanaka M., Tresse L., Abbas U., Bottini D., Cappi A., Guzzo L., Koekemoer A. M., Leauthaud A., Maccagni D., Marinoni C., McCracken H. J., Memeo P., Porciani C., Scaramella R., Scarlata C., Scoville N., 2010. *Astronomy & Astrophysics*, **523**, A13.

Riess A. G., Filippenko A. V., Challis P., Clocchiatti A., Diercks A., Garnavich P. M., Gilliland R. L., Hogan C. J., Jha S., Kirshner R. P., Leibundgut B., Phillips M. M., Reiss D., Schmidt B. P., Schommer R. A., Smith R. C., Spyromilio J., Stubbs C., Suntzeff N. B., Tonry J., 1998. *The Astronomical Journal*, **116**(3), 1009.



- Robotham A. S. G., Driver S. P., 2011. *Monthly Notices of the Royal Astronomical Society*, **413**(4), 2570.
- Robotham A., Driver S. P., Norberg P., Baldry I. K., Bamford S. P., Hopkins A. M., Liske J., Loveday J., Peacock J. A., Cameron E., Croom S. M., Doyle I. F., Frenk C. S., Hill D. T., Jones D. H., van Kampen E., Kelvin L. S., Kuijken K., Nichol R. C., Parkinson H. R., Popescu C. C., Prescott M., Sharp R. G., Sutherland W. J., Thomas D., Tuffs R. J., 2010. *Publications of the Astronomical Society of Australia*, **27**(01), 76.
- Rodriguez-Gomez V., Genel S., Vogelsberger M., Sijacki D., Pillepich A., Sales L. V., Torrey P., Snyder G., Nelson D., Springel V., Ma C.-P., Hernquist L., 2015. *Monthly Notices of the Royal Astronomical Society*, **449**(1), 49.
- Rodriguez-Gomez V., Pillepich A., Sales L. V., Genel S., Vogelsberger M., Zhu Q., Wellons S., Nelson D., Torrey P., Springel V., Ma C.-P., Hernquist L., 2016. *Monthly Notices of the Royal Astronomical Society*, **458**(3), 2371.
- Ruiz P., Trujillo I., Marmol-Queralto E., 2014. *Monthly Notices of the Royal Astronomical Society*, **442**(1), 347.
- Safranek-Shrader C., Montgomery M. H., Milosavljević M., Bromm V., 2016. *Monthly Notices of the Royal Astronomical Society*, **455**(3), 3288.
- Salim S., Rich R. M., Charlot S., Brinchmann J., Johnson B. D., Schiminovich D., Seibert M., Mallery R., Heckman T. M., Forster K., Friedman P. G., Martin D. C., Morrissey P., Neff S. G., Small T., Wyder T. K., Bianchi L., Donas J., Lee Y.-W., Madore B. F., Milliard B., Szalay A. S., Welsh B. Y., Yi S. K., 2007. *The Astrophysical Journal Supplement Series*, **173**(2), 267.
- Sanders D. B., Salvato M., Aussel H., Ilbert O., Scoville N., Surace J. A., Frayer D. T., Sheth K., Helou G., Brooke T., Bhattacharya B., Yan L., Kartaltepe J. S., Barnes J. E., Blain A. W., Calzetti D., Capak P., Carilli C., Carollo C. M., Comastri A., Daddi E., Ellis R. S., Elvis M., Fall S. M., Franceschini A., Giavalisco M., Hasinger G., Impey C., Koekemoer A., Le Fevre O., Lilly S., Liu M. C., McCracken H. J., Mobasher B., Renzini A., Rich M., Schinnerer E., Shopbell P. L., Taniguchi Y., Thompson D. J., Urry C. M., Williams J. P., 2007. *The Astrophysical Journal Supplement Series*, **172**(1), 86.
- Santini P., Fontana A., Grazian A., Salimbeni S., Fontanot F., Paris D., Boutsia K., Castellano M., Fiore F., Gallozzi S., Giallongo E., Koekemoer A. M., Menci N., Pentericci L., Somerville R. S., 2012. *Astronomy & Astrophysics*, **538**, A33.

- Schaye J., Crain R. A., Bower R. G., Furlong M., Schaller M., Theuns T., Dalla Vecchia C., Frenk C. S., McCarthy I. G., Helly J. C., Jenkins A., Rosas-Guevara Y. M., White S. D. M., Baes M., Booth C. M., Camps P., Navarro J. F., Qu Y., Rahmati A., Sawala T., Thomas P. A., Trayford J., 2015. *Monthly Notices of the Royal Astronomical Society*, **446**(1), 521.
- Schechter P., 1976. *The Astrophysical Journal*, **203**, 297.
- Scoville N., Aussel H., Brusa M., Capak P., Carollo C. M., Elvis M., Giavalisco M., Guzzo L., Hasinger G., Impey C., Kneib J., LeFevre O., Lilly S. J., Mobasher B., Renzini A., Rich R. M., Sanders D. B., Schinnerer E., Schminovich D., Shopbell P., Taniguchi Y., Tyson N. D., 2007. *The Astrophysical Journal Supplement Series*, **172**(1), 1.
- Sérsic J. L., 1963. *Boletín de la Asociación Argentina de Astronomía*, **6**(0).
- Somerville R. S., Lee K., Ferguson H. C., Gardner J. P., Moustakas L. A., Giavalisco M., 2004. *The Astrophysical Journal*, **600**(2), L171.
- Somerville R. S., Hopkins P. F., Cox T. J., Robertson B. E., Hernquist L., 2008. *Monthly Notices of the Royal Astronomical Society*, **391**(2), 481.
- Springel V., White S. D. M., Jenkins A., Frenk C. S., Yoshida N., Gao L., Navarro J., Thacker R., Croton D., Helly J., Peacock J. A., Cole S., Thomas P., Couchman H., Evrard A., Colberg J., Pearce F., 2005. *Nature*, **435**(7042), 629.
- Strateva I., Ivezić ., Knapp G. R., Narayanan V. K., Strauss M. A., Gunn J. E., Lupton R. H., Schlegel D., Bahcall N. A., Brinkmann J., Brunner R. J., Budavári T., Csabai I., Castander F. J., Doi M., Fukugita M., Györy Z., Hamabe M., Hennessy G., Ichikawa T., Kunszt P. Z., Lamb D. Q., McKay T. A., Okamura S., Racusin J., Sekiguchi M., Schneider D. P., Shimasaku K., York D., 2001. *The Astronomical Journal*, **122**(4), 1861.
- Tasca L. A. M., Le Fèvre O., López-Sanjuan C., Wang P.-W., Cassata P., Garilli B., Ilbert O., Le Brun V., Lemaux B. C., Maccagni D., Tresse L., Bardelli S., Contini T., Charlot S., Cucciati O., Fontana A., Giavalisco M., Kneib J.-P., Salvato M., Taniguchi Y., Vergani D., Zamorani G., Zucca E., 2014. *Astronomy & Astrophysics*, **565**, A10.
- Taylor E. N., Hopkins A. M., Baldry I. K., Brown M. J. I., Driver S. P., Kelvin L. S., Hill D. T., Robotham A. S. G., Bland-Hawthorn J., Jones D. H., Sharp R. G., Thomas D., Liske J., Loveday J., Norberg P., Peacock J. A., Bamford

- S. P., Brough S., Colless M., Cameron E., Conselice C. J., Croom S. M., Frenk C. S., Gunawardhana M., Kuijken K., Nichol R. C., Parkinson H. R., Phillipps S., Pimbblet K. A., Popescu C. C., Prescott M., Sutherland W. J., Tuffs R. J., van Kampen E., Wijesinghe D., 2011. *Monthly Notices of the Royal Astronomical Society*, **418(3)**, 1587.
- Taylor E. N., Hopkins A. M., Baldry I. K., Bland-Hawthorn J., Brown M. J. I., Colless M., Driver S., Norberg P., Robotham A. S. G., Alpaslan M., Brough S., Cluver M. E., Gunawardhana M., Kelvin L. S., Liske J., Conselice C. J., Croom S., Foster C., Jarrett T. H., Lara-Lopez M., Loveday J., 2015. *Monthly Notices of the Royal Astronomical Society*, **446(2)**, 2144.
- Toomre A., Toomre J., 1972. *The Astrophysical Journal*, **178**, 623.
- Torrey P., Wellons S., Machado F., Griffen B., Nelson D., Rodriguez-Gomez V., McKinnon R., Pillepich A., Ma C.-P., Vogelsberger M., Springel V., Hernquist L., 2015. *Monthly Notices of the Royal Astronomical Society*, **454(3)**, 2770.
- Trujillo I., Forster Schreiber N. M., Rudnick G., Barden M., Franx M., Rix H.-W., Caldwell J. A. R., McIntosh D. H., Toft S., Haussler B., Zirm A., van Dokkum P. G., Labbe I., Moorwood A., Rottgering H., van der Wel A., van der Werf P., van Starkenburg L., 2006. *The Astrophysical Journal*, **650(1)**, 18.
- Trujillo I., Conselice C. J., Bundy K., Cooper M. C., Eisenhardt P., Ellis R. S., 2007. *Monthly Notices of the Royal Astronomical Society*, **382(1)**, 109.
- Tully R. B., Fisher J. R., 1977. *Astronomy and Astrophysics*, vol. 54, no. 3, Feb. 1977, p. 661-673., **54**, 661.
- van der Wel A., Bell E. F., van den Bosch F. C., Gallazzi A., Rix H.-W., 2009. *The Astrophysical Journal*, **698(2)**, 1232.
- van der Wel A., Franx M., van Dokkum P. G., Skelton R. E., Momcheva I. G., Whitaker K. E., Brammer G. B., Bell E. F., Rix H.-W., Wuyts S., Ferguson H. C., Holden B. P., Barro G., Koekemoer A. M., Chang Y.-Y., McGrath E. J., Häussler B., Dekel A., Behroozi P., Fumagalli M., Leja J., Lundgren B. F., Maseda M. V., Nelson E. J., Wake D. A., Patel S. G., Labbé I., Faber S. M., Grogin N. A., Kocevski D. D., 2014. *The Astrophysical Journal*, **788(1)**, 28.
- van Dokkum P. G., Whitaker K. E., Brammer G., Franx M., Kriek M., Labbé I., Marchesini D., Quadri R., Bezanson R., Illingworth G. D., Muzzin A., Rudnick G., Tal T., Wake D., 2010. *The Astrophysical Journal*, **709(2)**, 1018.

- Vogelsberger M., Genel S., Springel V., Torrey P., Sijacki D., Xu D., Snyder G., Nelson D., Hernquist L., 2014a. *Monthly Notices of the Royal Astronomical Society*, **444**(2), 1518.
- Vogelsberger M., Genel S., Springel V., Torrey P., Sijacki D., Xu D., Snyder G., Bird S., Nelson D., Hernquist L., 2014b. *Nature*, **509**(7499), 177.
- Wake D. A., van Dokkum P. G., Franx M., 2012. *The Astrophysical Journal*, **751**(2), L44.
- White S. D. M., Frenk C. S., 1991. *The Astrophysical Journal*, **379**, 52.
- Williams R. J., Quadri R. F., Franx M., van Dokkum P., Labbé I., 2009. *The Astrophysical Journal*, **691**(2), 1879.
- Williams R. J., Quadri R. F., Franx M., 2011. *The Astrophysical Journal*, **738**(2), L25.
- Xu C. K., Zhao Y., Scoville N., Capak P., Drory N., Gao Y., 2012. *The Astrophysical Journal*, **747**(2), 85.
- Zepf S. E., Koo D. C., 1989. *The Astrophysical Journal*, **337**, 34.
- Zwicky F., 1933. *Helvetica Physica Acta*, Vol. 6, p. 110-127, **6**, 110.